University of Southampton

Studies of measurement techniques for indirect chemical sensing based on fluorescence spectroscopy and applications for fibre-optic sensors

Edward Alfred Denzil Austin

A thesis submitted for the degree of PhD

Faculty of Engineering and Applied Science
Department of Electronics and Computer Science
Optoelectronics Research Centre

September 2002

UNIVERSITY OF SOUTHAMPTON

ABSTRACT

FACULTY OF ENGINEERING AND APPLIED SCIENCE

Optoelectronics Research Centre

Doctor of Philosophy

Studies of measurement techniques for indirect chemical sensing based on fluorescence spectroscopy and applications for fibre-optic sensors

By Edward Alfred Denzil Austin

This thesis describes experimental and theoretical studies of interrogation systems for determining fluorescent decays of order a few microseconds. The studies have enabled optimised design of interrogators for sensing oxygen using a fluorescent polymer-encapsulated ruthenium complex. Two basic interrogation methods were explored, using blue LED excitation.

The Rapid Lifetime Detection (RLD) scheme, a fluorescence interrogation method based on direct interrogation of the decay curve following pulsed excitation was generalised, and a novel method for optimising measurement precision derived. The effect of background light on the optimum was quantified. Dissolved (aqueous) oxygen concentration was measured to a precision of 1 part per billion using a 1 second response time (the peak fluorescence power was only 12.5±0.5pW).

A second interrogation method, where the phase delay between an intensity modulated excitation source and the resultant fluorescence is processed to make measurements, was for the first time, fully analysed for measurement of exponential decays. When measuring fluorescence lifetimes in the range 2.9-3.3μs, a precision of 2.3×10^{-10} s $Hz^{-0.5}$ was achieved. (The peak fluorescence power was 500±25pW).

A novel combination of ruby optical temperature sensor insert and oxygen sensing layer was demonstrated as a simultaneous temperature and oxygen sensor.

A new fluorescence calibration standard consisting of thermally stabilised titanium-doped-sapphire sample was constructed to calibrate and test the indicators.

This work was sponsored by a BRITE EuRam European project, which helped determine the priorities of the research.

CONTENTS

CONTENTS **3**

ACKNOWLEDGEMENTS **9**

PUBLICATIONS LIST **10**

1 INTRODUCTION **11**

1.1 Background to this Research **11**

1.2 Introduction **12**

1.3 Outline of Indirect sensing using fluorescent indicators **12**

1.4 Dissolved Oxygen Sensing **14**

1.4.1 Traditional, non-optical dissolved oxygen sensing 15

1.4.2 Optical oxygen sensing 17

1.4.3 State of the Art Optical Oxygen Sensing Research. 18

1.4.4 Note on Measurement Units 21

1.5 Research work presented **21**

1.5.1 Sensing Schemes 24

1.6 References for Chapter 1 ..... **27**

2 CHARACTERISTICS OF FLUORESCENT INDICATORS **31**

2.1 Introduction **31**

2.2 Oxygen sensitive optical chemical indicators **32**

2.2.1 Indicator Chemistry 33

2.2.2 Encapsulation of the dye 34
2.2.3 Chosen Fluorescent Oxygen Indicator 35
2.2.4 Stern-Volmer formulas 35
2.2.5 Multi-site or 'two site' model 39
2.2.6 Log Gaussian distributions in κ and τ model 41
2.3 Fluorescence of Ti-doped-sapphire crystal – a calibration aid 44
2.3.1 The Ti:sapphire calibration reference probe. 45
2.4 Conclusions from chapter 2 48
2.5 References for chapter 2 50
3 OPTICAL ARRANGEMENT FOR THE INTERROGATION OF FLUORESCENT INDICATORS 53
3.1 Introduction 53
3.2 Excitation source 54
3.3 Coupling to the Indicator 56
3.3.1 General Aspects 56
3.3.2 The preferred coupling system 58
3.4 Fluorescence Detector 60
3.5 Optical Filtering 60
3.5.1 Optimal filter identification 62
3.5.2 Excitation source filter 63
3.5.3 Dichroic beam-splitter 64
3.5.4 Detection filter 65
3.5.5 Rejection of Filters 66
3.6 Excitation Light level and fluorescence produced 67
3.6.1 Delay-monitoring modulated source interrogator 67

3.6.2 Direct fluorescence decay curve interrogator 68

3.7 Precautions to Ensure Adequate Sensor Stability 69

3.7.1 Time response of the excitation source 69

3.7.2 Minimisation of unwanted background fluorescence 71

3.7.3 Thermal dependence of optical components 72

3.8 Conclusions from chapter 3 76

3.9 References for chapter 3 77

4 FLUORESCENCE INTERROGATION BY DIRECT ANALYSIS OF THE DECAY CURVE 78

4.1 Introduction 78

4.1.1 Direct fluorescence decay curve interrogation compared with modulated-excitation source sensing schemes. 79

4.2 Single photon detectors 80

4.2.1 The Photomultiplier Tube 80

4.2.2 The APD detector 82

4.2.3 The chosen detector 83

4.3 Optimised Direct Decay Curve Interrogation by Extended Rapid Lifetime Detection (RLD) 83

4.3.2 Interrogation System Design Outline 85

4.3.3 Sensing Scheme Model – Exponential Fluorescence Decay 86

4.3.4 Zero-bass line (background-less) situation 87

4.3.5 The effect of constant background light 95

4.3.6 The effect of unwanted background fluorescence decays 98

4.3.7 Sensing Scheme Model – Oxygen Indicator Fluorescent Decay 101

4.4 Confirmation of RLD model by comparison with Experimental results 104

4.4.1 Simulated RLD sensor using ‘Noise Generator’ 105

4.4.2 Laboratory bench tests 105
4.4.3 Verification of model by comparison at multiple setup vectors 108
4.4.4 Results 110
4.5 Real time wide range dissolved oxygen sensor measurements 112
4.5.1 Oxygenation Rig 112
4.5.2 Experimental results 114
4.6 Conclusions from chapter 4 116
4.7 References for chapter 4 118
5 FLUORESCENCE INTERROGATION BY MONITORING THE MEASURED DELAY RELATIVE TO AN INTENSITY MODULATED EXCITATION SOURCE 120
5.1 Introduction 120
5.2 Sensing Scheme 121
5.3 The measured phase-delay (idealised interrogation system) 122
5.3.1 Sinusoidal excitation modulation 122
5.3.2 Square wave modulation 123
5.4 Interrogation hardware 125
5.5 Optical detection preamplifier requirements 126
5.6 Expected progression of waveforms through the interrogation instrument and expected detected values 130
5.6.1 Simulation of section (a) and section (b) 131
5.6.2 Predicted progression of waveforms 134
5.7 Response of modulated source interrogation systems to exponential lifetime 139
5.8 Optimal detection of exponential fluorescence indicators 141

5.8.1 Contributions to noise in measurements 141

5.8.2 Identifying the optimal excitation modulation frequency 145

5.8.3 Optimal measurement assuming sin-shaped excitation modulation 146

5.9 Experimental measurements 148

5.10 Conclusions from chapter 5 150

5.11 References for chapter 5 152

6 COMBINED OXYGEN AND TEMPERATURE MEASUREMENT 153

6.1 Introduction 153

6.2 Dual oxygen and temperature sensing schemes 156

6.2.1 Combined optical temperature and oxygen measurement probe. 157

6.2.2 Dual temperature and oxygen sensing using modulated excitation source. . 157

6.2.3 Extended Rapid Lifetime Detection Sensing Scheme for Dual Temperature and Oxygen Measurement 162

6.3 Proof of principle – First Simultaneous, real-time, temperature and dissolved oxygen measurements 163

6.4 Conclusions from chapter 6 164

6.5 References for chapter 6 166

7 CONCLUSIONS AND FURTHER WORK 167

7.1 Background 167

7.2 Direct decay-curve analysis by enhanced Rapid Lifetime Detection (RLD) . 168

7.2.1 Possible further studies of the RLD sensing scheme. 169

7.3 Fluorescence Interrogation by Monitoring the Delay Relative to an Intensity Modulated Excitation Source 170

7.3.1 Further Studies of the modulated source interrogator 171

7.4 Optical Temperature Compensation in Fluorescence Interrogation systems 172

7.4.1 Further Work to improve the dual measurement system 172

7.5 Ongoing New Work 173

7.5.1 Ageing of optical oxygen sensors 173

7.5.2 Measurement of pH using alternative fluorescent indicators 176

7.6 References for chapter 7 179

8 APPENDIX 180

8.1 First measurements with anti-fouling coated membranes 180

8.1.1 Procedure 180

8.1.2 Results 181

8.1.3 Conclusions 182

8.2 Fluorescence interrogation by direct decay curve analysis technical description 183

8.2.1 Circuit description 183

8.2.2 Circuit diagrams 187

8.2.3 Software description 190

8.3 Phase-delay resolving fluorometer design detail 191

8.4 Optimisation of exponential measurements using the RLD method – Mathcad sheet 194

8.5 Published Papers 199

ACKNOWLEDGEMENTS

First of all, I'd like to thank John Dakin for giving me the chance to be involved with this project in the first place, his constant stream of ideas, and his jokes, which have often inspired me to return to the laboratory. Everyone involved with the BOSS programme also deserves thanks for putting up with my questions and making my work stays abroad so enjoyable. Thanks is also deserved by all the people who have worked directly with me on this project over the years; Andy, Jianhua, Carsten, Jo, Jane, John, Steve and Lisa.

Many friends inside and outside the ORC have supplied time, selfless advice, and absorbent shoulders whenever I have needed them; Toby, Beckett, Ali, Nic, Deb, Corin, Sally, Mark and all the rest of you – thanks a lot. Stu deserves special thanks for always having time for heated technical arguments, and for his helpful criticism of this thesis. Anna's invaluable contribution deserves wine. Instead, thanks.

My family, for as long as I can remember, have encouraged, forced, and blackmailed me into trying my best. This is exactly what I have needed – thank you.

PUBLICATIONS LIST

1. Austin, E., Dakin, J. and Strong, A. *Design of a photon-counting interrogation unit for monitoring Ru2+ Oxygen sensors*. in *EUROPT(R)ODE V* 16-19 April 2000 Lyon, France, P82,

2. Austin, E., Dakin, J. and Strong, A.P. *Use of transition-metal-doped sapphire crystals to calibrate and thermally compensate fluorescent-lifetime chemical detectors (keynote communication)*. in *EUROPT(R)ODE V* 16-19 April 2000 Lyon, France, KC9,

3. Austin, E. and Dakin, J. *Simultaneous sensing of dissolved oxygen and probe-tip temperature, using a ruby insert and compact photon counting receiver (postdeadline paper)*. in *Optical Fibre Sensors 13* 11-13 October 2000 Venice, Italy,

4. Austin, E. and Dakin, J. *Recent measurements with Ru2+ oxygen sensors, using doped sapphire crystals, both as a calibration aid and an integral temperature sensor (invited paper)*. in *SPIE: Fiber Optic Sensor Technology II* 5-8 November 2000 Boston, USA: SPIE, 4204A-44, 1-10

5. Austin, E.A.D. and Dakin, J.P. *Opto-electronic systems for addressing Ru oxygen sensors:their design optimization and calibration process (invited)*. in *SPIE: Fiber Optic Sensor Technology and Applications* 28 October - 2 November 2001 Boston,USA, 4578-06,

6. Austin, E., Dakin, J., Lobnik, A. and Uray, G. *Interrogation of optical pH sensor based on sol-gel doped new luminexcent europium chelate with compact photon counting system*. in *EUROPT(R)ODE VI* 7-10 April 2002 Manchester, UK, P15,

1 INTRODUCTION

1.1 Background to this Research

This thesis describes work funded by the Brite-Euram research project [1], Bio-compatible Optical Sensor Systems (BOSS). BOSS was an investigative programme conducted by a consortium of eight Europe-wide research and industrial partners. The project demonstrated the possibility of using biocompatible, anti-fouling coatings to enhance optical sensors. Reducing the build up of surface fouling on optical surfaces makes optical sensors more suitable for use in water monitoring, medical diagnostics, and bioreactor process control applications. In particular, the programme investigated adding the coating to fluorescent indicator membranes, which are commonly used for optical chemical sensing. The BOSS collaboration was completed in February 2001.

During the first two and half years of work, this research was constrained by the requirements of its funding programme, which were to rapidly construct interrogation units to monitor the fluorescent indicators, and thereby, for the first time, make measurements on anti-fouling coated indicators (see appendix). Fluorescent indicators for sensing dissolved oxygen concentration were used. Studying the chemistry necessary to synthesise the fluorescent indicators, and providing the facilities and testing to determine the performance of the anti-fouling coatings, were the responsibilities of the other partners, so in depth details of these are beyond the scope of this thesis.

To interrogate the indicators, time domain processing of the fluorescence signal was chosen, thus avoiding any intensity related problems, which will be discussed later. Two basic sensing schemes were used (again, these are described in detail later), firstly direct monitoring of the fluorescent decay curve following pulsed excitation, and secondly monitoring the phase delay between modulated excitation source and the resultant fluorescence. Instrumentation was constructed using both these methods, which involved significant research to minimise intrinsic error sources. The novel use of crystal inserts to add thermal compensation to oxygen measurements and to calibrate the instruments, using a simulated ‘ideal’ stable probe was also explored during this period.

During the final year of research, freed from the constraints of the BOSS programme, efforts have been focussed on greatly enhancing this sensing instrumentation, by developing new optimisation methods for the sensing algorithms used. The majority of this thesis describes this later study. The inclusion of anti-fouling coatings on the fluorescent indicators was not required for this, more general work.

1.2 Introduction

A sensor is required in environmental, medical, scientific and industrial process monitoring applications whenever monitoring of a physical parameter (or measurand) is required. In particular, chemical sensors are often used for the measurement of a wide variety of chemical compounds, radicals and ions present within gaseous or liquid test samples.

Often sensing tasks have been accomplished by exploiting a convenient mechanical phenomenon (for example, the mercury thermometer or the spring balance for weight measurements). For chemical sensing, electrochemical methods have often been used, which function by monitoring the interrelation between an electrical circuit and a chemical reaction. Alternative methods based on optical sensing have been the subject of intensive research since initial investigations in the late 1970s. There now exist optical probes for determining many parameters, such as temperature, pressure, pH, strain, oxygen concentration and others. Besides providing alternatives to traditional sensors, optical methods have allowed hitherto impossible or impractical sensing applications to be explored, for example, two dimensional oxygen flux imaging [2] (which will be described later).

Optical chemical sensing methods fall into two main groups; those that function by direct spectroscopy of the analyte (for example, sensing of Raman scattering, absorption changes or fluorescence from the analyte itself), and those that sense the measurand indirectly by monitoring the state of a suitable indicator, which itself is sensitive to the analyte. This latter method is considered here.

Optical chemical sensing has been revolutionised by the advent of optical fibres, which have allowed interrogation of the analyte or indicator remotely via a connecting lead. This has the advantage that the sensor head itself can usually be a low-cost passive device, alleviating the problems and cost associated with active electronic versions.

1.3 Outline of Indirect sensing using fluorescent indicators

Fluorescence occurs when a chemical species or material emits radiation (usually light) as a result of appropriate excitation. As will be seen, fluorescence can often be strongly affected by the prevailing environment, so the fluorescence from a chemical species or material can be monitored for indirect sensing. This sensing approach is shown schematically in Figure 1.1, where changes in the fluorescence of a suitable indicator are

monitored via an optical fibre connecting lead. The changes are monitored by appropriate instrumentation, which then provides a measure of the state of an analyte.

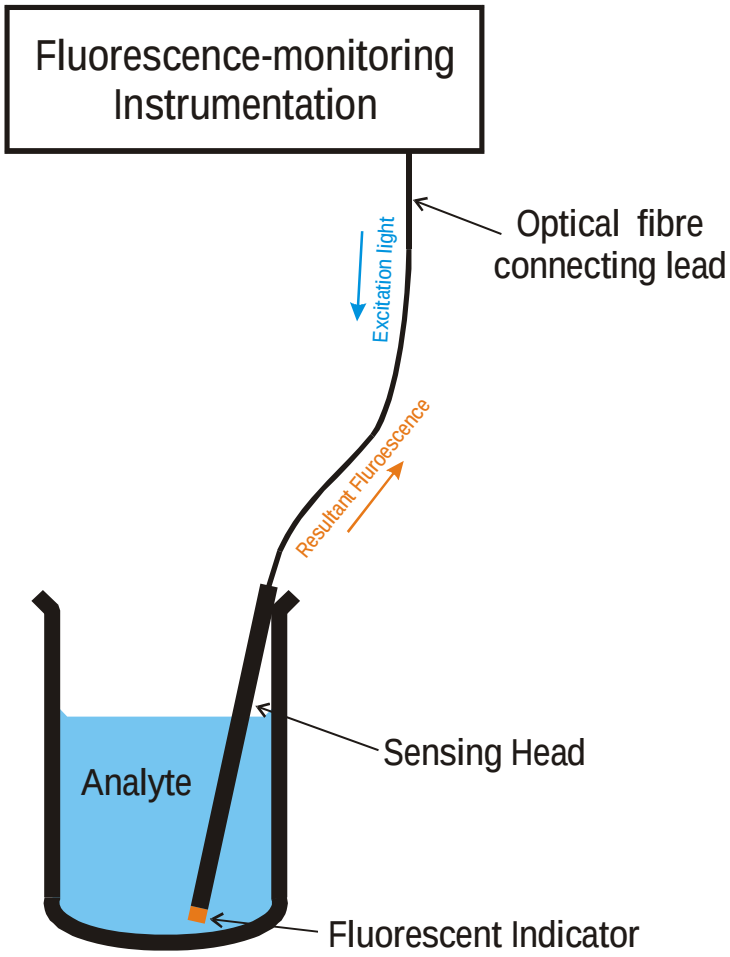

Figure 1.1 Indirect chemical sensing by monitoring the fluorescence of a suitable indicator

Indirect fluorescence sensors have been developed for many sensing areas, some of these are listed below.

Measurement of both molecular and dissolved oxygen concentration is one such example area. Molecular oxygen monitoring is used for sensing biological oxygen demand [3], in clinical applications (e.g. blood gas analysis, [4]), and for combustion analysis [5], whilst dissolved oxygen sensing is necessary in many other areas, which will discussed later. For most of these applications, the Clark oxygen sensor, an electrochemical probe based on amperometric interrogation of the oxygen flux through a membrane, first suggested in 1959 [6], is still most widely used. (The Clark cell design will be discussed in more detail later). As will be seen, there now exist optical alternatives, which have several compelling benefits, such as easy miniaturisation probe tip (sensing probe tips with OD 500µm, FOXY-AL300, are commercially available) and, unlike Clark cells, lack of oxygen consumption.

Another important measurement parameter to be interrogated using fluorescent indicator is pH. Accurate, continuous, and rapid measurement of pH is vital both for industrial process control and for scientific measurement in chemistry, medicine and biology. The traditional electrochemical 'glass electrode' pH sensor has for decades been a popular choice for continuous measurements, but susceptibility to electrical interference, corrosion of electrical leads and the presence of an electrical current flow through the monitored solution all adversely affect the precision of measurements. Research is continuing into the development of optical alternatives for physiological measurements, functioning via monitoring the colour change of a pH indicator [7] and energy transfer to a pH sensing dye [8], as well as by monitoring the fluorescence of an indicator layer [9].

Temperature is often measured by mechanical designs based on the thermal expansion of mercury or by electrical alternatives such as the thermocouple or thermistor, but many optical sensors, some based on fluorescence interrogation, also exist. The most useful of these, for remote measurements, are optical fibre based. The thermal sensor is then either extrinsic, where a temperature indicator (e.g. fluorescent crystal) is attached to the end of a connecting fibre, or intrinsic, where the sensing mechanism is included within the fibre itself, perhaps exploiting thermally dependent optical scattering within the fibre [10] or by interrogating Bragg grating structures imprinted inside the fibre [11]. Other proposed optical systems have employed optical interrogation of mechanical phenomena, for example by measuring thermally induced fluctuations in the reflections from a suitable surface[12].

As stated above, this work is primarily focussed towards measurement of dissolved oxygen, so this area is now discussed in greater detail.

1.4 Dissolved Oxygen Sensing

Measurement of Dissolved Oxygen (DO) is hugely important in many industrial, social and clinical applications.

The concentration of DO in natural water is, of course, of prime importance to the health of flora and fauna existing within. It is related to the delicate equilibrium between biochemical depletion and continued re-oxygenation, because organisms living within the water consume oxygen, whilst aeration and photosynthesis replaces it. DO concentration measurements have been an indispensable indication of the state of this equilibrium, as photosynthesis dominance can be diagnosed by correlations between variations in DO and

prevailing light level, whilst falling DO concentration can indicate deterioration in organism activity, perhaps due to increased pollution.

Industrial control of sewage treatment plants is another area where knowledge of the DO concentration is essential, because a balance between minimising the costly use of artificial aeration, and providing adequate oxygen to fuel bacterial treatment of the waste must be maintained. Accurate, continuous measurement of DO, at every stage in the treatment process is therefore vital to achieving efficient operation.

DO is used for transportation of oxygen within animals, usually in blood, so knowledge of the distribution of DO can help diagnose problems and enhance physiological understanding. Instruments have been designed for *in vivo* DO measurement, interrogation of extracted blood samples, and measurement of DO within the heart and other organs. Interrogation of oxygen consumption by cells and tissues is also used when studying tumour development.

DO measurements are also important in food and drug preparation applications. In food, high DO concentration can lead to oxidisation or degradation of quality, so measurement of this parameter is necessary to find methods for minimising this. DO concentration must also be regulated for efficient fermentation, fruit ripening, meat curing and drug preparation.

DO sensors are required for all these applications, so new designs and improvements have been the subject of continued research interest. In the following sections, first traditional, non-optical oxygen sensors are discussed, then optical alternatives described.

1.4.1 Traditional, non-optical dissolved oxygen sensing

Since his U.S. Patent in 1959 [6], Clark's electrochemical membrane covered electrode oxygen probe has dominated DO sensing. The operating theory behind the Clark sensor is covered in detail in many texts (see, for example [13]), so only a brief explanation will be given here.

Figure 1.2 shows a schematic representation of the basic cell, where a thin polyethylene membrane separates the sensor components from the analyte solution. An electrolyte solution, encapsulated by the membrane is held in contact with anode and cathode electrodes. Oxygen diffuses through the membrane into the electrolyte. The cathode is held at sufficient negative potential with respect to the anode to ensure electrochemical reduction of all the dissolved oxygen at the cathode surface (by (1.1)), so that the oxygen

flux flowing past the membrane is proportional to the oxygen concentration within the analyte at the probe surface. The resultant current flowing between the electrodes is governed by the rate of oxygen reduction at the cathode, and therefore an indication of the O_2 concentration in the analyte. The Clark cell is therefore an 'amperometric' sensor.

The Clark cell has the considerable disadvantage of consuming all the oxygen that is reduced at the cathode and therefore altering the measured oxygen concentration simply by measuring it. This is particularly troublesome for trace oxygen concentration measurements or where O_2 transport by diffusion or fluid movement is restricted, (e.g. in viscous fluids or thick sewage).

$$O_2 + 2H_2O + 4e^- \rightarrow 4OH^-$$

(1.1)

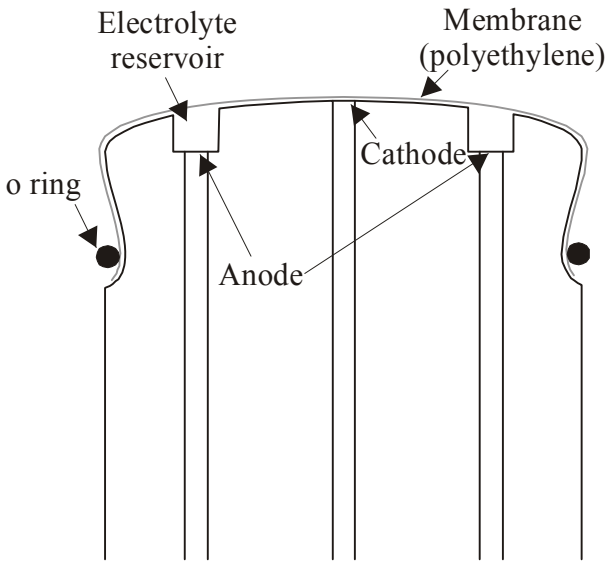

Figure 1.2 Clark's electrochemical oxygen sensor

Clark cell type oxygen sensors are available from many manufacturers. For reference, the published specification of one typical example, the YSI model 58, is shown in Table 1.

Sensing Range	0.0 to 20.0 mg l^{-1}
Accuracy	±0.3%,
Resolution	0.1% or 0.01mg l^{-1}, whichever is greater

Table 1 Published performance of the YSI model 58, a typical Clark cell oxygen sensor

Research to enhance electrochemical oxygen sensors has lead to continued development of new methods, some of which have been commercialised, such as the fast response oxygen sensor based on a miniaturised Clark cell [14] or the Zirconia oxygen sensor [15],

and other amperometric sensors [16], [17]. Work has been published based on further miniaturisation and integration of the Clark cell by employing a screen printing method [18]. Many gaseous phase O_2 sensors have also been developed for specific applications (e.g. automobile engine exhaust gas analysis), where environmental extremes (heat etc.) render the optical alternatives discussed below impractical [19], [20].

Interest in potentiometric electrochemical sensors for oxygen sensing where no current flows between the electrodes (and hence no oxygen is consumed), is evident in the literature. One example incorporating an E-MOSFET was described in [21].

Electrochemical oxygen sensors, though simple in concept and well-established in the market place, hold significant disadvantages when compared with optical alternatives.

1.4.2 Optical oxygen sensing

Optical oxygen sensing has received significant scientific attention over the last three decades, due to the advantages it holds over traditional electrochemical methods. It is only in the last 10 years that it has become a commercial competitor to electrochemical alternatives, finding market share in many clinical and environmental monitoring applications and allowing development of previously impractical or impossible sensors (this will be discussed later). Work on bulk optical detection systems (e.g. [22] 1995, [23] 1996), has lead to much more useful remote sensors, incorporating optical fibres, e.g.[24] (1996), or [25] (1998).

The attractive features normally associated with optical oxygen sensing are:-

No O_2 consumption in the sensing process. Amperometric measurement systems such as the Clark cell consume oxygen during the sensing process, reducing the level of oxygen dissolved in the analyte. This makes Clark cell sensors unsuitable for on-line measurements in many biological and trace gas measurement applications. Optical oxygen sensors do not consume oxygen.

No requirement for electrodes or electrolyte. *I*nterrogation of the indicator is purely optical.

No dependence on sample flow rate or stirring speed. Because Clark sensors consume and sense oxygen through an oxygen permeable membrane, the speed of analyte flow next to the membrane affects the oxygen level measured. An oxygen indicator rapidly reaches equilibrium with the analyte, requiring only a small quantity of oxygen to diffuse through

it, so stirring speed does not effect the levels measured (though of course, the time taken to reach the measured value is improved with agitation).

Immunity to electromagnetic interference. As connection to the remote sensing cell is made with optical fibre, there is no possibility of electromagnetic interference with sensor readings, if the interrogation equipment is well screened.

Low cost and easy replacement of passive probe head. This advantage makes the sensors particularly useful for multi-point measurement with multiplexing (polling) via optical fibre switches.

Good immunity to shock and high external pressure. In many Clark cell based designs a pressure equalisation system is necessary to equalise the pressure across the delicate membrane. This is not required for optical alternatives. Also the solid state indicator cannot be damaged so easily by shock.

Fibre-coupled remote probe allows monitoring in remote, hazardous or *in vivo* applications

Enhanced selectivity. Unlike micro-electro-chemical sensors, they are not influenced by Ca^{2+} and Mg^{2+}.

Micro-gravity operation Without electrolyte, operation in space or micro-gravity conditions is possible.

1.4.3 State of the Art Optical Oxygen Sensing Research.

Optical oxygen sensing is a growing research area. The state of the art is perhaps best defined by considering the new specialist sensors developed for previously impossible or impractical applications.

New oxygen sensors for clinical applications is one such area. For gaseous-phase measurement, sensors designed with fast enough response for real-time interrogation of human respiration have been investigated. In 1997 Kolle *et. al.*[26] published a study of sensor systems offering a t_{90} (time taken to achieve 90% of the full-scale response) of better then 100ms for respiration measurement. They concluded a platinum (II) - octaethylporphyrin – ketone indicator could be used to construct a rapid response oxygen sensor for breathe gas analysis with a t_{90} of 20ms.

Real-time oxygen concentration and flux 2-D imaging systems are becoming commonplace following work by Harmann *et. al.* in 1996 [27], where the fluorescence of

an indicator was interrogated by a gated CCD camera. This technique allowed quantitative imaging of oxygen flux or distribution at, or flowing through, a surface, and is of interest in engineering and medical applications (e.g. by measuring the oxygen flux through human skin).

Oxygen sensors for oceanographic applications must provide reliable measurements over extended time periods without recalibration. Most off-shore sensors cannot realistically be visited more than twice in a month due to the prohibitive cost and effort involved with retrieving the sensor. Membrane covered sensors, such as the Clark cell, rely on the fact that the oxygen flow rate through the membrane is proportional to the prevailing oxygen concentration, so fluctuations in the diffusion characteristics of the membrane, caused either by bio-fouling or thermal changes require - re-calibration. Optical sensors are now being developed for this purpose. In 1997 Gouin [28] *et. al.* published work describing an optical surveillance sensor to monitor pollution in coastal water. Based on monitoring the luminescence lifetime of an oxygen indicator (in this case a complex of ruthenium), they found the sensor to be adequate for this purpose, as it had no dependence on water salinity (a known problem for Clark cells) and only 10% dependence on hydrostatic pressure over a range 0-200 bar, (compensation of hydrostatic pressure is required for Clark cells). By 1999, a review report [29] explained that optical oxygen sensing for oceanographic applications had been developed into remote fibre-based designs with up to 50 detection channels and a lower Limit Of Detection (LOD) of 3 parts per billion (ppb). For improved bio-fouling, resistance, anti-fouling coated sensors have been developed as part of the BOSS programme. (Some first measurements from these are given in the appendix).

Another interesting new application involves the incorporation of optical oxygen indicators within paint to form Pressure-Sensitive Paints (PSPs) [30] for aerodynamic structure testing. The operating principle is shown in Figure 1.3, where the test structure (e.g. an aerofoil) is coated with an oxygen permeable paint, which includes an oxygen indicator. In this way, the air pressure at the paint surface is correlated with the oxygen partial-pressure presented to the indicator, so, by interrogating the observed fluorescence with a camera, pressure variations at the surface may be inferred. Using a CCD camera for this allows real-time pictorial representation of the pressure distribution across the aerofoil.

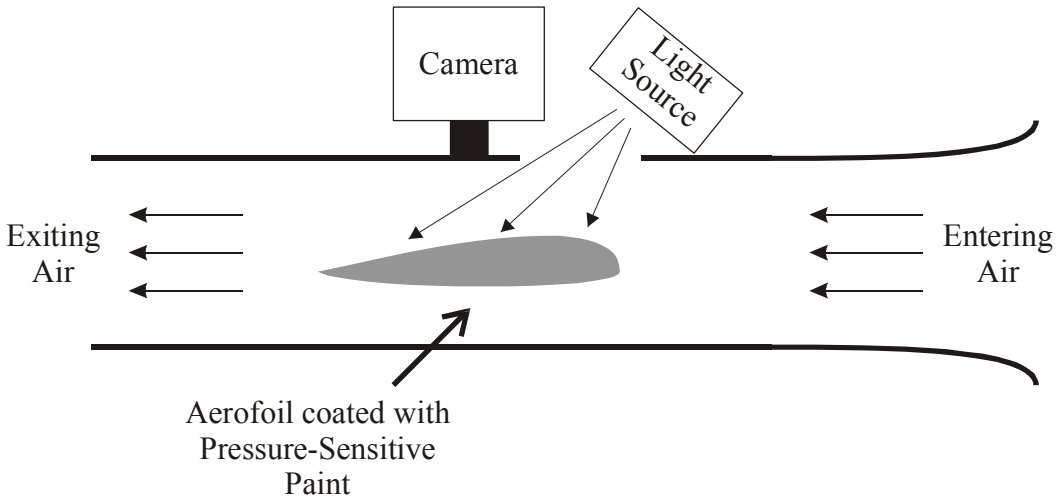

Figure 1.3 Wind tunnel tests of an aerofoil by coating with Pressure-Sensitive Paint.

1.4.3.1 State of the Art Commercial Optical Oxygen Sensors

For sensors at least, evidence of the development of research studies into commercial products is generally a good indication of a thriving area. To date, one probe-based commercial optical oxygen sensor is slowly gaining market share from traditional electrochemical counterparts - the FOXY (Fibre Optic Oxygen Sensor) [31], which has been available since 1998.

	YSI model 58	**FOXY optical probe**
Sensing Range	0.0 to 20.0 mg l^{-1}	0 to 40.7ppm
Accuracy	±0.3%,	0.1% (for 0-1.7ppm)
Resolution	0.1% or 0.01mg l^{-1}, whichever is greater	0.003 ppm at 0 ppm, rising to 0.02 ppm at 8.5 ppm

Table 2 Performance of YSI model 58 (electrochemical Clark cell), and FOXY optical dissolved oxygen sensors (ppm and mg l^{-1} units are essentially identical, see below). The optical alternative out-performs the traditional sensor in all parameters other than accuracy. The accuracy of the FOXY probe could probably be improved by monitoring fluorescence lifetime rather than intensity.

The performance of the FOXY optical and YSI electrochemical probes is compared in Table 2. The FOXY sensor has wider dynamic range and can make better resolution measurements, but has slightly inferior accuracy. (Accuracy could probably be improved by measuring fluorescence lifetime rather than intensity.)

Other optical sensors, e.g. [32], are currently in the research and development phase.

1.4.4 Note on Measurement Units

Measurement units used for sensing dissolved oxygen are sometimes confusing, so these are discussed separately here.

Dissolved oxygen is perhaps best measured in units of mg l^{-1} which is, to a high degree of accuracy, equal to oxygen concentration measured in ppm (because water has practically unit density at laboratory temperatures). At 760 torr ambient pressure, and 25°C, the concentration of oxygen present in a water sample in equilibrium with water-saturated air is 8.2 mg l^{-1}. DO is also sometimes measured as a 'percentage of air-saturated' value, and given the symbol [O_2]. This is perhaps a misleading practice, as the symbol does not emphasise that this is a proportion of **air**-saturated value.

1.5 Research work presented

The aim of the current work in this thesis was to devise, using work initiated during the BOSS programme, and continued since, methods to enhance the precision, response time and stability of measurements made by interrogation of fluorescence. For oxygen sensors this would increase the attractiveness of the optical alternative by improving present performance. Enhanced sensing could also lead to the development of new application areas, such as optical sensing of trace oxygen concentrations, which is presently only a research topic [33].

To achieve this, fluorescence interrogation instrumentation, designed and constructed for testing the anti-fouling-coated membranes used in the BOSS programme, was used to investigate and improve present measurement techniques. The hardware was constructed in a small benchtop 250x340x70mm enclosure (pictured, with sensing probe in Figure 1.4).

Figure 1.4 A prototype fluorescence interrogation instrument, with probe. The compact instrument measures 250x340x70mm

This thesis considers, in the following chapters, methods for enhancing or optimising each operational section within the instrument. Figure 1.5 shows schematically how these operational sections combine to make measurements, and the chapters that describe each of them.

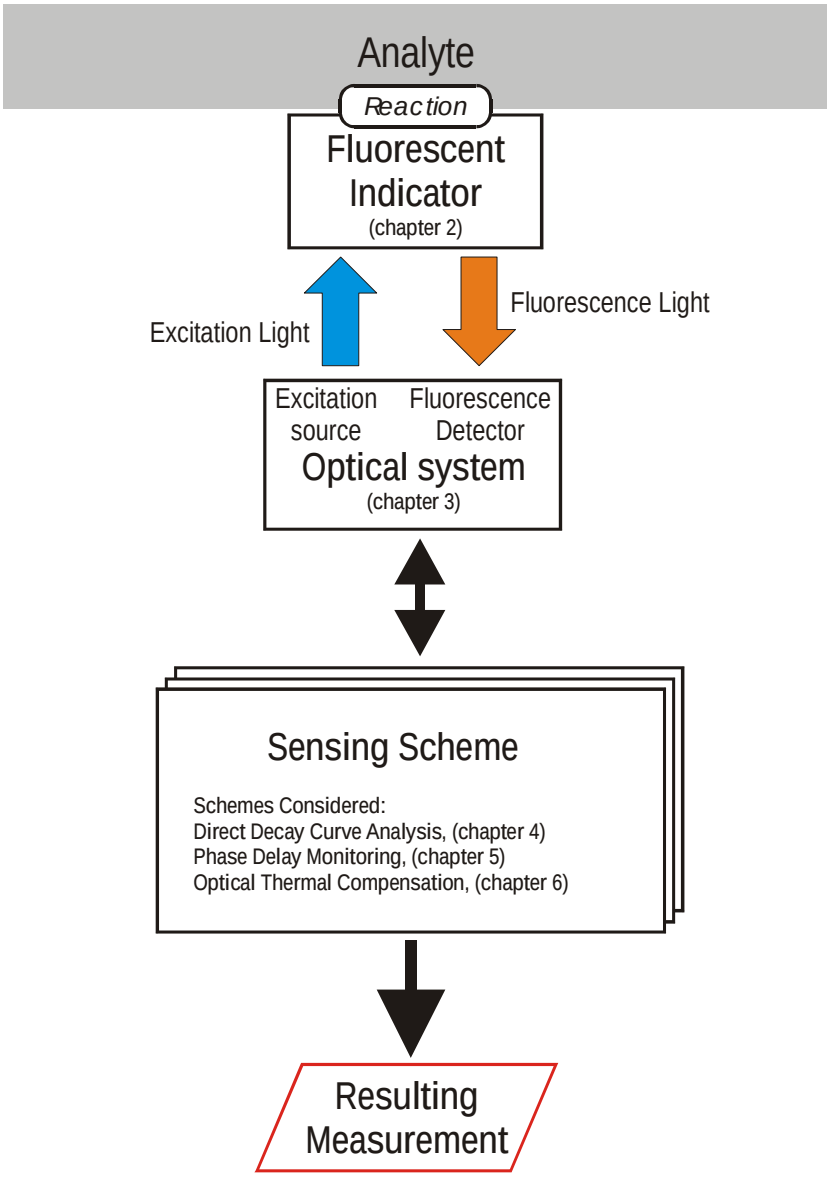

Figure 1.5 Schematic of operational elements for indirect sensing by interrogation of a fluorescent indicator. An indicator with measurand-dependent fluorescence is required (discussed in chapter 2). An optical system produces suitable excitation light and detects the resulting fluorescence (chapter 3). A 'sensing scheme', which dictates the excitation source drive signal, and decodes the measurand level from the detected fluorescence is chosen. Sensing schemes, and their enhancement and optimisation (which forms the main focus of this work) are discussed in chapters 4, 5 and 6. The resulting measurement is thereby attained.

First, a suitable fluorescent indicator is required. The material and its chemical composition would be chosen or engineered to have fluorescence characteristics dependent upon the measurand desired. The ultimate performance of the sensor is limited by the properties of the fluorescent indicator, so intensive effort has been devoted, by other BOSS partners, and by research groups around the world, to improving and developing these. Further study was therefore not attempted here, as greater gains in sensor performance were expected by focussing on other, less well-researched areas.

Fluorescent indicators, and particularly their fluorescence response will be fully described and characterised in chapter 2. Indicators for measuring dissolved oxygen, and a novel exponential fluorescence calibration standard using a titanium-doped-sapphire crystal will be described. This calibrator is one of the major novel contributions of this work.

Illumination of the indicator with appropriate excitation light, and detection of the resultant fluorescence, is fundamentally required to interrogate the indicator. An optical system comprising light source, optical filters, sensing head and optical detector similar to some previous systems was developed. Several often-overlooked precautions (for instance, measurement of the thermal response of the excitation source) were taken to ensure adequate optical interrogation of the indicator. This optical section will be described in chapter 3.

These initial chapters are necessary for providing the reader with background information and illuminating certain important design aspects. The main novel contributions will be described in chapters 4, 5 and 6.

The 'sensing scheme' governs the choice of excitation source and drive current and how the detected light is processed to decode the state of the fluorescent indicator, and therefore obtain the resulting measurement. Optimisation and enhancement of the sensing scheme can clearly improve performance of the sensor irrespective of the fluorescent indicator used. Despite this, the area has received little specific attention. Methods to achieve optimal measurements using enhanced versions of existing sensing schemes (chapters 4 and 5), and suggested new sensing schemes (chapter 6) were developed.

1.5.1 Sensing Schemes

Both the overall fluorescence intensity and the fluorescence decay curve with time from an indicator, after initial excitation are usually affected by the measurand value (see chapter 2), so sensing schemes have been devised to monitor each of these. Monitoring changes in the fluorescence intensity, by applying constant excitation light, is the simplest optical method (e.g. [34], where fluorescence from pharmaceuticals in blood was directly interrogated), but, for indirect sensing particularly, this can lead to stability problems due to ageing of the membrane, coupling to it and thermal dependency (see chapter 3). To alleviate this, where possible most modern sensing schemes have interrogated the shape of the fluorescence decay curve.

One such sensing scheme, the Rapid Lifetime Detection (RLD) method, is based on direct analysis of the fluorescence decay curve following an excitation light pulse, and will be

considered in chapter 4. This sensing scheme, suitable for ultra-low level detection, and, if desired, for plotting out the fluorescent decay function, detects the rate of receiving individual photons emitted by the fluorescent indicators, as a function of time, following excitation by a pulsed source. The number of photons arriving during two, pre-defined time intervals are accumulated, then the ratio of these measurements is used as a derived indication of the state of the indicator. Many repeat measurements can be accumulated to provide a more accurate measurement. Clearly, detecting individual photons gives excellent sensitivity at low light levels.

Several new optimizations and enhancements of the RLD method have been suggested by this study [35], [36]. A new calculation method, for determining the conditions for optimal high-repetition rate measurements was developed. An analytical error-propagation approach was adopted to model the precision of measurements, as a function of the various parameters used to set up the sensing scheme. This was the first time an analytical model, taking into account all of these relevant set up parameters, had been developed. The effectiveness of varying the interrogator conditions to suit the fluorescence decay and background ambient light was considered and an almost doubling in measurement precision when compared with that expected from conditions previously believed to be optimal was quantified. The new method has been extensively verified by comparison with not only a computer simulation of the sensor, but also with experimentally derived measurements from real indicators. The excellent agreement confirmed validity of the new model.

In chapter 5, interrogation of the phase delay between a modulated excitation source and the resultant detected fluorescence will be investigated as a sensing scheme.

The drive current through an LED (which excites the membrane) is modulated, at frequency f_m. The returning weak fluorescence from the indicator would also be modulated at frequency $f_{m,}$ but returns with a total delay arising from a combination of electronics delays, optical propagation delays, and a variable phase delay, which is a function of the fluorescence lifetime of the indicator. The value of this delay is then a derived indication of the state of the indicator.

This is perhaps the most widely used scheme, principally due to the simplicity of the instrumentation required and its intrinsic tolerance to background light (this is discussed later). The traditional (sinusoidal shaped excitation) sensor response will be modelled for ideal conditions. The enhanced (dual phase, square-wave modulation) sensing scheme, which is preferable in many applications, will then be considered. A novel, more-realistic

model, which includes the optical delays, electronic delays and band limiting effects measured from the real sensor hardware will be developed, showing the implication of these effects on measurements. By characterising noise sources in the hardware, the expected measurement precision will be calculated and compared with achieved values, thereby verifying correct operation of the model. Settings for achieving optimal precision measurements will be calculated, and compared with previously published results. The expected measurement precision will be calculated and compared with the achieved value to verify this analysis.

Cross-sensitivity of fluorescent indicators to temperature is a commonly encountered problem – one oxygen indicator giving a 4% $°C^{-1}$ error [37]. Thermal compensation by measuring the analyte temperature has been therefore required in most applications. This is usually achieved using an electrical thermometer. For instance, the FOXY probe makes temperature readings by adding a thermocouple at the sensing head, which is connected to the interrogation system via an electrical connecting lead. An optical alternative based on adding a second indicator and slightly modifying the sensing scheme is preferable, and was suggested by this research [38]. In chapter 6, this will be described. The indicator combination used will be justified, then sensing schemes for dual measurements of both indicators, based on direct fluorescence decay analysis and on delay monitoring using modulated excitation source will be suggested. The principle will be proved by experimental measurements at multiple temperatures.

Chapter 7 concludes this thesis, by describing the enhancements and optimisations explored, then suggesting areas where further work could lead to greater understanding or further performance gains. Finally, some areas only briefly explored during this study, but which could form the basis of interesting new work, will be described. This includes initial work to develop a compact optical pH sensor, and first studies to characterise the ageing process of the oxygen indicator, which determines the operational lifetime of the sensor.

1.6 References for Chapter 1

1. BOSS, *(Biocompatible Optical Sensor Systems), BRITE RuRAM Project no BE-4311*. Jan. 1997 - Dec 2000

2. Stucker, M.*, et al.*, *FLIM of luminescent oxygen sensors: clinical application and results.* Sensors and Actuators B, 1998. **51**: p. 171-175.

3. Preininger, C., LKlimant, I. and Wolfbeis, O., *Optical Fiber Sensor for Biological Oxygen Demand.* Anal. Chem., 1994. **66**(11): p. 1841-1846.

4. Baldini, F. *Optical Fibre Chemical Sensors at IROE for Medical Applications*. in *Biochemedical Medical Sensors.*: SPIE, 2085, 104-108

5. NI, T. and Melton, L., *Fuel equivalence ratio imaging for methane jets.* Applied Spectroscopy, 1993. **47**(6): p. 773-781.

6. Clark, L.C., *Electrochemical device for chemical analysis,* Patent, U.S.,1959, 2913386

7. Goldstein, S.R., Peterson, J.I. and Fitzgerald, R.V., *A miniature fibre-optic pH sensor for physiological use.* Journal of Biomedical Engineering., 1980. **102**: p. 141-146.

8. Jordan, D.M., Walt, D.R. and Milanovich, F.P., *Physiological pH Fibre-Optic Chemical Sensor Based on Energy Transfer.* Analytical Chemistry, 1987. **59**: p. 437-439.

9. Lobnik, A., Majcen, N., Niederreiter, K. and Uray, G., *Optical pH sensor based on the absorption of antenna generated europium luminescence by bromothymolblue in a sol-gel membrane.* Sensors and Actuators B, 2001. **74**: p. 200-206.

10. Dakin, J.P., Pratt, D.J., G.W., B. and Ross, J.N., *Distributed optical fiber Raman temperature sensor uysing a semiconductor light source and detector.* Electronics Letters, 1985. **21**: p. 569.

11. Rao, Y.J.*, et al.*, *In-fiber Bragg-Grating temperature sensor system for medical applications.* Journal of Lightwave Technology, 1997. **15**: p. 779-785.

12. Grattan, K.T.V., *Fiber optic techniques for temperature sensing*, in *Fiber Optic Chemical Sensors and Biosensors*, O.S. Wolfbeis, Editor. 1991, London:CRC Press. p. 151-192. ISBN 0-8493-5509-5

13. Hitchman, M.L., *Measurement of Dissolved Oxygen*. Chemical Analysis, ed. P.J. Elving and J.D. Winefordner. Vol. 49. 1978: John Wiley and Sons. 0-471-03885-7

14. *Fast Dissolved Oxygen & Temperature Sensor*. 2000, PME fast response sensors and systems www.pme.com/oxsensor.htm.

15. *Model 1234 Oxygen Sensor*., Novatch Controls www.novatech.com.au/html/1234.htm.

16. Sotiropoulos, S. and Wallgren, K., *Solid-state microelectrode oxygen sensors.* Analytica Chemica Acta, 1999. **388**: p. 51-62.

17. Demin, A.K., Zhuravlev, B.V. and Somov, S.I., *Sensor for measuring the oxygen concentration in gas mixtures with unsteady pressure.* Solid State Ionics, 1998. **112**: p. 355-359.

18. Glasspool, W. and Atkinson, J., *A screen-printed amperometric dissolved oxygen sensor utilising an immobalised electrolyte gel and membrane.* Sensors and Actuators B, 1998. **48**: p. 308-317.

19. Gibson, R.W., Kumar, R.V. and Fray, D.J., *Novel sensors for monitoring high oxygen concentrations.* Solid State Ionics, 1999. **121**: p. 43-50.

20. Yulong, X., Xiaohua, Z. and O., S., *Oxygen sensors based on semiconducting metal oxides : an overview.* Sensors and Actuators B, 2000. **65**: p. 2-4.

21. Hendrikse, J., Olthuis, W. and Bergveld, P., *The E-MOSFET as an oxygen sensor: constant current potentiometry.* Sensors and Actuators B, 1999. **59**: p. 35-41.

22. Trettnak, W., Gruber, W., Reininger, F. and Klimant, I., *Recent progress in optical oxygen sensor instrumentation.* Sensors and Actuators B, 1995. **29**: p. 219-225.

23. Trettnak, W.*, et al.*, *Miniaturized luminscence lifetime-based oxygen sensor instrumentation utilizing a phase modulation technique.* Sensors and Actuators B, 1996. **35**: p. 506-512.

24. Murtagh, M., Ackley, D. and Shahriari, M., *Development of a Highly Sensitive Fibre-Optic O2/DO sensor based on a phase modulation technique.* Electronics Letters, 1996. **32**(5): p. 477-479.

25. Trettnak, W.*, et al.*, *Optical Oxygen Sensor Instrumentation Based on the Detection of Luminescence Lifetime.* Advances in Space Research, 1998. **22**(10): p. 1465-1474.

26. Kolle, C. and al., e., *Fast Optochemical sensor for continuous monitoring of oxygen in breath-gas analysis.* Sensors and Actuators B, 1997. **38**: p. 141-149.

27. Hartmann, P. and Ziegler, W., *Lifetime Imaging of Luminescent Oxygen Sensors Based on All-Solid-State Technology.* Analytical Chemistry, 1996. **68**: p. 4514-4514.

28. Gouin, J.F., Baros, F., Birot, D. and Andre, J.C., *A fibre-optic oxygen sensor for oceanography.* Sensors and Actuators B, 1997. **38-39**: p. 401-406.

29. Kronfeldt, H. and Schmidt, H., *Submersible Fiber-Optic Sensor System for Coastal Monitoring*. 1999. p. 51-55 Sea Technology.

30. Gouterman, M., *Oxygen Quenching of Luminescence of Pressure Sensitive Paint for Wind Tunnel Research.* Journal of Chemical Education, 1997. **74**(6): p. 697-702.

31. Ocean-Optics, *FOXY Fiber Optic Oxygen Sensor - www.oceanoptics.com/products/foxysystem.asp*. 1996

32. *Van-Essen Instruments, 'O2 sensor for ground and surface water monitoring' - www.vanessen.com/*. R&D phase

33. Trinkel, M., Trettnak, W. and Kolle, C., *Oxygen trace analysis utilising a miniaturised luminescence lifetime-based sensor instrumentation.* Quimica Analitica, 2000. **19 (suppl 1)**: p. 112-117.

34. Gu, Y. and al., e., *A new fiber optic sensor for detecting in situ the concentrations of pharmaceuticals in blood.* Sensors and Actuators B, 2000. **66**: p. 197-199.

35. Austin, E.A.D. and Dakin, J.P. *Opto-electronic systems for addressing Ru oxygen sensors:their design optimization and calibration process (invited)*. in *SPIE: Fiber Optic Sensor Technology and Applications* 28 October - 2 November 2001 Boston,USA, 4578-06,

36. Austin, E. and Dakin, J., *Optimization Method for Rapid Lifetime Detection (RLD) Interrogation of fluorescent Decay Sensors - submitted July 2002.* Analytical Chemistry, 2002.

37. Wolfbeis, O., *Oxygen Sensors - temperature effects*, in *Fiber optic chemical sensors and biosensors, volume II*, O. Wolfbeis, Editor. 1991, CRC Press, Inc. p. 27-28. ISBN 0-8493-5509-5

38. Austin, E., Dakin, J. and Strong, A.P. *Use of transition-metal-doped sapphire crystals to calibrate and thermally compensate fluorescent-lifetime chemical detectors (keynote communication).* in *EUROPT(R)ODE V* 16-19 April 2000 Lyon, France, KC9,

1. CHARACTERISTICS OF FLUORESCENT INDICATORS

1.1. Introduction

Fluorescence occurs when a chemical species or material emits radiation (usually light) as a result of appropriate excitation. Often the quantity and lifetime of the fluorescence is altered by environment; perhaps by temperature, pressure, oxygen concentration, or pH. In this case, the fluorescent chemical species or material is called an 'indicator', because the state of an external parameter is indicated by the state of its fluorescence.

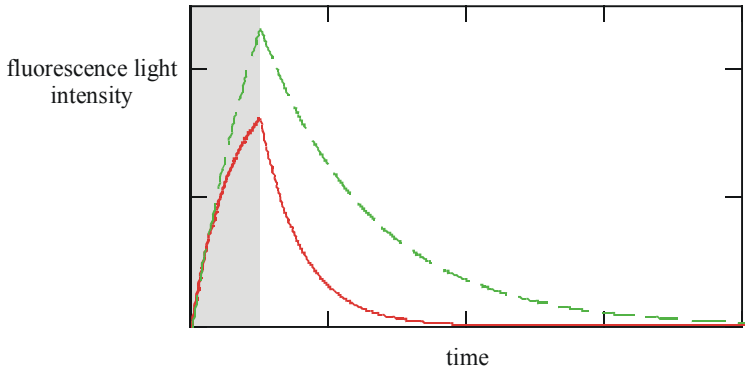

Figure 1.1 The fluorescence response from an indicator. Fluorescence light, excited during the shaded area is then released. For fluorescent indicators, this fluorescence response is dependent upon an environmental variable, such as temperature. As this is increased so the fluorescence response evolves from the dotted to the solid response. Interrogation equipment can monitor this change and thereby infer the value of the environment variable.

This situation is illustrated in Figure 1.1, where the fluorescence observed from an indicator has been plotted as a function of time. Consider firstly the dashed line. Luminophores (fluorescence emission sites) within the indicator, excited by a suitable source, eventually release their excess energy as fluorescence light, relaxing to a ground state. When the excitation source is switched on (during the shaded area), progressively more luminophores become excited and start to fluoresce, so the observed fluorescence intensity initially increases (eventually equilibrium would be reached). When the excitation is switched off (beyond the shaded box), luminophores are no longer excited to replace the relaxing (fluorescing) ones, so the observed fluorescence intensity dies away. As the environmental parameter is altered (e.g. the temperature increased) so the fluorescence lifetime and intensity of the indicator change, causing the fluorescence

response to evolve perhaps from the dotted to the solid line. The mathematical description of this process will be dealt with later.

Various sensing schemes have been suggested for monitoring the observed fluorescence, and thereby inferring the state of the environment variable in question - these will be discussed in future chapters. Here, the relationship between the fluorescence decay shape and environment parameter is discussed firstly for a chemical complex developed to sense oxygen, then for a titanium-doped-sapphire crystal material with intrinsic thermally dependent fluorescence.

1.2. Oxygen sensitive optical chemical indicators

In this section, the effect of oxygen concentration on the fluorescence of a suitable indicator will be investigated.

Oxygen affects the fluorescence of certain molecules by prohibiting (or quenching) the normal radiative decay process, which is responsible for producing fluorescence. By monitoring the degree of quenching, the oxygen concentration present can be measured.

An in depth explanation of the fluorescence process is given below, but in simplified form, the chemical scheme is this. An incident photon promotes the luminophore to an excited state. The luminophore may relax to the ground state by several mechanisms, but of particular interest is when the excess energy is emitted as a fluorescence photon, which has lower energy and therefore longer wavelength than the incident photon (the difference between excitation and fluorescence wavelength is known as the ‘Stokes shift‘). When oxygen molecules are present, there is a finite possibility of energy-transfer between the excited luminophore and oxygen molecule, resulting in relaxation of the luminophore without radiative emission, (the oxygen molecule ascends to a singlet state).

To sense oxygen, many luminophores are required, each contributing to the observed fluorescence. The time luminophores spend in the excited state following excitation follows a statistical distribution, so after an excitation pulse, the fluorescence decays with a characteristic, usually exponential, decay. The concentration of oxygen present defines the proportion of luminophores interacting with the oxygen molecules, and thus effects the observed fluorescence intensity (by non-radiative relaxation of some of the luminophores) and decay characteristic lifetime (by altering the mean time for which a luminophore may remain excited without interaction with oxygen). Usually, the luminophores must be

immobilised within a support matrix to provide a mechanical harness to hold the otherwise liquid sensing dye, and to separate it from other interfering species (this is discussed later).

A large amount of research has been done to enhance the properties of oxygen indicators (e.g. [1], [2], [3], [4]). The chemical complex used has been optimised for sensitivity, selectivity, dynamic range, response time, photo-stability, shelf life, durability and ease of synthesis. The support matrix has been studied to improve permeability to oxygen, mechanical, thermal and chemical strength, transmittance of the required absorption and fluorescence bands, and addition of functional groups for electrostatic or covalent immobilisation of the luminophore complex. As part of the BOSS program, the ability to withstand biological conditions (biocompatibility), of the sensing membrane was enhanced [5] for applications in physiological, industrial and environmental monitoring.

Due to this large volume of previous work, only a brief study of the indicator chemistry, then the requirements and consequences of immobilising the dye in a support matrix will be discussed. As previously noted, the oxygen indicator itself is not the main centre of the work presented here. The fluorescence response of the indicator as a function of oxygen concentration, and models for this complex behaviour will then be investigated.

1.2.1. Indicator Chemistry

Several luminophores have been investigated for their suitability as oxygen indicators. The desirable sensor characteristics of sensitivity, selectivity, dynamic range, response time and extended working life are achieved by a fluorescent indicator possessing high stokes shift, high fluorescence quantum yield, vigorous quenching response to oxygen, long fluorescence lifetime, and strong absorbance in bands emitted by convenient solid-state light sources.

Though dye molecules based on polycyclic aromatic hydrocarbons (e.g. pyrene, pyrenebutyric acid, fluoranthene, decayclene, etc), and porphyrins (e.g. encapsulated in sol-gel [6], and optimised for long-lived (~0.5ms) phosphoresce [7]) have been used as fluorescent oxygen indicators, metal-organic complexes are most attractive. Since the discovery of energy transfer between luminescent transition metal complexes and oxygen in 1977 [8], and the suggestion of using this for sensing applications in 1986, [9], complexes of ruthenium, osmium, iridium, platinum and lead have been developed. The Ruthenium metal-organic complexes tris(2,2'-bipyridyl)ruthenium(II) ($[Ru(bpy)_3]^{2+}$) and tris(4,7-dipenyl-1,10-phenanthroline)ruthenium(II) ($[Ru(dpp)_3]^{2+}$) have gained the principle share of research activity because of their highly efficient luminescence

production (0.30 for $[Ru(dpp)_3]^{2+}$), relatively long-lived excited states (~5μs for $[Ru(dpp)_3]^{2+}$) fast response times (t_{90}<<30s), spectral absorption of blue light (~470nm – readily produced by blue LEDs), high photochemical stability (in comparison with organic dyes), and large Stokes' shift resulting in emission of orange-red fluorescence (~600nm). Blue LEDs and modern detectors are ideally suited to these absorption and emission characteristics.

1.2.2. Encapsulation of the dye

Measurements could be made by dissolving the indicator dye into the analyte solution itself, but for most applications this is either inconvenient or impossible, so the indicator dye must instead be encapsulated within a solid support matrix, which is placed in contact with the analyte. (Clearly, encapsulation is necessary to make gaseous measurements). The support matrix must be oxygen-permeable to allow passage of oxygen to the indicator dye, have high solubility of the indicator and be chemically and mechanically resilient enough to withstand the intended operating environment. Usually the combination of dye and support matrix together are termed the 'membrane'. As discussed in detail later, encapsulation strongly effects the fluorescence response of the dye to oxygen.

Polymers are usually chosen for encapsulation of ruthenium complexes due to their low-cost, high solubility of the sensing dye, ease of synthesis, and versatile molecular composition. Other encapsulating matrices include sol-gel for porphyrins [6], and for ruthenium complexes, Zeolite Y [10], and gelatin, which is particularly suited to dissolved concentration measurements in organic solvents [11]. Encapsulation can improve sensor selectivity by being impermeable to other quenchers, notably heavy metal cations and certain anions. For most studies, a ruthenium complex has been immobilised within silicones. The silicone-encapsulated indicator forms a convenient flexible membrane that may be easily deposited or glued onto many substrates or sensing probes.

For aqueous measurements silicone has many attractive features including an extraordinarily high permeability to oxygen (being 2 orders of magnitude greater than for any other organic polymers and resulting in high quenching efficiencies), as well as excellent chemical and mechanical stability. Because of its hydrophobic character, ionic species cannot penetrate silicone rubber improving selectivity. Silicone is also considered to be mechanically an appropriate support material for the preparation of most oxygen sensors, as it can be easily spread in thin layers and then bonded to curved probe tips. Thermoplastic matrixes, such as PVC and polystyrene (PS) are also sometimes used.

These are especially suitable for investigations on absorption spectral changes, since they are highly transparent (low light scattering, unlike silicone supports incorporating silica gel).

1.2.3. Chosen Fluorescent Oxygen Indicator

The oxygen sensing membrane chosen for this study was an example of the most commonly used variety; an $[Ru(dpp)_3]^{2+}$ complex embedded in a silicone (Dow-Corning 3140, a poly(dimethysiloxane)-based formulation) support matrix with 10% by weight silica gel, which absorbs the ionic indicator. These were synthesised by one of the BOSS research partner groups, (Professor G. Orellana's group at the Universidad Complutense in Madrid) as described in [5]. Although the BOSS programme was aimed at sensors with anti-fouling coatings, most of the membranes used for this study were left uncoated as this was not required (or desired) for verification of new sensing schemes, the main focus of this study. In fact inclusion of an anti-fouling coated would have made comparison with other published results using conventional uncoated membranes impossible.

The spectral absorption and emission from the membranes are discussed in chapter 3. Here, the fluorescence response of the membrane as a function of oxygen concentration is discussed.

1.2.4. Stern-Volmer formulas

The Stern-Volmer formulas are the well-known traditional relationships, which express fluorescence intensity and the fluorescence lifetime as a function of quencher concentration. A brief derivation of the formula for fluorescence intensity is given here for completeness. (Though such a derivation surely exists in the literature, it could not easily be found, so it was derived from first principles again here).

Fluorescence production is governed by bimolecular quenching kinetics between the dye molecule (S) and the excitation photon (of energy $h\nu_e$). The possible outcomes from the reaction in the presence of quencher (Q) and their rate constants are described in the sequence (1.1) (excited species are denoted with an asterisk).

excitation	$S + h\nu_e \rightarrow S^*$	E
fluorescence emission	$S^* \rightarrow S + h\nu_f$	α_1
non - radiative emission	$S^* \rightarrow S + \Delta$	α_2
energy transfer	$S^* + Q \rightarrow S + Q^*$	β_1
catalytic deactivation	$S^* + Q \rightarrow S + Q + \Delta$	β_2
electron transfer	$S^* + Q \rightarrow S^+ + Q^-$	β_3
electron transfer	$S^* + Q \rightarrow S^- + Q^+$	β_4

(1.1)

The reactions with rates α_1 and α_2 represent unquenched decay of the dye molecule (i.e. no reaction between the excited dye molecule (S^*) and the quencher). α_1 is the rate of the decay which produces fluorescence light, α_2 is the intrinsic (i.e. unquenched) rate of non-radiative decay. All the decays designed with rates β are reactions influenced by the quencher. These reactions are; energy transfer between excited luminphore and quencher at rate β_1; catalytic deactivation of S^* at rate β_2 and electron transfer reactions between excited luminophores and quencher at rates β_3 and β_4.

Let us now consider a number of dye molecules operating in the presence of the quencher. Let us denote the number of dye molecules in the relaxed state, for a quencher concentration of Q as S(Q), and the number in the excited state as $S^*(Q)$. We will also group the rate of unquenched deactivations together as α, and assume that all unquenched reactions result in fluorescence emission (i.e. $\alpha=\alpha_1$, $\alpha_2=0$). Similarly, let us call the rate of quenched deactivations (i.e. those not leading to fluorescence production) β, (i.e. $\beta=\beta_1+\beta_2+\beta_3+\beta_4$). The change in the number of excited dye molecules per unit time is then the number excited by the excitation light, minus the number relaxing. Relaxation can occur either by quenched or unquenched deactivations to the ground state. We can say that the number of deactivated molecules S(Q) times the activation rate E, minus the number of excited state dye molecules $S^*(Q)$ times α (unquenched relaxations) minus the number of excited state dye molecules times the quenched deactivation rate β times the number of quenching molecules present in the dye sample (Q). This is expressed mathematically in (1.2).

At steady state, the number of excited dye molecules does not change hence (1.2) is equated to zero.

$$\frac{dS^*(Q)}{dt} = E.S(Q) - \alpha.S^*(Q) - \beta.Q.S^*(Q) = 0$$

(1.2)

(1.2) quickly leads to (1.3).

$$E.S(Q) = (\alpha + \beta.Q)S^*(Q)$$

(1.3)

Let us now consider the situation when no quencher is present, and then the situation when quencher concentration Q is present. The overall number (excited plus unexcited) of luminophores, of course must remain constant, so,

$$S^*(0) + S(0) = S^*(Q) + S(Q)$$

(1.4)

and the fluorescence intensity I_0 produced in the quencher less state is

$$I_0 = \alpha.S^*(0)$$

(1.5)

and in the presence of quencher concentration Q, the intensity I is

$$I = \alpha.S^*(Q)$$

(1.6)

We can write

$$\frac{I_0}{I} = \frac{\alpha.S^*(0)}{\alpha.S^*(Q)} = \frac{E.S(0).(\alpha + \beta.Q)}{\alpha.E.S(Q)} = \frac{S(0)}{S(Q)}(1 + \frac{\beta}{\alpha}.Q) = 1 + \mathrm{K}_{sv}Q$$

(1.7)

where we have used (1.3), (1.4), (1.5) and (1.6), assumed that the number of unexcited dye molecules is very large compared to the number of excited ones, so that S(0)=S(Q), and defined the Stern-Volmer constant K_{sv} as β/α.

We have derived the well-known, Stern-Volmer Equation written here for oxygen quenching reactions as

$$\frac{I_0}{I} = 1 + K_{SV} \cdot pO_2$$

where
I_0 is the fluorescence intensity in the absence of oxygen
I is the fluorescence intensity in the presence of oxygen
K_{SV} is the overall dynamic quenching constant = $k \cdot \tau_0$ (k is the bimolecular constant, and
τ_0 is the natural lifetime of the indicator dye in the absence of oxygen)
pO_2 is the oxygen partial pressure (proportional to concentration)

A similar equation for fluorescence decay lifetime may be derived by considering, rather than the steady state situation, the response to delta-function (i.e. short pulse) excitation light. The Stern-Volmer equation for fluorescence lifetime is:

$$\frac{\tau_0}{\tau} = 1 + K_{SV} \cdot pO_2$$

where
τ_0 is the fluorescence lifetime in the absence of oxygen
τ is the fluorescence lifetime in the presence of oxygen

The Stern-Volmer equation holds for sensors when the indicator dye is dissolved in the analyte and is thus homogeneously dispersed, with each indicator molecule exposed to identical conditions. However, in most sensing applications, as explained above, it is necessary to immobilize the indicator in an encapsulating solid substrate. For such sensors, the response of. τ_0/τ or I_0/I against pO_2 is no longer linear, as given by Stern-Volmer, but instead the sensitivity of the indicator falls with increased oxygen concentration, leading to a downward sub-linear increase in the otherwise linear Stern-Volmer plot (which is I_0/I or τ_0/τ plotted against pO_2). Stern-Volmer (or S-V) plots for four common dyes encapsulated in various support matrices are presented in Figure 1.2 (reproduced from [12]). A non-linear downward droop is clearly distinguishable.

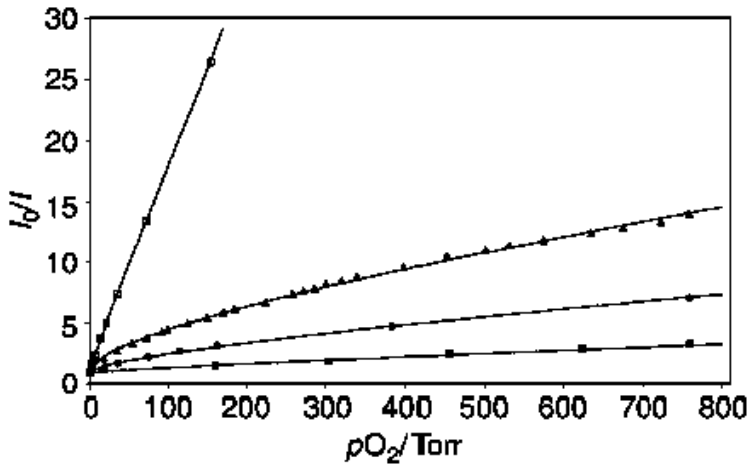

Figure 1.2 Stern-Volmer plots (I_0/I versus pO_2) for some common optical oxygen indicators reproduced from [12]. The indicators are (from most elevated plot to least) Pd(II)OEPK in PVC, Pt(dpp)(CN-)$_2$ in silicone rubber, Ru(dpp)$_3^{2+}$(DS-)$_2$ in silicone rubber and Ru(dpp)$_3^{2+}$(Ph$_4$B-)$_2$ in cellulose acetate. Reductions in the slope of these curves (sub-linear behaviour) is clearly observed as partial-pressure rises for all of these dyes, showing reduced sensitivity as pressure rises.

Various models for extending or even replacing the Stern-Volmer relationship have been suggested to explain this behaviour, these are briefly explained below. An accurate model of the indicator response is essential for predicting the response from the membrane, which is needed for computer simulation of oxygen sensors.

1.2.5. Multi-site or 'two site' model

This model assumes that, when encapsulated in a support matrix, the dye molecules are bonded to a number of spectroscopically-heterogeneous sites, with a separate Stern-Volmer equation applying at each site.

This situation may be described as

$$\tau_i = \frac{\tau_{0,i}}{(1+\tau_{0,i}\cdot k_{q,i}\cdot pO_{2,i})}$$
$$I_i = \frac{I_{0,i}}{(1+\tau_{0,i}\cdot k_{q,i}\cdot pO_{2,i})}$$

(1.8)

where the index 'i' is added to the Stern-Volmer equation to denote fluorescence from a single site *i* within the sensing membrane (it is assumed that the oxygen partial pressure is identical at the sites).

In the two-site model, it is assumed that only two types of site exist within the membrane, one with natural lifetime and bimolecular constants $\tau_{0,1}$, k_1, at site 1, and $\tau_{0,2}$, k_2. at site 2. By aggregating the contribution from each type of site the fluorescence intensity is modelled to be

$$I = I_0\left[\frac{f_1}{1+\tau_{0,1}\cdot k_1\cdot pO_2}+\frac{1-f_1}{1+\tau_{0,2}\cdot k_2\cdot pO_2}\right]$$

(1.9)

where f_1 is the proportion of the fluorescence sites of type 1.

As the contributions from each site type are exponential, the total time-resolved response of the fluorescent intensity of the membrane would be bi-exponential:

$$I(t)=\alpha_1 e^{-t/\tau_i}+\alpha_2 e^{-t/\tau_2}$$

(1.10)

where we have defined pre-exponential terms α_1 and α_2, (these are, of course, different to the earlier definitions) which describe the contribution from site type 1 and 2 respectively.

The two-site model may be related to experimentally measured lifetimes via the weighted mean lifetime,

$$\tau_M=\frac{\alpha_1\tau_1+\alpha_2\tau_2}{\alpha_1+\alpha_2}$$

It can be shown that

$$\frac{I_0}{I}=\frac{\tau_{0,M}}{\tau_M}$$

(1.11)

relating measured effective fluorescence lifetimes to the standard Stern-Volmer formulas.

As noted in [13] and [12], it follows from (1.10), that the proportion of light returning with exponential time constant τ_1 (i.e. $\alpha_1/\alpha_1+\alpha_2$) should equal the proportion of fluorescence intensity received from site type 1 as defined in (1.9), (i.e. f_1)).

Unfortunately, discrepancies arise when $\alpha_1/\alpha_1+\alpha_2$ (as measured by fitting bi-exponentials to time-resolved fluorescence plots), is compared with f_1 (as measured empirically by fitting data to (1.9)). In a study of an ruthenium complex dye encapsulated

in silicone rubber[13], values of 0.16-0.31 depending on pO_2 for $\alpha_1 / (\alpha_1 + \alpha_2)$ were contrasted with a fitted f_1 value of 0.4 over the same measurement range, questioning the validity of this physical model.

This strongly empirical model, though adequate in certain situations, does not synthesise oxygen sensor response satisfactorily in all cases.

1.2.6. Log Gaussian distributions in κ and τ model

Rather than assuming only a few differing sites exist within the matrix, this extended model (first suggested in 1998 by Mills in [12], then extended in 1999 again, by Mills in [14], [15]) assumes that the fluorescent sites cannot be sorted into a few discrete groups, but instead that they must be described by a log-Gaussian shaped distribution in quenching parameters τ_0 and κ_q. Mills showed that his model gave satisfactory agreement between measured and expected fluorescence decays, for many sensors. This is therefore the model used here.

The fluorescence intensity response of an oxygen sensing membrane, following delta-function excitation, is modelled, by the log-Gaussian, model as

$$I(t) = \mathrm{I_s} \frac{\int_{-\infty}^{\infty} e^{-x^2} e^{-\left[(1+\kappa.q.e^{(\rho_1+\rho_2).x}).t.e^{(-\rho_1.x)}\right] / \tau_{0,mdl}} dx}{\int_{-\infty}^{\infty} e^{-x^2} dx} . \frac{\int_{-\infty}^{\infty} \frac{e^{\rho_1.x}.e^{-x^2}}{1+\kappa.q.e^{(\rho_1+\rho_2).x}} dx}{\int_{-\infty}^{\infty} e^{\rho_1.x}.e^{-x^2} dx}$$

(1.12)

where the contribution from the continuum of sites are integrated to form the time and intensity response of the indicator. κ and $\tau_{0,mdl}$ are the Stern-Volmer constant and unquenched fluorescent lifetime for the modal number of sites (i.e. the most common), ρ_1 and ρ_2 are the widths of the log-Gaussian shaped distributions of the unquenched decay lifetimes and the Stern-Volmer constants of the sites respectively. Finally I_s specifies the intensity of the fluorescence.

1.2.6.1. Calibration of oxygen sensing membrane

Referring to (1.12), we see the parameters (I_s, ρ_1, ρ_2, κ, $\tau_{0,mdl}$) must be recovered in a calibration stage to model the response from an oxygen sensor. Each indicator used must

be separately calibrated, as the heterogeneity of the support sites varies widely between membranes. The calibration parameters recovered for each membrane will be quoted when results from the membrane are used, but the method used for extracting them is given here.

To calibrate the indicator against the model, the fluorescence decay from the indicator at (at least) two known dissolved oxygen concentrations was required. These curves were measured when needed using a photon-counting fluorescence interrogator to resolve the decay curve and the water oxygenation rig, (which bubbles mixtures of nitrogen and air through 100ml water sample) to attain arbitrary DO concentrations. These are both discussed in detail in chapter 4.

1.2.6.2. Estimation of $\tau_{0,mdl}$ and ρ_1

As noted by Mills [15], the parameters $\tau_{0,mdl}$ and ρ_1 may be easily fitted from the fluorescence decay of the indicator measured in the absence of oxygen, because the modelled response reduces to

$$I_{q=0}(t) = \mathrm{I_s} \frac{\int_{-\infty}^{\infty} e^{-x^2} e^{-\left[t.e^{(-\rho_1.x)}\right] / \tau_{0,mdl}} dx}{\int_{-\infty}^{\infty} e^{-x^2} dx}$$

(1.13)

Bubbling nitrogen through a test water sample displaces the dissolved oxygen present thereby de-oxygenating the water (this process is discussed in chapter 4). An experimentally measured $I_{q=0}(t)$ captured under these conditions was therefore used to obtain these parameters, by simply fitting the measured decay response to a (1.13) via a non-linear regression algorithm.

1.2.6.3. Estimation of κ and ρ_2

Values for κ and ρ_2 were extracted by capturing further fluorescence decay curves at different known DO concentrations. Fluorescence decays were captured at 0%, 25%, 50%, 75% and 100% [O_2], using the oxygenation rig.. Having captured these fluorescence decays, values for κ and ρ_2 were estimated by non-linear regression at each measured oxygenation level and averaging of the results from each regression.

It was found that an extension to the originally suggested model was required, due to a slight quencher dependence of the Stern-Volmer constant κ. Figure 1.3 plots typical fitted

values for κ plotted as a function of concentration showing an excellent linear relationship. The physical importance of this reduction in sensitivity with increasing concentration is unclear, but it is thought to arise from the unusually high concentration of dye molecules present in the oxygen indicators used.

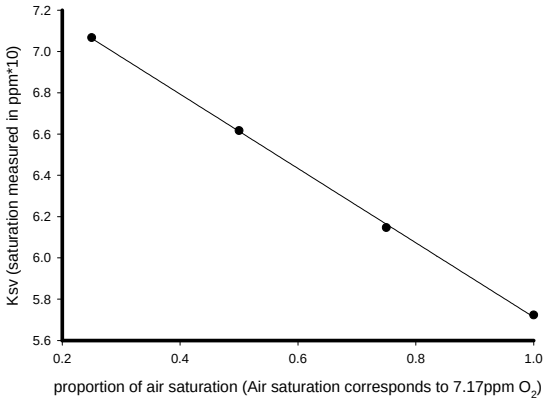

Figure 1.3 κ plotted as a function of Oxygen concentration

The model was updated to include this by re-defining κ as

$$\kappa(q) = \kappa_0 - \kappa q$$

(1.14)

where κ_0 and κ could be estimated from a linear fit of κ(q) to q (shown in Figure 1.3).

1.2.6.4. Recovery of I_s

I_s was deduced from the measured fluorescence intensity I_p measured at a known oxygen level, at some arbitrary time t_p (usually just after the excitation pulse). The value of I_s could be extracted such that the expected intensity at time t_p was equal to the measured value, i.e:

$$I_1(t_p) - I_p = 0$$

(1.15)

Using these calibration techniques, the model input parameters were estimated for each membrane used. Approximate values for effective (i.e. equivalent mono-exponential) lifetime where 3.3μs at 100%[O_2] falling to 1.1μs at 0%[O_2]. (The concept of an 'effective' mono-exponential response, is perhaps misleading when the decay curve is actually far from exponential.)

1.3. Fluorescence of Ti-doped-sapphire crystal – a calibration aid

Thankfully, some fluorescent indicators, and many fluorescent glasses and crystals, have simpler fluorescent responses than that of the oxygen indicator described above. A titanium-doped-sapphire crystal (Ti:sapphire), is one such example. This crystal has a pure exponential fluorescence decay, with a convenient and thermally dependent lifetime. Provided its temperature is controlled, this crystal therefore forms a useful calibration standard, which may be used whenever a known and stable exponential fluorescence is required. Its optical stability even under intense excitation (e.g. within laser cavities), its hard, robust, mechanical properties and its insensitivity to chemical species (such as gases, liquids, ions, etc.), make it ideal for this purpose.

The novel use of Ti:sapphire, as a convenient calibration standard for fluorescence interrogation instrumentation was first suggested and published during this research [16], then its suggested calibration role extended in [17]. This was one of the major novel contributions of the current work.

Successful fibre optic chemical sensors will require extensive calibration both at the time of construction (e.g. during industrial quality assurance), and at frequent intervals during use. Ideally at any time, all the performance parameters of the sensor, such as accuracy, detection limit, linearity etc. must either be known or be easily verified. Though the fluorescent indicator response and the interrogator have often been calibrated together in one step, it is preferable to first independently verify the interrogation system, as it may have internal electronic or opto-electronic delays, or optical cross-talk from excitation system to detection system. Unexpected interrogator performance could indicate a malfunction within the unit itself.

Previous work (e.g. [18]) had suggested a calibration processes by either placing the sensing probe or an alternative known dye (e.g. rhodamine 6G) in a precisely controlled chemical environment. Such methods, though unavoidable in certain circumstances, are inconvenient and unreliable for the purpose of checking the interrogator, because the response of the chemical indicator used can vary in many ways, e.g, due to changes in composition, support matrix, temperature, ageing effects (e.g. photobleaching) and chemical environement. The accuracy to which these environment variables can be stabilised effects the accuracy of the overall calibration process itself. This is avoided with

the Ti:sapphire calibration probe. Simply by careful thermal control of the crystal (close to room temperature), a fluorescence lifetime fluctuation of only 1.3ns (0.04%) was achieved, over a 100s measurement period.

The Ti:sapphire calibration crystal was also a convenient test sample, used in this study, whenever an exponential decay characteristic was required, e.g. for verification of new sensing schemes. Its design is discussed here.

1.3.1. The Ti:sapphire calibration reference probe.

The fibre coupled Ti:sapphire probe provided an optically-suitable plug-in replacement for a fibre probe using ruthenium-based oxygen sensors. Its spectral absorbance and fluorescence are sufficiently similar to that of the Ru^{2+} indicator to allow interrogation of it using the same blue LED excitation source, PMT or silicon detector and same optical filter system. The absorbance and fluorescence spectra of both indicators are plotted in Figure 1.4 and Figure 1.5 respectively. These standard results for the properties of Ti:sapphire are reproduced from [19] and [20], and for the oxygen indicator were provided by G.Orellana's group in Madrid (measurement apparatus details will be given in chapter 3).

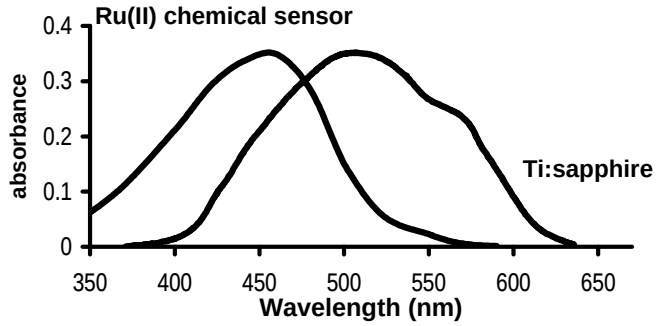

Figure 1.4 Absorption spectra of the oxygen indicator and ti-doped-sapphire

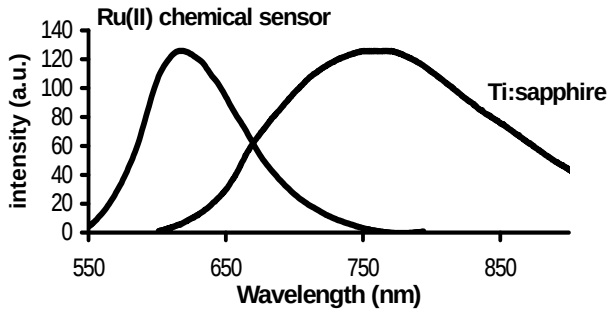

Figure 1.5 Fluorescence spectra of the oxygen indicator and Ti-doped sapphire

The overlap between the oxygen indicator and Ti:sapphire absorbance spectra means that an excitation source (e.g. blue LED) for promoting fluorescence from the oxygen indicator would also excite fluorescence from the crystal. Similarly the fluorescence spectra of the Ti:sapphire crystal could be evaluated with the oxygen indicator interrogation instrumentation (given that a long-pass optical filter is employed in the sensing instrument). Furthermore the crystal's fluorescence lifetime (Figure 1.6, reproduced from [21]) is of the same order as the effective lifetime range of the oxygen indicator (which was found to vary between 1 and 3.3μs, as discussed above). These properties make the Ti:sapphire crystal calibration probe a suitable plug-in replacement for the oxygen indicator.

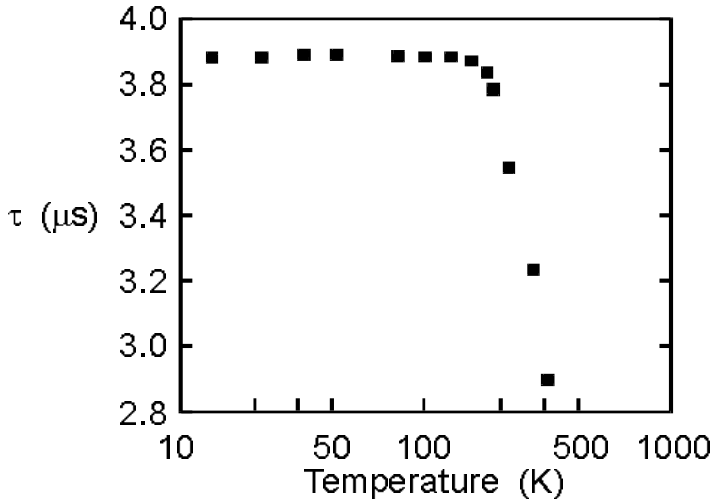

Figure 1.6 Variation of fluorescent lifetime of a Ti-doped sapphire crystal with temperature. Reproduced from [21]

The probe was physically constructed by simply potting a small (2 x 2 x 23mm) cuboid of the crystal, bonded to the distal end of a 600 μm core 630μm cladding, connectorised silica fibre into a brass housing. The potting adhesive used was a highly efficient optical scattering formula including glass bubbles (3M Scotchlite C15/250) mixed into a standard 2-part epoxy (Permabond 'double bubble fast-cure'). The epoxy filled with glass bubbles scatters stray light emerging from the crystal back into it, giving a miniature integrating "sphere" effect, thereby improving the fluorescence production efficiency of the probe. This arrangement is shown in Figure 1.7 with a photograph given in Figure 1.8.

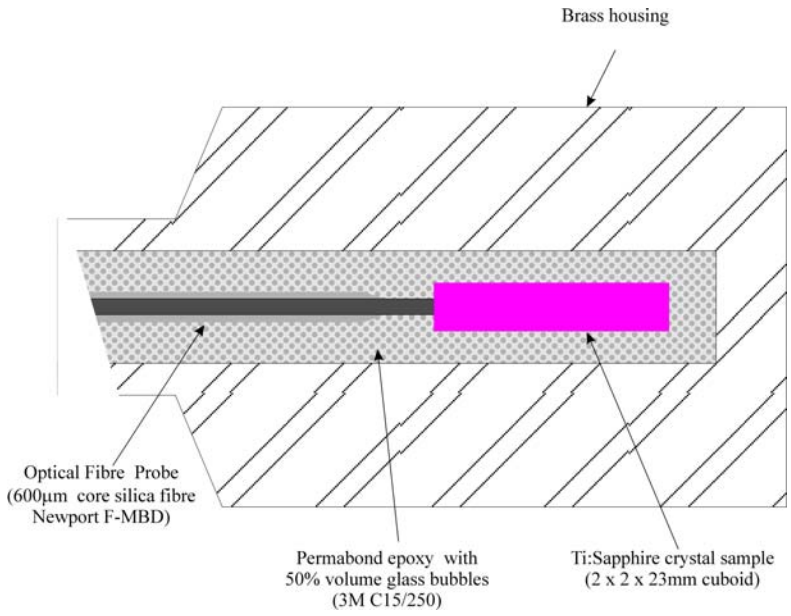

Figure 1.7 Mechanical design for simple Ti-doped-sapphire calibration standard probe

To set its temperature, the arrangement was heated or cooled by a 2-stage 30W Peltier heat pump. Temperature control was achieved by an ILX Lightwave temperature controller (LDT-5412) which monitored the temperature of the brass housing (and therefore the Ti:sapphire sample) by means of a thermister (10K 25°C miniature bead type). By altering the current flowing through the Peltier heat pump, the temperature controller heated or cooled the assembly until the thermister resistance reached a preset set-point. The temperature controller was specially modified to allow external control of this set-point from a control PC.

The temperature of the housing was logged by a control computer, using a separate, integrated circuit based thermometer bonded to the brass housing. National Instruments type LM35CZ having ±0.1°C accuracy was used, which has the convenient output voltage characteristic of 10mV $°C^{-1}$. The assembly is pictured in Figure 1.8.

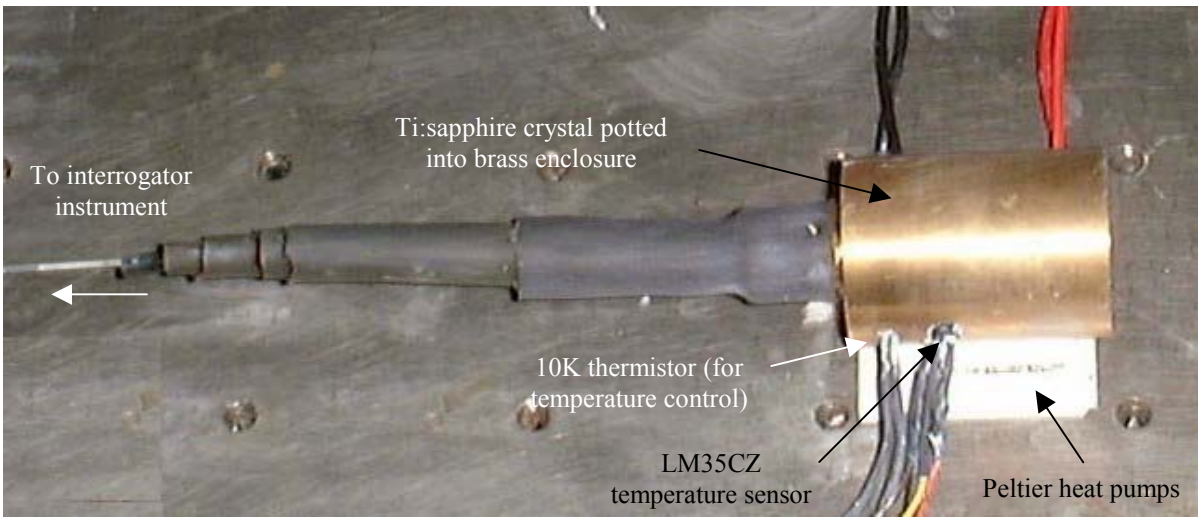

Figure 1.8 Ti:Sapphire calibration standard with Peltier heat pump and dual temperature sensors for separate temperature control feedback and temperature logging.

The reference probe could be used to provide exponential lifetimes in the range 2.9µs and 3.3µs, depending on the desired set temperature. For most experiments, a lifetime of 3µs, was used, which, for this Ti:sapphire crystal, was obtained at a set temperature of 21.6°C. By computing the standard deviation of a temperature log, while the calibrator temperature was held steady over a 100 second experimental run, a temperature fluctuation of **less than ±0.1°C** (i.e. limited by the thermometer itself) was measured. This corresponds to a lifetime fluctuation of **less than 1.3ns** (i.e.0.04%).

1.4. Conclusions from chapter 2

In this chapter, the basic scientific principle of generalised fluorescence indicators, then more specific oxygen sensing types, was given, including a description of common dye encapsulation mediums. The chosen test membrane for oxygen measurements was described. This was an example of the most popular variety, an $[Ru(dpp)_3]^{2+}$ complex absorbed on silica gel within a silicone support matrix. The standard Stern-Volmer formulas for the fluorescence response of a sensitive dye in the presence of quencher (oxygen in this case) was derived. It was pointed out that dye encapsulation has a complicating effect on fluorescence response due to heterogeneity at the fluorescing sites, so a true Stern-Volmer relationship is often not observed. Some of the suggested mathematical models for describing encapsulated dye behaviour were described. The 'log-Gaussian distributions in κ and τ' model was identified as the most appropriate for describing the selected sensing membrane, and a method for estimating the model parameters from a membrane sample was described. Each indicator membrane required

separate calibration, so the extracted parameters will be quoted in future chapters when necessary.

In future chapters, a standard fluorescence decay will be required for verification of new and newly optimised sensing schemes. As the fluorescence decay function of the oxygen indicator is complicated and dependent on many variables, a titanium–doped-sapphire crystal, which has highly predictable behaviour, was employed to check the interrogator. In this chapter, the Ti:sapphire 'calibration reference' was described, which, by controlling the crystal temperature, provides an exponential fluorescence decay of lifetime between **2.9 and 3.3μs**, **stable to 1.3ns Hz$^{-0.5}$** over a 100s test log. The use of a Ti:sapphire probe for calibration of optical sensors was first suggested as part of this work [16], and is one of the major novel contributions.

1.5. References for chapter 2

1. Draxler, S.*, et al.*, *Effects of Polymer Matrices on the Time-Resolved Luminescence of a Ruthenium Copmplex Quenched by Oxygen.* Journal of Physical Chemistry, 1995. **99**: p. 3162-3167.

2. Xu, W., Kneas, K.A., Demas, J.N. and Degraff, B.A., *Oxygen Sensors Based on Luminescence Quenching of Metal Complexes: Osmium Complexes Suitable for Laser Diode Excitation.* Analytical Chemistry, 1996. **68**(15): p. 2605-2609.

3. Xu, W.*, et al.*, *Oxygen Sensors Based on Luminescence Quenching: Interactions of Metal Complexes with the Polymer Supports.* Analytical Chemistry, 1994. **66**(23): p. 4133-4141.

4. Klimant, I. and Wolfbeis, O.S., *Oxygen-Sensitive Luminescent Materials Based on Silicone-Soluble Ruthenium Diimine Complexes.* Analytical Chemistry, 1995. **67**(18): p. 3160-3166.

5. Navarro-Villoslada, F.*, et al.*, *Fiber-Optic Luminescent Sensors with Composite Oxygen-Sensitive Layers and Anti-Biofouling Coatings.* Analytical Chemistry, 2001. **73**(21): p. 5150-5156.

6. Lee, A. and Ohura, I., *Porphyrin-doped sol-gel glass as a probe for oxygen sensing.* Analytica Chemica Acta, 1997. **342**: p. 181-188.

7. Mills, A. and Lepre, A., *Controlling the Response Characteristics of Luminescent Porphyrin Plastic Film Sensors for Oxygen.* Analytical Chemistry, 1997. **69**(22): p. 4653-4659.

8. Demas, J.N., Harris, E.W. and Mcbride, R.P., *Energy transfer from luminescent transition metal complexes to oxygen.* Journal of the American Chemical Society, 1977. **99**(11): p. 3547-3551.

9. Meyer, T.J., *Photochemistry of metal coordination complexes: metal to ligand charge transfer excited states.* Pure and Applied Chemistry, 1986. **58**(9): p. 1196-1206.

10. Meier, B., Werner, T., Klimant, I. and Wolfbeis, O.S., *Novel oxygen sensor material based on a ruthenium bipyridyl complex encapsulated in zeolite Y: dramatic differences in the efficency of luminescence quenching by oxygen on*

going from surface-absorbed to zeolite-encapsulated fluorophores. Sensors and Actuators B, 1995. **29**: p. 240-245.

11. Choi, M.M.F. and Xiao, D., *Oxygen-sensitive reverse-phase optode membrane using silica gel-absorbed ruthenium(II) complex embedded in gelatin film.* Analytica Chemica Acta, 1999. **387**: p. 197-205.

12. Mills, A., *Optical sensors for oxygen: a log-gaussian multisite-quenching model.* Sensors and Actuators B, 1998. **51**: p. 69-76.

13. Carraway, E.R., J.N., D., DeGraff, B. and Bacon, J.R., *Photophysics and photochemistry of oxygen sensors based on luminescent transition-metal complexes.* Analytical Chemistry, 1991. **63**: p. 337-342.

14. Mills, A., *Response Characteristics of Optical Sensors for Oxygen : models based on a distribution in torr0 or kq.* Analyst, 1999. **124**: p. 1301-1307.

15. Mills, A., *Response characteristics of optical sensors for oxygen : a model based on a distribution in torr0 and kq.* Analyst, 1999. **124**: p. 1309-1314.

16. Austin, E., Dakin, J. and Strong, A.P. *Use of transition-metal-doped sapphire crystals to calibrate and thermally compensate fluorescent-lifetime chemical detectors (keynote communication).* in *EUROPT(R)ODE V* 16-19 April 2000 Lyon, France, KC9,

17. Austin, E.A.D. and Dakin, J.P. *Opto-electronic systems for addressing Ru oxygen sensors:their design optimization and calibration process (invited).* in *SPIE: Fiber Optic Sensor Technology and Applications* 28 October - 2 November 2001 Boston,USA, 4578-06,

18. Choi, M. and Xiao, D., *Single Standard calibration for an optical oxygen sensor based on luminescence quenching of a ruthenium complex.* Analytica Chemica Acta, 2000. **403**: p. 57-65.

19. Nelson, D.F. and Sturge, M., *Relation between absorption and emission in the Region of the R lines of Ruby.* Physical Review, 1965. **137**(4A): p. A1117-A1130.

20. Zhang, Z., Grattan, K. and Palmer, A., *Temperature dependences of fluorescence lifetime in Cr3+ doped insulating crystals.* Physical Review B, 1993. **48**(11): p. 7772-7779.

21. Byvik, C.E. and Buonchristiani, A.M., *Analysis of Vibronic Transitions in Titanium Doped Sapphire using the temperature of the Fluorescence Spectra.* IEEE Journal of Quantum Elelectronics, 1985. **QE-21**(10): p. 1619-1626.

2. OPTICAL ARRANGEMENT FOR THE INTERROGATION OF FLUORESCENT INDICATORS

2.1. Introduction

As explained in the introduction, for real-world verification of the new and newly optimised sensing schemes, a fluorescence interrogation instrument was required. All sensing schemes must illuminate the indicator with appropriate excitation light, and detect the resultant fluorescence. Suitable optical arrangements will be described in this chapter.

The elements required are; an excitation light source, a light directing, guiding and filtering system to convey this to the indicator and to collect the resulting fluorescence, and an optical detector to measure the fluorescence. Many previous researchers have achieved this by constructing large experimental setups on the optical bench. For example the work by Xiao *et. al.* in 1999 [1], used a nitrogen laser to verify millisecond lifetime fluorescence from lanthanides, or the study by Chan *et. al.*[2], where a 20kW pulsed nitrogen laser was used to verify their newly proposed sensing scheme. Large commercial fluorometer instruments are also sometimes used. These intractable arrangements would be impractical in most real-world sensing applications, where lightweight or portable and low power instrumentation is required, so, for this study, only the light levels and signal processing schemes that could be achieved within a single (250x340x70mm) bench-top format enclosure, and standard PC computer, were considered. To achieve this, special instrumentation was designed and built with these constraints in mind, similar to that available commercially, to provide test-bed systems for verifying the new and newly optimised sensing schemes presented in following chapters. These instruments were also used for quantifying the effectiveness of anti-fouling layers as part of the BOSS research programme (see appendix).

Many important, but often neglected, effects where considered, such as the thermal response of the optical components (which introduce errors in measurement, dependent upon ambient temperature), the undesirable additional fluorescence generated by the optical components and cements used to bond them together (called ‘auto-fluorescence’), and minimisation of cross-talk between excitation source and fluorescence detector. By

verifying these characteristics, correct operation of the optical arrangement was guaranteed.

The last of these, (minimisation of cross-talk between excitation and detection systems) was perhaps the most difficult to successfully avoid. Although various optical arrangements can optimise it, the fluorescence light returning from the indicator is usually very weak. In the system to be described here (where a single optical fibre was used for both conveying excitation and collecting fluorescence from the indicator) an incident 14.1μW of excitation light guided to the indicator resulting in only 500pW peak of fluorescent to the detector (i.e. 14dB less). This means that when the sensing scheme requires the fluorescence signal to be measured at the same time as the outgoing excitation source is illuminated (e.g. the intensity modulated source interrogator, chapter 4), then the component of excitation light reaching the detector must be attenuated by much greater than 14dBs, (at least 30dBs) so that the measured unwanted excitation light contribution is much smaller than the fluorescence signal itself.

In the following chapter, first the excitation light source, then the optical coupling system which conveys excitation light to the indicator, then the optical detector used for measuring the resulting fluorescence are discussed in turn. Optical filters were required to separate excitation and fluorescence light; these are then considered. Finally the precautions taken to ensure correct operation of the interrogator are discussed.

A Ruthenium based oxygen indicator having spectral absorption in the blue region (peaking at 460nm) and orangy-red resulting fluorescence (peaking at 620nm) was assumed.

2.2. Excitation source

To excite fluorescence from the indicator, a light source with suitable blue (400-500nm, to excite the indicator) output was required. Bulk laser sources (mainly Argon-Ion or N_2 type) are widely used in the laboratory, due to the large number of available lasing lines (which allows tuning of the excitation wavelength to the peak absorption wavelength of the indicator), the high output power available (which maximises resulting fluorescence) and the lack of significant out-of-band emissions (which could be confused with fluorescence). Their size, weight, and complexity make them unsuitable for portable or lightweight sensing applications. Current state of the art blue laser diodes exist and are small and light, but still rather rare and expensive and would probably give more problems

of photo-bleaching (due to elevated excitation power). Nichia Chemical Industries have produced a gallium-nitride laser diode, available only for evaluation, but at a cost of $3000 and with an expected operational lifetime of only 500 hours. This leaves either high intensity blue LEDs or perhaps filtered flashlamps. Flashlamps, though capable of providing short (<1μs) high-intensity pulses of light (up to 0.1J/pulse), are housed in very high-pressure bulbs, and require a high voltage power supply and a special charging capacitor to operate effectively. Few models are capable of greater than 100Hz repetition frequency, which does not allow optimal interrogation of most oxygen indicators with microsecond lifetimes (see chapter 4 for discussion of optimal repetition rate). Another likely disadvantage of the flashlamp is the greater auto-fluorescence from the optical filtering required to select the blue output from the white light and near-UV flashlamp output.

For these reasons, InGaN blue LEDs are currently the most favourable source for fluorescence interrogation systems due to their unrivalled low cost (<$1), small size (available in 5x7mm or smaller connectorised packages), simple drive requirements (a current of around 50mA at a saturated voltage of around 3V), reasonably high output power (some are now multi-milliwatt) extended operational lifetime (well over 1K hours), and rapid and thermally independent switching characteristics. (One study [3] showed the output from the LED resulting from a 10ns wide pulse had disappeared after 40ns.) In comparison to these compelling features, their disadvantages (principally, low output power), are generally considered acceptable. LEDs are employed in the vast majority of fluorescence interrogation instrumentation. They were also chosen for this study.

To identify the best LED for this application, examples manufactured by Nichia industries (NSPB300 series), CEL (the L-513UBC-S), the MBB51TA-L from Micro Electronics Corporation, the E474 from Gilway Technical Lamps, and the Hewlett Packard HLMP-CB15 were purchased and compared for brightness, viewing angle (i.e. degree of collimation of the output beam), and output power. Following these investigations, the HP HLMP-CB15 was selected, as it has higher output power (a luminous intensity of 765mcd, which is equivalent to a radiative flux of $10mWsr^{-1}$ was specified by HP), and emits the most collimated beam, removing the need for an external collimating lens (a viewing angle of 15° was specified in the manufacturer's data).

It is well documented that blue InGaN LEDs produce significant (though weak) UV and orange-red light side emissions (e.g. [4], and [5]). Both of these components are unwanted and must be removed by the use of appropriate optical filters. Red spectral output

components are particularly troublesome as they are spectrally indistinguishable from the fluorescence emission produced by the indicator itself, so if coupled back to the detector, can cause cross-talk. In the absence of adequate filtering, such coupling is likely to occur as a result of reflections or elastic scattering at the probe itself, at polished fibre ends and due to any other spurious reflection or diffuse scattering within the instrumentation. For this reason, it has been necessary to attenuate these emissions by placing optical filters in front of the LED. The UV and short-wavelength emissions from the blue LEDs were thought to be potentially damaging to the indicator dye or support matrix, principally due to their higher photon energy (see chapter 7), and they are more likely to excite fluorescence in fibres, filters and bonding cements, so it was desired to also attenuate these wavelengths from the LED output. The optical filters will be discussed later.

2.3. Coupling to the Indicator

2.3.1. General Aspects

To convey excitation light to the fluorescent indicator next to the analyte and collect the resulting fluorescence, an optical coupling arrangement (termed the 'sensing head') is required.

Many arrangements have been described in the literature. The simplest of these have been based on bulk (i.e. no optical fibre) optics, where the LED light shines, via a suitable optical filter, onto the fluorescent indicator, whilst the resulting fluorescence is conveyed to the detector again via optical filtering. As an example, a bulk optics arrangement was used, in conjunction with a platinum (II) - octaethylporphyrin – ketone indicator in a rapid response oxygen sensor for real-time breathing gas analysis, with a t_{90} (time to achieve 90% of intended value) of 20ms [6]. Their sensing head design (shown schematically in Figure 2.1), incorporated an additional reference photodiode to compensate for fluctuations in the excitation LED intensity.

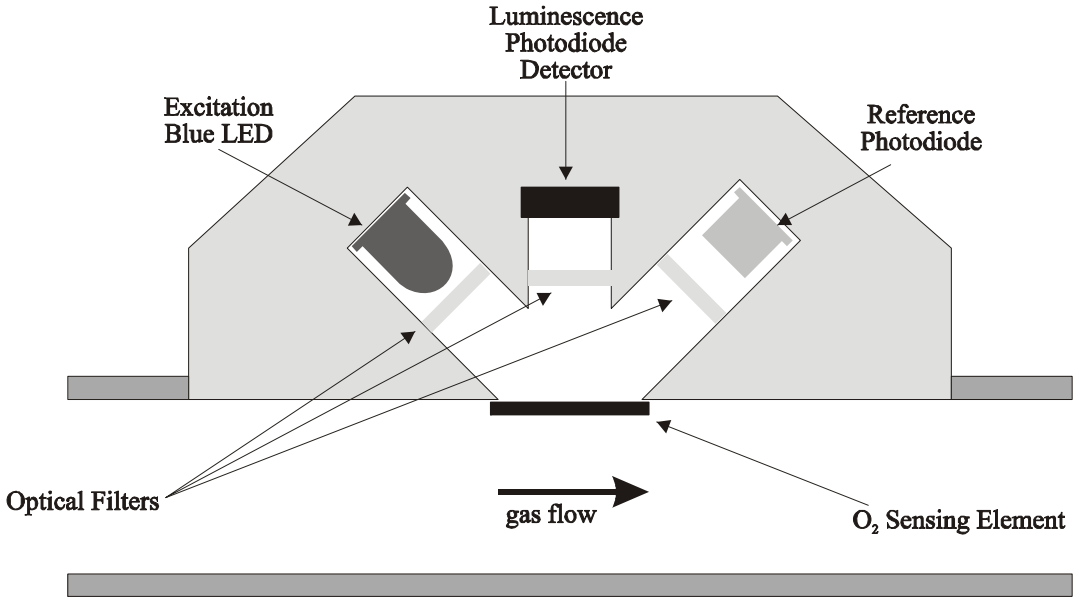

Figure 2.1 Oxygen sensor for real-time breathing gas analysis, employing bulk-optics employed in [6]. Fibre remoted systems are preferred in most applications, but this work needed the highest possible optical intensities to allow the shortest possible averaging times for rapid analysis.

Although useful for achieving the highest fluorescence intensity and best optical coupling to maximise the ratio of detected fluorescence to emitted excitation, bulk systems have many drawbacks when compared with fibre-based solutions. In particular, a fibre connecting lead conveniently separates the electro-optic interrogation unit and optical sensing head. This brings all the advantages of remote fibre-based detection – immunity to electromagnetic interference at the sensing point, possibility of a very large (>10m) distance between interrogator and probe (e.g. for operation in remote inaccessible or hazardous conditions), miniaturisation of sensing head and the possibility to multiplex many probes via a simple optical fibre switch. Remote detection has been a feature of most modern optical chemical sensing research, either by using a dual or bifurcated fibre system, where one fibre carries the excitation light and the other guides back the resulting fluorescence, or a single fibre, where the same fibre carries excitation and fluorescence light. For reasons of low cost, flexibility of connection fibre, simplicity of miniature probe fabrication, and possibility of simpler probe multiplexing, a single fibre system was used in this study. Generally, large core diameter multimode fibres are advisable with LED sources to maximise excitation and fluorescence power.

To launch excitation light along the connecting fibre, and to couple the resulting fluorescence to an optical detector, a bulk optical arrangement was required within the interrogator unit housing. Several arrangements have been proposed, two of which are described in Figure 2.2. On the left of the figure, a mirror, mounted at 45° to the fibre,

reflects returning fluorescence into the detector. A small hole at the mirror's centre allows passage of the excitation beam into the fibre. On the right, the excitation light beam is reflected into the fibre by a small mirror mounted at 45° into the fibre. The returning fluorescence is collected by the remaining unobscured portion of a collimating lens and hence observed by the detector. These methods offer no intrinsic spectral selectivity to aid separation of excitation and fluorescence light, and require a highly collimated (e.g. laser) excitation light beam.

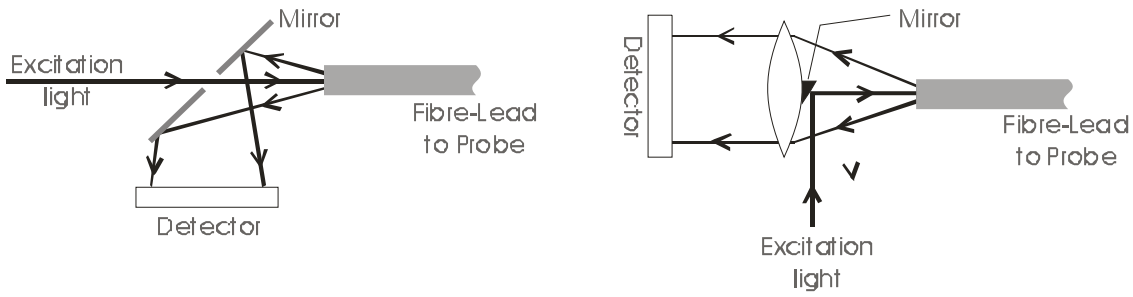

Figure 2.2 Alternative arrangements for coupling excitation and collecting fluorescence to and from the fibre connecting lead. These schemes require highly collimated (e.g. laser) excitation light and offer no intrinsic spectral selectivity.

2.3.2. The preferred coupling system

We will now describe the preferred method, which was used in the interrogation units described here.

The coupling system incorporated a dichroic filters, as shown in Figure 2.3. The dichroic filter itself will be described in detail later in this chapter, so here it is simply noted that, when mounted at 45°, the filter operates like a wavelength-selective beam-splitter. The excitation light was reflected to the fibre launch lens by the dichroic filter. The red fluorescence signal, (returning from the same fibre), was transmitted by the dichroic filter to impinge, (via a final optical filter) on a suitable optical detector. Together, this arrangement was termed the 'optical filter block' and was constructed in a custom built aluminium block of dimension 50x25x25mm. An 'FC' type fibre connector (Sieko instruments) was employed to allow simple exchange of fibre probes. A pure silica high OH fibre with 600µm core diameter 630µm cladding diameter (Newport type F-MBD) with a high N.A. of 0.37, was identified as the largest core diameter fibre available (therefore the best fluorescence coupling possible) which retaining adequate mechanical flexibility.

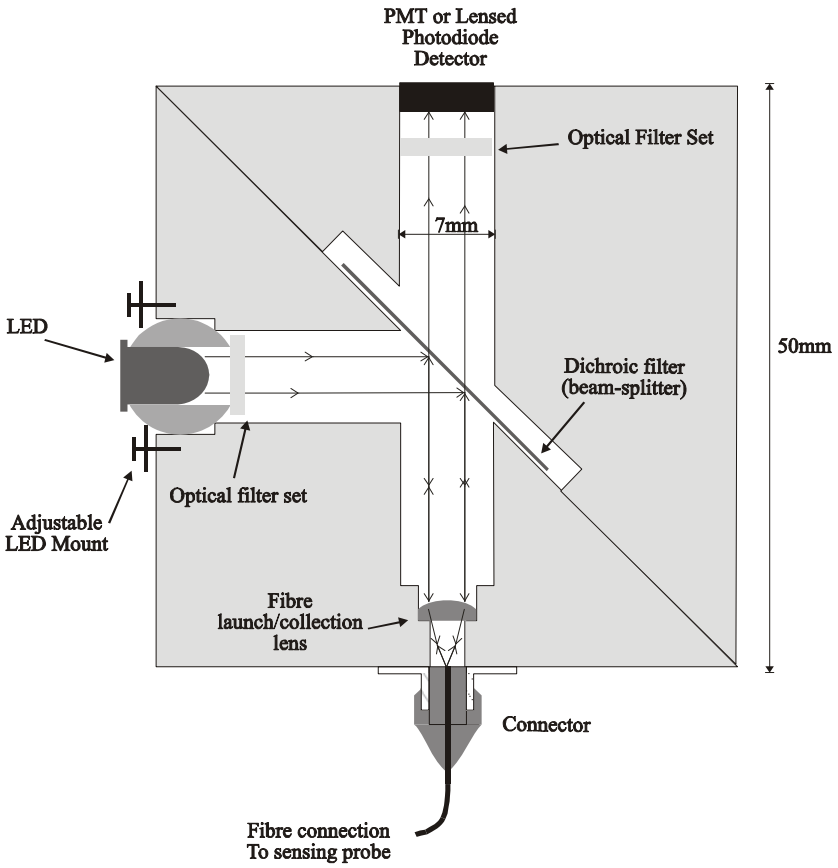

Figure 2.3. The 'Optical Filter Block'; a coupling system to convey excitation light to the fibre and to detect returning fluorescent light. An FC type connector (at the bottom of the figure) was used to connect the lead to the sensing probe.

A probe was required to suspend the membrane (cut to a 6mm disc) and connecting fibre, such that the membrane was in contact with the analyte solution and the fibre tip. In this way, excitation light was directed onto the sensing membrane and some of the resulting fluorescence collected. The probe is shown in Figure 2.4.

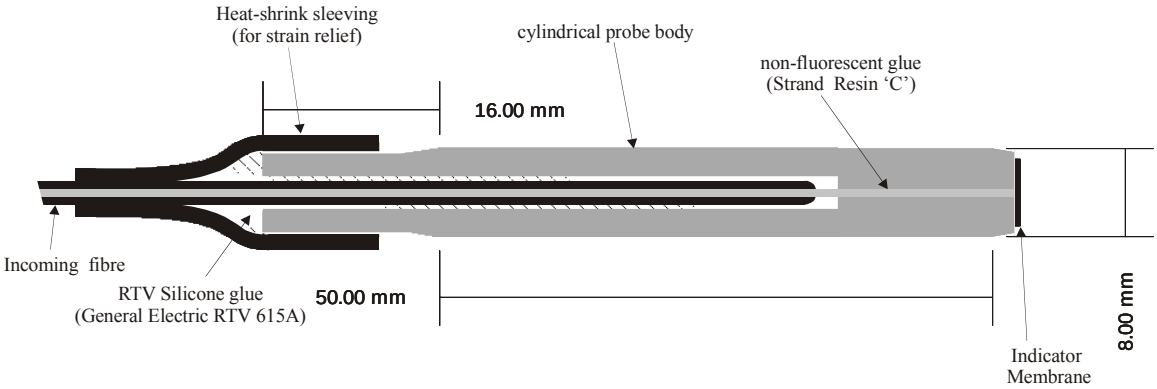

Figure 2.4 Probe for dissolved oxygen measurements. The probe provided support so that the membrane could be placed in contact with the analyte, whilst fluorescence (promoted by excitation light from the fibre), was in part guided back into the fibre.

A 2m length of fibre (jacketed in black non-fluorescent opaque sleaving) with a custom-modified 'FC' type connector (adhesive with a very low fluorescence under blue excitation was required, see later) formed the remainder of the sensing probe. This arrangement is pictured in Figure 2.5.

Figure 2.5 Probe (left), 2m connecting fibre lead, and modified (for low auto-fluorescence) 'FC' type fibre connector (right). The probe body measured 70x8mm.

2.4. Fluorescence Detector

An optical detector was then required to measure the returning fluorescence intensity. Different optical detectors were required for each of the two main sensing schemes considered. For interrogation by direct decay curve analysis (which will be described in chapter 4), a Photo-Multiplier Tube configured as a photon counter was employed. This selection will be justified in chapter 4, but here it is simply noted that this detector had a large enough sensitive area (8mm diameter, circular) to not require any additional lensing (a Hamamatsu H7155-01 integrated photon counter was used). For interrogation of fluorescence from modulated-excitation, a Centronic type BPX65RT photodiode (with 1mm^2 active chip area) was chosen (see chapter 5). This model came factory fitted with focussing lens, so that its effective sensing area for collimated light was a 5mm in diameter. Again no further lensing was required.

2.5. Optical Filtering

The use of well-selected optical filters is crucial to the effective design of a fluorescence monitoring system.

Optical filters are used to selectively transmit certain parts of the optical spectrum (the in-band wavelengths), whilst blocking other parts (out-of-band wavelengths). Filters

transmitting long wavelengths and blocking shorter wavelengths are ‘long-pass’ filters, those transmitting a defined intermediate range of wavelengths are called ‘bandpass’ filters, and those blocking long wavelengths, but transmitting short, are called ‘shortpass’ filters.

Optical filtering was required here to attenuate unwanted out-of-band emissions from the LED excitation source, to form the dichroic beam-splitter itself, and to attenuate non-fluorescence light before falling on the detector.

Due to the need for compact, inexpensive instrumentation, only two types of optical filter were considered. ‘Absorbance’ or ‘coloured glass’ filters are made from glass engineered, by adding dopant, to attenuate certain wavelengths. These are available in a wide range of types and are characterised by high (more than 50dB) out-of-band attenuation. The degree by which wavelengths are attenuated may be conveniently tuned by specifying filter thickness, and hence the interaction length between the absorbing coloured glass and incident light. The thermal properties of the filters were adequate for the purposes of this study, as most filters present a linear increase in cross-over (50% transmission) wavelength of between 0.020nm and 0.024nm per °C [7] (as the stokes’ shift of the oxygen indicator is of order 200nm, this drift is negligible). The main disadvantages of coloured glass filters for this application are is that they can exhibit auto (or self)-fluorescence (which is created by relaxation from the excited states of the absorbance glass itself following excitation by absorbed incident light) and their in-band attenuation. Although not serious for longer wavelengths in long-pass filters, in-band attenuation can be quite severe for certain coloured glass filters when a wide thickness is required (the Schot Glas BG12 filter, at 5mm thickness, transmits only 47% of incoming light at 400nm, its peak transmission wavelength). Auto-fluorescence is discussed in more detail later, so here it will simply be noted that extra fluorescence generated by the optical filters themselves is highly undesirable.

The second type of optical filter considered was the ‘dichroic’ or ‘interference’ filter, where a transparent substrate is coated with thin films of dielectric material. A fraction of incident light is reflected at the boundary between each film, so by altering the thickness and number of coatings, the reflections can be engineered to give constructive or destructive interference according to wavelength. In this way, filters with almost any spectral characteristic can be produced. Blocked wavelengths of incident light are reflected (not absorbed, as in coloured glass filters) so dichroic filters produce negligible auto-fluorescence. Unfortunately, most available dichroic filters generally do not attenuate

out-of-band wavelengths as effectively as coloured glass alternatives (usually around 30dBs is achieved), possibly due to imperfections in the film deposition process and limitations on film quantity.

As stated above, the main function of the optical filters was to; minimise the cross-talk signal (i.e. the blue excitation light reaching the detector), maximise the level of excitation light that reaches the sensing layer, maximise the returning fluorescence signal and produce negligible self-fluorescence. A dichroic filter was necessary for splitting the excitation and fluorescence light, but the emission and fluorescence filters could be made from absorbance or dichroic types. The high out-of-band attenuation characteristic of absorbance filters was required, but the auto-fluorescence produced was unacceptable. Similarly, the negligible auto-fluorescence from dichroic filters was desirable, but their poorer out-of-band attenuation was not sufficient.

These different performance strengths were combined by cementing combinations of absorbance and dichroic filters next to each other, to form filter 'sandwiches'. When a short-wavelength-passing, long-wavelength-blocking filter was required (i.e. the excitation filter in front of the LED), an absorbance filter was placed first (to strongly attenuate the unwanted long-wavelength light), followed by a short-pass dichroic filter to block the weaker auto-fluorescence from the filter (which has longer wavelength, due its Stokes' shift). When a long-wavelength-pass filter was required (i.e. to block stray excitation light from the detector), a long-pass dichroic filter was placed before the absorbance filter to attenuate short wavelengths before they reach the absorbance filter, thereby reducing the auto-fluorescence produced.

2.5.1. Optimal filter identification

Optimal operation of the interrogator was dependent upon selecting appropriate optical filters from the myriad of available options, to form appropriate sandwich filters for blocking unwanted emissions from the excitation LED, for making the dichroic beamsplitter, and for blocking unwanted excitation light from the fluorescence detector. To identify this optimum, the absorbance spectra of filters from Schott Glas, OCLI, Omega Optical and Andover were first measured in the range 200-1200nm using a Perkin-Elmer Lambda 9 spectrophotometer, which is capable of measuring an absorbance of 5 (i.e. an optical density of 50dB) from 200-860nm, falling to an absorbance of 3 at 1200nm (this is due to a change of excitation lamps within the instrument at 860nm). The dichroic beam-splitter alternatives were placed in the spectrophotometer at 45° to simulate their

angle of incidence in the filter block. Manufacturer's published data could not easily be used because in most cases this was incomplete, or it did not extend over this complete spectral range. (Filters, particularly dichroic types, often have inconvenient transmittance of wavelengths far from their transmission peak). A computer simulation was devised to aid optimal selection from the possible combinations, by simulating the spectral transmittance effects of each filter on the LED spectral curve and power. In this way, for any combination of optical filters, the excitation spectrum and power, and the proportion of crosstalk to fluorescence signal expected at the detector was modelled.

2.5.2. Excitation source filter

The filter 'sandwich' chosen for blocking unwanted emissions from the LED is shown in Figure 2.6. The purpose, type, maker and model number of each filter is described within the figure.

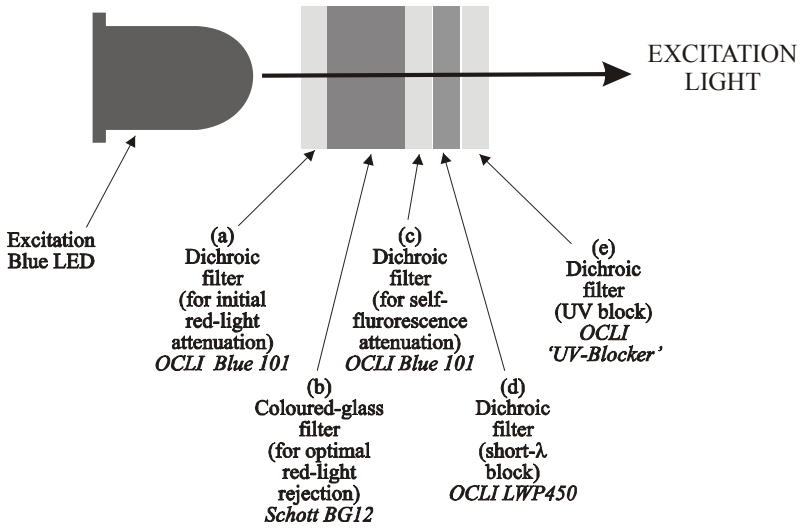

Figure 2.6 LED emission filter 'sandwich' to combine high attenuation of out-of-band emissions with low-auto-fluorescence. The purpose, type, maker and model number of each filter is described within the figure.

The absorbance spectra of these filters and the spectral output of the LED excitation source are plotted Figure 2.7. The filter measurements were measured in-house, as described above the LED spectral output was taken from manufacture's data. As we can see, when the filters are combined in a sandwich, wavelengths longer or shorter than the LED excitation maximum (470nm) are strongly attenuated (by absorbances of more than two). The resulting excitation spectrum, measured from the real interrogator, is given in a following section.

The LWP 450 and UV blocking filters were added for the decay-resolving instrument to reduce excitation power (discussed below), and possibly reduce excitation light induced degradation of the fluorescence indicator (see chapter 7).

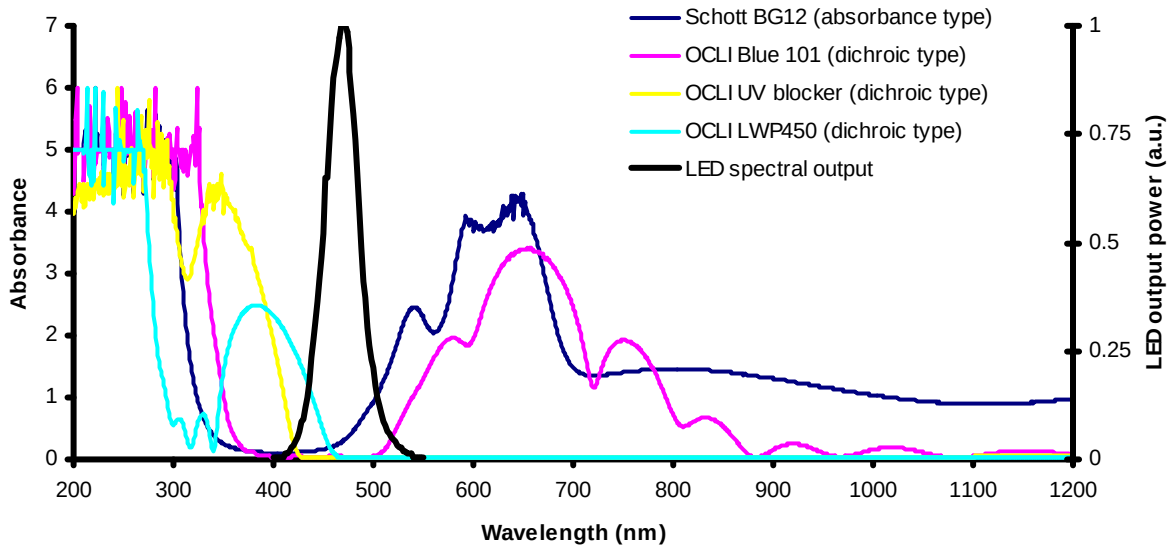

Figure 2.7 Spectral absorption of filters in the LED excitation sandwich and spectral output from the LED itself. The function of each of the filters is explained above. The OCLI LWP450 and UV blocker filters were added for the decay-resolving instrument to reduce excitation power, and possibly reduce excitation-light-induced degradation of the fluorescence indicator.

2.5.3. Dichroic beam-splitter

To reflect the blue excitation light into the fibre launch optics, and to transmit the resulting fluorescence to the detector, the Schott Yellow 604 filter having 510nm cutoff, (when measured at a 45° angle of incidence) was identified as the optimum filter, and is shown in Figure 2.8. The filter absorbance was measured at a 45° angle of incidence to simulate incident light in the transmission arm of the filter block assembly.

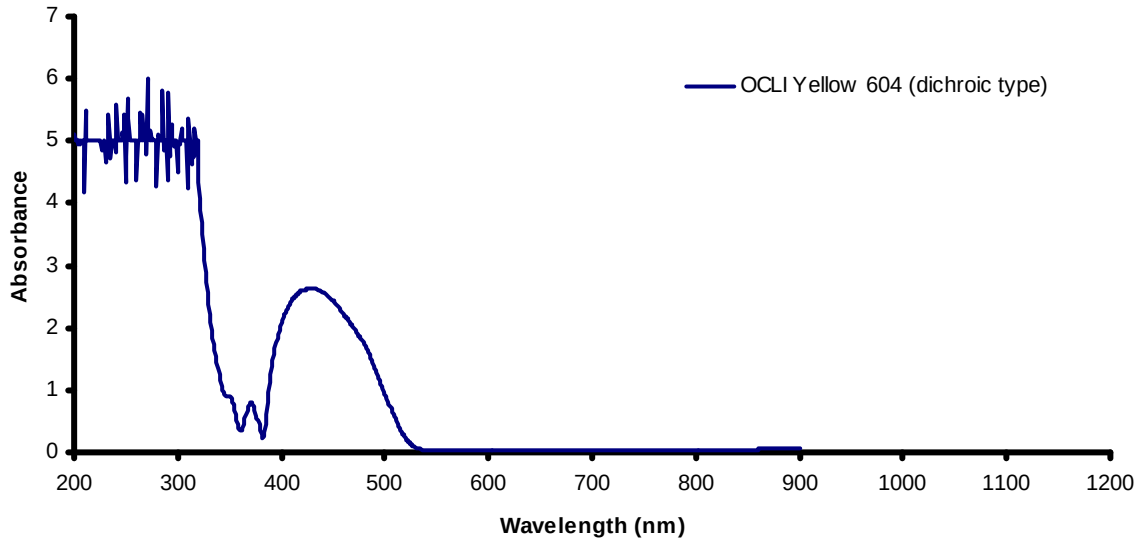

Figure 2.8 Spectral absorbance of the dichroic OCLI Yellow 604 filter used for beam splitter purposes. This plot was measured at a 45° angle of incidence, to simulate the transmission arm of the filter block.

2.5.4. Detection filter

The requirements for the optical filters in the fluorescence light path are simpler, as they should convey the fluorescent light wavelengths (the fluorescence spectrum is plotted in Figure 2.10) with little loss, prevent undesirable blue excitation light reaching the detector, and add minimum unwanted fluorescence from the optical filtering system itself. A filter combination consisting of blue blocking red passing dichroic filter (OCLI 'Yellow 604', 560nm cutoff with normal incidence) was placed before a (Schott OG590) red passing absorbance filter in front of the detector. The absorbance spectra of these filters is shown in Figure 2.9.

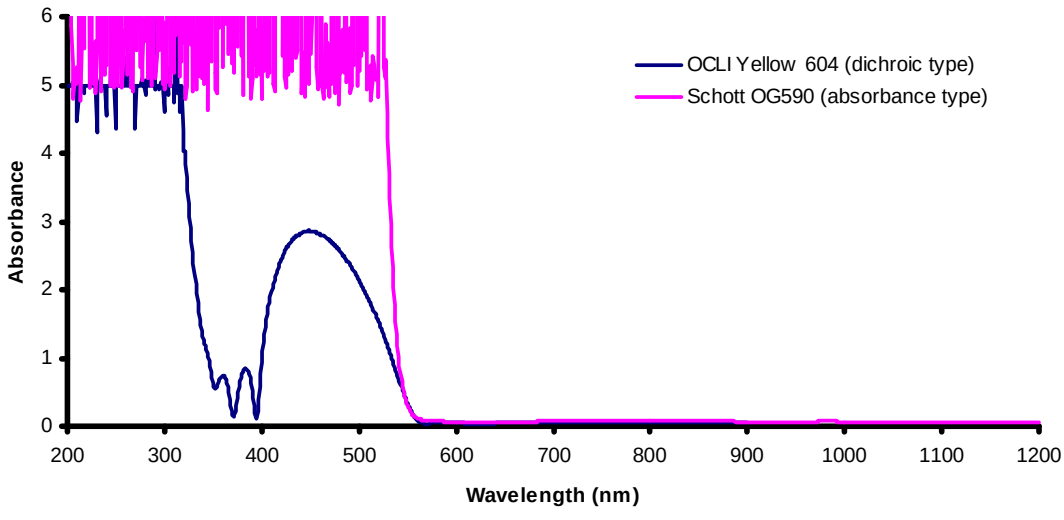

Figure 2.9 Spectral absorbance of the dichroic OCLI Yellow 604 filter used for initial blocking, and OG590 filter used for high attenuation of residual excitation light. (For this plot, the Yellow 604 filter was measured using normally incident light).

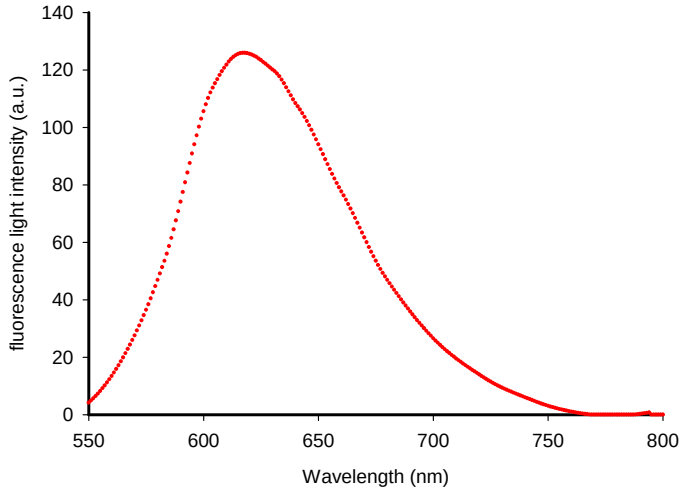

Figure 2.10 Fluorescence production spectra for $[Ru(dpp)_3]^{2+}$ oxygen indicator membrane under blue light excitation. (Provided by Professor G. Orellana's group from Universidad Complutense in Madrid, measured using a custom-made CCD device, LAP-1000).

2.5.5. Rejection of Filters

To check for adequate rejection between the excitation light and the detector, the absorbance of all the optical filters used to filter the LED, split the beams and block stray light to the detector were sandwiched together, and their total absorption measured. The resulting spectrum is shown in Figure 2.11. An absorbance of more than 5 below 800nm, and more than 3 above 800nm, where the instrument changes light sources and detectors, was achieved. These figures represent the limit of detection of the spectrophotometer, proving excellent attenuation of excitation light in the range 200-1200nm range.

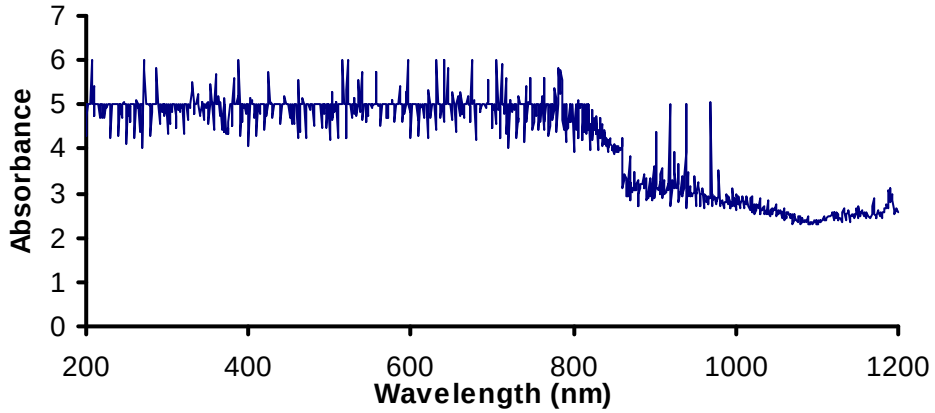

Figure 2.11 Total absorption of all the optical filters used. An attenuation in excess of the limitations of the spectrophotometer was measured throughout the 200-1200nm range, showing excellent rejection of excitation light.

2.6. Excitation Light level and fluorescence produced

We shall now describe the excitation light levels and spectra produced and the resulting fluorescence collected from the instruments. Two optical arrangements were fabricated, one for each of the distinct sensing schemes explored; modulated excitation source delay interrogation (in chapter 5), and direct decay analysis (in chapter 4). The results from each set of measurements are given here.

2.6.1. Delay-monitoring modulated source interrogator

The UV blocking and long-wave pass (LWP450) filters were omitted from the excitation filter sandwich to optimise excitation power and hence increase the fluorescence power falling on the insensitive photodiode detector. A peak excitation power of **14.1±0.1μW** (measured with an Ando AQ-6315A optical spectrum analyser, estimated error) was launched into the fibre (the LED drive current was 76±0.5mA during the peak of its modulation). This lead to **500±25pW** of fluorescence light power arriving at the detector. This was calculated from the voltage present at the detector pre-amplifier output, knowing the detector responsivity and the total gain of the receiver (to an accuracy of 5%) – again see chapter 5. The excitation spectrum achieved is plotted with the absorption spectrum (i.e. proportion of incoming light absorbed by the membrane) of the oxygen sensing membrane in Figure 2.12. The LED drive current was reduced to 40±0.5mA, its maximum continuous drive current value. The absorption spectrum of the membrane was measured using a UV-VIS spectrophotometer by Professor G. Orellana's group from Universidad

Complutense in Madrid. The excellent overlap between the two curves ensures efficient excitation of the membrane. Note the larger than 50dB difference between the peak 470nm excitation power (at –32dBm), and the residual undesirable red excitation power (less than -85dBm, below the noise limit of the ANDO measurement instrument). This helped to ensure a low level of excitation-light induced cross-talk during fluorescence measurements.

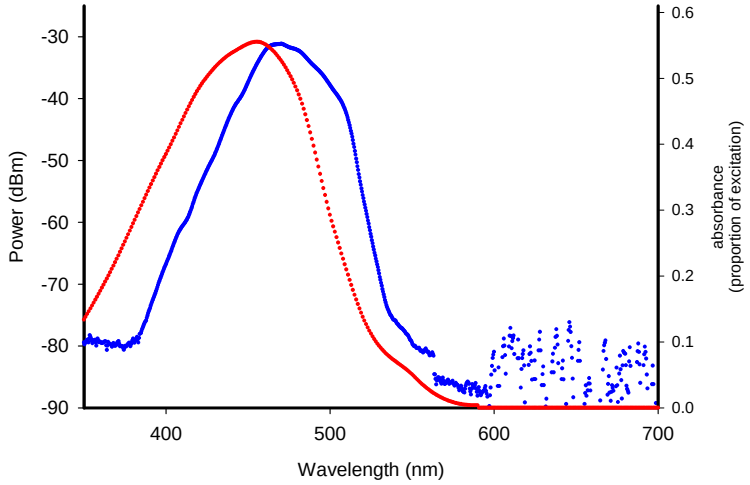

Figure 2.12 Modulated source interrogator excitation spectrum (blue, left y-axis), and absorption of $[Ru(dpp)_3]^{2+}$ oxygen indicator membrane (red, right y-axis). The excitation spectra was measured using a fibre-coupled OSA, Ando AQ-6315A OSA. The capture resolution was 5nm, and the LED drive current was 40mA (the maximum continuous drive current possible). The overlap ensures adequate excitation of the oxygen indicator.

2.6.2. Direct fluorescence decay curve interrogator

As stated above, the Hamamatsu H7155-01 photon counting PMT detector was chosen for direct decay curve interrogation. The reasons for this choice, and the principle of photon counting detection will be described in chapter 4, but here we simply note that significant 'pulse-coincidence', or saturation of the detector, occurs whenever light levels in excess of 15pW are presented to the detector. Hence, the 500pW fluorescence signal produced by the modulated-source interrogation optical arrangement would be far too great for the PMT detector. The returning fluorescence power was therefore reduced to a more moderate level by significantly lowering the LED drive current (to 150±15μA) and by adding the UV blocking and long-wave pass (LWP) filters into the excitation filter sandwich Figure 2.6. This resulted in a new excitation power of **7.4±0.5nW** (again measured with the Ando AQ-6315A optical spectrum analyser, estimated error), and a resulting fluorescence of (at peak) **12.5±0.1pW** (error estimated from possible variation in

detection efficiency). (The ratios between fluorescence and excitation power are different for the two interrogators, because the excitation spectrum from the direct fluorescence decay interrogator differs from that of the modulated source interrogator.) The excitation spectrum is plotted with the absorption of the membrane for this interrogator in Figure 2.13. The overlap between the two curves again ensures efficient excitation of the membrane.

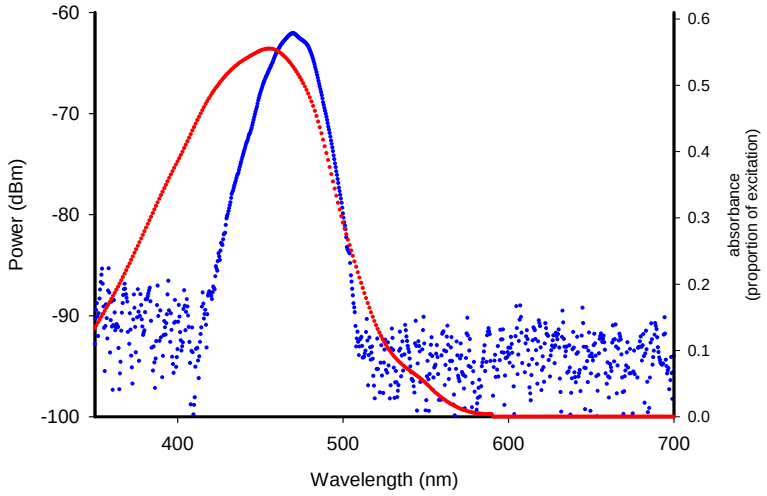

Figure 2.13 Excitation spectrum used for the fluorescence decay curve measurement (blue, left y-axis), and absorption of $[Ru(dpp)_3]^{2+}$ oxygen indicator membrane (red, right y-axis). The excitation spectra was measured using an Ando AQ-6315A OSA. The capture resolution was 5nm, and the LED drive current was 146μA. The overlap ensures adequate excitation of the oxygen indicator.

2.7. Precautions to Ensure Adequate Sensor Stability

Several often-overlooked precautions were taken to ensure stable and expected operation of the interrogators. These are discussed here.

2.7.1. Time response of the excitation source

The excitation source (an InGaN blue LED from HP), should respond to changes in drive current much more rapidly than the characteristic response time (fluorescent decay time) of the indicator. Any significant time delay in the response of the LED itself could introduce unwanted decays indistinguishable from the fluorescence itself. The short time scale behaviour of such devices was investigated by Choa *et. al*. in [3], where the output from a Nichia InGaN LED was captured by a polychromatic streak camera (a device based on deflection of photo-electrons, capable of resolving spectral snapshots at repetition intervals of just a few ns) whilst driven with 10ns duration pulses. This work showed how

the spectral output from the LED evolved in time. An initial UV output gave way to the main blue emission after around 20ns. After 40ns, 30ns after the drive current switched off, the LED's output was completely extinguished. The results from their studies are reproduced in Figure 2.14. Their work was focussed toward exploring the UV emission during the first moments of the LED's output, concluding that it was produced by a less favourable reaction within the LED, which quickly gave way to the more stable blue producing reaction. However, their study also conveniently captured the impulse response (i.e. the output following a very short pulse) from the LED with a high speed detection system. The output response time (the time between the start of the current pulse and the blue output reaching half its maximum value) of the LED was around 25ns, so for the purposes of this study, the LED can be thought of as having instantaneous response, as the shortest fluorescence lifetime to be measured was 1μs, much longer than 25ns.

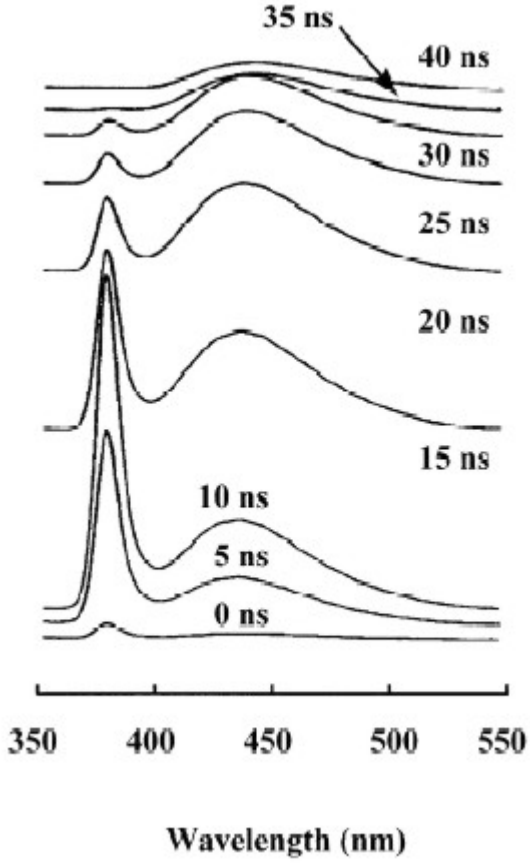

Figure 2.14 Time-resolved spectra of Nichia InGaN blue LED resulting from 10ns input pulse. Reproduced from [3] This shows the response time of the LED was less than 25ns.

The possibility of thermally induced variation in the output of the LED will be investigated later.

2.7.2. Minimisation of unwanted background fluorescence

As stated above, it was extremely undesirable to have fluorescent materials in the optical path other than the fluorescent indicator itself. This adds decay signals that provide, at best, a constant offset, and at worst, a temperature dependent drift in measurements. Background fluorescence always complicates characterisation and calibration of measurements. As explained above, the inherent auto-fluorescence from optical filters was minimised by constructing filter 'sandwiches'.

Another important source of unwanted fluorescence was found to be optical adhesive. Even the epoxy used by Newport (a large and reputable optics company) to secure their fibre inside connector ferules was found to be strongly fluorescent when illuminated with the blue excitation light. To alleviate this, an alternative non-fluorescent optical adhesive was required.

A simple experiment was devised to compare the fluorescence outputs from different commonly available adhesives. Several different clear transparent adhesives (including silicones, UV cure optical cements, and two-part epoxies) were cured in 10x5x5mm sample holders and exposed to 90mW of blue (476nm) excitation light from an argon-ion laser. The resultant fluorescence was measured by placing a strongly blue absorbing filter (in this case the lens from a pair of laser safety goggles, Laser-guard type 'argon') in the light path between the glue sample and detector, a Newport optical power meter fitted with a silicon detector head. The specifications of the filter (OD>9 at 476nm) ensured excellent rejection of excitation light, leaving only the fluorescence light progressing to the detector. The fluorescence produced by the cements varied considerably, ranging from 5μW produced by a West System two part epoxy, to negligible (i.e. immeasurable by this method) fluorescence produced by Norland type N61 UV curing epoxy. This N61 type was measured to produce 115nW, whilst an empty sample holder control was measured to produce 150nW of fluorescence! (This was believed to be due to additional reflection of the excitation light within the empty sample holder, causing more stray blue light.) Three adhesives were selected for use in the interrogators; Strand, Resin 'C' type styrene glue (designed for clear casting applications) for applications where a hard-setting epoxy was required (e.g. cementing the fibre into its ferule), a two-part room temperature vulcanising silicone rubber glue (General Electric type RTV615A) for use when more elastic adhesive is required (e.g. when fixing long lengths of fibre into test probes), and Norland N61 for when highly optically transparent bonding was required.

2.7.3. Thermal dependence of optical components

The predictable and stable operation of a fluorescence interrogation system is in great part dependent upon the thermal stability of the optical and electronic components within it. If any of these have thermally dependent characteristics then ambient temperature will effect measurements. Though this could be compensated for by the addition of an electrical thermometer to monitor the instrumentation temperature, this complication is undesirable.

The slight thermal dependence in the transmission spectra of optical filters (discussed above) was negligible for this application, but other components could have their own variability.

An experiment was devised to characterise the thermal dependence of the LED response time.

2.7.3.1. Thermal dependence of InGaN LED response

As mentioned earlier, all light sources have a characteristic response time required to establish a change in light output following a change in drive current. An experiment (see Figure 2.15) was devised to quantify the thermal dependence of the response time of the LED. The blue LED (HP type HLMP-CB15, as used in the interrogator optics), was placed inside a temperature controlled environmental chamber. The LED was driven (via 33R current limiting resistor) by a 5V square wave of frequency 100KHz, achieving a peak drive current of 50mA. The resultant light output was conveyed through the window of the chamber to a detector and transimpedance amplifier. The 1KΩ feedback resistor gives adequate gain and sets the bandwidth of the detection system to around 5MHz (measured by increasing the LED modulation frequency until the detector output was half its low-frequency value). Only an approximate measure of the detection bandwidth was required.

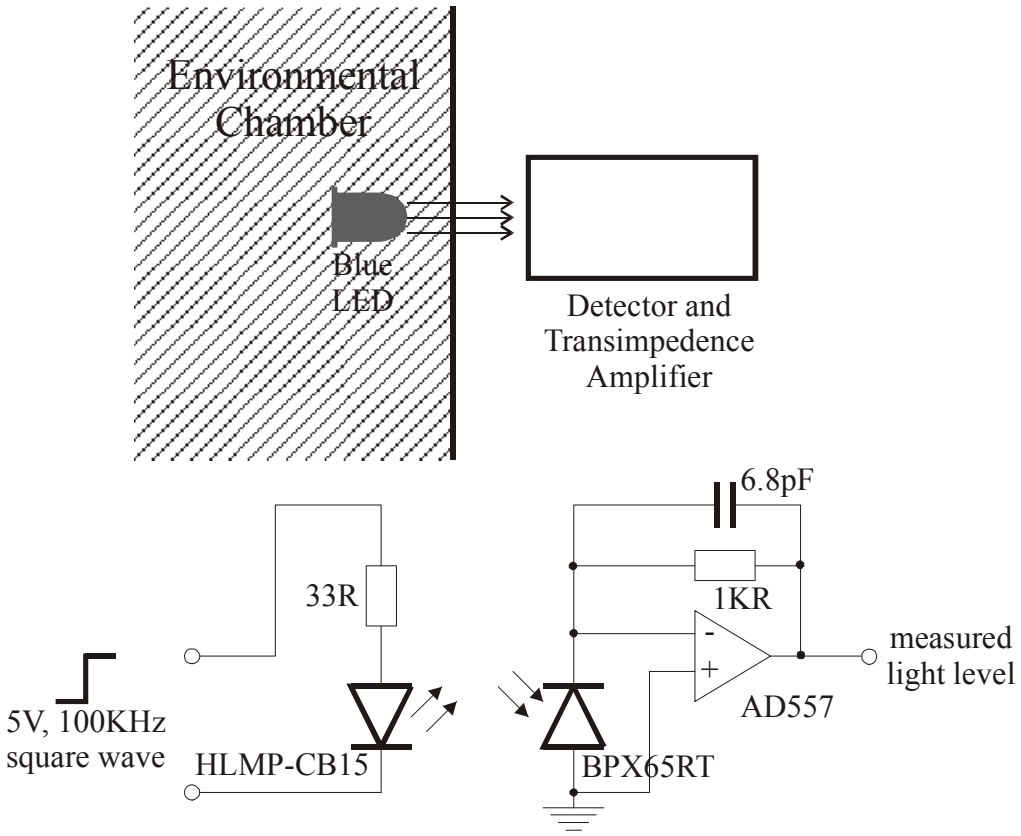

Figure 2.15 Testing the thermal dependence of LED output. The LED was placed inside a temperature controlled environmental chamber with glass door, such that its light output passed through the door to fall on the silicon photodiode detector. The output from the detector was monitored to measure changes in the response of the LED to temperature.

The LED extinction characteristic was captured at 25, 10, 40 and 50°C (Figure 2.16) and 25, 50 then returning to 25°C in Figure 2.17. A fall time of around 200ns was evident in all plots, which is similar to that expected from the measured bandwidth of the detector system itself. Hence any thermally induced change in the LED response time occurred on a time scale much smaller than 200ns, and is hence negligible.

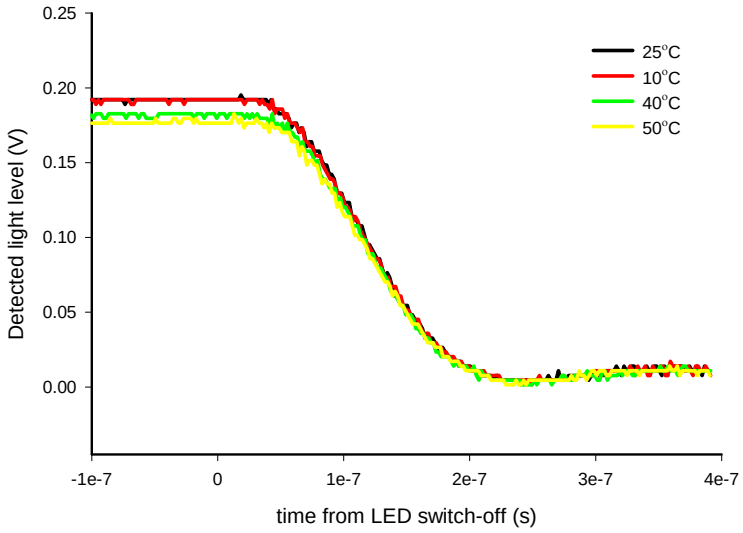

Figure 2.16 Measured LED switch-off characteristic as a function of LED temperature. Negligible time response was observed.

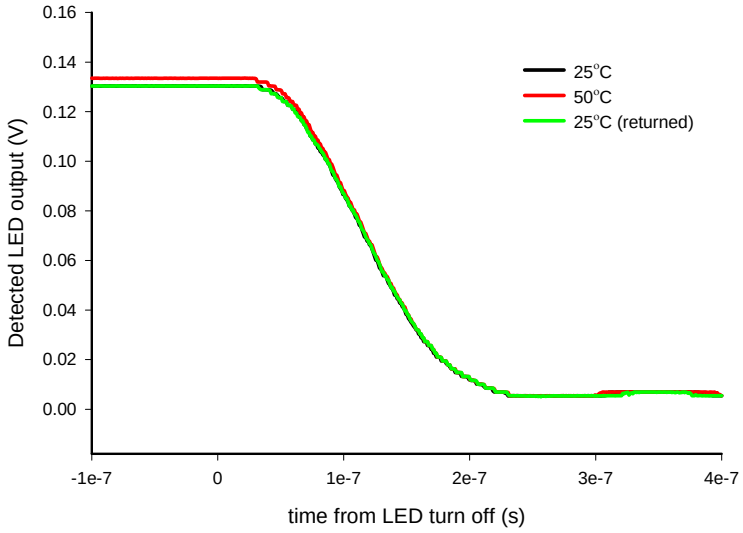

Figure 2.17 Measured LED switch-off characteristic as a function of temperature (second test to confirm results). Again negligible response time change was observed.

2.7.3.2. Thermal response of silicon detector and pre-amplifier module

The temperature response of the silicon detector, and associated OEM pre-amplifier module was measured using the same experimental arrangement, but with the pre-amplifier and detector placed inside the environmental chamber and the LED placed outside. The results, (Figure 2.18), showed significant thermal dependence.

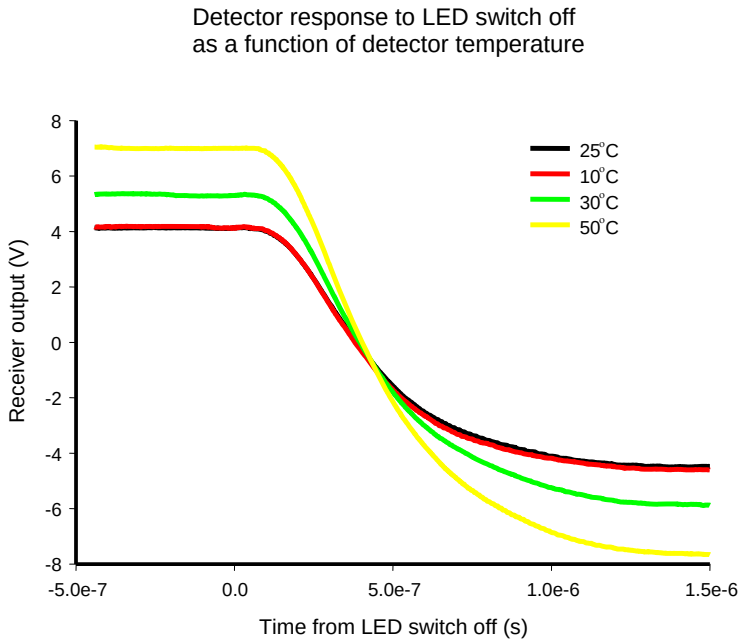

Figure 2.18 Thermal response of silicon detector and first preamplifier module. A strong thermal dependence was observed.

This result was not expected to arise from the photodiode itself. The speed of response of a photodiode detector, is dependent upon the collection time of photon induced electron hole pairs and the RC time constant arising from the combination of resistances and capacitances in the diode itself and the associated circuit. The charge collection time is comprised from two components. Firstly the faster component is dependent on the transit time of electron hole pairs through the depletion region under the influence of the electric field therein. The second slower component occurs when photons are absorbed outside the depletion region but produce carriers by diffusion. This diffusion component is dominant at low bias voltages. The fast component of collection time has minor temperature dependence, due to the temperature term in the electron-hole drift velocity, but for this application where high gain is required, the overall detector response time is limited by the much slower RC time constant, and therefore should be negligibly temperature dependent.

The problem was traced to one of the gain stages inside the preamplifier module, which had its own undesirable thermal dependence. The OEM module was suitably redesigned, and the new version (which is described in detail in chapter 5) had no observable temperature variation, even when exposed to an extreme temperature increase (around 40°C) using a heat gun.

The temperature dependence (e.g. photon detection efficiency, dark count rate, and maximum detectable count rate) of PMT detectors in photon counting mode should

generally be negligible at room temperature conditions, (because the discriminator circuit should allow for changes in PMT module, see chapter 4). As no discernable measurement drift was observed even over several hour tests using the Ti:sapphire calibrator (see chapter 4), this temperature dependence was not investigated.

2.8. Conclusions from chapter 3

To verify the novel and newly optimised sensing schemes described in forthcoming chapters, test bed fluorescence interrogation systems were required. To provide realistic testing, the interrogation instrumentation was limited to a bench-top format, similar to that available in the marketplace. Conducting these tests on bulky laboratory setups would be unrealistic, as most sensing applications require small or portable instrumentation. This chapter described the optical portion of the design.

The various design decisions were justified by comparison with other work and the many complications encountered were investigated. A fibre remoted design was preferred. Several often ignored but nevertheless important factors were considered; the time response of the excitation source, minimisation of unwanted background fluorescence and the thermal dependence of the optical components were all reduced to negligible levels. (Any residual temperature dependence would have caused drifts in the long term experiments – as will be seen, none were encounters).

The optical arrangement for modulated excitation source fluorescence delay interrogation (chapter 5), produced an excitation power of 14.1±0.1μW leading to 500±25pW of fluorescence at peak. For direct decay curve analysis (chapter 4), the excitation power was reduced to 7.4±0.5nW leading to a peak of 12.5±0.1pW of detected fluorescence light (a lower excitation power was required to prevent saturation of the detector).

2.9. References for chapter 3

1. Xiao, M. and Selvin, P., *An improved instrument for measuring time-resolved lanthanide emission and resonance energy transfer.* Review of Scientific Instruments, 1999. **70**(10): p. 3877-3881.
2. Chan, S., Fuller, Z., Demas, J. and DeGraff, B., *Optimized gating scheme for Rapid Lifetime Determinations of Single-Exponential Luminescence lifetimes.* Analytical Chemistry, 2001. **73**: p. 4486-4490.
3. Choa, F.S.*, et al.*, *Time-resolved-spectrum studies of GaN light emitting diodes.* Applied Physics Letters, 1996. **69**(24): p. 3668-3670.
4. Holst, G., Koster, T., Voges, E. and Lubbers, D., *FLOX - an oxygen-flux-measuring system using a phase-modulation method to evaluate the oxygen-dependent fluorescence lifetime.* Sensors and Actuators B, 1995. **25**: p. 231-239.
5. Trettnak, W.*, et al.*, *Optical Oxygen Sensor Instrumentation Based on the Detection of Luminescence Lifetime.* Advances in Space Research, 1998. **22**(10): p. 1465-1474.
6. Kolle, C.*, et al.*, *Fast Optochemical sensor for continuous monitoring of oxygen in breath-gas analysis.* Sensors and Actuators B, 1997. **38**: p. 141-149.
7. *Andover Corporation - Optical Filter Guide.* http://www.andcorp.com/Web_store/General_info/Technical.html.

3. FLUORESCENCE INTERROGATION BY DIRECT ANALYSIS OF THE DECAY CURVE

3.1. Introduction

Interrogation of fluorescence from a suitable chemical indicator or crystal has been widely employed as an indirect optical sensing method. Initial systems monitored fluorescence intensity changes induced by the measurand whilst undergoing constant excitation, but for greater stability and reproducibility of measurements ([1] and [2]) monitoring of changes in the fluorescence decay shape is the preferred method. Usually, in portable or small bench top instrumentation, fluorescence decay lifetime has been derived by monitoring the phase delay between intensity modulated excitation light and the resulting modulated fluorescence light returning from the indicator [3], [4]. An alternative sensing scheme is discussed here, were the decay curve shape of the fluorescence following excitation with a light flash directly is inspected to derive the state of the measurand.

Until recently, though often used in laboratory experiments, portable commercial sensors (e.g. [5], [6]) have not employed direct decay curve analysis, principally due to the additional expense and bulk of the optical detector, (usually a photo-multiplier tube, PMT is required) and the need for sophisticated real-time curve-fitting to derive the state of the indicator. Recently new compact and low-cost, modular PMT-based photon counting heads (e.g. Hamamatsu type H6180 and new red-sensitive modified versions, described later), provide highly compact relatively-inexpensive detection. When combined with the Rapid Lifetime Detection (RLD) sensing scheme, (an elegant curve fitting algorithm requiring simple hardware and software), a highly attractive alternative to the modulated-source sensor is achieved. The RLD method, although having been extensively applied to evaluation of materials, particularly semiconductors, by luminescence microscopy and characterisation of chemical species, has not been widely employed as a means of chemical interrogation using fluorescent indicators. RLD techniques can be applied to gated CCD based fluorescence lifetime imaging systems.

In this study, use of the RLD method for fluorescence interrogation in optical sensing applications was for the first time fully analysed and optimised [7]. A new calculation method, for determining the conditions for optimal high-repetition rate measurement of exponential fluorescence decays using the RLD method, was developed. An analytical

error-propagation approach was adopted to model the precision of the RLD method, as a function of excitation pulse duration, window boundary times and experiment repetition rate. This new analytical model, taking into account all of these relevant system parameters, is developed below.

The effectiveness of varying the interrogator conditions to suit fluorescence decay lifetime and background ambient light was considered. The effect of background exponential decays (for example arising from fluorescent optical components in the interrogator or the presence of fluorescent materials at the probe tip) was then quantified. The optimisation method was then extended to include the sophisticated response expected from the ruthenium-based oxygen indicator.

Finally, results were verified by comparison with both a computer-simulation, (which assumed Poisson noise distribution in the detected fluorescence), but also with experimentally derived measurements from real sensors.

3.1.1. Direct fluorescence decay curve interrogation compared with modulated-excitation source sensing schemes.

Direct decay curve analysis with photon-counting fluorescence detection has several advantages when compared with modulated source sensing schemes (which usually employ photodiodes for detecting fluorescence).

Firstly, by counting individual photons, it is possible to work at light levels below the detection limit of a photodiode-based system (as will be seen in chapter 5, high detection bandwidth and therefore low sensitivity is required). This permits interrogation of dyes having poor photo-bleaching (by reducing the intensity of damaging excitation light) behaviour and/or very low quantum efficiencies. As less fluorescent light is required to make measurements there is more freedom of optical design (e.g. a single optical fibre rather that a thick fibre bundle may be required to connect to the sensing head).

Secondly, due to the time gated detection used, a photon counting system may more easily separate excitation light from fluorescence. In conventional fluorescence measurement systems, some cross-talk light, albeit significantly attenuated by a well-designed filtering system, will inevitably appear at the detector and change the apparent phase of the returning fluorescence. This can occur due to imperfect filters or due to fluorescence in adhesives, etc, which generally have very much shorter decay time. By only using

fluorescence occurring after the excitation light pulse is extinguished, a direct decay interrogator can be intrinsically immune to such cross-talk, as the elastic scattering signal and the short-decay fluorescence signals disappear as soon as the excitation light source is extinguished.

Thirdly, a photon counting system can more easily be configured to capture the fluorescence decay curve of the indicator, (multi-channel systems already immediately recover decay curves, and time gated systems display curves by setting the control algorithm to build up a curve by sequential "boxcar" detection). To achieve the required sensitivity, a photodiode detector must usually be strongly band-limited, and is therefore not capable of detecting high bandwidth components in the fluorescence decay curve.

The disadvantages of the direct-curve analysis are generally, the expense of the detector itself, and sensitivity to background light (modulated source systems are frequency selective, and thus are not effected by small incoherent background light).

3.2. Single photon detectors

A single-photon detector has been often used for direct fluorescence decay analysis. Two alternatives, the photo-multiplier tube (PMT) and the Avalanche PhotoDiode (APD) are discussed here.

3.2.1. The Photomultiplier Tube

Since its discovery in 1887 by Herts [8], the photo-electric effect, where a photon, incident on a material liberates an electron (sometimes called a photo-electron), has been very widely exploited. In a photomultiplier tube (PMT), photo-electrons, freed from a suitable photo-cathode are multiplied at each of a subsequent series of voltage-biased dynodes and detected at the anode. At high light levels, the photoelectrons resulting from each detected incident photon overlap, producing an analogue current at the anode proportional to the received light intensity. At low incident light levels (<~10 M photons s^{-1}), the electrons arriving at the anode arising from each detected photon may be separately detected via an electronic discriminator circuit, then shaped into convenient digital pulses (usually of order 10ns duration), ready for subsequent digital processing. The photon count per second is then related to the light intensity in a highly linear manner. The total pulse frequency is the addition of those arising from detected fluorescence, from background ambient light, and from unavoidable (though cooling can reduce it) 'dark counts' (mainly thermally induced electrons produced at the anode or dynodes). Poisson counting statistics

dictates that the intrinsic uncertainty in measuring n randomly-occurring events (in this case, anode pulses) is $\sqrt{n}$.

3.2.1.1. Spectral response of the PMT

The spectral response of a PMT is determined by the material chosen for the photo-cathode, and the absorption of the detector window material.

The photo-cathode is usually an alkali metal, chosen for low work function (highly efficient conversion of incident light into photo-electrons) at the required detection wavelengths. The various photo-cathode materials lead to widely differing spectral responses as shown in Figure 3.1. For red light detection, a multialkali photo-cathode (comprised Na-K-Sb-Cs) gave optimal response, with long wavelength limit at 930nm (see Figure 3.1, where the spectral responses of several photo-cathode materials are plotted on the same set of axis).

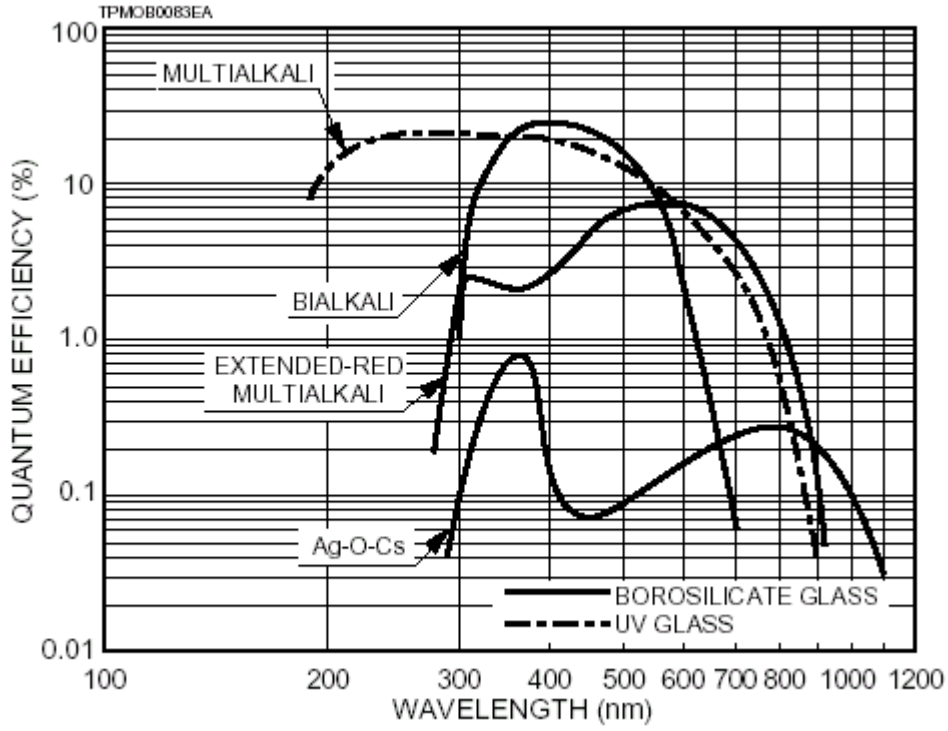

Figure 3.1 Photo-cathode spectral response characteristics, reproduced from [9].

The spectral response of the detector can also be tailored by altering the detection window material. Various materials have been used for improved UV response, but in applications where detection of UV light is not required, a borosilicate glass is favourable. Borosilicate glass can be produced with very low potassium composition, which leads to optimum 'dark' count frequency. (Some dark pulses are produced by stray electrons causing

scintillations on the glass envelope, and this effect is minimised when the glass has lowest potassium concentration).

3.2.1.2. Integrated photon counter modules

There are many areas where high-sensitivity optical detection is required, e.g. spectrophotometry, various medical instrumentation and of course fluorescence measurement. Unfortunately, for compact or portable applications, the sophisticated nature of the photo-multiplier, combined with the need for HT supply (for biasing the dynodes and anode) has hampered miniaturisation efforts. The situation is changing with the appearance of highly miniaturised integrated photon-counting modules, where PMT tube, HT supply, and, for photon counting applications, pulse discriminator are all combined into a single compact box (50x50x22mm versions are available from Hamamatsu). These new modules pave the way to the use of high-sensitivity PMT detectors in compact or portable instrumentation.

3.2.2. The APD detector

The Avalanche PhotoDiode (APD) is a special type of photodiode optical detector with high-speed and high-sensitivity characteristics. An internal gain mechanism is powered by applying a large reverse voltage.

When photons of sufficient energy enter a photodiode, electron-hole pairs are generated in the depletion region. If a reverse voltage is applied to the PN junction, an electric field is established, causing the electrons to drift towards the N type and the holes toward the P type. There is a finite probability of drifting electrons and holes colliding with the underlying crystal lattice within the depletion layer, so there exists an upper boundary on the average speed an electron or hole may attain without collision. If the applied voltage is increased beyond that necessary for the electron-holes to gain this saturation speed, the carriers possess significant excess energy when they collide with the crystal lattice, causing ionisation of the crystal, and creation of new electron-hole pairs. Hence amplification occurs.

APDs may be operated in a photon counting mode, and are therefore commonly used as replacements for PMT photon-counting detectors, but they hold disadvantages when compared with PMTs. Firstly, the gain mechanism itself is a statistical process, hence the multiplication factor is not the same for every electron-hole that is created. This leads to an ‘excess noise’ in the detected pulse frequency higher than the intrinsic Poisson (or shot) noise, which increases as the gain is increased. The second problem with APD detectors is

the requirement for re-biasing the device after each detected photon, which can take up to order of microseconds depending on the external circuit used. This limits the maximum photon count rate that can be detected to a much lower level than that of PMTs, which generally can detect a few Mcps before pulse co-incidence becomes relevant.

3.2.3. The chosen detector

For fluorescence interrogation, where very high sensitivity (to detect the weak fluorescence response) and very high bandwidth (to faithfully reproduce the fluorescence decay curve) are required, a PMT photon-counter was preferred. Furthermore, the almost shot-noise limited performance of the PMT detector allowed easier characterisation of the fluorescence response (see later).

The Hamamatsu type H7155-01 type integrated photon-counting PMT head was chosen for interrogation of the red fluorescence light. This compact (50x50x22mm), light (75g) integrated photon-counting detector, required only an external 5V supply, provides TTL specification 30ns duration output pulses. The R5613 PMT within uses borosilicate window and multi-alkali photo-cathode, achieving excellent wide-wavelength response. The sensitivity at 620nm (peak fluorescence output of the oxygen indicator) was 8 x 10^4 counts pW^{-1} (or overall photon detection rate of 2.5%), and the maximum count rate (allowing 10% pulse coincidence) was 1.5M counts s^{-1}.

3.3. Optimised Direct Decay Curve Interrogation by Extended Rapid Lifetime Detection (RLD)

The RLD method is a sensing scheme for rapidly determining the state of a fluorescence indicator from the shape of its decay curve. The fluorescence light arriving in two pre-defined time "windows" or intervals is accumulated and then ratioed (see Figure 3.2 where the fluorescence light intensity is plotted as a function of time after excitation by a pulse of excitation light). The results, firstly C_{ab} from the integrated light arriving in time interval A (between t_a and t_b), and secondly C_{cd} from those arriving in time interval B (between t_c and t_d) are processed to derive the state of the fluorescent indicator, based on assumptions regarding its decay function. This method, (a generalised version of that first suggested with equal and concurrent window intervals by Ashworth in 1984 [10]), allows extremely rapid interrogation of fluorescence decays, and is therefore termed the Rapid Lifetime Determination (RLD) method.

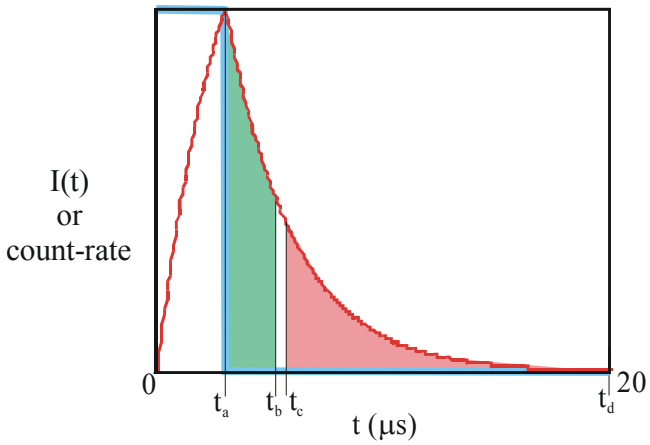

Figure 3.2 The RLD method for rapid determination of fluorescence lifetime. Following an excitation pulse (of duration t_{off}), the resulting fluorescence light arriving within two time intervals (t_a to t_b, is termed interval A and t_c to t_d, interval B) is integrated and processed to derive the fluorescence decay lifetime. In its first conception, the time intervals were assigned consecutive and equal durations, but in this work, they may be assigned any duration and any start time.

3.3.1.1. Previous RLD studies

In 1994 Soper *et. al.*[11] showed that the RLD method could measure lifetime with similar precision to the harder to implement, but popular, maximum-likelihood-estimator (MLE) method, where lifetime and intensity is calculated from a sampled decay curve. A disadvantage of the MLE method is that analysis of the whole decay curve is necessary, rather than merely integrating signals for selected periods under the curve. This immediately complicates the interrogation system. Therefore, as it has already been done, the precision of the RLD method will not be compared with that of competing sensing schemes here.

Various work, aiming to improve the precision of RLD measurements, based on direct computer simulation of 'noisy' fluorescence decay curves, has been published. In 1991 Ballew and Demas[12] performed a study of the RLD method for detection of exponential decays, using consecutive time windows, in the presence of constant background light. Then, in 1993, Waters and Burns[13] considered optimised detection of exponential decays with ***equal duration*** time windows, concluding that allowing a short time gap between the two windows, during which no fluorescence light signal is accumulated, can lead to an improved precision of decay lifetime measurement. Demas *et. al.*[14] considered equal-duration ***overlapping*** windows in a study of the RLD method. In 2001 Chan et al. [15] extended this work to differing duration time windows, arriving at the surprising result that overlapping windows provided the optimised gating scheme. The analysis presented here concludes that use of overlapping windows is not the true optimal

configuration, agreeing with Waters and Burns. In [16] by Chan *et. al.*, the RLD method has been extended to operate with square-wave-modulated excitation light. Fluorescence light was measured both during and after the rectangular excitation waveform, leading to errors if there is cross-talk of light from the excitation lamp into the detection system. In this work, only fluorescence light occurring after the excitation pulse has ceased is measured, reducing the impact of such cross-talk.

3.3.1.2. New Enhancements Resulting from this Study

During this study, the RLD method was modelled and an optimisation algorithm devised for sensor applications, where continuous on-line monitoring of longer lived (>1μs) fluorescent indicators (e.g. the ruthenium complex oxygen indicator) was required. It is assumed that, for these applications, the experimental setup parameters of excitation pulse duration and repetition period, and detection window boundary times may be easily adjusted to their optimum values. Previous optimisation studies (above) have been almost exclusively directed towards measurements of rapid fluorescence decays (much shorter than 1μs) for direct chemical analysis. Under these conditions, it was much more difficult to vary window boundaries, excitation pulse rate, and excitation pulse duration with sufficient resolution to optimise the process. For longer fluorescence lifetimes (>1μs) this becomes progressively easier.

A full **analytical** approach to modelling the sensing scheme and fluorescence indicator response (which in itself leads to novel results), taking account of all these setup parameters has, to our knowledge, never been explored before. A multi-dimensional numerical-minimization algorithm was applied to identify optimal setup configuration for RLD of fluorescent decays.

3.3.2. Interrogation System Design Outline

As mentioned above an interrogation system was constructed to test the newly optimised sensing schemes. This is briefly described here – the interested reader is referred to the appendix section for a complete description.

Digital electronics was used to accumulate the photons arriving during the time intervals. The two accumulated values C_{ab} from the detected photons arriving in time interval A, and C_{cd} from those arriving in time interval B, were passed to a control PC (see Figure 3.3). The ‘digital synchronization electronics’ incorporated a RAM lookup table, allowing

flexible computer controlled allocation of window intervals, excitation pulse duration and overall repetition rate. Wide variation in averaging time was also possible.

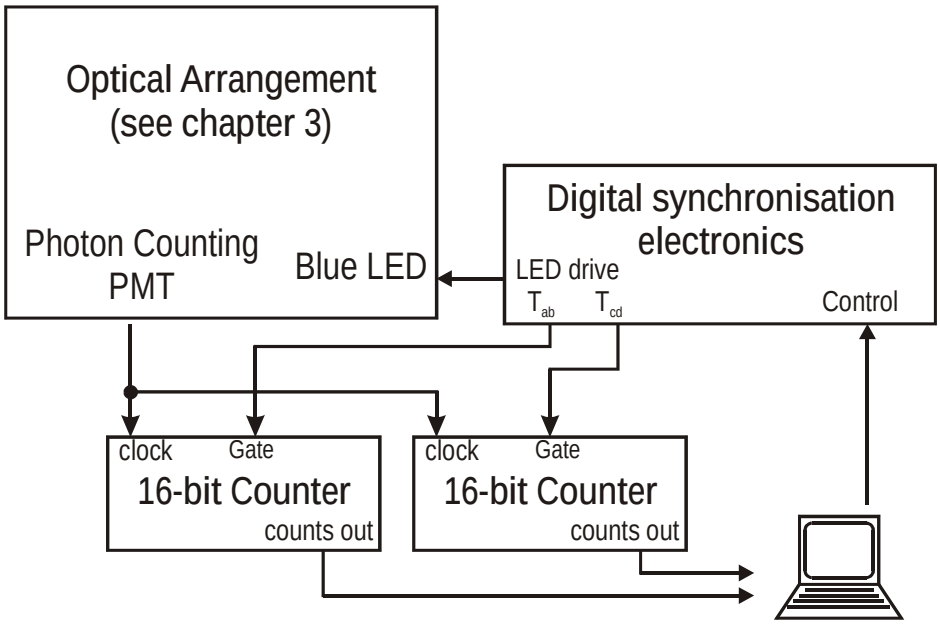

Figure 3.3 Schematic arrangement of direct decay curve interrogator. The 'digital synchronization electronics' incorporated a RAM lookup table, allowing flexible computer controlled allocation of window intervals, excitation pulse duration and overall repetition rate. Wide variation in averaging time was also possible. Please refer to the appendix section for more details.

3.3.3. Sensing Scheme Model – Exponential Fluorescence Decay

Fluorescent indicators with exponential (sometimes called single-exponential or mono-exponential) decay curves are first considered, then the model is extended to the much more complex decay observed from oxygen indicators.

If we denote the intensity versus time profile of the excitation light reaching the indicator as K(t) and the intensity of the fluorescence that returns from the indicator following impulse excitation as $I^0(t)$, then the observed fluorescence intensity, I, at time t, may be written as:-

$$I\ (t) = \int_{-\infty}^{t} I^0(t-t').K(t')dt'$$

(3.1)

(i.e. the fluorescence intensity at time t is the accumulation of the remaining fluorescence excited at times before t)

3.3.4. Zero-base line (background-less) situation

For a mono-exponential decay, the fluorescence decay curve following impulse excitation is:-

$$I^0(t) = I_s e^{-t/\tau}$$

(3.2)

where I_s is an intensity term.

In some cases the response of the excitation light source to a rectangular pulse drive signal could be an important factor, but here we shall assume the source (a blue LED for our experiments), responds essentially instantaneously, and with negligible thermal dependence (see chapter 2 for experimental justification of this). K(t) is then simply the excitation source drive signal - typically a low duty-cycle rectangular waveform. If we first consider one excitation waveform period (i.e. a single pulse), (beginning at time t=0, and ceasing at $t=t_{off}$) then K(t) is

$$K(t) = \begin{cases} 1 & 0 < t \le t_{off} \\ 0 & t \le 0, t > t_{off} \end{cases}$$

(3.3)

When the indicator has lifetime τ, then the fluorescence intensity observed at a time t (> t_{off}) is, from (3.1), given by:-

$$I_1(t) = \tau . I_s . e^{-t/\tau} . (e^{t_{off}/\tau} - 1).$$

(3.4)

or, by re-arranging:-

$$I_1(t) = \left[\tau . I_s . (1 - e^{t_{off}/\tau}) \right] . e^{-(t - t_{off})/\tau}$$

(3.5)

We see that as the excitation pulse duration (t_{off}) is increased, the peak fluorescence intensity increases exponentially towards a maximum value.

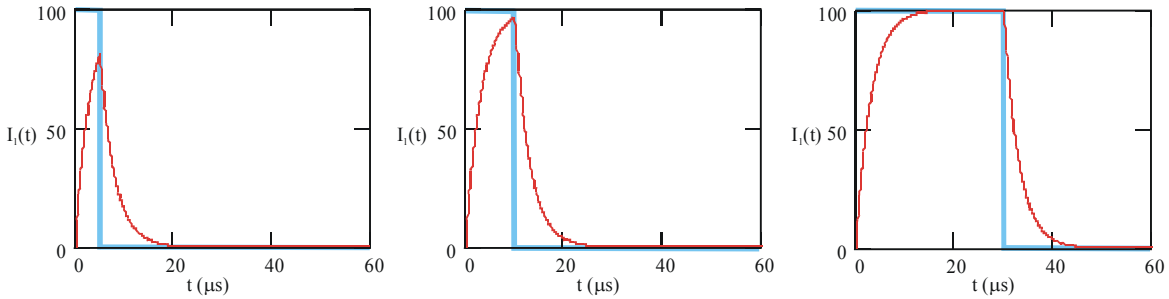

Figure 3.4 Theoretically observed fluorescence decay profiles from a fluorescent indicator having 3µs decay lifetime, when exposed to an excitation pulse of 5, 10, or 30µs. Note that increasing the duration of excitation pulses does not yield a linearly proportional increase in returning fluorescence intensity.

Figure 3.4 shows the expected response from an indicator having a 3µs lifetime, when excited by pulses of 5,10 and 30µs duration. An increase in the excitation-pulse duration does not yield a proportionate increase in the received post-excitation fluorescence intensity, because the peak fluorescence intensity soon approaches an equilibrium value, once the excitation rate of fluorescent sites equals the rate of these relaxing to a lower state. Once this point is reached, increasing the excitation pulse width then has the undesirable effect of decreasing the possible excitation pulse repetition rate, without useful increase in the fluorescent light intensity, so this tends to reduce the signal to noise ratio, and hence the measurement precision. There therefore exists an optimal excitation pulse duration, where the best trade-off between fluorescence intensity and repetition rate is achieved. This important result has apparently not been observed or noted in previous studies.

When the probe is exposed to a periodic series of excitation pulses at high repetition rates, the model must be extended to account for the weak, but finite, residual fluorescent "tail" from previous excitation pulses. Again, this important aspect does not appear to have been explored in other published work. To simplify analysis of this, only decays from the previous four excitation pulses are considered, as the residual fluorescence from a time greater than four repetition periods previously is usually negligible, certainly using any likely range of practical setup parameters. If the excitation repetition period is around 20µs, and the fluorescence decay lifetime is 3µs, then after four repetition periods (80µs), the fluorescence intensity remaining from the original excitation pulse has decayed to 10^{-12} of its original intensity. If the excitation pulse repetition period is $t_{rep,}$ then the observed fluorescence intensity is given by

$$I(t) = \sum_{i=0}^{4} \tau . I_s (e^{t_{off}/\tau} - 1).e^{-(t+i.t_{rep})/\tau}$$

(3.6)

Figure 3.5 illustrates the effect of fluorescence remaining from previous excitation pulses in high repetition rate systems. In red, the fluorescence light characteristic expected from a single excitation pulse is plotted, whilst in green, the decay characteristic that would be observed from a high repetition rate system is plotted, for an 8µs repetition period, 3µs excitation pulse and 3µs fluorescence lifetime.

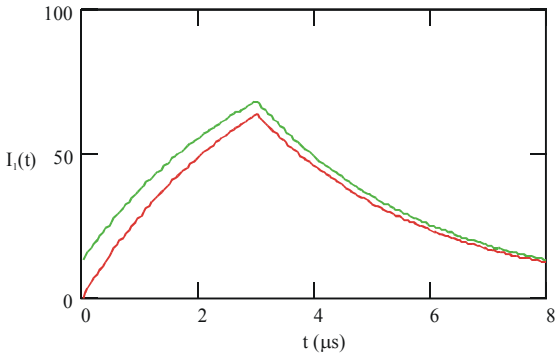

Figure 3.5 Modelled observed fluorescence from a single excitation pulse (lower curve, in red) and repetitive pulses (upper curve, in green)

We shall now model the RLD sensing scheme itself. Consider again Figure 3.2, where all times were defined with respect to the beginning of the excitation pulse. The time t_{off} is the duration of the excitation pulse, t_a the start time of the first window, t_b the end time of the first window, t_c the start time of the second window, t_d the end time of the second window, and t_{rep} the repetition period of the excitation pulses.

If we call C_{ab} the number of counts received between t_a and t_b, and C_{cd} the number between t_c and t_d, we can write

$$C_{ab} = \int_{t_a}^{t_b} I(t)dt$$
$$C_{cd} = \int_{t_c}^{t_d} I(t)dt$$

(3.7)

For exponential decays, fluorescence intensity and decay lifetime may be computed from these measurements [17], but, as mentioned previously, fluorescence decay is the preferred measurement, so the dimensionless, intensity independent ratio of the accumulated count values, R, is required; given by

$$R = {}^{C_{ab}}\!/_{C_{cd}}$$

(3.8)

The 'setup vector' **p** is now defined as the set of all pre-selected parameters; window boundary times, excitation pulse duration, and excitation pulse repetition period.

$$\mathbf{p} \equiv \begin{pmatrix} t_{off} \\ t_a \\ t_b \\ t_c \\ t_d \\ t_{rep} \end{pmatrix}$$

(3.9)

To simplify the preceding expressions, all functions have so far been written without their arguments. Let us now write them in their full form, so the count ratio, R, can be shown as a realistic function of setup vector **p** and fluorescence lifetime τ ; R(**p**,τ).

For each measurand value (e.g. oxygen concentration, or temperature) there exists a setup vector, $\mathbf{p}_{max}$, that corresponds with the maximum Signal-to-Noise Ratio (SNR) in measurements. The first step in computing this vector was to calculate, by error propagation arguments, the expected error in measurement of decay lifetime τ as a function of setup vector and fluorescence intensity.

As the errors in the measurements of C_{ab} and C_{cd} are independent, they add incoherently (i.e. in quadrature), so the error, $\delta R(\mathbf{p},\tau)$, in R(**p**,$\tau$), in terms of C_{ab} and C_{cd} and their errors, $\delta C_{ab,}$ and $\delta C_{cd,}$ is given by:-

$$\pm \delta R(\mathbf{p},\tau) = \pm \sqrt{\left(\frac{\partial R(\mathbf{p},\tau)}{\partial C_{ab}}\right)^2 .(\delta C_{ab})^2 + \left(\frac{\partial R(\mathbf{p},\tau)}{\partial C_{cd}}\right)^2 .(\delta C_{cd})^2}$$

(3.10)

If we firstly ignore dark counts and ambient background light, the errors in C_{ab} and C_{cd} are simply (by Poisson statistics):

$$\delta C_{ab} = \sqrt{C_{ab}}$$
$$\delta C_{cd} = \sqrt{C_{cd}}$$

(3.11)

rewriting (3.10)

$$\delta R(\mathbf{p},\tau) = \sqrt{\frac{R(\mathbf{p},\tau)(1+R(\mathbf{p},\tau))}{C_{cd}}}$$

(3.12)

Though it is impossible to analytically derive an expression for τ in terms of R for this extended RLD method, we may easily write an expression for R in terms of τ, and the known setup parameters (i.e. the setup vector **p**). In this way τ may be numerically approximated from the measured value of R and the function R(**p**,τ) (perhaps via a look-up table). The uncertainty (or noise) in the count ratio measurement (3.12) may be equated to uncertainty in the resultant measurement of fluorescence decay constant, $\delta\tau(\mathbf{p},\tau)$ simply by multiplying by the rate of change of τ with R

$$\pm\,\delta\tau(\mathbf{p},\tau) = \pm\left|\delta R(\mathbf{p},\tau).\left(\frac{\partial R(\mathbf{p},\tau)}{\partial\tau}\right)^{-1}\right|$$

(3.13)

which may be computed from (3.7), (3.8), and (3.12)

The SNR in the measurement of τ over a measurement time t_{rep} (i.e. one excitation pulse period) is simply $\frac{\tau}{\delta\tau(\mathbf{p},\tau)}$, but ($1/t_{rep}$) periods occur in every second, so the signal to noise ratio, ϕ(**p**,τ), achievable in 1s is improved by a factor $\sqrt{\frac{1}{t_{rep}}}$. Hence:-

$$\phi(\mathbf{p},\tau) = \sqrt{\frac{1}{t_{rep}}}.\frac{\tau}{\delta\tau(\mathbf{p},\tau)}$$

(3.14)

In sensing applications, this could be related to SNR in the required sensing parameter via the sensor calibration function.

As an example, consider interrogation of a fluorescent indicator with a decay lifetime 3μs where the returned fluorescence intensity is such that I_s=1Mcps.

A computer simulation (written in Mathsoft Mathcad 2000, see appendix) was used to identify the optimum setup vector ($\mathbf{p}_{max}$) by numerical maximization of ϕ(**p**,τ) with respect to the 6D vector **p**. The resulting optimum $\mathbf{p}_{max}$ is displayed in Figure 3.6, which should give a SNR in lifetime measurement of $490\text{Hz}^{0.5}$ (this is the expected SNR given 1s averaging time).

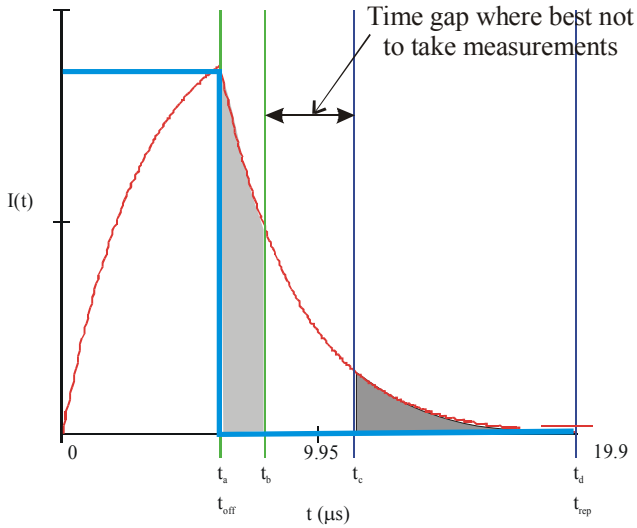

Parameter	*Value (µs)*
t_{off}	*6.06*
t_a	*6.06*
t_b	*7.80*
t_c	*11.2*
t_d	*19.8*
t_{rep}	*19.8*

Figure 3.6 Optimum configuration for the determination of a 3µs fluorescence decay lifetime using the RLD method

Figure 3.6 shows that, to achieve the most favourable measurement condition, there should be a short time gap between the first and second windows, during which no counts should be accumulated. Thus, it is actually **advantageous** to not use some of the available photon counts. Previously, Demas *et. al.*[14] and Chan et al. [16] (this model suggests incorrectly) asserted that the optimum conditions occurred with overlapping windows, but they did not consider gaps between windows in their analysis. An SNR of 120 $Hz^{0.5}$ (inferior to the presented optimum) would be expected from operating at their preferred configuration. Walters and Burns[13] did consider gaps, and, like this work, realized their advantages, but they did not allow the possibility of differing time window durations, as considered here. Operating at their preferred condition would yield an SNR of 240 $Hz^{0.5}$. None of the workers considered the repetition rate consequences of changing excitation pulse width, and also did not take into account the overlapping "tails" from earlier decays.

τ (μs)	$t_{off} = t_a$		t_b		t_c		$t_{rep} = t_d$		SNR in τ measurement (I_{sat}=1Mcps)
	t_{off} (μs)	norm. (t_{off}/τ)	t_b (μs)	norm. (t_b/τ)	t_c (μs)	norm. (t_c/τ)	t_{rep} (μs)	norm. (t_{rep}/τ)	
1.00	2.02	2.02	2.60	2.60	3.74	3.74	6.60	6.60	283
1.50	3.02	2.01	3.89	2.59	5.60	3.73	9.88	6.59	346
2.00	4.04	2.02	5.20	2.60	7.50	3.75	13.18	6.59	400
2.50	5.04	2.02	6.49	2.60	9.34	3.74	16.47	6.59	447
3.00	6.06	2.02	7.79	2.60	11.22	3.74	19.77	6.59	490
3.50	7.07	2.02	9.09	2.60	13.09	3.74	23.07	6.59	529
4.00	8.07	2.02	10.39	2.60	14.95	3.74	26.35	6.59	565
4.50	9.08	2.02	11.69	2.60	16.82	3.74	29.66	6.59	599
5.00	10.07	2.01	13.00	2.60	18.67	3.73	32.91	6.58	632

Table 3 Optimum system setup conditions as a function of fluorescence lifetime (τ) in the absence of background light. As expected, t_a=t_{off}, and t_d=t_{rep} at all lifetimes. The system times are also expressed as a normalised value by dividing by the fluorescence lifetime, showing, as expected, the optimal settings vary linearly with fluorescence lifetime in the absence of background signal. (Note, small differences in the normalized values between lifetimes reflect the convergence criteria selected for the optimisation algorithm)

Clearly a different $\mathbf{p}_{max}$ exists for every fluorescence lifetime. For lifetimes in the range 1-5μs, $\mathbf{p}_{max}$ was calculated and is displayed in Table 3. As expected, t_a=t_{off}, and t_d=t_{rep} at all lifetimes, and the optimal values for t_a, t_b, t_c and t_d vary linearly with fluorescence lifetime. The optimum measurement conditions occur when the pulse has duration 2.02τ, the first window has duration 0.58τ, the gap between windows is 1.14τ and the second window has longer duration 2.85τ.

Next, a sensor designed to measure the lifetime of an indicator with fluorescence lifetime varying between 1-10μs was considered. For every lifetime value, there exits a new optimum setup vector. Figure 3.7 plots the optimum time window boundaries ($\mathbf{p}_{max}$) for maximum SNR determination of decay lifetime as a function of sensor decay lifetime. The optimum SNR $\phi(\mathbf{p}_{max},\tau)$ is also plotted (using the axis on the right). (Note this plot is not linear, because, though the SNR achieved in one experiment repetition varies linearly with

lifetime, the number of repetitions possible in 1s also varies with increasing t_{rep}, giving an overall curved plot). To maintain the optimum lifetime determination over a 1 to 10µs decay time range requires large changes in the setup parameters.

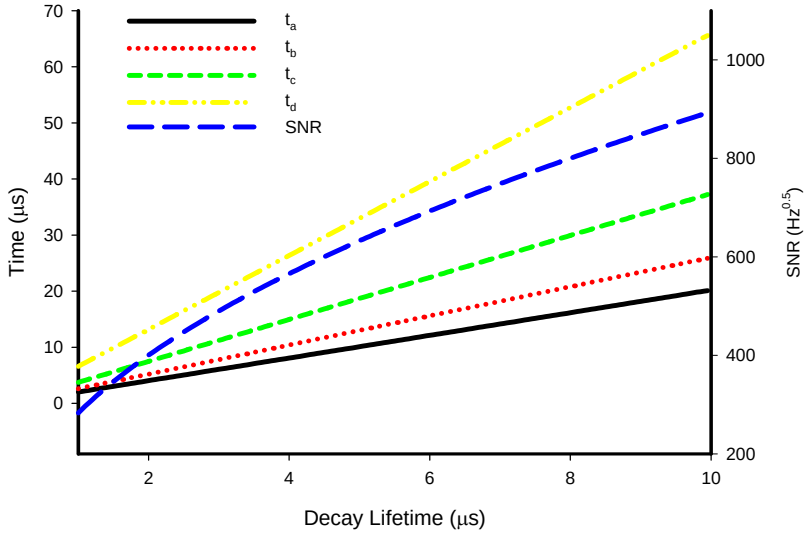

Figure 3.7 Theoretical values of the optimum time window boundaries, plotted as a function of a fluorescence decay lifetime. The value of optimum SNR for determination of decay time is also plotted.

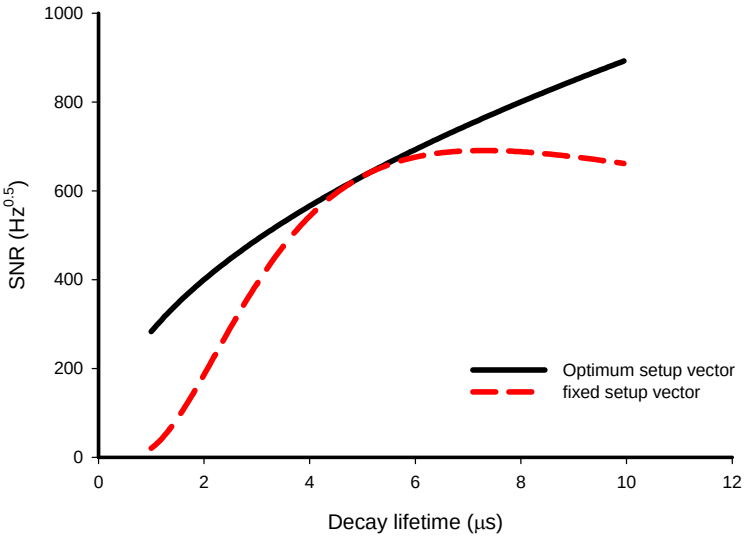

Figure 3.8 Comparison of the optimum SNR achievable when using a variable optimisation routine to the SNR achievable using a fixed setup vector.

The variation in optimal setup cannot be ignored if a wide range of lifetimes is expected. Figure 3.8 (dotted line) illustrates the SNR penalty if only one fixed setup vector were to be used over the entire measurement range (i.e. if the window boundaries are held constant). Also plotted (full line) is the optimum SNR that would be attainable assuming we can ***vary*** the setup vector, (i.e. use the optimum $\mathbf{p}_{max}$) to suit the expected or prevailing

decay lifetime. There is a clear improvement over the non-optimum SNR. For the fixed algorithm, it is noted that, at shorter lifetimes than the pre-selected optimum (in this case 5μs), the SNR achievable will quickly approach zero. For wide range measurements, selection from a set of setup parameters pre-calculated by prior optimisation at each lifetime in the range, would be necessary to achieve best SNR (perhaps via an auto-ranging algorithm, controlled by a PC or dedicated processor unit).

3.3.5. The effect of constant background light

The model described so far, although comprehensive in many ways, has still been incomplete, as we have taken an idealized case, neglecting the effect of background ambient light on the readings. In reality, the presence of a small amount of unwanted constant background is inevitable. This can arise from both undesirable ambient light (there is no cross-talk component when the excitation light source is off), and from the unavoidable 'dark count' from the PMT used in the detection system. By including a "background" term in the model, the effect of dark counts and background-light counts on the SNR in determination of τ can be determined and taken into account for both optimisation and performance prediction.

First we define the expected accumulated count values in the presence of background light as:-

$$C'_{ab} = \int_{t_a}^{t_b} I(t)dt + B_{ab}$$
$$C'_{cd} = \int_{t_c}^{t_d} I(t)dt + B_{cd}$$

(3.15)

where B_{ab} and B_{cd} are the background contributions. (These have been usually measured "on-the-fly" during an experimental run, and then used to form part of the input to the sensing algorithm.)

The background-compensated count ratio would then be calculated as part of the sensing algorithm (again neglecting function arguments for simplicity) as:-

$$R' = \frac{C'_{ab} - B_{ab}}{C'_{cd} - B_{cd}}$$

(3.16)

As there is an uncertainty term arising from both the fluorescence and background measurements, the uncertainty in measurement of the background corrected count ratio must be re-written as

$$\pm \delta R' = \pm \sqrt{\left(\frac{\partial R'}{\partial C'_{ab}}\right)^2 .(\delta C'_{ab})^2 + \left(\frac{\partial R'}{\partial C'_{cd}}\right)^2 (\delta C'_{cd})^2 + \left(\frac{\partial R'}{\partial B_{ab}}\right)^2 (\delta B_{ab})^2 + \left(\frac{\partial R'}{\partial B_{cd}}\right)^2 (\delta B_{cd})^2}$$
$$= \pm \frac{1}{C'_{cd} - B_{cd}} \sqrt{C'_{ab} + B_{ab} + [C'_{cd} + B_{cd})]R'^2}$$

(3.17)

where we have used that fact that, due to Poisson counting error, the uncertainties can be written as

$$\delta C'_{ab} = \sqrt{C'_{ab}}, \delta C'_{cd} = \sqrt{C'_{cd}}, \delta B_{ab} = \sqrt{B_{ab}}, \delta B_{cd} = \sqrt{B_{cd}}$$

(3.18)

This can then be converted to an uncertainty in measurement of decay lifetime by multiplying by the rate of change in τ with respect to ratio, as before

$$\delta \tau = \left(\frac{\partial R}{\partial \tau}\right)^{-1} \delta R$$

(3.19)

If we assume a constant ambient background light level resulting in N_d photon count rate, then we can write:

$$B_{ab} = N_d .(t_b - t_q) \text{ and } B_{cd} = N_d .(t_d - t_c)$$

(3.20)

Once again, to account for overall experiment time, the uncertainty in τ must be multiplied by the square root of the experiment frequency to obtain the time-compensated SNR in τ:-

$$\phi(\mathbf{p}, \tau, N_d) = \frac{\tau}{\delta \tau(\mathbf{p}, \tau, N_d)} \sqrt{\frac{1}{t_{rep}}}$$

(3.21)

where arguments have been included once again.

The effect of varying background light levels on the SNR in lifetime was modelled. We assumed a decay of lifetime τ = 3μs, and again a high intensity term I_s = 1Mcps. Figure 3.9 shows (solid curve) the maximum attainable SNR in determination of τ, after 1s of averaging, plotted as a function of background light level in Kcps (N_d). Background levels

of between 0% (N_d=0 Kcps) and 10% (N_d=300 Kcps) of the peak fluorescence response were considered. The dotted line shows the SNR achieved when the setup parameters are fixed at their optimum values for the zero-base line situation. The improved measurement situation, achieved by optimising setup parameters to suit the prevailing background level, leads to significantly superior SNR, underlining the importance of this optimisation process.

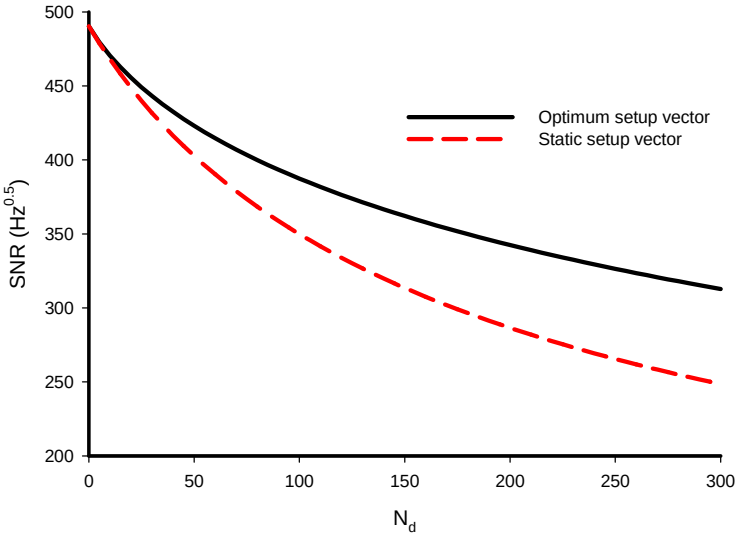

Figure 3.9 The effect of background light on the value of SNR for lifetime measurement. The optimum curve, with a variable setup vector routine (solid line), is plotted on the same set of axis as the poorer SNR predicted to be possible merely with fixed parameters (dotted line).

Figure 3.10 shows the optimum setup vector as a function of background light level, showing that optimum values of the parameters t_d and t_c are most effected by background light. (This is expected as the fluorescent light intensity returning during interval B would be far lower than the light level received just after the end of the excitation pulse, so is far more greatly influenced by background light.)

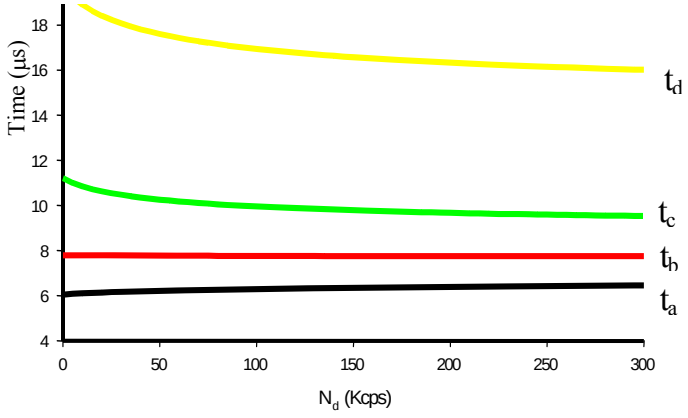

Figure 3.10 Optimum interrogation settings in the presence of increasing background light. As expected, the optimum results always occurred when $t_{off} = t_a$ and $t_d = t_{rep}$.

3.3.6. The effect of unwanted background fluorescence decays

As explained in chapter 2, the excitation light pulse promotes not only the intended fluorescence from the indicator, but also other decays from auto-fluorescence of optical components and bonding cements, the excitation light source itself (usually short-lived), or the fluorescence response of material close to the probe tip (e.g. chlorophyll fluorescence in biological measurements). To assess the impact of these unwanted decays on an RLD interrogator, the lifetime determined from an indicator in the presence of background decays of varying lifetime and intensity was calculated. The indicator fluorescence lifetime was assumed to be 3.29μs, and the interrogator was optimised for measurement of this decay.

The fluorescence response from delta-function excitation, previously given by (3.2), must be updated to include the background term:

$$I_0(t, p_b, \tau_b) = I_s\left[(1 - p_b).e^{-t/\tau} + p_b.e^{-t/\tau_b}\right]$$

(3.22)

So a proportion p_b of the initial fluorescence intensity arises from a background fluorescence of lifetime τ_b.

The count ratio (R) was determined by computer simulation for a variety of background decay proportions and lifetimes. The decay lifetime that would be measured by the RLD scheme was calculated and the percentage fall in this relative to the intended (or principle) lifetime (i.e. 3.29μs) calculated. This was plotted as a function of the proportion (fraction of initial fluorescence, p_b) and lifetime (τ_b) of the background in Figure 3.11.

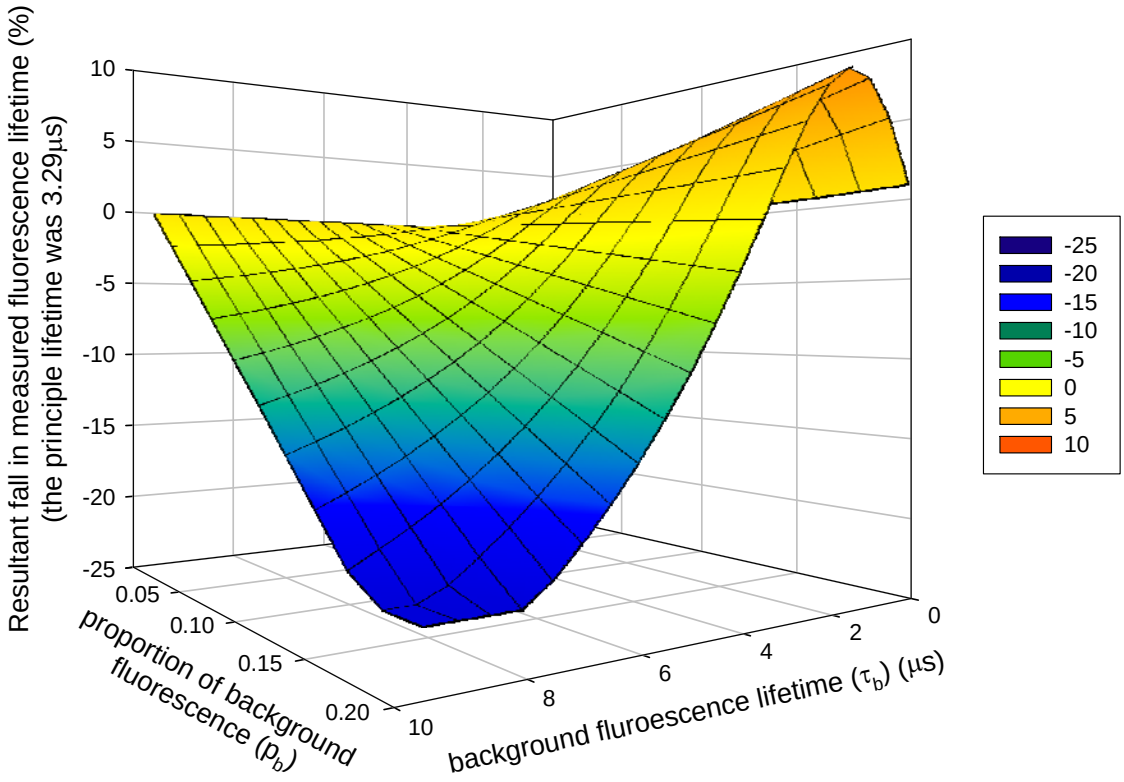

Figure 3.11 The effect on measured fluorescence lifetime of unwanted background fluorescence decays. The percentage fall in measured fluorescence lifetime is plotted as a function of the proportion and lifetime of the background decay.

Very short decays do not strongly effect the measured lifetime, as they add only a few counts to C_{ab} before decreasing to a negligible level. Obviously an unwanted background decay with the similar lifetime as the dominant lifetime does not alter the measured lifetime, so there must exist a peak lifetime between 0µs and 3.29µs that leads to maximum reduction in measured lifetime (i.e. a background lifetime that causes the largest error in measurement). The computer-simulated results shown in Figure 3.11 show such a peak occurs at 1.49µs. Background fluorescence decays of this lifetime must therefore be particularly avoided. Background fluorescence of longer lifetime than the principal lifetime obviously increase the measured value.

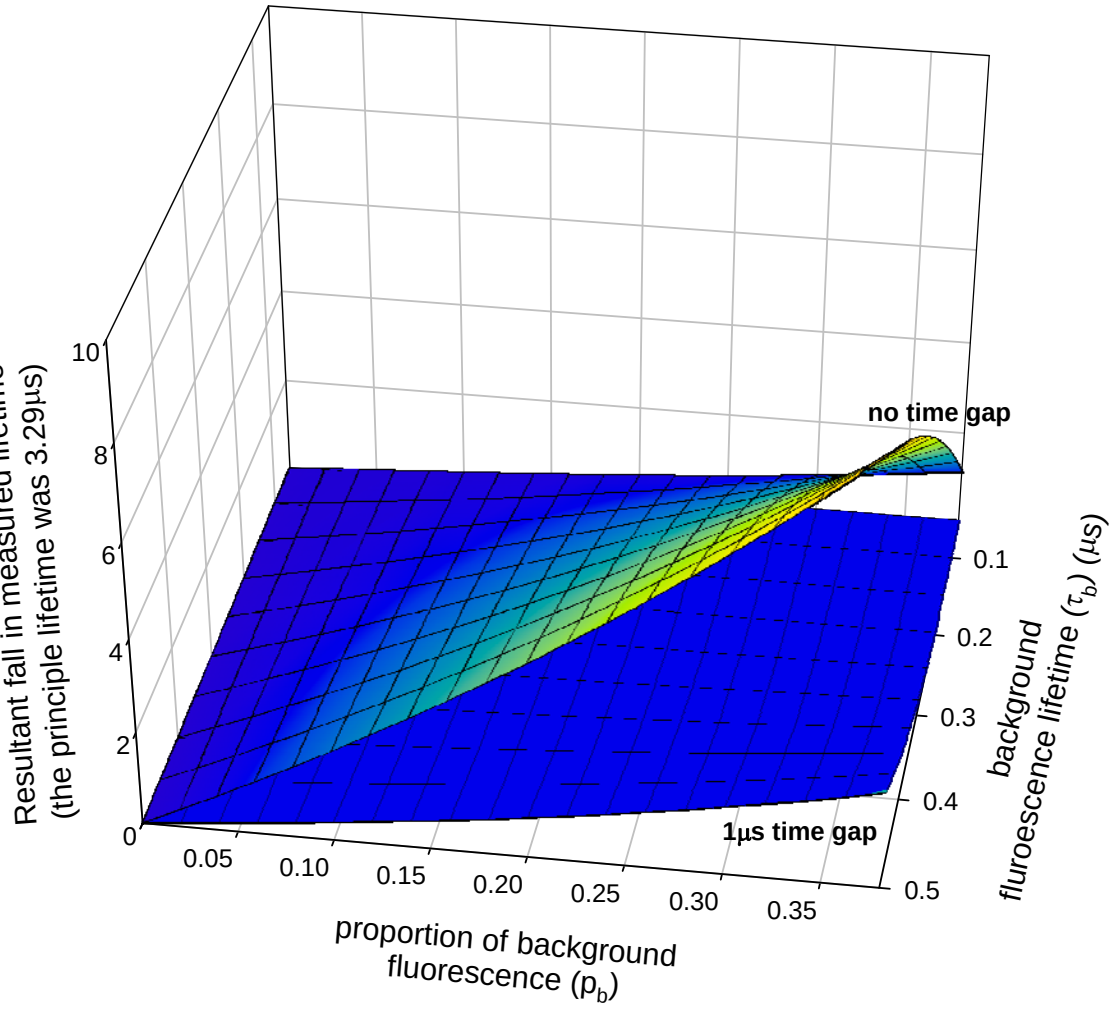

Figure 3.12 The effect on measured fluorescence lifetime of short-lived unwanted background fluorescence decay. The percentage fall in measured fluorescence lifetime is plotted as a function of the proportion and lifetime of background decay. The effect of short lived decay can be significantly reduced by introducing a time gap between the end of the excitation pulse, and the opening time of the first window.

To investigate the effect of very short-lived background fluorescence in more detail, the effect of background lifetimes ranging between 100ns and 500ns was simulated and displayed in Figure 3.12. Short-lived decays are most likely to arise from the decay of the source, or from fluorescent species in the analyte. Introducing a time delay between the end of the excitation pulse and the first interrogation window is suggested as a way of reducing these errors. We can see from the figure that the addition of a 1µs time gap reduces the effect of the short decay on the measured lifetime by 10^4 for lifetimes of less than 300ns. (This gain is possibly at the expense of reduced measurement precision, though this could be accounted for by increasing the excitation power.) Further work is required to fully analyse this suggested sensing scheme.

The effect on the principal measurement of long-lived (3-10ms) background fluorescence decays was also calculated and plotted in Figure 3.13. Here we see that long backgrounds have much less impact on the measured decay, as the change in photon arrival rate from the background is only very slight within the time scale of measurements. (This will be discussed further in chapter 6).

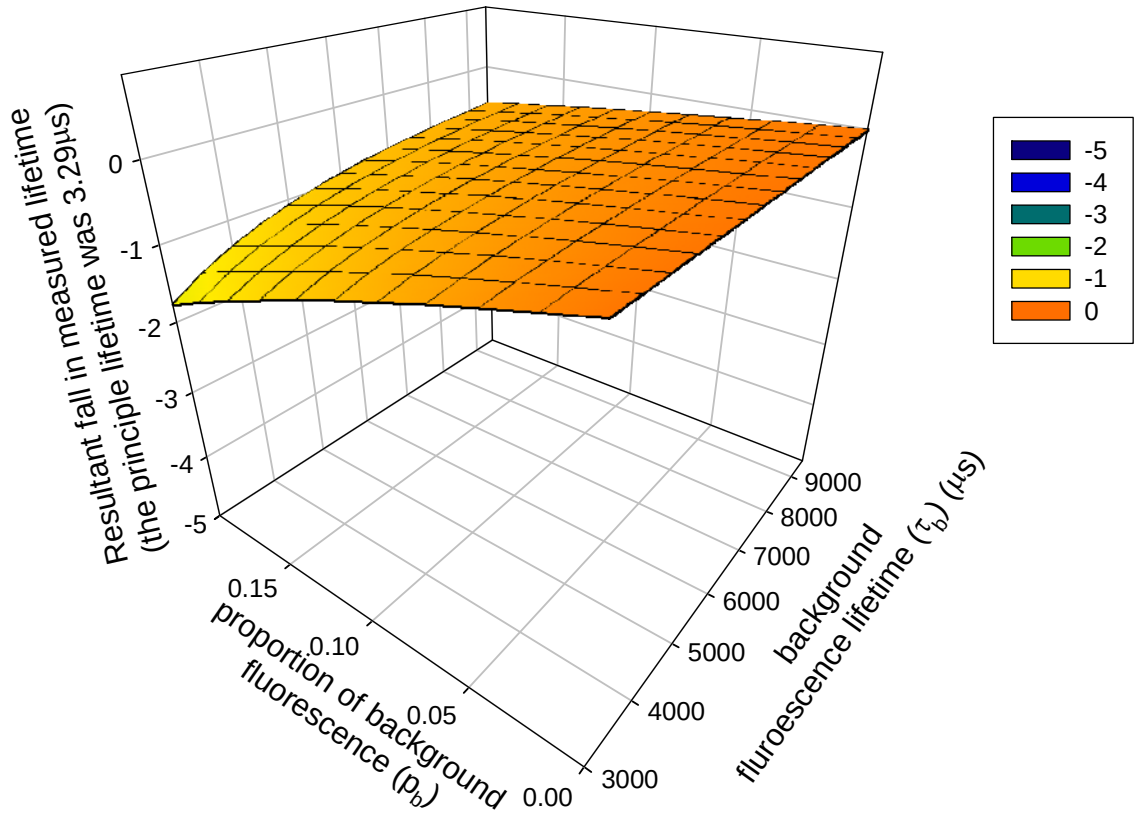

Figure 3.13 The effect on measured fluorescence lifetime of long-lived unwanted background fluorescence decay. The percentage fall in measured fluorescence lifetime is plotted as a function of the proportion of the initial fluorescence arising from the unwanted decay, and the fluorescence lifetime of the unwanted decay.

3.3.7. Sensing Scheme Model – Oxygen Indicator Fluorescent Decay

An exponential fluorescence decay has been assumed so far. The model will now be extended to the more complex decay from an oxygen indicator.

As explained in chapter 2, when a fluorescent oxygen indicator is encapsulated within a support matrix (e.g. silicone), its observed fluorescence decay curve is far from exponential. Many models have been developed to describe this sophisticated response, but the most successful so far is the 'log-gaussian distribution in τ_0 and κ_q' model

suggested by Mills in 1999 [18], which accounts for heterogeneity in the support matrix by assuming a mathematical distribution of quenching sites exist. (This was discussed in more detail in chapter 2).

The predicted fluorescence decay curve from a membrane may be described by (this equation was already stated in chapter 2):

$$I(t) = \mathrm{I_S} \frac{\int_{-\infty}^{\infty} e^{-x^2} e^{-\left[(1+\kappa.q.e^{(\rho_1+\rho_2).x}).t.e^{(-\rho_1.x)}\right] / \tau_{0,mdl}} dx}{\int_{-\infty}^{\infty} e^{-x^2} dx} . \frac{\int_{-\infty}^{\infty} \frac{e^{\rho_1.x}.e^{-x^2}}{1+\kappa.q.e^{(\rho_1+\rho_2).x}} dx}{\int_{-\infty}^{\infty} e^{\rho_1.x}.e^{-x^2} dx}$$

(3.23)

3.3.7.1. Optimised interrogation of Oxygen indicators

To update the RLD model for interrogation of oxygen, (3.13) must be re-written thus:

$$\pm \delta q(\mathbf{p}, q) = \pm \left| \delta r(\mathbf{p}, q) . \left(\frac{\partial r(\mathbf{p}, q)}{\partial q} \right)^{-1} \right|$$

(3.24)

because the uncertainty in measured oxygen concentration (δq) is now the parameter to be minimised.

To identify the $\mathbf{p}_{max}$ at which oxygen may be measured with minimum uncertainty the function $\theta(\mathbf{p},q,N_d)$, which is the time normalised uncertainty in oxygen measurement must be minimised with respect to **p**:

$$\theta(\mathbf{p}, q, N_d) = \delta q(\mathbf{p}, q, N_d) / \sqrt{t_{rep}}$$

The complex sensor response function (3.23) makes numerical identification of $\mathbf{p}_{max}$ time consuming, even with modern computer power. To minimize computation time whilst still achieving accurate results, a program was written using Microsoft Visual C++. The program performed the following steps. The expected fluorescence impulse response curve was calculated using I(t) for t between 0μs and 90μs in steps of 10ns (9000 points) and the results stored in an array. This minute time step was required to ensure negligible time-quantisation of the results. The infinite integrals expressed in (3.23) were calculated in steps of 0.1 between –4 and 4, (as recommended in Mills' paper[18]: integrating over larger limits was found to alter results only in the fourth most significant figure). $\mathbf{p}_{max}$ was

identified by minimising $\theta(\mathbf{p},q,N_d)$ with respect to $\mathbf{p}$ using Powell's iterative multi-dimensional minimisation algorithm [19]. As for the exponential case, this procedure was verified by comparison with computer model and laboratory experiment (see below).

Just as with exponential indicators, the optimal setup vector varies considerably with oxygen concentration. This means that when a wide range of measurements is required, either the interrogation settings should be adjusted on-line to suit the prevailing oxygen concentration, or a compromise static setup vector must be identified (for instance when the hardware is only capable of operation at a single setup vector). To investigate this further, the optimal setup vectors for measuring at 0.1ppm, ($\mathbf{p}_{max}^{0.1}$) and 8.2ppm (air saturated), ($\mathbf{p}_{max}^{8.2}$) O_2 were computed, and the expected noise in measurements calculated as a function of oxygen concentration for operation at each of these.

The expected noise in measurement of oxygen is plotted as a function of oxygen concentration for the setup vectors in Figure 3.14, with a zoomed x-axis version in Figure 3.15. The open circles represent expected noise in measurements while set to $\mathbf{p}_{max}^{0.1}$, while closed circles assume the $\mathbf{p}_{max}^{8.2}$ setting. The figures show that though, as expected, noise in measurement of very low oxygen concentrations benefits from operation at $\mathbf{p}_{max}^{0.1}$, the situation is very quickly reversed as concentration is increased, with very significantly superior noise performance expected from $\mathbf{p}_{max}^{7.17}$ at slightly higher concentrations. This arises from the highly non-linear response of the indicator. The presence of even trace levels of oxygen quenches the fluorescence strongly, reducing the effective lifetime and fluorescence intensity observed. As oxygen concentration increases, so the quantity of light captured (and hence the measurement precision) at the $\mathbf{p}_{max}^{0.1}$ setup rapidly decreases. Hence, in this case, to achieve best performance over the widest measurement range with a single static setup vector, $\mathbf{p}_{max}^{8.2}$ would be chosen.

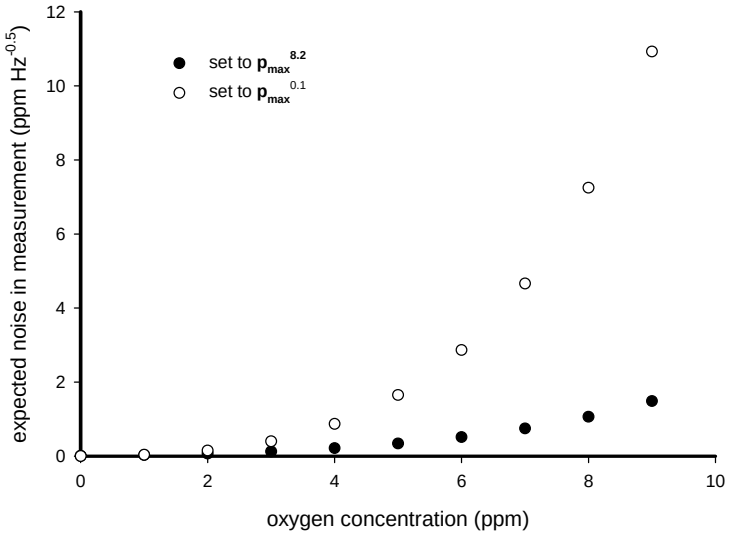

Figure 3.14 expected noise in measurement of dissolved oxygen for setups optimised for measurement at 0.1ppm and 8.2 ppm.

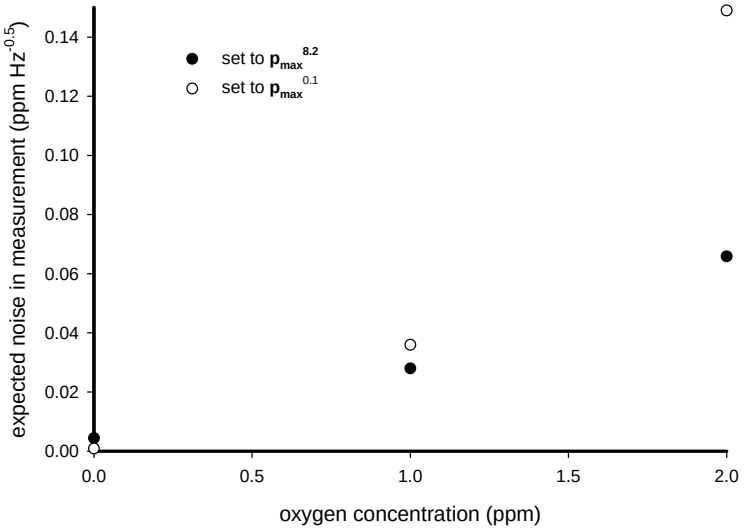

Figure 3.15 same as Figure 3.14 but with zoomed in low concentration measurements

3.4. Confirmation of RLD model by comparison with Experimental results

A series of computerised and laboratory bench experiments were conducted to verify, by comparison, results from the new theoretical models. First, the computerised model, which was included because it operates in a similar fashion to the numerical models favoured by previous studies, will be described. Then the laboratory tests, which employed the Ti:sapphire fluorescence indicator for exponential tests, and a ruthenium-based indicator for oxygen tests, will be described. Finally, the results from these tests will be presented.

3.4.1. Simulated RLD sensor using 'Noise Generator'

For computerized verification of the analytical model, synthesized 'noisy' data was used. This was termed the 'noise generator model'. In the simulation, fluorescence counts C_{ab}, C_{cd} and background counts B_{ab} and B_{cd}, were computed by integration of the expected fluorescence decay over the required time windows. Simulated noise was then added to these results by a Poisson noise-generator, to emulate the noise arising from photon counting detection. A 'measured' value of count ratio R was then calculated and stored. By repeating this process one thousand times, an averaged value of R and an estimate of the standard deviation in the data set of 'measured' values of R was calculated.

To reduce computation time over multiple setup vectors, I(t), (the expected fluorescence decay function) was calculated and stored for t=0 to t=90μs in steps of 10ns, before running the simulation.

3.4.2. Laboratory bench tests

The prototype sensor for direct decay analysis (which has already been described) was used to perform the laboratory tests. Before comparative tests could be performed, it was necessary to calibrate the two indicators to obtain the indicator model parameters (e.g. the I_s term and the fluorescent lifetime). The optimal setup vectors could then be computed for each indicator.

3.4.2.1. Exponentially shaped decay

For experimental comparison with the single-exponential indicator model, a crystal of Ti:sapphire, a material with well-defined, mono-exponential fluorescent behaviour, was employed as the fluorescent indicator. For this experiment the crystal temperature was held constant at 21.6±0.1°C (3μs decay time) using the apparatus described in chapter 2.

The calibration parameters (I_s, N_d and τ) were required to compare the computer models with the laboratory experiment. To measure these values, the fluorescence decay curve from the indicator was required. This was captured by running a series of sequential experiments with narrow sequential windows, thereby operating in 'boxcar' mode.

The excitation light pulse duration (t_{off}) was set to 12μs (approximately four times the maximum effective natural lifetime of the indicator), so that the fluorescence intensity was guaranteed to attain its saturation equilibrium during the excitation pulse. This occurs when the rate of promotion of dye molecules to the excited state is equal to the rate of relaxation to the ground state. To obtain low-noise decay plots, the fluorescence light

resulting from several excitation pulses was accumulated to achieve an average decay curve. The instrument was capable of very high repetition rate measurements, but for obtaining calibration curves, this was set to 33μs so the effect on each decay of the residual fluorescence "tail" from previous decays was negligible. The window width (the accumulation time or resolution for each point on the decay curve) was set to 0.167μs and the total accumulation time for each point was 8.7ms, to ensure excellent signal-noise in the measurements. The resultant fluorescence decay response is shown in Figure 3.16.

As the indicator will have attained saturated fluorescence during the excitation pulse, (because $t_{off} >> \tau$) equation (3.6) may be re-written as

$$I_1(t) = [\tau . I_s] e^{-(t - t_{off})/\tau}$$

(3.25)

and the intensity measured at time t_{off}

$$I_1(t_{off}) = \tau . I_s$$

(3.26)

This allows I_s to be resolved from the captured decay curve.

The background ambient light rate N_d was measured by simply running the experiment with the excitation light flashes extinguished.

The fluorescence decay lifetime τ was measured from the fluorescence decay tail using traditional processor-intensive least-squares fit.

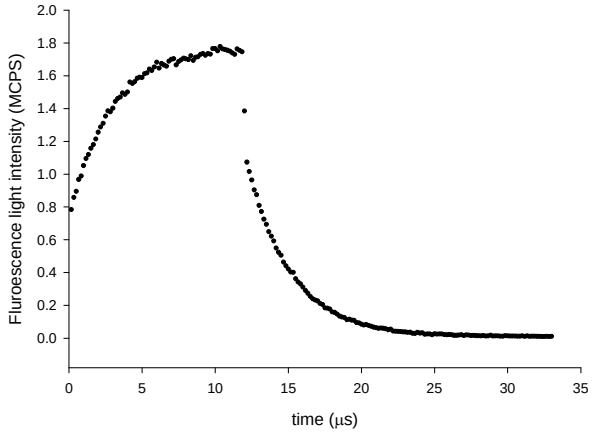

Extracted parameters

Parameter	*Value*
I_s	400 KCps
N_d	9.3 KCps
τ	2.99 ±0.01μs

Figure 3.16 Fluorescence decay of Ti:Sapphire crystal at 21.6±0.1°C. The LED excitation pulse length was 12μs and the excitation repetition rate was 33μs.

The optimum setup vector $\mathbf{p}_{max}$ (t_{off}, t_a, t_b, t_c, t_d and t_{rep}) was then numerically calculated by an implementation of the Powell multi-dimensional method (written in Borland C++ Builder 4) for maximisation of SNR in lifetime measurement, as described above. The optimal setup vector (as expected t_{off}=t_1 and t_4 = t_{rep} at the optimal point) was:-

Parameter	*Value (μs)*
t_a	6.15
t_b	7.77
t_c	10.5
t_d	18.2

An identical optimum result was obtained from a simulation written in Mathsoft Mathcad 2000. The optimal SNR in fluorescence lifetime was $280Hz^{0.5}$.

3.4.2.2. The oxygen indicator

As with the mono-exponential case, the calibration parameters were required to compare the analytical error-propagation model with a laboratory bench-top instrument. To allow

calibration of the oxygen indicator, the computer-programmable oxygenation rig described in later was used. For this comparative test, the probe was immersed in deoxygenated water held at 30°C. To ensure de-oxygenated conditions, N_2 was bubbled at a rate of 0.5 l/min through a 200ml water sample.

The membrane under test was calibrated as in chapter 2, but for this test in deoxygenated water, only the parameters $\tau_{0,mdl}$=5.61μs, ρ_1=0.434, I_s= 1.33 x 10^4 cps and N_d=2 x 10^2cps where required. The expected optimum setup vector $\mathbf{p}_{max}$ (t_{off}, t_a, t_b, t_c, t_d and t_{rep}) was numerically calculated, as before, by an implementation of the Powell multi-dimensional method (written in Microsoft Visual C++), to be:

Parameter	*Value (μs)*
t_a	15.44
t_b	18.39
t_c	29.40
t_d	48.95

leading to an optimal oxygen concentration uncertainty of 1.1ppb $Hz^{-0.5}$.

3.4.3. Verification of model by comparison at multiple setup vectors

The exhaustive test used for comparison of the analytical model, the computer-based 'noise generator' model, and laboratory experiment will now be described. Firstly, expected values for the count ratio (R), and expected SNR in determination of R were calculated for each of 130 setup vectors (including the expected optimum vector and overlapping window configurations) using the analytically-derived error-propagation model described above. Count ratio rather than derived value (i.e. decay lifetime or oxygen concentration) was chosen for comparison to simplify the study and to remove possible additional errors introduced by the calibration process itself. All points satisfied the necessary inequalities, where t'_{rep} is the previously calculated optimal repetition period:

$$t_{off} > 0$$
$$t_{off} = t_1$$
$$t_a < t_b$$
$$t_b < t_d$$
$$t_b < t_c < t_d$$
$$t_d = t_{rep}$$
$$t_{rep} < t'_{rep} + 10\mu s$$

The 'noise-generator' computer simulated RLD sensor was programmed, for the exponential case, to calculate simulated values for R and SNR in R at each setup vector, and the results compared with the previously calculated (expected) values from the analytical computer model. (Verification of the oxygen sensor analysis with the noise generator model was not required in view of the excellent agreement obtained with the exponential indicator.)

The laboratory based test instrument was configured to perform 1000 experiments, each with 1850 excitation-pulse repetitions, at each of the setup vectors. (1850 experiment repetitions were chosen to fill the run time of the interrogation hardware). The background level N_d was measured before each experiment by simply running a test with no excitation pulse, thereby accumulating background counts in the time windows. For each experiment in a set of 1000, the count ratio was calculated and stored. The SNR achieved in measurement of R (over the 1850 repetition averaging time), and the average measured R were calculated from this stored data. For the n'th experiment in a set of 1000, the count ratio, R'_n (where a dash is used to indicate the presence of background light) was measured and stored. For each setup vector, the average count ratio was simply

$$\overline{R'} = {}^{1}\!/_{1000} \sum_{n=1}^{1000} R'_n$$

(3.27)

and the uncertainty in measurement of $\overline{R'}$ was the RMS deviation

$$\delta R' = s = \sqrt{\frac{\sum_{n=1}^{1000} (R'_n - \overline{R'_n})^2}{1000}}$$

(3.28)

and the SNR in measurement of count ratio (achieved during an experiment period of 1850 experiment repetitions) was

$$\frac{\overline{R'}}{\delta R'} = \overline{R'}.\sqrt{\frac{1000}{\sum_{n=1}^{1000}(R'_n - \overline{R'})^2}}$$

(3.29)

For oxygen indicator measurements, due to drifts in experimental measurement conditions it was impossible to take measurements for very long periods, hence the number of setup vectors was limited to 35.

3.4.4. Results

The values of count ratio and SNR in count ratio from the three sources; the analytical model, the noise generator direct simulation, and the laboratory experiment are compared for interrogating an exponential decay in Figure 3.17 and Figure 3.18. Figure 3.17 compares noise generator simulation on the x-axis and error propagation model on the y-axis. If the models agree, all points would lie on the 45°, x=y line. It can be seen that there is excellent quantitative agreement between the two models, both for the count ratio, and for SNR in count ratio measurements.

Figure 3.18 compares the noise-generator simulation and real experimentally measured results. Again, there is excellent agreement, especially at high SNR values. At lower SNR values, unpredictable non-Poisson errors are evident, but these are only to be expected when statistical errors are high. Sensors would not normally operate under such poor SNR conditions. Importantly, the calculated setup vector optimal SNR in measurement of R returned the highest precision measurements. Converting to 1s measurement time, the SNR in R predicted was $972Hz^{0.5}$ and achieved was $1092Hz^{0.5}$. This is satisfactory agreement for a noise-based measurement. As the modelled and experimentally measured SNRs in R agree, the optimal SNR in lifetime of $280Hz^{0.5}$ was achieved.

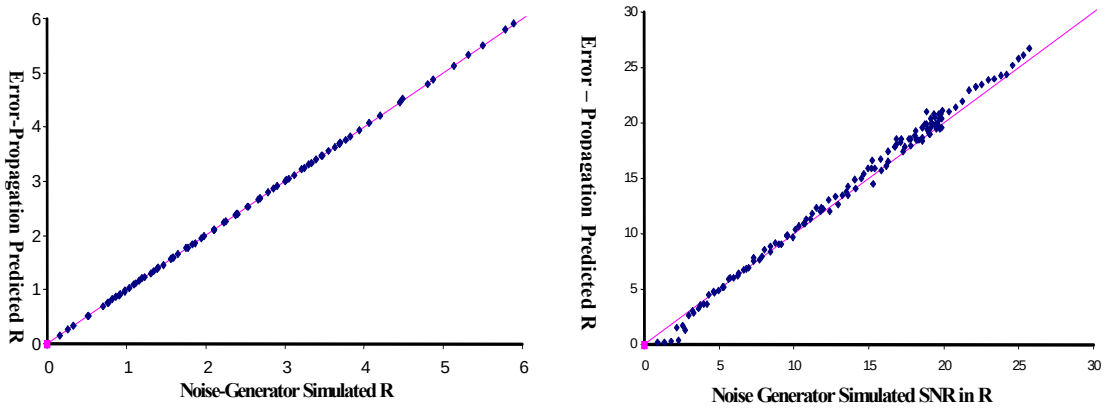

Figure 3.17 Comparison between the count ratio (R) and the signal-to-noise ratio in count ratio simulated using the 'noise generator' model with same expected from the error-propagation model for an exponential fluorescence. The excellent agreement verifies similarity between results obtained by error-propagation arguments and those from traditional simulation of noisy data.

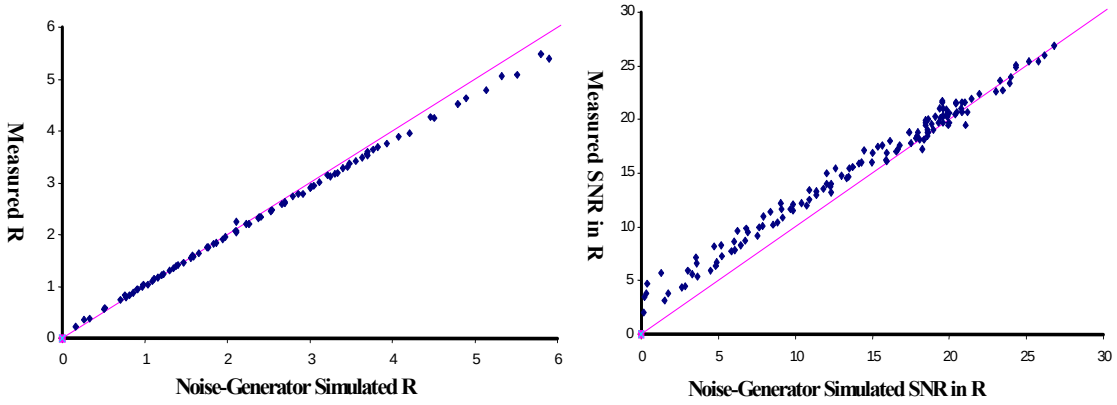

Figure 3.18 Comparison between the count ratio (R) and the signal-to-noise ratio in count ratio simulated using the 'noise generator' model with same achieved by real measurements made with the Ti:sapphire exponential fluorescence reference. The excellent agreement verifies correct operation of the model, and importantly shows that the predicted optimum measurement condition does in fact result in the maximum signal to noise in measurements.

Figure 3.19 show comparisons between the error-propagation expectedand measured results for an oxygen indicator. As before the error-propagation model results are plotted on the horizontal-axis, while the measured values are plotted on the y-axis. The theoretical and experimentally measured count ratio and signal to noise in count ratio show excellent quantitive agreement, verifying the presented RLD model. Importantly, the optimal setup vector for measurement of count ratio does indeed lead to optimal signal to noise in measurements. Again, converting to 1s measurement time, the SNR in R predicted was $109Hz^{0.5}$ and achieved was $111Hz^{0.5}$. This again is satisfactory agreement for a noise-based measurement. As the modelled and experimentally measured SNRs in R agree, the optimal oxygen measurement precision of 0.0013% [O_2] or **1.1ppb $Hz^{-0.5}$** (i.e. 1.1ppb in 1s averaging time) was achieved.

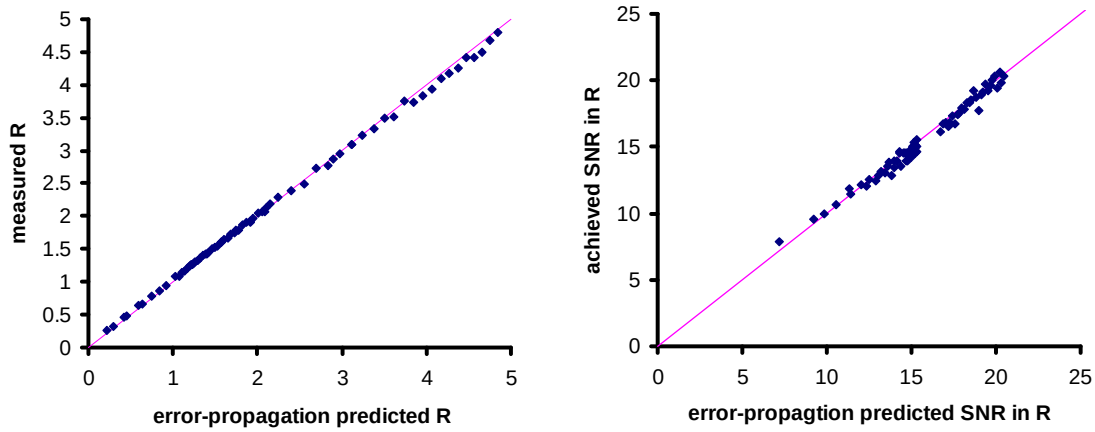

Figure 3.19 Comparison between the count ratio (R) and the signal-to-noise ratio in count ratio achieved, with same expected from the error-propagation model for an oxygen indicator response. The excellent agreement again verifies similarity between results obtained by error-propagation arguments and those from real experimental measurements.

3.5. Real time wide range dissolved oxygen sensor measurements

This section presents more results from the oxygen sensor, this time logged in real time as the oxygenation concentration is altered between 0% and 100%[O_2]. The indicator was interrogated by the optimised RLD method. To perform these measurements, a high-speed DO test rig was developed.

3.5.1. Oxygenation Rig

An experimental arrangement was required to vary the dissolved oxygen concentration with a test water sample, and thereby calibrate and test the oxygen sensor. To do this, a computer-controlled oxygenation rig was constructed to allow the concentration of dissolved oxygen in a 100ml water sample to be regulated by bubbling mixtures of air and (oxygen free) nitrogen gases through it. By placing the optical sensor probe (the sensor under test SUT) next to a commercial electro-chemical probe in the water sample whilst bubbling different gas mixtures, the response from the SUT could be compared with that of a commercially available alternative.

Pressurised gas cylinders with regulators, followed by two computer-controlled mass-flow controllers (both Brooks, Model 5850TR, ±1% accuracy over full range), set the required nitrogen/air ratio, allowing automated cycling through the desired oxygen concentration profiles. To allow more rapid changes in oxygen level then previous systems, a special high-speed bubbler was custom built. A custom-built glass beaker (University of

Southampton, Chemistry Department, glass workshop) was divided in two by fusing a large area (100mm diameter, 10mm thickness) sintered glass filter (a commercial porous material made by sintering powdered glass), at a height of 25mm from its base. The enclosed gas volume below the filter was pressurised with the nitrogen/air mixture so that the gas was forced to pass through the filter, forming many tiny bubbles in the water sample above. A combined flow-rate of 1 l/min was used, giving an expected oxygenation accuracy of ±3%. The commercial probe used was a standard YSI 5739 (Clark cell) type. This arrangement is shown in Figure 3.20. For temperature control, the bubbler was placed in a thermally-controlled water bath. A photograph of the high speed bubbler is shown in Figure 3.21.

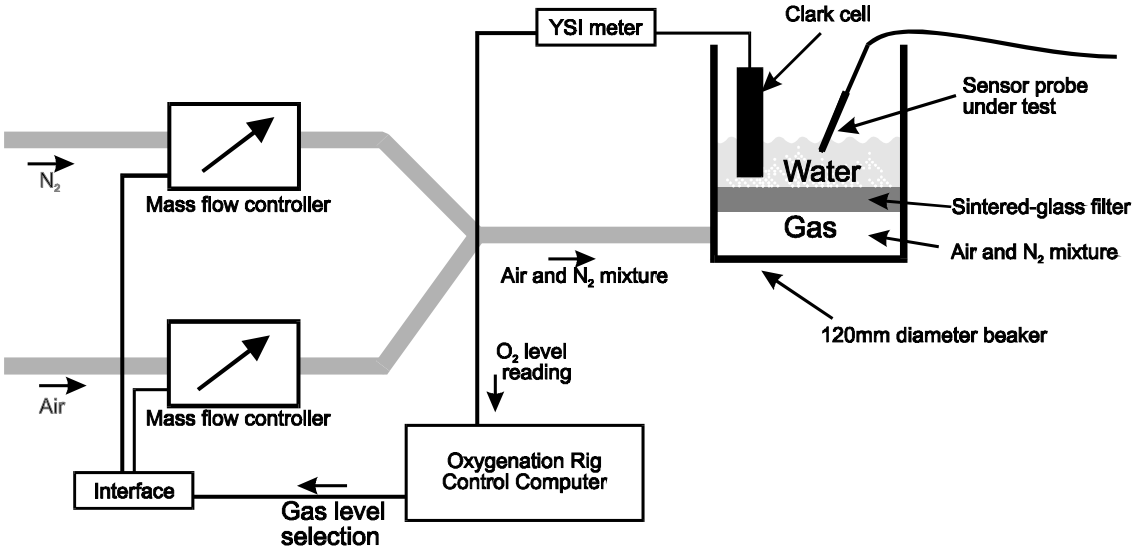

Figure 3.20 Schematic of Oxygenation Rig for testing of the example oxygen probes

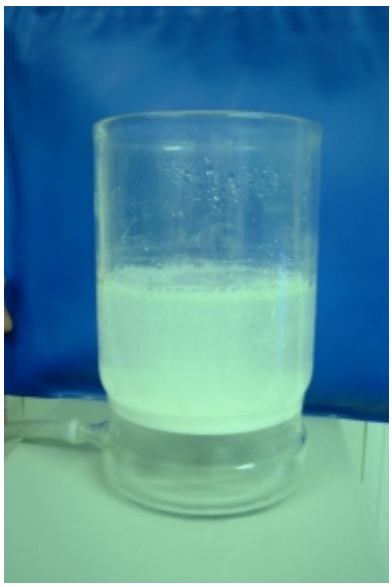

Figure 3.21 The fast response gas bubbler in operation. A beaker is divided by a large-area glass sinter. The lower chamber is pressurised with an air/nitrogen mixture which bubbles into the water sample above. The bubbler was photographed while an air/nitrogen mixture was bubbled through the test water sample.

Tests showed that a dissolved oxygen concentration change from 0% [O_2] to 100%[O_2] was achieved in less than 1 minute.

3.5.2. Experimental results

A ruthenium probe was calibrated with the log-Gaussian model then the optimal measurement conditions calculated using the new optimisation algorithm. As explained above, for best full-range operation, the sensor was optimised for air-saturated measurement. The sensor was then tested using the oxygenation rig above. A DO concentration profile ranging from 100-0% [O_2] in 10% steps, was programmed into the control computer, with a hold time of 20 minutes at each step. The measured values from the oxygen sensor and the Clark sensor were simultaneously logged, and the results are displayed in Figure 3.22. An averaging time of 5s was used for the optical measurement.

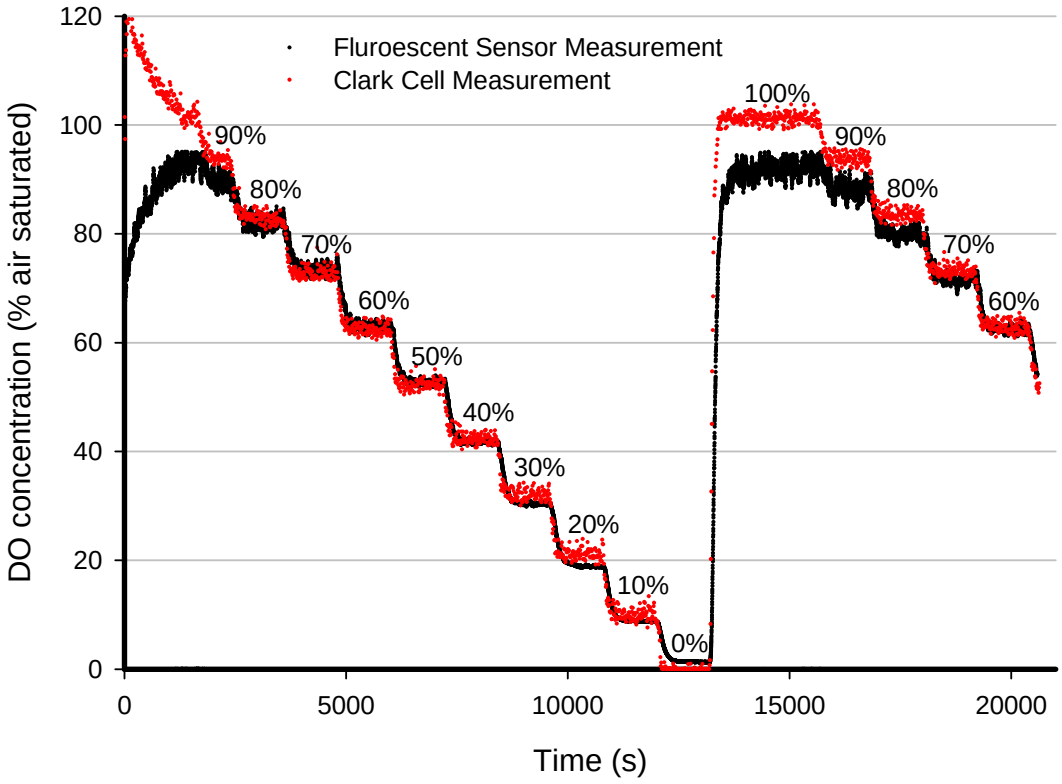

Figure 3.22 Experimental measurements taken with an optimised optical oxygen sensor and conventional Clark cell sensor as a 10% step oxygenation profile was performed. After an initial stabilisation period (until 1000s, 15 minutes), both sensors responded well to dissolved oxygen concentration changes. The optical sensor provides lower noise measurements than the Clark cell at low oxygen concentrations, but above 70%, the low fluorescence signal present distorts the optical measurement.

After a stabilisation period of 17 minutes, both sensors responded well to the oxygen concentration changes. At DO concentrations below 50%, the optical alternative clearly out-performs the Clark cell, with a measurement precision of 5ppb achieved by the optical sensor at 0% oxygen. (A more modern Clark cell would have equalled this performance, see chapter 1). Above 80% [O_2], the optical sensor response became non-linear, with a 10% measurement error appearing at 100% [O_2]. It is thought that the very low fluorescence collected under high quencher concentrations (one twentieth of that collected at the 0%, unquenched condition, see Figure 3.23) causes other factors, such as background light to become more significant and cause the error. The sensor model is also least accurate at high quencher concentrations, when the non-linear effects mentioned above are most relevant. There is also a slight drift in the optical reading over the 5 hour test. This is thought to arise from temperature fluctuations in the water sample, caused by the differing temperature of the air and nitrogen gas supplies. The thermal cross-sensitivity

of fluorescent oxygen indicators, and a novel method for compensating for them, will be discussed in chapter 6.

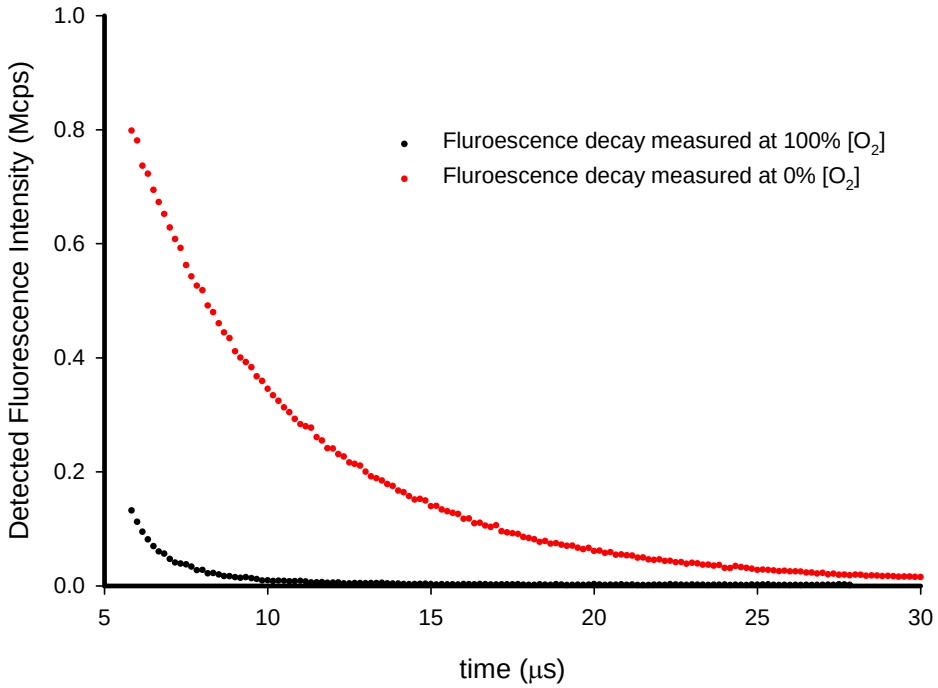

Figure 3.23 Fluorescence decay curves captured at 100% and 0% [O_2]. Only one twentieth of the photons collected at 0% (unquenched) conditions are collected at 100% (air-saturated) conditions.

3.6. Conclusions from chapter 4

In this chapter, fluorescence interrogation by direct analysis of the decay curve was considered. The RLD method was identified as a suitable method for interrogation of indicators with exponential decays (Ti:sapphire was used as an exponential fluorescence indicator) and oxygen indicators (a ruthenium-based indicator was assumed, see chapter 2 for description of this) with considerably more complicated decay shape. A novel analytical error-propagation-based model for the precision of an enhanced RLD method as a function of excitation pulse length, window boundary times and experiment repetition rate was described. Using the model, for the first time the conditions for optimal high-repetition rate measurements of both indicators using the enhanced RLD method were identified. This work showed that allowing a time gap between windows lead to the most favourable condition (disagreeing with studies by Demas *et. al.*[14] and Chan et al. [16], which did not consider all windowing conditions, but agreeing in principle with work by Walters and Burns[13]). The optimal setup condition considered here is expected to more than double the SNR ($490Hz^{0.5}$ compared with next best $243Hz^{0.5}$) expected when operating at conditions previous asserted to be optimal.

This novel work allowed study of the effectiveness of varying interrogator conditions to suit measurand level and background ambient light. The effect of background fluorescence decays (e.g. from auto-fluorescence of optical components or fluorescence species in the analyte) was also quantified. A method for reducing this effect (by up to 10^4 for short (<300ns) background decays) was discussed.

The new theoretical model was verified by comparison with both a computer-based random (Poisson) noise generator (similar to that used by previous studies), and with experimentally derived measurements with real Ti:Sapphire and oxygen indicators. The excellent agreement showed validity of the model. The optimal signal-to-noise ratio in measurement of a 3μs, pure exponential with peak fluorescence power 12.5pW was **280 $Hz^{0.5.}$**

For oxygen measurements, a measurement precision of **1.1ppb $Hz^{-0.5}$** was achieved whilst measuring de-oxygenated water, (with the sensor optimised for de-oxygenated measurements).

A test over the full 0-100% [O_2] range was performed with a sensor optimised for wide-range measurements. A dissolved oxygenation rig was used to vary the DO concentration in a 100ml water sample through 10% steps by bubbling a precisely controlled mixture of air and nitrogen gases through it. A measurement precision of **5ppb in 5s** was achieved, outperforming the observed precision of a standard Clark cell. (This precision is inferior to that achieved in de-oxygenated water above, because for these wide range measurements, the sensor was optimised for air-saturated rather than de-oxygenated measurements.)

3.7. References for chapter 4

1. Draxler, S. and Lippitsch, M., *Fluorescence Decay Time Measurement - a New Optical Sensing Scheme.* SPIE Biochemical Medical Sensors, 1993. **2085**: p. 61-67.

2. Trettnak, W.*, et al.*, *Optical Oxygen Sensor Instrumentation Based on the Detection of Luminescence Lifetime.* Advances in Space Research, 1998. **22**(10): p. 1465-1474.

3. Murtagh, M., Ackley, D. and Shahriari, M., *Development of a Highly Sensitive Fibre-Optic O2/DO sensor based on a phase modulation technique.* Electronics Letters, 1996. **32**(5): p. 477-479.

4. Trettnak, W.*, et al.*, *Miniaturized luminscence lifetime-based oxygen sensor instrumentation utilizing a phase modulation technique.* Sensors and Actuators B, 1996. **35**: p. 506-512.

5. Ocean-Optics, *FOXY Fiber Optic Oxygen Sensor - www.oceanoptics.com/products/foxysystem.asp*. 1996

6. *photosense LLC - real-time respiration sensor - www.photosence.com/oos.html*. currently in R&D phase

7. Austin, E. and Dakin, J., *Optimization Method for Rapid Lifetime Detection (RLD) Interrogation of fluorescent Decay Sensors - submitted July 2002.* Analytical Chemistry, 2002.

8. Herts, H., Ann.Physik, 1887. **31**: p. 983.

9. *Hamamatsu Photonics K.K. - Photon Counting Using Photomulitplier Tubes, Technical publication*. 1998.

10. Woods, R. and Ashworth, H., *Transient Digitizer for the Determination of Microsecond Luminescence Lifetimes.* Analytical Chemistry, 1984. **56**: p. 1395-1400.

11. Soper, S. and Legendre, B., *Error Analysis of Simple Algorithms for Determining Fluorescence Lifetimes in Ultradilute Dye Solutions.* Applied Spectroscopy, 1994. **48**(3): p. 400-405.

12. Ballew, R. and Demas, J., *Error analysis of the rapid lifetime determination method for single exponential decays with a non-zero baseline.* Analytica Chemica Acta, 1991. **245**: p. 121-127.

13. Waters, P. and Burns, D., *Optimized gated detection for lifetime measurement over a wide range of single exponential decays.* Applied Spectroscopy, 1993. **47**(1): p. 111-115.

14. Sharman, K.*, et al.*, *Error Analysis of the Rapid Lifetime Determination Method for Double-Exponential Decays and New Windowing Schemes.* Analytical Chemistry, 1999. **71**(5): p. 947-952.

15. Chan, S., Fuller, Z., Demas, J. and DeGraff, B., *Optimized gating scheme for Rapid Lifetime Determinations of Single-Exponential Luminescence lifetimes.* Analytical Chemistry, 2001. **73**: p. 4486-4490.

16. Chan, S.*, et al.*, *New Method of Rapid Luminescence Lifetime Determination Using Square-Wave Excitation.* Appied Spectroscopy, 2001. **55**(9): p. 1245-1250.

17. Pack, S., Renfro, M., King, G. and Laurendeau, N., *Photon-counting Technique for Rapid Fluorescence-Decay Measurement.* Optics Letters, 1998. **23**(15): p. 1215-1217.

18. Mills, A., *Response characteristics of optical sensors for oxygen : a model based on a distribution in torr0 and kq.* Analyst, 1999. **124**: p. 1309-1314.

19. Press, W., Teukolsky, S., Vetterling, W. and Flannery, B., *Chapter 10: Minimisation or Maximisation of Functions*, in *Numerical Recipes in C*. 1996, Cambridge University Press ISBN 0-521-43108-5. p. 396-455. ISBN 0-521-43108-5

4. FLUORESCENCE INTERROGATION BY MONITORING THE MEASURED DELAY RELATIVE TO AN INTENSITY MODULATED EXCITATION SOURCE

4.1. Introduction

Interrogation of the delay in the re-emitted fluorescence signal following excitation by a suitably intensity modulated source was briefly discussed in chapters 1 and 4. It has been a widely used sensing scheme for indirect sensors using fluorescence measurement since 1993, when it was suggested as a preferable alternative to simple intensity measurements [1]. It remains the most popular sensing scheme both in scientific research systems [2], [3], [4] and industrial applications [5], principally due to the simplicity of the instrumentation required and intrinsic tolerance to background light.

In this chapter, the sensing scheme itself is first explained and modelled for an idealised interrogation system and sinusoidal excitation modulation. This will then be extended to the case of square-wave modulation (which is preferable in many applications). Then a novel more practically realistic model, including the inevitable optical delays, electronic delays and band limiting effects of real components, will be developed, using computer simulation of real interrogation hardware that has been built for the project. Using the model, the expected response from a realistic dual-phase, square-wave modulated interrogator will be explored for the first time. By characterising noise sources in the hardware, the expected measurement precision is then calculated and compared with achieved values, thereby verifying correct operation of the model. Settings for achieving optimal precision measurement using dual and single-phase interrogators will be calculated, and compared with previously published results.

4.2. Sensing Scheme

Consider first a fluorescent indicator exposed to a constant continuous optical excitation source. After an initial fluorescence build-up period, an equilibrium is reached where the rate of luminophores excited by the source becomes equal to the rate of their relaxation to the ground state. If the indicator were to be excited instead with a source of periodically varying intensity of appropriate modulation frequency, then this equilibrium would never be reached, and the fluorescence light intensity would vary in a manner determined by the excitation modulation waveform. By monitoring the delay between the excitation modulation and the subsequent returning fluorescence modulation, the fluorescence decay lifetime could be inferred.

This arrangement is shown in Figure 4.1, where an idealised interrogator is described. Here, a sinusoidal excitation light modulation, of frequency f_m (and hence period $1/f_m$) (Figure 4.1 (a)) results in a delayed fluorescence signal (Figure 4.1 (b)). An exponential fluorescence decay or a band limited detection system, where all components other than f_m are not admitted, is assumed.

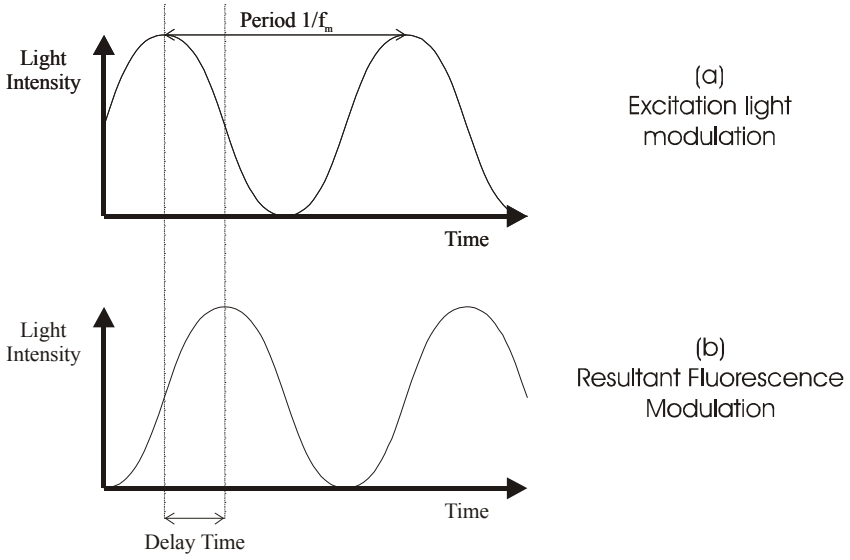

Figure 4.1 Ideal delay monitoring fluorescence interrogator.

In the case of a sine-wave modulated excitation source of frequency f_m, falling on an indicator having exponential fluorescence decay lifetime τ, the phase delay ϕ is given by (this relationship is proved later):-

$$\tan(-\phi) = 2\pi f_m \tau$$

(4.1)

Pure sinusoidal modulation of most excitation light sources is inconvenient (when the source has non-linear intensity response, e.g. the LED) or impossible (e.g. when a flashlamp is used, where an arc between two electrodes inside a pressurized bulb triggers a flash of light). Non-linear sources require complicated drive electronics and may only deliver pure sinusoidal modulation when modulation depths are kept low to linearise the source response. Conversely, square-wave, (or 'on-to-off-to-on') modulation is much easier to achieve, either by modulating the source drive itself (e.g. for LEDs), or by placing a shutter (e.g. LCD) in front of a continually illuminated source (e.g. halogen bulb). The delay is no longer related to fluorescence lifetime by (4.1) when a square-wave shaped modulation is chosen, as a higher bandwidth detector should be used, and higher frequency components exist in the detected waveform.

The expected phase delay firstly from sinusoidal, then from square-wave excitation is discussed in the following section. The argument is then extended to include the delays and the limited frequency response of the detection system itself.

4.3. The measured phase-delay (idealised interrogation system)

In this section, the expected phase-delay measured by a fluorescence interrogator is modelled. A fluorescence indicator having an exponential decay function is assumed.

4.3.1. Sinusoidal excitation modulation

First we consider the sinusoidal excitation modulation case to derive (4.1), the well-known relationship between the phase delay and the fluorescence decay lifetime.

When the excitation source is sinusoidally modulated at an angular frequency ω (so $\omega = 2\pi f_m$), we can describe the fluctuating part (i.e. ignoring any continual residual excitation light) as:

$$\upsilon(t) = \upsilon_s \sin(\omega t)$$

(4.2)

If the indicator has an exponential fluorescence decay with a lifetime τ, then the expected impulse response (which is the fluorescence decay that would be seen if the excitation source where to emit a single short pulse) is

$$I^0(t) = I_s e^{-t/\tau}$$

(4.3)

The detected fluorescence I(t) at time t is then an accumulation of all the remaining un-decayed fluorescence light excited before time t, i.e. the convolution of υ(t) with $I^0(t)$

$$I(t) = I^0 * \upsilon(t) = \int_0^t I^0(t-\eta).\upsilon(\eta).d\eta$$

(4.4)

where we have applied the definition of convolution. By inserting (4.2) and (4.3) into (4.4), and performing the integration, we obtain

$$I(t) = I_s.\upsilon_s.\left[-\frac{\tau(\omega\tau\cos(\omega t) - \sin(\omega t)) + \omega\tau^2.e^{-t/\tau}}{1+\omega^2.\tau^2}\right]$$

(4.5)

at sufficiently large t (i.e. after the response from the indicator has become established), we may re-write this as

$$I(t) = K.[\sin(\omega t) - \omega.\tau.\sin(\omega.t + 90°)]$$

(4.6)

where the various constants are grouped together in K.

So I(t) is made up of a sine wave, of angular frequency ω, and intensity K, plus a 90° phase shifted contribution of intensity -K.ωτ. This observation leads to the well-known formulae for the phase delay ϕ between the intensity modulation waveform of the excitation, and the returning fluorescence modulation:

$$\tan(\phi) = \frac{90° \text{ phase} - \text{shifted component}}{\text{in - phase component}} = -\omega\tau \text{ or } \tan(-\phi) = \omega\tau \text{ or } \tan(\text{-}\phi) = 2\pi f_m \tau$$

(4.7)

i.e. the same as (4.1).

4.3.2. Square wave modulation

As explained above, it is often preferable to employ simple on-off square-wave intensity modulation, although this alters the measured phase delay.

When the excitation light is a 50% duty cycle 100% modulation depth (i.e. on-off-on-off) square wave, it can be expressed as the infinite Fourier series expansion:-

$$\upsilon(t) = \upsilon_s.\left[\frac{1}{2} + \frac{2}{\pi}\left(\frac{\sin(\omega t)}{1} + \frac{\sin(3\omega t)}{3} + \frac{\sin(5\omega t)}{5} + ...\right)\right] = \upsilon_s\left[\frac{1}{2} + \frac{2}{\pi}\sum_{m=0}^{\infty}\frac{\sin((2m+1)\omega t)}{2m+1}\right]$$

(4.8)

once again, we must apply a convolution to obtain the received fluorescence intensity waveform I(t), so

$$I(t) = \int_0^t I^0(t-\eta).\upsilon(\eta).d\eta = \frac{I_s.\upsilon_s}{e^{t/\tau}}\int_0^t e^{\eta/\tau}.\left[\frac{1}{2} + \frac{2}{\pi}\sum_{m=0}^{\infty}\frac{\sin((2m+1)\omega\eta)}{2m+1}\right].d\eta$$

(4.9)

using the identities:

$$\int_0^t e^{t/\tau}.\frac{\sin(n\omega\eta)}{n}.d\eta = \frac{\omega\tau^2}{1+n^2\omega^2\tau^2} - \tau.e^{t/\tau}.\frac{\left[n\omega\tau\cos(n\omega\tau) - \sin(n\omega\tau)\right]}{(1+n^2\omega^2\tau^2)n}$$

(4.10)

and

$$\int_0^t e^{\eta/\tau}.d\eta = \tau^2(1-e^{t/\tau})$$

(4.11)

we complete the integration and obtain:

$$I(t) = \frac{I_s.\upsilon_s}{e^{t/\tau}}.\left[\frac{\tau^2}{2}.(1-e^{t/\tau}) + \frac{2}{\pi}\sum_{m=0}^{\infty}\left[\frac{\omega.\tau^2}{1+(2m+1)^2\omega^2\tau^2} - \tau.e^{t/\tau}.\frac{\left[(2m+1)\omega\tau\cos((2m+1)\omega\tau) - \sin((2m+1)\omega\tau)\right]}{(1+(2m+1)^2\omega^2\tau^2).(2m+1)}\right]\right]$$

(4.12)

in the limit of increasing t (i.e. once the fluorescence is established), this equation may be reduced to

$$I(t) = I_s.\upsilon_s.\left[\frac{-\tau^2}{2} - \frac{2}{\pi}\sum_{m=0}^{\infty}\left[\tau.\frac{\left[(2m+1).\omega\tau\cos((2m+1)\omega\tau) - \sin((2m+1)\omega\tau)\right]}{(1+(2m+1)^2\omega^2\tau^2).(2m+1)}\right]\right]$$

(4.13)

If the detection system introduces no additional delays, and is low-pass filtered such that it measures only the fundamental of the modulation frequency (i.e only the angular frequency of ω is admitted), then only the m=0 Fourier component will be included, so the measured waveform is:

$$I_{LP}(t) = I_s.\upsilon_s.\left[\frac{-\tau^2}{2} - \frac{2}{\pi}\left[\tau.\frac{\left[(\omega\tau\cos(\omega\tau) - \sin(\omega\tau)\right]}{(1+\omega^2\tau^2)}\right]\right]$$

(4.14)

and, as in the sine wave excitation case, the fluorescence lifetime may be related to the phase delay by the familiar function (4.7).

In the general case, more applicable to real world applications, the detection system has limited bandwidth but does not perfectly attenuate all non-fundamental harmonics, and usually has its own delay. Then, a more complicated numerical model specific to the measurement apparatus is required to predicted the expected phase delay. To explore this interrogation hardware was built. Its design is now discussed.

4.4. Interrogation hardware

Here the system components within the interrogator are briefly described. More analysis will be given later, when the theoretical model is updated to reflect the non-ideal response of the hardware. For a complete circuit description, please refer to the appendix section.

The system design is shown in Figure 4.2. The optical parts of the instrument have already been described in (chapter 3). The excitation source (an InGaN blue LED) is driven by a square-wave signal, derived by division of a master clock signal. For low-cost and high-sensitivity, the resulting fluorescence was detected by a silicon photo-diode (the most commonly used detector in these sensors), and amplified by a special transimpedance based pre-amplifier. The transimpedance stage (required for lowest noise, highest gain combination for a given response bandwidth), was followed by a high-pass filter then a secondary gain stage. This was then further amplified by a variable gain stage, having a maximum gain of 30. The amplified detected waveform is fed to a pair of electronic multiplier circuits, configured to multiply by either +1 or –1 according to the state of their digital reference input. TTL square waves, one in phase with the excitation modulation (termed D_0) and one delayed by 90 degrees to it,

(called D_{90}) are conveyed to the reference inputs of the multipliers. Each multiplier was followed by an analogue low-pass filter of bandwidth 10Hz before acquisition by the control computer, where further digital filtering (of software adjustable cut-off frequency) was performed. As two electronic multipliers were used, for separately decoding in-phase and out-of-phase components, this sensing scheme has been called the 'dual-phase' or 'quadrature' phase-detection system, [6]. The detected components may be processed to allow intensity independent measurement of phase angle.

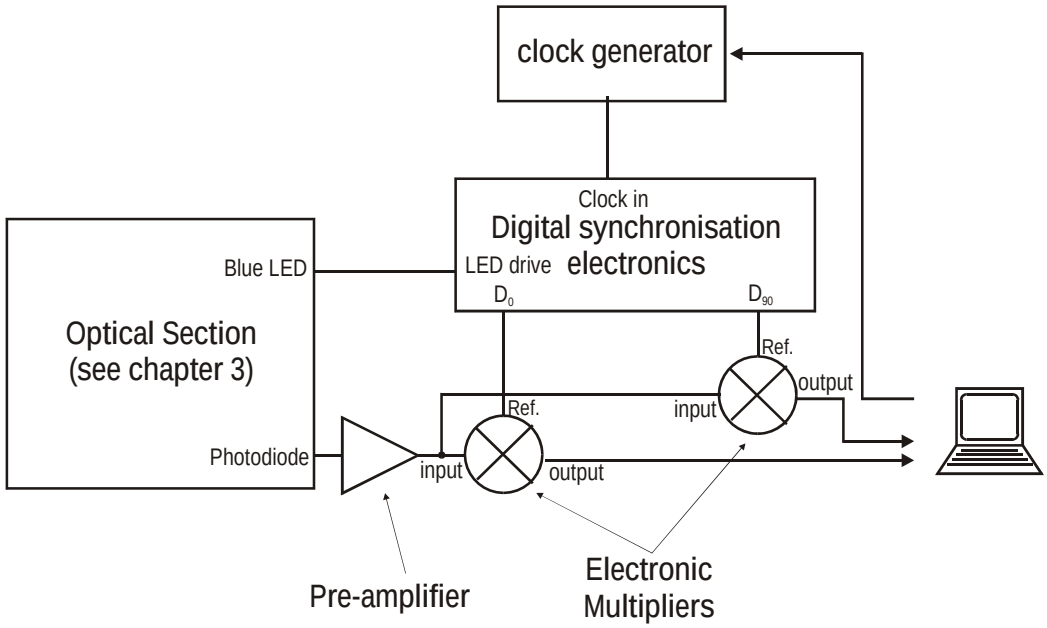

Figure 4.2 Schematic diagram, showing the electronic elements in the phase-delay monitoring fluorescence lifetime interrogator. Fluorescence resulting from square wave excitation was interrogated with a dual-phase (sometimes called "in-phase and quadrature") electronic multiplier system.

The apparatus allows computer settable excitation frequencies, based on division of a 12MHz clock, leading to modulation waveform periods of 10.667, 21.3333, 42.667 etc. μs

4.5. Optical detection preamplifier requirements

Here a basic overall design of the optical detector preamplifier will be discussed. Later, other aspects, such as noise considerations, will be considered.

The operating principle of photodiode optical detectors was outlined in chapter 3. In simplified terms, a current is produced by the photodiode proportional to the measured light intensity. A pre-amplifier module was required to convert this tiny current into a useable signal.

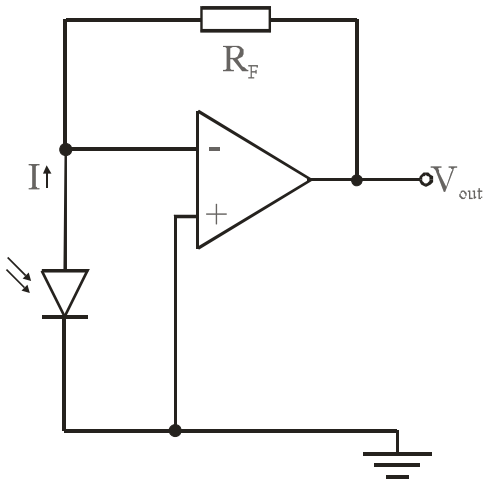

Figure 4.3 The transimpedance amplifier. It is the preferred topology for high-gain photodiode pre-amplification.

The transimpedance amplifier is shown in Figure 4.3. It has been described in detail in many core texts (e.g. Gowar [7]). Light incident on the depletion region of a photodiode causes excitation of the semiconductor material and production of electron-hole pairs, which, given sufficient energy, can escape to form a measurable current I. At equilibrium, the voltages at the negative and positive terminals of the operational amplifier (see Figure 4.3) must be equal (and therefore zero), so the voltage V_{out} appearing at the amplifier's output must be equal to the voltage produced across the 'transimpedance' resistor $R_{f.}$, which is equal to $I.R_f$. Hence the current, I, produced by the photodiode is amplified by factor R_f.

As explained in chapter 3, only 500pWr.m.s of fluorescence light was expected to reach the detector, so a current of around 250pAr.m.s would be produced (assuming a responsivity of $0.5AW^{-1}$). To amplify this to a reasonable level with a transimpedance amplifier, (say 1V r.m.s = 2.8V peak-peak), a transimpedance of $1/250x\ 10^{-12} = 4x10^9$ Ω would be required. It can be readily shown from a discussion of the idealised transimpedance amplifier, (i.e. assuming an ideal operational amplifier) that the bandwidth of detection (i.e. the light modulation frequency at which the gain of the amplifier is half its low frequency value) occurs (at maximum) when $f = \frac{A}{2\pi C.R_F}$,

where f is the frequency of light modulation, C is the combined detector capacitance, A is the open-loop gain of the amplifier, and R_F the transimpedance itself. If A is 70dB and C is 30pF (typical values), then the detection bandwidth would be only 5.7KHz (i.e. a response time of 175μs, much slower than the 1μs effective lifetime of the indicators). This makes a simple transimpedance amplifier alone unsuitable for this application.

Another disadvantage of operating with such a large transimpedance would be reduced immunity to background light, as the pre-amplifier could be easily saturated. As explained previously, one of the main advantages of the frequency selective fluorescence interrogator is thus immunity to background light. As the transimpedance amplifier is DC coupled (hence cannot intrinsically block continuous light) any continuous background signal (or offset in the amplifier itself) would be amplified with the same gain as the signal, and so could saturate the amplifier. This situation has been described in Figure 4.4, where the detected waveform in the presence of three background light levels is plotted. 100% modulation depth was assumed. In Figure 4.4 (a), the background-less situation is given, where only the fluorescence light itself was detected. In Figure 4.4 (b), a tolerable background level, that would be isolated from the detected signal by the frequency selective filter is assumed. In Figure 4.4 (c), the background level is so large that when combined with the peak fluorescence signal, the amplifier is saturated and its output can no longer reflect the detected light level. This would lead to significant errors in the detected phase delay. With a transimpedance of 4GΩ, the maximum background permitted (assuming 10V saturation voltage) would only be about 1.3nW. (The same problems would occur if the amplifier had a DC offset of its own.)

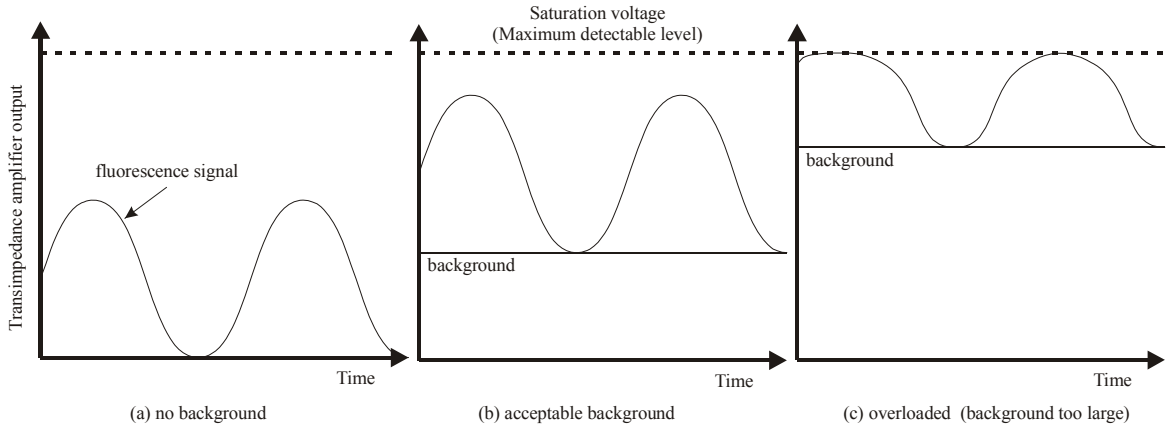

Figure 4.4 Saturation of transimpedance amplifier with background light

These problems were alleviated by splitting the gain into two stages; first a lower transimpedance gain amplifier, then a second stage amplifier, separated by a high-pass filter. This approach required lower gain from the transimpedance stage, which, then gives a higher bandwidth in the detection system. This was preferable, because the choice of modulation frequency was more flexible if the limiting factor was not the detection bandwidth itself. Operating close to the detection bandwidth could also introduce unwanted, possibly thermally dependent delays. An analysis of the effect of the detection amplifier on the fluorescence waveform will therefore be required because (as noted above) harmonics of higher frequency than the modulation fundamental could be present in the detected waveform, altering the measured phase shift. Due to the expected modulation frequency of around 100kHz, (to allow significant fluorescent decay during each modulation half-period) a target detection bandwidth of 200kHz was chosen.

The highest transimpedance possible whilst still retaining the desired bandwidth of 200kHz was 85MΩ (see earlier transimpedance bandwidth calculation), so a transimpedance of 100MΩ (giving 170kHz theoretical cut-off frequency) was chosen, as this was the closest readily available component value.

After a high pass filter section (based on DC servo circuitry), a 30x current feedback amplifier was employed to give the same overall gain as would be possible with the single 3GΩ transimpedance stage.

The two-stage pre-amplifier was constructed by a specialist supply company (Theoptics, Romsey, Hampshire). The design was based on their TA10 amplifier, and

was allocated serial number 133. It will be fully characterised, including a noise analysis, later.

4.6. Expected progression of waveforms through the interrogation instrument and expected detected values

To adequately model the expected measurement, the progression of waveforms through the system was modeled for a given fluorescence lifetime.

Rather than developing a cumbersome analytical model for the interrogator, a numerical approach was adopted, to predict the measured phase angle, as a function of fluorescence decay and modulation frequency.

The first step was to model the expected fluorescence intensity waveform resulting from square wave excitation modulation. This procedure was described in detail in chapter 4, so it is not considered again here. Let us assume this fluorescent modulation is a periodic fluorescence intensity waveform I(t), appearing at the detector as a result of the modulated excitation light. The effect on this waveform of each of the amplification and multiplying elements was modelled in turn.

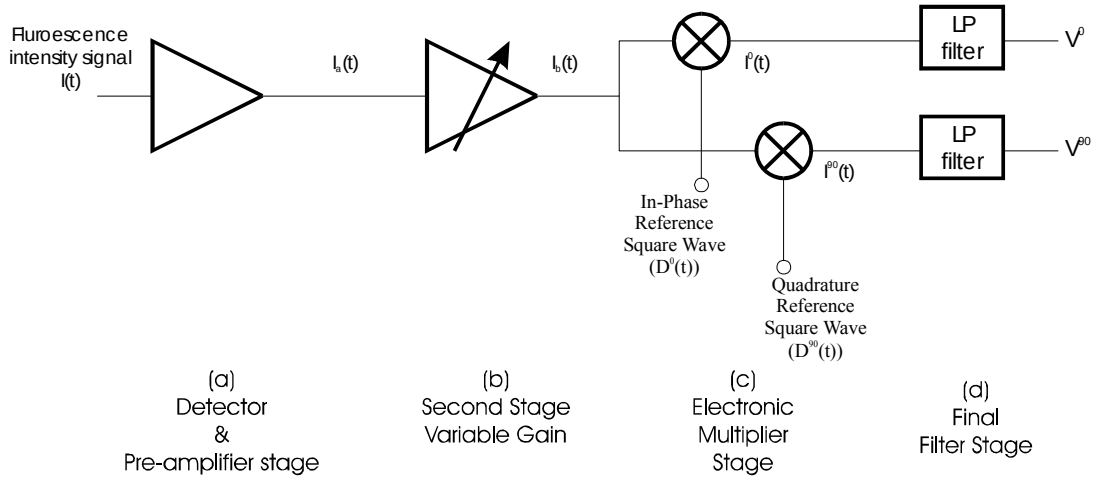

Figure 4.5 System level description of the detection electronic elements within the interrogator. The system has been divided into four stages. Section (a) and (b) include optical and detector pre-amplification stages, followed by twin electronic multipliers, (section (c)), for dual phase detection. These are followed by low-pass filters (section (d)) to provide appropriate decoding and averaging of the detected phase-angle.

Here the detection electronics is described in slightly more detail, before each stage is characterised and modelled. A simplified schematic representation of the analogue circuitry is given in Figure 4.5. First the response of optical sections, detector, and pre-amplifier are grouped in section (a), which comprises InGaN blue LED, optical filters, and preamplifier discussed above. This two stage-amplifier and high pass filter is expressed using a single amplifier symbol in Figure 4.5.

Section (b), a variable gain inverting amplifier, was included to allow extra gain when interrogating very weak fluorescence intensities, but not required for this work. This pre-amplified signal was then passed through the twin electronic multipliers (section (c)) referenced to the overall synchronisation signals D^0 and D^{90} (this was explained previously). The two low-pass filters (section (d)), (with time bandwidth 10Hz), provide the average voltages V^0 and V^{90}, which were passed to the control computer for further averaging and processing.

4.6.1. Simulation of section (a) and section (b)

The effect of the optical filters, detector, transimpedance amplifier and secondary amplifier was applied to the fluorescence waveform I(t) by convolution with an impulse response measured from the system. The theoretical principle of convolution, where the response, measured at the output of a channel, when a delta-function (short) pulse is applied at its input, is used to predict the output of the channel resulting from any arbitrary input waveform has been discussed in many texts [8], so is not covered in detail here. This principle will be used here to model the hardware systems. A linear transfer function at each stage is therefore assumed.

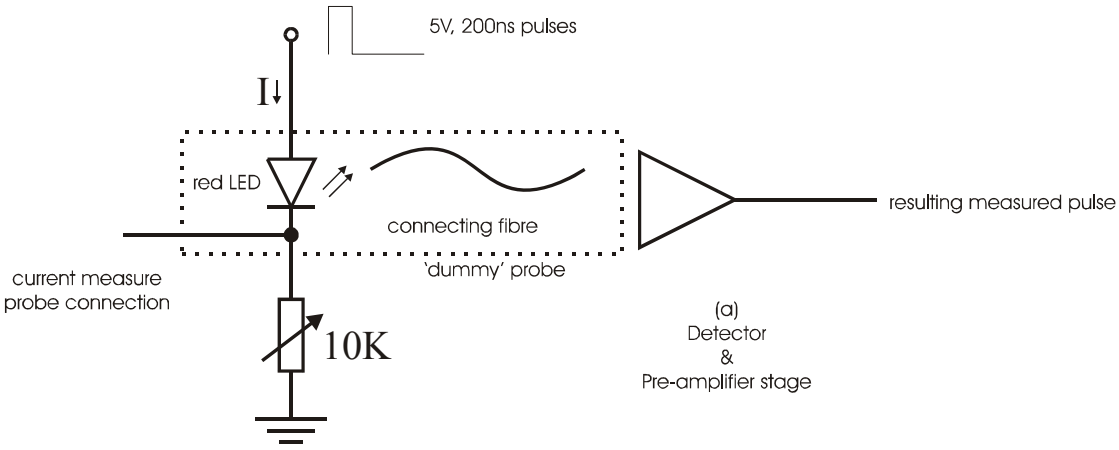

Figure 4.6 Experimental setup for measuring the impulse response of section (a). A 'dummy' probe comprising standard optical fibre bonded to a red LED was used to mimic the fluorescence signal.

The impulse response of section (a) and (b) (set to unity gain) was obtained by de-convolving the waveform observed at its output with that of 200ns duration drive current pulse, applied to an LED coupled to the optical input. To do this, a special test probe or 'dummy' probe was fabricated and connected to the interrogation instrument, as shown in Figure 4.6. The 'dummy' probe consisted of the same fibre lead used for other probes (Newport F-MBD), but instead of a fluorescent indicator, a red LED (a GaP LED from 'Fibre Data' type L05R5000E1, 700nm peak output wavelength) was bonded to its distal end to thereby mimic the fluorescence light. As the intensity of fluorescence light returning from a real indicator was very weak (<500pW), optimal coupling between the LED and fibre lead was not required to achieve this power, so the cleaved fibre was simply bonded with styrene cement (Strand, Resin 'C', a polymer resin having negligible auto-fluorescence was used, see chapter 2) into a 1x4mm hole drilled in the plastic casing of the LED. 5V, 200ns pulses with 5KHz repetition rate, derived from a bench-top pulse generator (Lyons Instruments type PG23), were applied via a 10KΩ variable resistor to the red LED, thereby allowing adjustable attenuation of the LED drive current. The LED drive current was adjusted so the intensity of the test probe output was 500pW (measured using an Ando AQ-6315A optical spectrum analyser).

Obviously, any significant time delay between the drive current pulse applied to the test LED and the resultant light pulse, or any induced fluorescence signal produced by the test probe itself, would be extremely undesirable. A test was therefore performed

to confirm rapid response of the test probe. Light from the probe was conveyed to a separate wide-bandwidth red-sensitive detection system, comprising Hamamatsu type H6780 PMT module and Theoptics TA10 transimpedance amplifier, with 100KΩ feedback resistance. The transimpedance amplifier effectively presents a very low impedance to the PMT, maximizing operating bandwidth. The detector PMT module itself has a specified anode pulse rise time of 0.65ns, and the transimpedance amplifier stage has specified response time <50ns, giving an overall detection bandwidth of over 20MHz.

All three measured waveforms are shown in Figure 4.7, with the LED drive current (measured by monitoring the voltage across the series resistor) plotted in solid dark line, the high bandwidth optical measurement for verification shown as the dashed line, and the resultant pulse at the output of the instrumentation preamplifier (i.e. the measured output of section (b) within the instrument) as the dotted trace.

The wide bandwidth measurement from the PMT detector shows a rise and fall time of 50ns (i.e. 20MHz). This implies the wide-bandwidth verification measurement was limited by the bandwidth of the detection system, so the test probe itself must have a response time much shorter than 50ns, as required. No significant fluorescence from the test probe was observed.

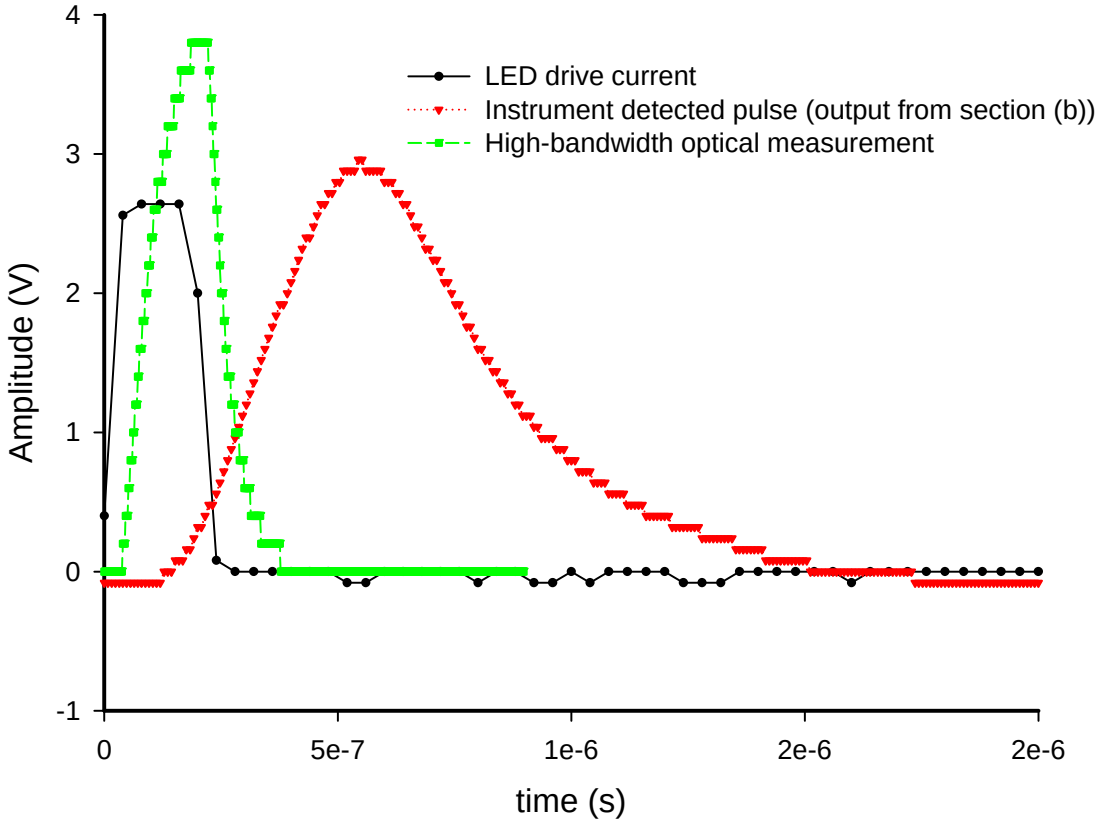

Figure 4.7 Measurements to derive the impulse response of the instrumentation's detection system. An LED was driven with a 200ns pulse. The current flowing through the LED is plotted (solid line). A high-bandwith measurement of the resultant optical pulse was taken (dashed line, squares), to confirm rapid response and negligible fluorescence of the test probe. Finally, the resultant detected pulse by the instrumentation pre-amplifier (i.e. the output of section (b)) is given (dashed line, triangles).

The impulse response of the detection system was then calculated by performing the appropriate de-convolution.

4.6.2. Predicted progression of waveforms

A numerical computer simulation for predicting the response of the progression of waveforms through the instrument was written in Mathsoft Mathcad 2000. A pure exponential (or 'mono-exponential') decay from the indicator was assumed.

The numerical model simulated, for an assumed fluorescence lifetime and excitation light frequency, the expected fluorescence intensity waveform (I(t)). The effect of the pre-amplification stages (section (a) and section (b)) were simulated by convolving I(t) with the impulse response of section (a) and (b), obtaining $I_c(t)$.

To test the fidelity of the numerical model, a comparison was made between an expected and experimentally measured waveform. This was achieved by connecting the interrogator to the Ti:Sapphire calibration probe (described in detail in 2), which returned exponential fluorescence decay.

The calibration probe was thermally stabilised in the custom oven with its temperature control system (see chapter 2). Its fluorescence lifetime was then determined accurately by curve fitting to its captured fluorescence response, which was obtained using the photon-counting fluorescence interrogator (see chapter 4). The results from this measurement are shown in Figure 4.8, where a non-linear regression algorithm (within Sigma-Plot 2000) was used to fit a mono-exponential decay curve to the measured fluorescence decay. The fluorescence lifetime of the probe was determined as 3.05 ± 0.02μs.

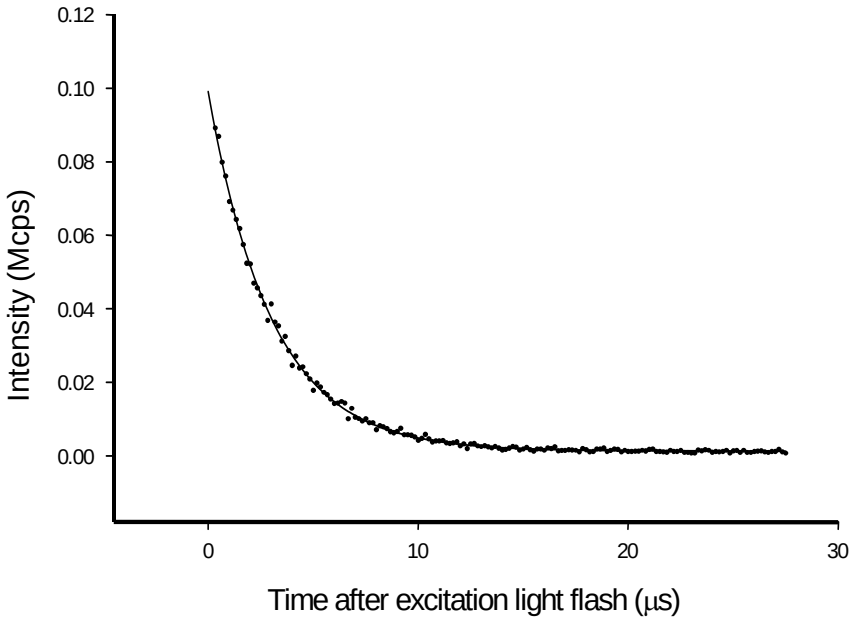

Figure 4.8 Ti:Sapphire probe fluorescence response curve at 21.0°C. A non-linear regression analysis gave the response time as 3.05 ± 0.02μs.

The computer simulation was set to simulate the expected fluorescence waveform resulting from exciting a probe with an exponential lifetime of 3.05μs (i.e. equal to the measured Ti:Sapphire probe lifetime), with a square wave intensity modulated excitation source, with a drive-signal period of 10.66μs (i.e. equal to one of the excitation periods that can be generated by the interrogation instrument).

The resultant analytically derived fluorescence waveform I(t) is shown in Figure 4.9.

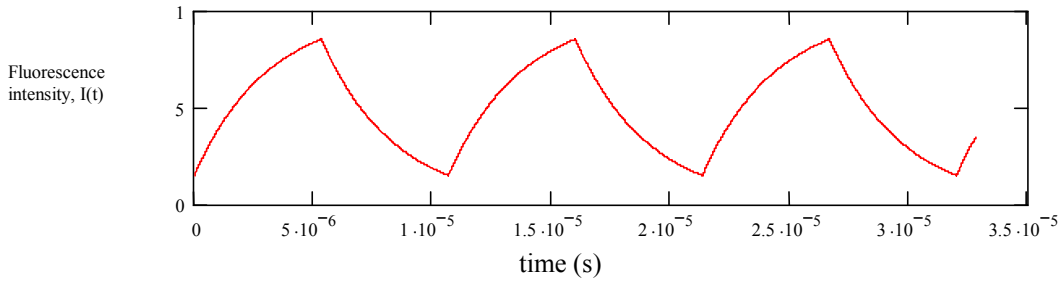

Figure 4.9 Simulated fluorescence intensity I(t) returning from a probe of lifetime 3.05µs, excited with a square wave modulation having a period of 10.67µs.

The response of section (a) and section (b) to this waveform was calculated by convolution with the impulse response, leading to the band-limited waveform (filtered waveform, dotted line) plotted in Figure 4.10. The original undistorted waveform (I(t)) is plotted on the same axis (full line). To achieve this, the analytically derived waveform I(t) was 'sampled' by the computer, at a sampling period of 8ns (i.e. much faster than any other likely effects within the system) then performing the convolution. Another point to note is that section (b) is an inverting amplifier, so that where the fluorescence intensity (as plotted in Figure 4.9) rises, then $I_c(t)$ falls in Figure 4.10. As can clearly be seen, the simulation shows a delay between the undistorted fluorescence and the 'detected' waveform. The band limiting affect of the detector is also evident from the "rounded corners" showing low-pass filtering of the response.

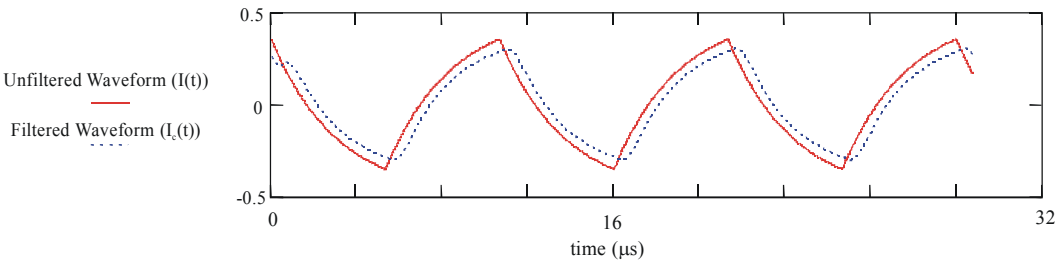

Figure 4.10 Simulated fluorescence signal following section (a) and (b) ($I_c(t)$) . The undistorted fluorescence intensity waveform I(t) is plotted on the same axis for reference. We can clearly see the delay presented by the electronics. (The sampling period used for this analysis was 8ns)

In Figure 4.11, the simulated fluorescence lifetime (blue dotted line in Figure 4.10) is plotted on the same set of axis as a real measured waveform. As we see, there is excellent agreement between the simulated and the measured curves, showing the computer model predicts the real system with very high fidelity.

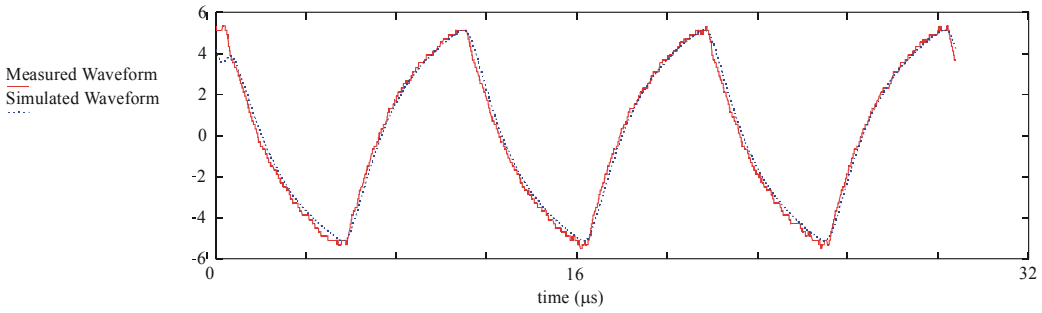

Figure 4.11 Simulated detected fluorescence signal, $I_c(t)$ (dotted line) plotted for comparison with measured same (full line). This plot verifies faithful simulation of first the fluorescence response characteristic itself, then the band-limiting effect of excitation source, detector, and detector pre-amplification stages. (The sampling period was 8ns)

Next section (c) (the electronic multiplier section) was modelled. First, simulated versions of the in-phase (D_0) and quadrature (D_{90}) waveforms, which form the control inputs to the electronic multipliers, were generated. The electronic multipliers were then simulated by multiplying the waveform $I_c(t)$, by either +1 or –1 according to the state of the reference signals. The resulting waveform expected $V^0(t)$ is plotted as the solid line in Figure 4.12.

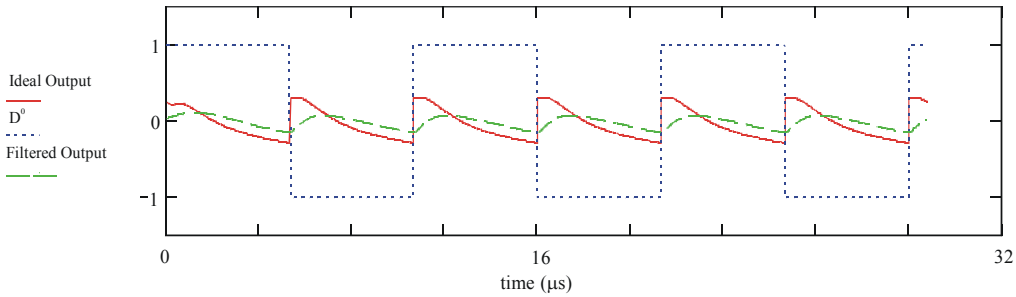

Figure 4.12 Idealised and band-limited in-phase electronic multiplier output. The ideal $V^0(t)$ (full line), and a band limited version (dashed line) are plotted.

Unfortunately, a real electronic multiplier circuit is in practice not ideal. The circuit design used is discussed in detail in the appendix, but for here it is important simply to note that the design was optimised for low measurement drift and accuracy, at the expense of limitations to bandwidth (130KHz), and low slew rate ($1V\mu s^{-1}$).

To assess the effect on the signal of the electronic multipliers, their frequency response, whilst fixed in non—inverting mode, was measured and is shown in Figure 4.13. The curve shows an approximate bandwidth of 130KHz, with subsequent roll off of 13dB/Octave.

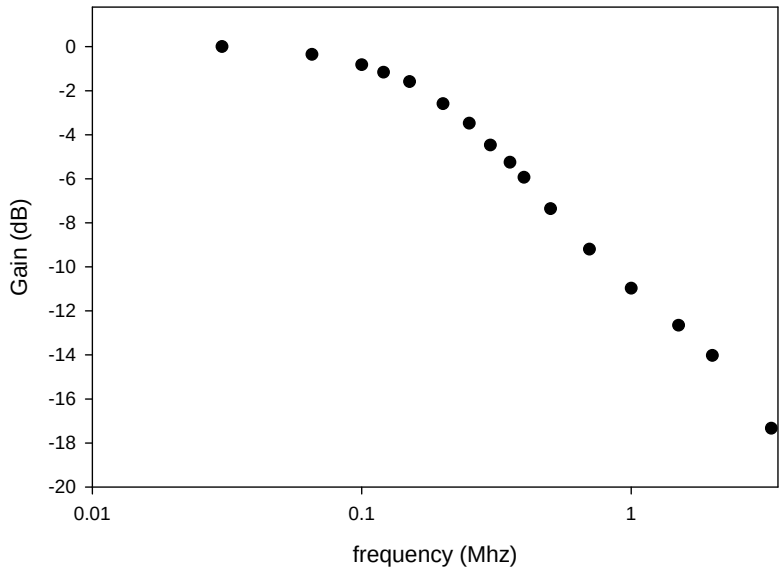

Figure 4.13 Measured frequency response of electronic multiplier circuit. The curve shows, in approximate terms, a 130KHz bandwidth with 13dB/Octave roll-off.

To try to model this effect by convolution, the waveform resulting at the output of the multiplier from 200ns pulses at its input was captured then de-convolved with the originating 200ns pulse waveform. The ideal (infinite bandwidth) electronic multiplier output (full line Figure 4.12) was then convolved with this measured impulse response of the multipliers, yielding the band-limited waveform (dashed line Figure 4.12). This waveform (dotted line) is compared with a real measured version (full line) waveform in Figure 4.14. If the electronic multiplier stage had been successfully modeled, then the two waveforms would be identical, but this is far from the case; there is still a large discrepancy between the simulated and measured traces.

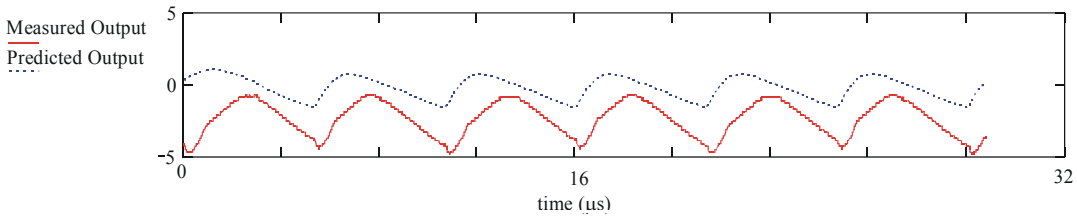

Figure 4.14 Simulated (dotted line) and measured (full line) output from 'in-phase' electronic multiplier. Note the model does not adequately reflect the measured waveform due to the limiting slew-rate of the multiplier circuits.

This discrepancy occurred due to the limiting slew-rate of the multiplier circuits, which comes into effect when they are switched between inverting and non-inverting modes. (This is a shortcoming of the electronic design.) This makes the computer model unsuitable for accurately modeling the electronic multiplier circuits. Modeling

this slew rate limited amplifier behavior is possible, but not by any means trivial. Such analysis is not attempted here.

4.7. Response of modulated source interrogation systems to exponential lifetime

In the absence of a satisfactory model for the effect of the electronic multipliers, it was impossible to fully predict the response from the physical interrogator hardware to exponential lifetime or an oxygen indicator. The model still has great value, because it allows comparison of hypothetical "realistic" interrogators with the ideal response (given below), and it is still adequate for a noise analysis (given later).

First, square-wave modulation, ideal detection amplifiers and perfect electronic multipliers with no delay and no bandwidth limitation were assumed. Simulated values for time-averaged versions of V^0 and V^{90} were calculated by averaging their expected waveforms over three modulation periods. The value of R, which is the dimensionless ratio of V^{90}/V^0, (which is used to infer phase-delay and therefore fluorescence lifetime) was calculated from these values. V^0, V^{90} and R are plotted as a function of fluorescence lifetime between 1 and 5μs for a 10.66μs excitation modulation period in Figure 4.15. The expected ratio R that would be observed had sinusoidal modulation been employed was plotted on the same axis as the square-wave case in the right-most diagram.

The difference between these plots therefore reflects the extra harmonics present in the detected signal when square-wave modulation is used. The plots diverge more at longer fluorescence lifetimes because the lower frequency harmonics produced by the indicator coincide with stronger harmonics produced by the modulation waveform itself, and are therefore captured by the interrogation system.

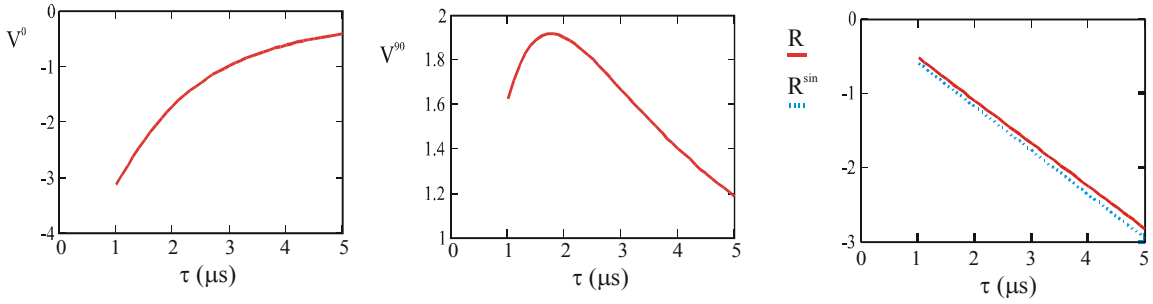

Figure 4.15 Predicted values for V^0, V^{90}, and their ratio R plotted as a function of fluorescence lifetime. Ideal detection system and electronic multipliers with unlimited bandwidth are assumed. The expected value of R for sinusoidal modulation (as predicted by (4.1)) is plotted for reference.

When the effect of the delays and limited response time of the detection amplifier are included using convolution, the simulated V^0, V^{90} and R responses shown in Figure 4.16 are expected. The response at 3.2μs lifetime, where the ratio goes through a discontinuity, occurred because the fluorescence signal delayed by its passage through detection amplifiers and optics, has zero in-phase component at this lifetime. This is analogous to the phase delay passing through 90° in a sinusoidal modulation system.

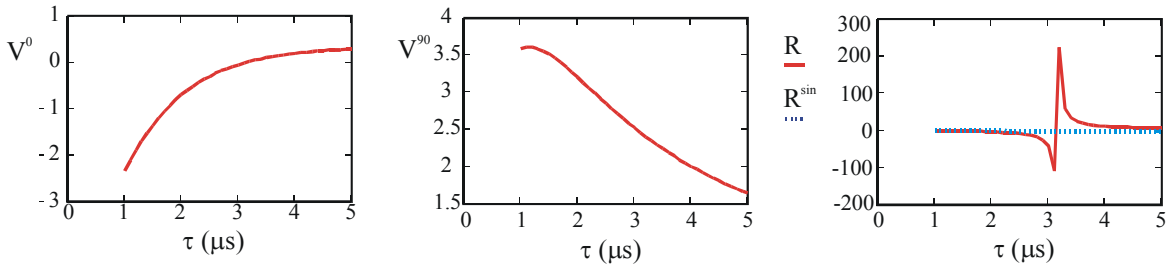

Figure 4.16 Predicted values for V^0, V^{90}, and their ratio R plotted as a function of fluorescence lifetime. Realistic detection and optical systems (characterised earlier) but ideal electronic multipliers are assumed. The expected value of R for sinusoidal modulation (as predicted by (1)) is also plotted for reference.

In Figure 4.17, the expected response of the system when the effects of the detection amplification system, and the 130KHz bandwidth of the electronic-multiplier circuits is included in the response by convolution.

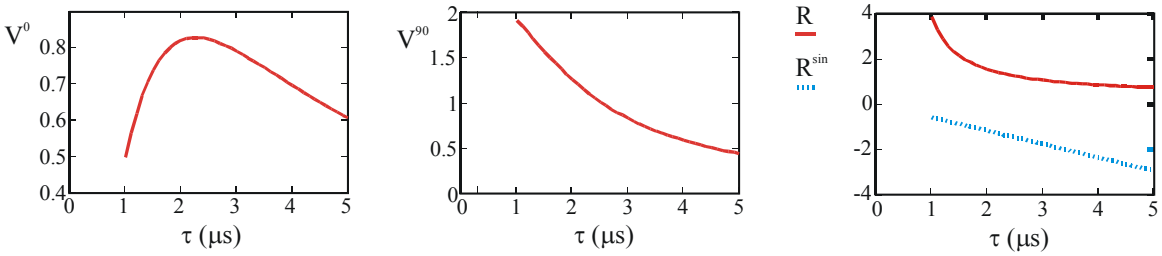

Figure 4.17 Predicted values for V^0, V^{90}, and their ratio R plotted as a function of fluorescence lifetime. The measured impulse response of the detection amplifiers and electronic multipliers are included. The expected value of R for sinusoidal modulation (as predicted by (1)) is plotted for reference.

We can see the effect of electrical and optical delays is greater than the effect of square-wave modulation. Though, in the absence of an adequate model for the electronic multiplier, it was impossible to predict measured values, this analysis is still valuable, because it shows, for the first time, the effect of square-wave modulation and realistic electronics and optics when exponential decays are detected. Further work is necessary to improve the interrogation system, thereby allowing verification of these results with measured values.

4.8. Optimal detection of exponential fluorescence indicators

Optimum operation of sine-wave modulation single-phase sensors for oxygen measurement, and identification of the most favourable modulation frequency has been considered before in [9].. The effects of detector frequency response, square wave modulation, and dual-phase interrogation have not been addressed, so, these aspects are explored here for the first time.

4.8.1. Contributions to noise in measurements

To identify the optimal measurement condition for the instrument, the expected noise in measurements from the hardware must be characterized. This is now done by analyzing each noise source. Results will then be verified by comparison with achieved values.

The main sources of noise in the detection system arose from the intrinsic noise in the fluorescence light itself plus contributions from the high-gain transimpedance

amplifier section. The secondary amplifier (with 30x gain), and the other stages, with no gain, should add negligible noise.

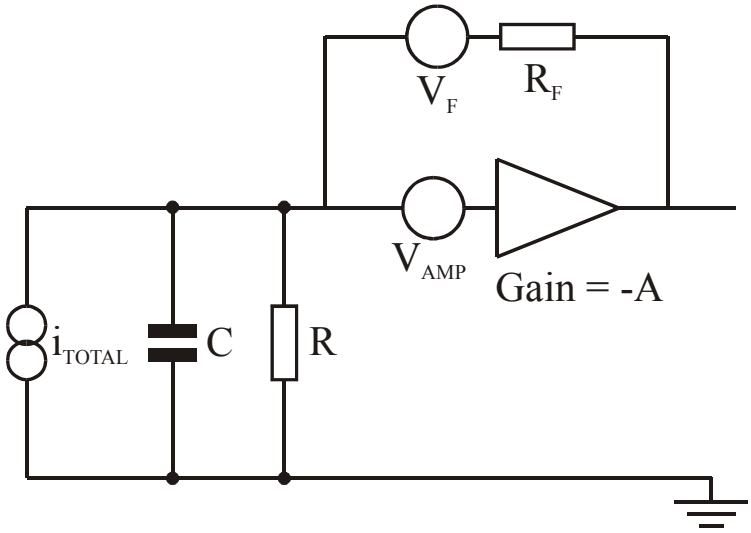

Figure 4.18 Noise sources for a transimpedance amplifier. I_{TOTAL} includes the shot noise, the current noise of the amplifier and the thermal noise arising the from amplifier and detector resistance (grouped as resistance R). V_F is the voltage noise created in the feedback resistor, V_{AMP} the amplifier input voltage noise, and C the combined capacitance of detector, amplifier, and stray capacitance.

To model the expected noise in the detected waveform, the noise sources were each considered then their contributions combined. Consider Figure 4.18, where the transimpedance amplifier is drawn for noise analysis.

First consider the intrinsic photon noise in the detected fluorescence light (this is sometimes called the shot noise). This is the unavoidable intrinsic minimum noise. The current $i_{in,}$ that is produced when a light intensity of 500pW falls on a detector of responsivity $0.42AW^{-1}$ (quoted value for BPX65RT detector at 620nm) is simply 500.10^{-12} x 0.42 = 2.1 x 10^{-10}Ar.m.s. The shot noise resulting from this is simply a current of $\sqrt{2e.i_{in}}$ = **8.2 x 10^{-15}Ar.m.s $Hz^{-0.5}$** or in voltage terms at the amplifier output **2.5 x 10^{-5}Vr.m.s $Hz^{-0.5}$.**

The feedback transimpedance creating voltage noise V_F which is equivalent to a current of $\frac{\sqrt{4.k.T.R_f}}{R_F}$ or **13 fA $Hz^{-0.5}$**. This is of similar order to the shot noise calculated above, so this must be considered important.

Current noise from an appropriate amplifier is typically a few fA $Hz^{-0.5}$ (Burr-Brown OPA655), and thus an order of magnitude smaller than the shot noise will be ignored.

The amplifier voltage noise is much larger, having equivalent current $2\pi V_{AMP} C.f$, where f is the detection frequency and C is the total input capacitance (this is derived in, for example [7]). At 100KHz, this corresponds to **11 fA $Hz^{-0.5}$**, i.e. of similar order to the shot noise. This will be considered.

The quoted noise equivalent power for the BPX65 detector (which is the a measure of the dark current produced by the detector) is 3.3 x 10^{-14}W $Hz^{-0.5}$, i.e. much smaller than the 500pW expected fluorescence light power, so can be safely ignored.

The thermal noise from the input resistance R, which is included in i_{TOTAL} is $\sqrt{\frac{4kT}{R}}$, which for a combined input resistance of around 2GΩ, negligible (<1fA $Hz^{-0.5}$).

The modelled voltage noise spectral density, at the output of the detector, at a frequency f when measuring an optical power p can therefore expressed as the addition in quadrature of the shot noise, transimpedance noise and amplifier noise

$$\eta(f, p) = R_F \sqrt{2eKp + \frac{4.k.T}{R_F} + (2\pi.V_{AMP}.C.f)^2} \text{ A. Hz}^{-0.5}$$

(4.15)

where K is the responsivity of the detector. Of course, this noise would be spectrally limited by the frequency response of the amplifier itself, but this is not important, as we will see.

The electronic multiplier section is frequency selective, so it can be shown that only the noise spectral density at the fundamental modulation frequency integrated over the overall measurement bandwidth is admitted to the final measurement. In general terms, noise components at even harmonics of the modulation frequency would also be admitted, as the modulation waveform is square-wave shaped, but these are strongly attenuated by the electronic multiplier circuits themselves, and are therefore negligible.

The expected noise in V^0 or V^{90} was therefore calculated by firstly integrating the fluorescence light intensity signal (I(t)) to obtain the total received power, then, by assuming all this power occurred at the modulation frequency (this approximation is

adequate for the purposes of a noise calculation), the expected noise η was calculated from (4.15).

The measurements V^0 and V^{90} should both contain identical noise, η, so the ratio $R=V^{90}/V^0$, contains a noise which is approximately:

$$\delta R = \sqrt{\left(\frac{\partial R}{\partial V^{90}}\right)^2 \eta^2 + \left(\frac{\partial R}{\partial V^0}\right)^2 \eta^2}$$
$$= \frac{\eta}{V^0}\sqrt{1+\left(\frac{V^{90}}{V^0}\right)^2}$$

(4.16)

(this is actually a slight approximation, because, even though the signals V^0 and V^{90} are processed separately, they are also correlated as they come from the same detected signal. Further investigation of this was not necessary for a noise calculation).

To test this noise analysis, a laboratory experiment to measure the noise in one of the outputs (V^0), whilst interrogating a stable fluorescence lifetime, was performed. The hardware interrogator was connected to the Ti:sapphire calibration standard, which was thermally tuned to return a lifetime of 3.05±0.02μs as before. The custom oven held the calibrator temperature steady to a long term accuracy of 0.1°C, which implies a lifetime noise of less than 1.3ns. Analysis of the fluorescence lifetime as a function of ratio V^0 (see Figure 4.17) predicted this would introduce a noise in V^0 of **1.3×10^{-5} V. $Hz^{-0.5}$**. The voltage V^0 was experimentally acquired at 1KHz via 12-bit National Instruments analogue interface card (type Lab-PC+) onto a standard PC computer. The noise arising from the acquisition itself was limited by the bit-width of the interface card over its input range (-5 to +5V, i.e. 10V) at 1KHz sampling rate, which is $\frac{10}{2^{12}} \cdot \frac{1}{\sqrt{1000}} = 7.5 \times 10^{-5} V.Hz^{-0.5}$ Once acquired, V^0 was further low-pass filtered by a roaming average algorithm to an overall response time of 5s, and the data stored at 5s intervals over an experimental run of 1080s. By calculating the standard deviation of these stored measurements then multiplying by the square root of the response time, 5s, the error in measurement of V^0 was measured as **0.6mV $Hz^{-0.5}$**. This value is much larger than the noise introduced by variations in the calibration probe temperature and noise introduced by the acquisition process, so it may be assumed it originated from the interrogation hardware itself.

The theoretically expected noise was calculated as **0.49mV Hz$^{-0.5}$** by evaluating (4.15) (the noise spectral density), at the modulation frequency (in this case 10.66μs) and detected fluorescence power (500pW). There was therefore good agreement between the theoretically expected achieved noise, proving validity of the model.

4.8.2. Identifying the optimal excitation modulation frequency

To estimate the error in measurement of lifetime from the error of measurement of R, we can say when δR<<R, then

$$\delta\tau \approx \delta R.\frac{\partial \tau}{\partial R} \approx \delta R.\left(\frac{\partial R}{\partial \tau}\right)^{-1}$$

(4.17)

which may be calculated from (4.16) and the numerical model for R, (which was given earlier). Identifying setup parameters for optimum measurement of lifetime is then the simple process of numerically identifying the modulation frequency which leads to minimum δτ via a minimisation algorithm.

To confirm (4.17), the error in measurement of the Ti:sapphire calibration crystal fluorescence lifetime was estimated. The measured ratio R was averaged with a response time of 5s and logged as the temperature of the calibration probe was progressed through a series of pre-set values. More than one temperature was required to relate ratio R to lifetime τ. Results from this are given later in the experimental results section. A dataset of results captured at 14.23±0.04°C, over a period of 450s, was extracted for error analysis. The observed error was unchanged throughout the measurement range. By determining the standard deviation per second of the dataset and relating this to a change in fluorescence lifetime via a derived calibration curve (see below), the error in measurement was determined to be **2.3 x 10^{-10}s Hz$^{-0.5}$**. The expected error (calculated using (4.17)) was determined to be **1.0 x 10^{-10}s Hz$^{-0.5}$,** (neglecting the effect of the electronic multipliers and assuming a received fluorescence intensity of 0.8Vr.m.s, as measured from experiment). Perfect estimation of experimentally received noise is not expected, because (as mentioned above) the effect of the electronic multiplier circuits could not be effectively modelled, so it was

assumed that (4.17) adequately describes the expected error in lifetime measurement and confirming expected operation of the interrogation hardware.

4.8.3. Optimal measurement assuming sin-shaped excitation modulation

Optimal experimental setup conditions were calculated by minimising $\delta\tau$ as a function of modulation frequency.

As stated above, the optimal modulation frequency for single-phase, sinusoidal modulation has already been considered by Orgurtsov et.al. [9]. Their optimum was derived by asserting that maximum precision in measurements occurs when the interrogator is most sensitive, that is when the maximum variation in phase shift with luminescence lifetime is observed or,

$$f_m = \frac{1}{2\pi\tau}$$

(4.18)

(where f_m is the optimal modulation frequency). The measured phase-angle is then 45°.

To make the presented model comparable with the assumptions in this published result, it had to be significantly simplified. Only photon, or shot noise was considered, with single-phase detection, and sin-shaped excitation modulation. The optimal modulation frequency was numerically determined for several fluorescence lifetimes by minimization of the noise in lifetime measurement ($\delta\tau$). The resulting derived optimal fluorescence lifetimes are displayed in Table 4 (right side of figure). We see excellent agreement between numerically predicted and traditionally assumed (using (4.18)) optimal excitation periods. (The slight discrepancy between numerical and traditional optimum periods arises because of the convergence criteria specified in the computer model). The numerically calculated error in lifetime measurements at each optimal point was also noted.

The model was then slightly extended to describe a dual-phase measurement system and the optimal excitation frequencies computed. A longer excitation period was required to provide optimal measurement from the dual-phase system. This result is best explained by considering Figure 4.19, where the response of a single-phase

interrogator monitoring a fixed fluorescence lifetime at a fixed modulation frequency is plotted, as a function of phase delay between the measured signal and the multiplication reference. The dotted line shows the effect on the sensitivity of measurements, clearly showing optimum sensitivity when the phase angle is 90°. (This differs from the optimal phase angle in the discussion above, because here we are assuming independent control of modulation frequency and phase delay). If a dual-phase measurement system was employed, then the optimal excitation period should be increased, so that both the in-phase and out-of-phase detectors operate closest to their optimal phase delay, as predicted by the model. This interesting result is believed to be novel.

Decay lifetime (μs)	Dual-phase (quadrature) measurement		Single-phase measurement		
	Optimal Excitation Period (μs)	Lifetime error (10^{-12} s)	Optimal Excitation Period (μs)	Lifetime error (10^{-12} s)	Conventional Excitation Period (4.18) (μs)
1	9.0	3.2	6.3	2.8	6.3
1.5	12.7	5.4	9.0	4.1	9.4
2	17.0	7.2	12.4	5.5	12.6
2.5	21.0	9.0	15.0	6.9	15.7
3	21.9	11.0	18.0	8.2	18.8

Table 4 Optimal excitation frequencies for analysis of exponential lifetimes with dual or single-phase measurement. Shot-noise limited detection is assumed. Excellent agreement exists between our numerically calculated optimal settings with single phase and the optimum setting predicted by the traditional relationship (4.18). This confirms the validity of the numerical model. Optimal settings for dual-phase detection were also calculated numerically.

Table 4 also shows a slight increase in lifetime measurement error when a dual-phase system is used. This is to be expected because the dual-phase measurement system described is intrinsically insensitive to returning fluorescence intensity, whilst a single phase version has intensity dependence, so some of the information present in the returning fluorescence is not used.

Another interesting feature to be noted in Table 4 is the less than 3 times increase in optimal excitation period for a fluorescence lifetime increase of 3 times. This occurred because, for the dual-phase measurement, the band-limiting effect of the detection electronics was included in the analysis. When resolving short fluorescence lifetimes, when the detected signal contained significant high-frequency information the detection system would therefore distort the measured waveform, requiring longer excitation periods for optimal lifetime measurements.

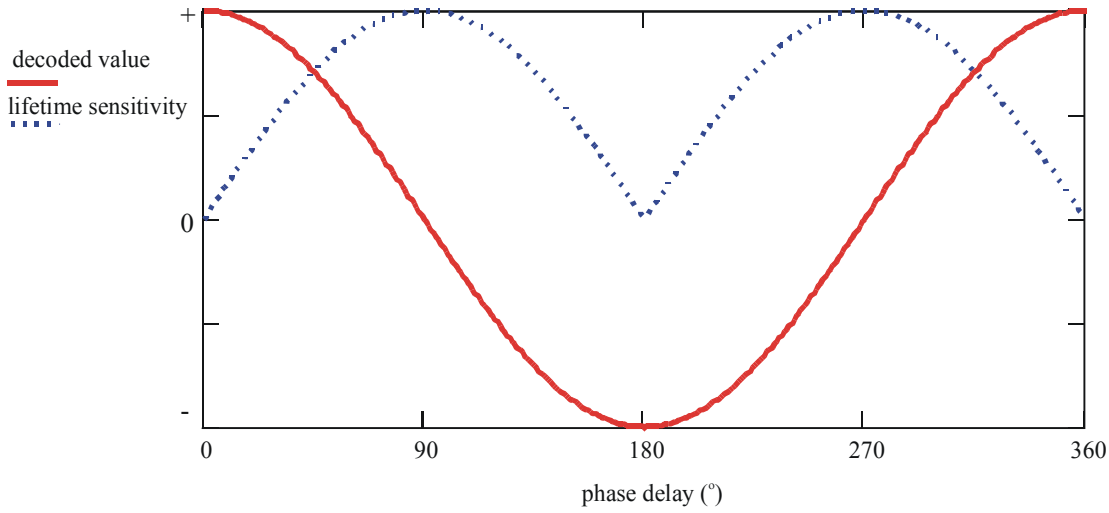

Figure 4.19 The response of a single-phase interrogator system using fixed frequency sin-shaped modulation interrogating a fixed exponential fluorescence as a function of phase delay. The solid line displays the decoded value as a function of phase-delay. The dotted line displays the sensitivity of the detector to changes in fluorescence lifetime.

4.9. Experimental measurements

The response of the fluorescence interrogator to exponential lifetimes in the range 2.9-3.2μs was measured. The results are given here.

The Ti:sapphire calibration sample was employed as a useful mono-exponential calibration aid (see chapter 2). The calibration probe was progressed through a series of set-point temperatures: **17.55±0.05, 14.23±0.04, 28.83±0.05** and **23.39±0.03°C.** Each was held for a period of 1800s (30 minutes). (These temperatures coincide with convenient resistances of the feedback thermocouple). The ratio R ($=V^{90}/V^{0}$) was determined with 5s response time and logged.

The resulting data are displayed in Figure 4.20, where measured temperature is plotted (solid line, left vertical axis) and measured ratio R (dashed line, right vertical axis).

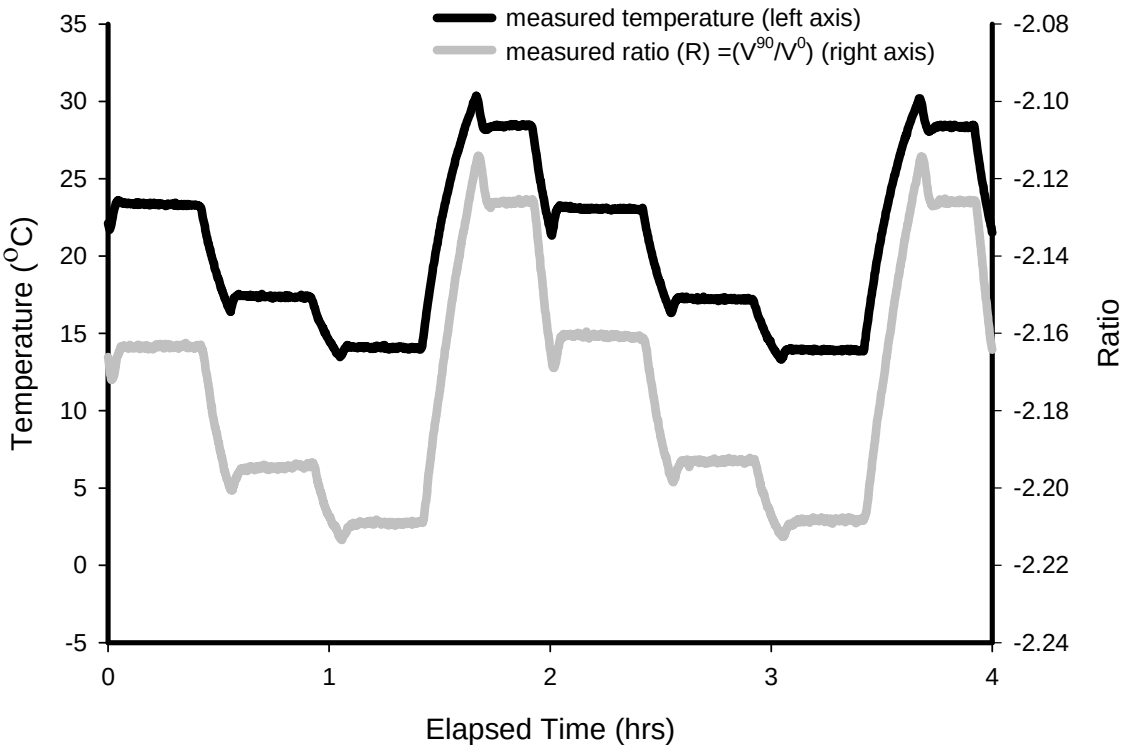

Figure 4.20 Measurements of ti:sapphire probe as the calibration probe temperature is varied

Calibration data were extracted from this test and are presented in Figure 4.21. A repeatable response is displayed, proving that the sensor had negligible measurement drift. This calibration curve was used to estimate the noise in fluorescence lifetime measurements to be **2.3×10^{-10}s $Hz^{-0.5}$** showing excellent high precision measurements are possible with the apparatus.

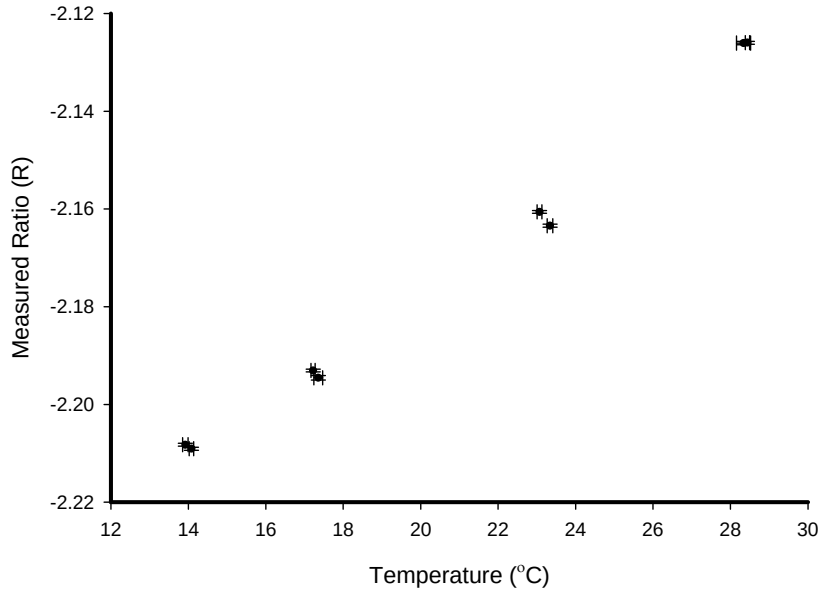

Figure 4.21 Extracted Calibration data from ti:sapphire test

As comparisons between logged results and predicted values would not be possible, further measurements using the oxygen indicators could not have lead to novel results. This was therefore not pursued, leaving more time for exploring other, more profitable areas.

4.10. Conclusions from chapter 5

In this chapter, fluorescence interrogation by monitoring the delay between an intensity modulated excitation source and the resultant fluorescence was investigated.

This technique has been widely used for the interrogation of fluorescent species, principally because of its modest instrumentation requirements, and favourable immunity to background light. The 'dual-phase' system, where twin electronic multipliers are used to simultaneously decode in-phase and out-of-phase components is the most popular sensing scheme, as phase-delay measurements can then be made independently from fluorescence light intensity. A benchtop interrogation system was custom built to aid the investigation.

Equation (4.1) has been traditionally used to convert the measured phase delay to implied fluorescence lifetime, but, as was explained in section 4.3.2, an adjustment is required for most real-world applications. When square-wave shaped modulation is used, and when the detection system does not strongly band-limit the detected fluorescence signal, then the relationship between apparent measured 'phase delay'

(in general, this measurement is not actually a phase delay) and fluorescence lifetime is much more complicated. For this reason, this type of sensor has in the past been calibrated in a strongly empirical manor, simply by measuring the response to the measurand to obtain a calibration curve. This does not require a full understanding of the system, and does nothing to reveal unexpected problems, such as unexpected delays, in the interrogation system. To improve on this standard technique a more analytical approach was developed here. The fluorescence signal, and the expected effect of the detection system on this signal, was calculated for any given modulation frequency and fluorescence lifetime by numerical simulation. This allowed, for the first time, inspection of the effect of square-wave excitation, and the various optical and electronic delays, without the need for experimental measurements. The effect of these factors on the overall response of the interrogator was demonstrated by comparison between ideal values and results from the new realistic model. This study showed, interestingly, that the effect of optical and electronic delays in the hardware interrogator was greater than the effect of using square-wave-shaped, rather than sine-wave-shaped, excitation modulation.

This modelling procedure was used to characterise the bench-top interrogator, and it was found to successfully predict the detected waveform. However, performance limitations in the high-frequency analogue signal processing stage of the interrogator prevented accurate modelling of the complete sensor, and for this reason, the analysis was not extended to oxygen measurements.

Optimal excitation frequencies for measurement of fluorescence lifetimes in the range 1-3μs, using dual and single-phase detection interrogation systems were calculated. For single-phase measurements, the results agreed with previously published results. A lower excitation frequency is required for optimal dual-phase measurements. This is believed to be a novel result.

The sources of random noise in the bench-top system were carefully identified and quantified as a function of detected fluorescence power. Using this expression, the expected precision of fluorescence lifetime measurements was calculated, and verified by comparison with experimental data. A lifetime precision of $\mathbf{2.3 \times 10^{-10} s\ Hz^{-0.5}}$ was achieved when measuring a fluorescence lifetimes in the range 2.9-3.3μs. The predicted precision was $\mathbf{1.0 \times 10^{-10} s\ Hz^{-0.5}}$, which confirms adequate operation of the model.

4.11. References for chapter 5

1. Draxler, S. and Lippitsch, M., *Fluorescence Decay Time Measurement - a New Optical Sensing Scheme.* SPIE Biochemical Medical Sensors, 1993. **2085**: p. 61-67.

2. Trettnak, W.*, et al.*, *Optical Oxygen Sensor Instrumentation Based on the Detection of Luminescence Lifetime.* Advances in Space Research, 1998. **22**(10): p. 1465-1474.

3. Murtagh, M., Ackley, D. and Shahriari, M., *Development of a Highly Sensitive Fibre-Optic O2/DO sensor based on a phase modulation technique.* Electronics Letters, 1996. **32**(5): p. 477-479.

4. McDonagh, C.*, et al.*, *Phase fluorometric dissolved oxygen sensor.* Sensors and Actuators B, 2001. **74**: p. 124-130.

5. Ocean-Optics, *FOXY Fiber Optic Oxygen Sensor - www.oceanoptics.com/products/foxysystem.asp*. 1996

6. Meade, M.L., *Two-phase lock-in amplifiers*, in *Lock-in amplifiers: principles and applications*. 1989, Peter Peregrinis Ltd on behalf of the Institution of Electrical Engineers. p. 81-96. ISBN 0906048 94 x

7. Gowar, J., *The receiver amplifier*, in *Optical Communication Systems*. 1984, Prentice/Hall. p. 403-429. ISBN 0-13-638156-1

8. Press, W., Teukolsky, S., Vetterling, W. and Flannery, B., *Chapter 13 Fourier and Spectral Applications*, in *Numerical Recipes in C*. 1996, Cambridge University Press ISBN 0-521-43108-5. p. 396-455. ISBN 0-521-43108-5

9. Ogurtsov, V. and Papkovsky, D., *Selection of Modulation Frequency of Excitation for Luminescence Lifetime-based Oxygen Sensors.* Sensors and Actuators B, 1998. **51**: p. 377-381.

5. COMBINED OXYGEN AND TEMPERATURE MEASUREMENT

5.1. Introduction

Both optical and electro-chemical oxygen sensors have an undesirable cross-sensitivity to temperature. The temperature dependence in Clark sensor was measured by Hitchman [Hitchman, 1976 #7] to lead to an increase of 1-6% $°C^{-1}$ in measurements. Thermal compensation has therefore been required in most applications.

For optical oxygen indicators, this thermal dependence is also important. Variations in temperature cause significant variations in response, as the luminescence quantum yield of the dye, the quenching constant, k_{sv}, the solubility of oxygen into the indicator support matrix, and the diffusion of oxygen into the membrane are all effected by temperature. Little research has been performed to further clarify these mechanisms, though its overall effect has been measured by a few studies. In 1988, Opitz *et. al.* [1] measured the thermal response of a pyrene butyric acid oxygen indicator encapsulated in a silicone rubber membrane. They showed that the response of their indicator to oxygen was adjusted by 20% in the range 300-500K. In [2], McDonagh *et.al.* have measured the thermal response of their ruthenium indicator ($Ru\text{-}(Ph_2phen)_3^{2+}$) (i.e. of similar composition to that used in this study), at temperatures between 5-30°C over a dissolved oxygen range 0-100% [O_2]. They recorded a change in lifetime of 0.6% $°C^{-1}$ in the absence of oxygen, rising to a lifetime change of 1.5% $°C^{-1}$ when measuring air saturated water (100%[O_2]). In his description of the temperature effect in optical sensors [3], Wolfbeis summarises results from temperature coefficient measurements made on various luminescent dyes and postulates reasons for these dependencies. The reader is referred to this volume for in-depth analysis – here it is simply noted that temperature may strongly effect the indicator response. For one dye (9,10 diphenylanthracene immobilised in polydimethyl siloxane), a temperature change from 2 to 48°C lead to a change in quenching constant of 37%, giving a 4% $°C^{-1}$ change in measured oxygen concentration.

The problem is compounded in applications where dissolved oxygen concentration measuremed in units of air saturated proportion (denoted [O_2]) because the air-saturated dissolved oxygen concentration has strong temperature dependence ([4]).

To compensate for these errors, knowledge of the analyte's temperature is required. Most commercial sensors have achieved this by mounting a solid-state electrical thermometer next to the oxygen sensing head. Ocean Optics employed a thermocouple for their FOXY (Fibre Optic Oxygen Sensor) [5] sensor. Another competing optical oxygen sensing system produced by PhotoSense [6] measures probe temperature with a Resistance Temperature Detector (RTD).

A more convenient method is to measure the prevailing temperature optically. This removes the need for a separate electrical connection to the sensing head, (which adds complexity, and susceptibility to electromagnetic interference). Though the thermal measurement could be accomplished by adding a separate optical sensor and connecting fibre, it is possible to accomplish measurement of both temperature and oxygen with a single optical fibre, by adding a fluorescent thermal indicator within the sensing head itself. This brings the advantage of a single fibre connection between interrogator and probe and all the well-known advantages of fibre-optic sensing (ease of miniaturisation, long distance interrogation, immunity to electro-magnetic interference, possibility of simple multiplexed analysis of several probes etc.).

The probe would be designed to convey excitation light to both temperature and oxygen indicators, and to collect resulting fluorescence light from both. Separation of the oxygen and temperature measurements is possible in two ways. Firstly, the two indicators could be chosen with widely differing spectral properties so their absorption or fluorescence bands were separable spectrally. Considerable additional interrogator complexity would be required to achieve this (either multiple excitation sources, or multiple detectors and complex optical filters would be required), so here the second more elegant method, where the two indicators have similar spectral properties, but widely differing fluorescence lifetime was investigated.

The use of ruby (Cr^{3+}-doped-sapphire) as a thermal indicator, to monitor the temperature of the Ru^{2+}[dip] oxygen indicator was first suggested by this research as a result of this investigation, [7]. Ruby has previously been used alone for temperature sensing applications [8], [9], because of its highly predictable and thermally dependent fluorescent lifetime. Ruby itself has not only stood the test of survival over geological time, but has also proven stability under intense illumination (e.g. ruby laser systems), and so is preferable to chemical dye-based thermal indicators. The fluorescence lifetime of the crystal is reproduced from **[10]** as a function of temperature in (Figure 5.1).

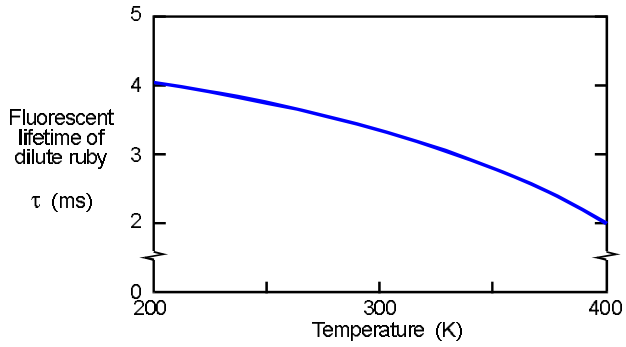

Figure 5.1 Fluorescent lifetime of ruby crystal plotted as a function of temperature. Note, around room temperature, the fluorescence lifetime is over one thousand times longer than the Ru^{2+} dye. Reproduced from [10].

The optical properties of ruby crystal are ideal for this purpose, because there is adequate overlap between the absorption (Figure 5.2), and fluorescence spectra (Figure 5.3) of ruby and the oxygen indicator. This allows optimal interrogation of both elements with existing oxygen sensor optics.

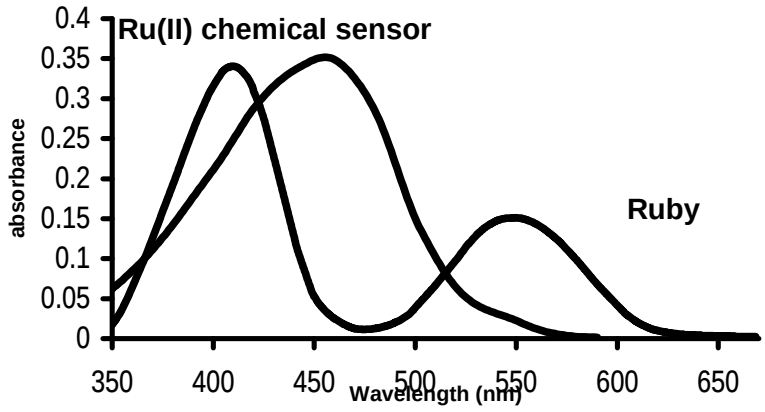

Figure 5.2 Absorption spectra of Ru membrane and ruby (reproduced from [10]). There is spectral overlap in the 470nm (blue LED) range, allowing excitation of ruby with existing membrane interrogation optics

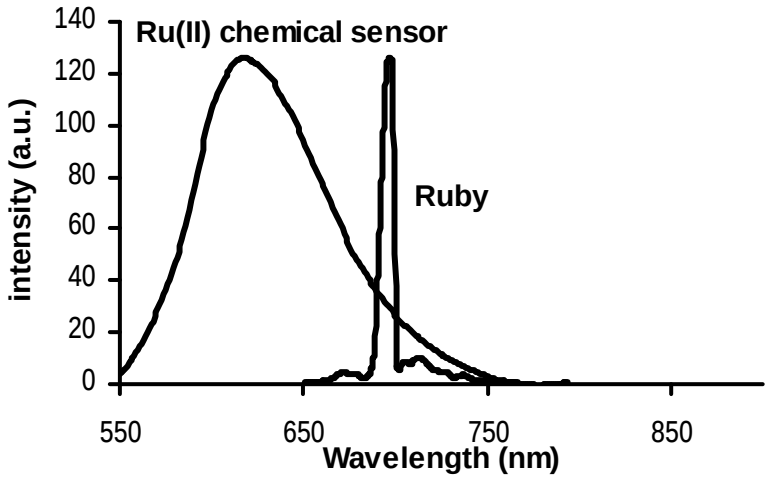

Figure 5.3 Fluorescence spectra of Ru membrane and ruby (reproduced from [10]). There is spectral overlap allowing easy interrogation of ruby with existing membrane interrogation optics.

A sensing scheme is required to interrogate the fluorescence from the temperature and oxygen indicators. Previously Liao *et. al.* [11] achieved this by frequency-domain processing of the returning fluorescence signal resulting from square-wave modulation at 488.3Hz. In their configuration, an alexandrite crystal was used to monitor the temperature of a platinum tetraphenylporphyrin (PTPP) oxygen indicator, while the interrogation system measured the electronic frequency spectrum of the detected fluorescent signal. This required a complicated high-frequency signal-processing scheme, as harmonics of the modulation frequency have increasingly less intensity. This disadvantage was avoided with the sensing scheme suggested here. Furthermore, this indicator combination has advantages over the previous alexandrite/PTPP system, as the ratio of temperature to oxygen indicator fluorescent lifetime is far greater, (1000 times as compared with 3.6 times in Liao's system) and ruby, unlike alexandrite, is non-toxic.

Using ruby, a much more convenient, high signal/noise, real time, temperature compensation system using the same LED source, detector, same optics, including the filter set, and even the same interrogation electronics as the oxygen indicator was realised.

5.2. Dual oxygen and temperature sensing schemes

To separately interrogate the oxygen and temperature indicators, a suitable sensing scheme was required. Two alternative methods; a modulated excitation source system, then a

direct decay curve analysis scheme will be shortly discussed. First, the sensing head (or probe), necessary to excite and collect fluorescence from both indicators, is described.

5.2.1. Combined optical temperature and oxygen measurement probe.

To prove the dual measurement principle a simple probe was sufficient. A single 600µm core 630µm cladding diameter fibre was used for excitation and collection. Figure 5.4 shows the flat-plate design used. A 10x1.5mm circular disc of ruby was bonded to the polished, fibre end. The 6mm diameter oxygen indicator was then bonded to the ruby disc.

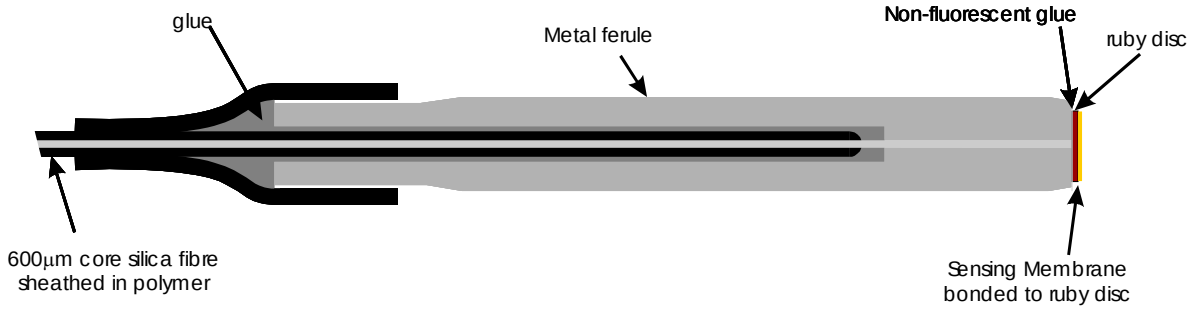

Figure 5.4 Temperature-compensated probe design, employing a simple disc of ruby bonded to the probe end, with the chemical sensing membrane bonded to the disc.

Incident light emerging from the fibre passes through the disc, exciting the ruby crystal, with the remaining light falling on the membrane. Fluorescence from both the membrane and the ruby is partially coupled back into the fibre.

5.2.2. Dual temperature and oxygen sensing using modulated excitation source.

The lifetimes of both the Ru^{2+}-based oxygen indicator and the ruby crystal can be measured using the sensing scheme outlined in Figure 5.5. This interrogator differs from that of the phase-based sensor described in chapter 5 only by the addition of a second clock generator and computer controlled switch, allowing dual square-wave-shaped modulation frequency operation. For an initial setup, the modulation frequencies could be chosen so that the LED was modulated with a square wave of half-period similar to the characteristic decay time of the oxygen indicator (that is of order 10µs period) when switched to high frequency mode, and with half-period similar to that of the ruby (that is of order 10ms period) when switched to low frequency mode.

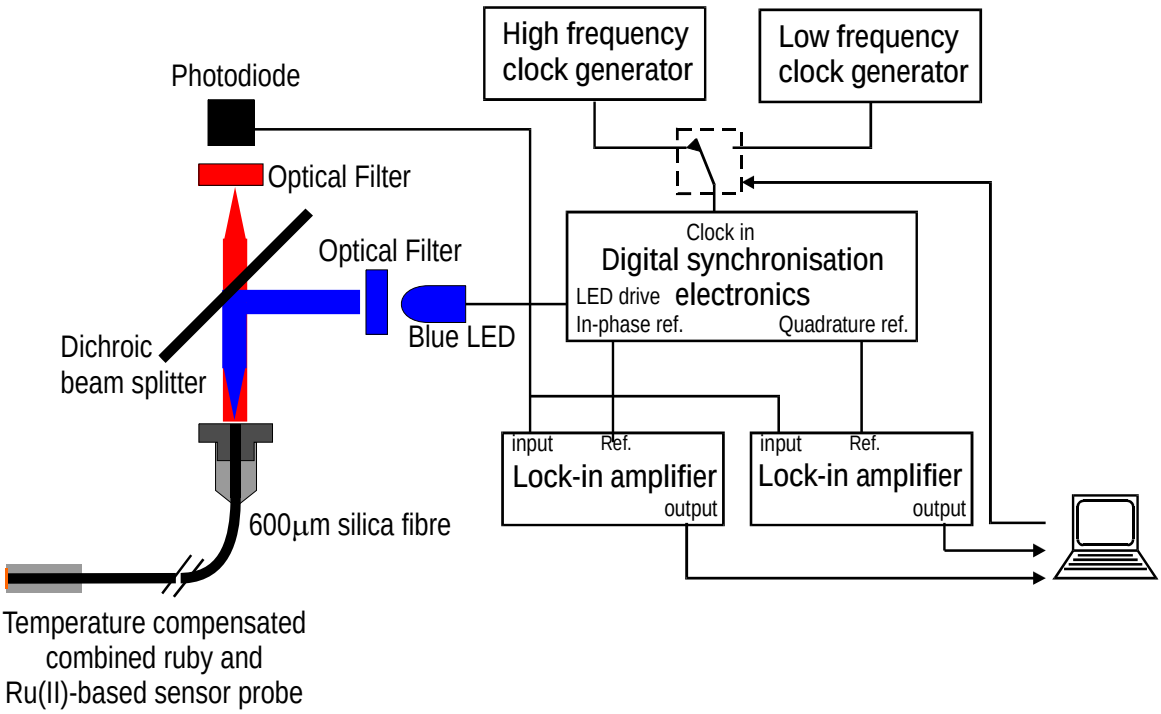

Figure 5.5 Interrogation of temperature and oxygen indicators by a dual excitation frequency modulated source configuration. This simple alteration to the previously described modulated source interrogator (chapter 5) allows independent measurement of the fluorescence from both indicators.

This sensing scheme will be explained by describing the circuit operation at each modulation frequency, neglecting complicating effects such as the detection bandwidth and optical or electronic delays.

5.2.2.1. High excitation frequency mode for indicator interrogation

Let us define t=0 as the time when the excitation source is first activated. Let us also define the modulation period when switched to high frequency mode, as T_{HF}, (which is of order 10µs). The fluorescence contribution from the ruby crystal must be practically constant due to its increased lifetime, (a fluctuation of only 0.16% in ruby fluorescence intensity would be possible over the excitation modulation period), so the fluorescence waveform observed is as shown schematically in Figure 5.6 (where the excitation source will be illuminated during $0<t<T_{HF}/2$ and extinguished during $-T_{HF}/2<t<0$).

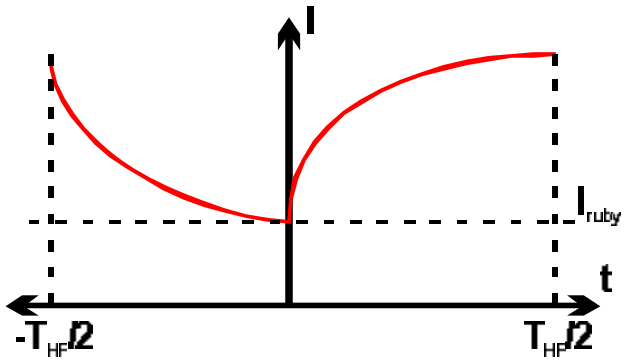

Figure 5.6 Fluorescence waveform expected when high-frequency modulation has been selected. I_{ruby} is the (almost) constant fluorescence contribution from the ruby crystal, which has long fluorescence lifetime. T_{HF} , the high-frequency modulation period would be of order 10μs.

If we call this combined observed fluorescence waveform I(t), the fluorescence waveform from the oxygen indicator alone $I_{oxygen}(t)$, and the (almost) constant contribution from the ruby crystal I_{ruby}, then the resultant decoded in-phase signal (termed V_0, see chapter 5) would be given by:

$$
\begin{aligned}
V_0 &= \int_0^{T_{HF}/2} I(t)dt - \int_{-T_{HF}/2}^{0} I(t)dt. \\
&= \int_0^{T_{HF}/2} I_{oxygen}(t)dt + T_{HF}/2 \,.I_{ruby} - \\
&\left(\int_{-T_{HF}/2}^{0} I_{oxygen}(t)dt + T_{HF}/2 \,.I_{ruby} \right) \\
&\text{so } I_{ruby} \text{ components cancel.} \\
&= \int_0^{T_{HF}/2} I_{oxygen}(t)dt - \int_{-T_{HF}/2}^{0} I_{oxygen}(t)dt
\end{aligned}
$$

Figure 5.7 Measured in-phase component at high modulation frequency

Similarly, for the out-of-phase component, termed V_{90}:

$$
\begin{aligned}
V_{90} &= \int_{-T_{HF}/4}^{T_{HF}/4} I(t)dt - \int_{T_{HF}/4}^{T_{HF}/2} I(t)dt - \int_{-T_{HF}/2}^{-T_{HF}/4} I(t)dt \\
&= \int_{-T_{HF}/4}^{T_{HF}/4} I_{oxygen}(t)dt + \left(T_{HF}/2 \right).I_{ruby} \\
&- \left(\int_{T_{HF}/4}^{T_{HF}/2} I_{oxygen}(t)dt + \left(T_{HF}/4 \right).I_{ruby} \right) \\
&- \left(\int_{-T_{HF}/2}^{-T_{HF}/4} I_{oxygen}(t)dt + \left(T_{HF}/4 \right).I_{ruby} \right) \\
&\text{so } I_{ruby} \text{ components cancel.} \\
&= \int_{-T_{HF}/4}^{T_{HF}/4} I_{oxygen}(t)dt - \int_{T_{HF}/4}^{T_{HF}/2} I_{oxygen}(t)dt - \int_{-T_{HF}/2}^{-T_{HF}/4} I_{oxygen}(t)dt
\end{aligned}
$$

Figure 5.8 Calculation of out-of-phase decoded component

Hence the I_{ruby} components cancel from both the decoded components, so the phase-delay measured at high-frequency modulation would not be affected by the ruby's fluorescence. Another way to think of this is to consider the fluorescence contribution from the ruby crystal as a constant background contribution.

5.2.2.2. Low excitation frequency mode for temperature interrogation

When an indicator is exposed to a constant excitation pulse of sufficient duration, an equilibrium is established where the rate of excitation of luminophores to the fluorescence state becomes equal to their rate of relaxation to the ground state, leading to a constant, or 'saturated' fluorescence intensity. This was discussed in chapter 4, where the time taken for this saturation to become established was shown to be approximately three times the fluorescence lifetime of the indicator. The oxygen indicator, which has an unquenched (maximum) effective lifetime of 3μs, would therefore attain saturated fluorescence after less than 10μs continuous excitation.

With the low frequency modulation frequency selected (with period T_{LF} of order 10ms), at time t=0, when the excitation source is switched on, the oxygen indicator would reach saturated fluorescence effectively within 10μs, which, when compared with the fluorescence from the ruby (or order 3ms) can be considered instantaneous. Similarly, with the excitation source extinguished (at time $t=T_{LF}/2$), the oxygen indicator fluorescence would, within 10μs, relax to a negligible value, leaving only the ruby fluorescence remaining. This would give a fluorescence waveform as shown schematically in Figure 5.9. Once again, it was assumed that the excitation source was illuminated during $0<t<T_{LF}/2$ and extinguished during $-T_{LF}/2<t<0$.

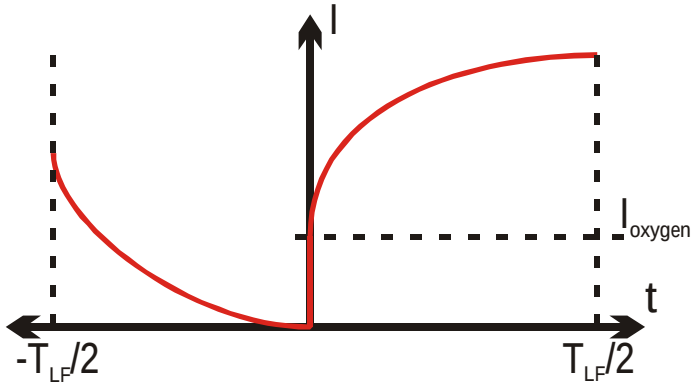

Figure 5.9 Fluorescence waveform expected when low excitation frequency mode (with period of order 10ms) is selected. I_{oxygen}, the contribution from the oxygen indicator, would quickly (within 10μs) attain saturated value following excitation source illumination, and similarly decay to a negligible degree following cessation of the excitation light.

If we call the fluorescence waveform returning I(t), (this is, of course, different to I(t) for high excitation frequency mode), and I_{oxygen} the saturated fluorescence intensity from the oxygen indicator, then the in-phase decoded component would be given by

$$V_0^{LF} = \int_0^{T_{LF}/2} I(t)dt - \int_{-T_{LF}/2}^{0} I(t)dt.$$

$$= \int_0^{T_{LF}/2} I_{ruby}(t)dt + T_{LF}/2 \,.I_{oxygen} -$$

$$\int_{-T_{LF}/2}^{0} I_{ruby}(t)dt$$

so I_{oxygen} components do not cancel.

Figure 5.10 Calculation of in-phase component decoded with low frequency modulation selected.

Though an I_{oxygen} term remains, this could be accounted for during sensor operation, by calculating the saturated oxygen intensity from measurements made at high-frequency mode.

No such complication exists for the out-of-phase decoded component, as the I_{oxygen} terms cancel, (because the oxygen indicator fluorescence is in phase with the modulation waveform):-

$$V_{90}^{LF} = \int_{-T_{LF}/4}^{T_{LF}/4} I(t)dt - \int_{T_{LF}/4}^{T_{LF}/2} I(t)dt - \int_{-T_{LF}/2}^{-T_{LF}/4} I(t)dt$$

$$= \int_{-T_{LF}/4}^{T_{LF}/4} I_{ruby}(t)dt + \left(T_{LF}/4\right).I_{oxygen}$$

$$-\left(\int_{T_{LF}/4}^{T_{LF}/2} I_{ruby}(t)dt + \left(T_{LF}/4\right).I_{oxygen}\right)$$

$$-\int_{-T_{LF}/2}^{-T_{LF}/4} I_{ruby}(t)dt$$

so I_{oxygen} components cancel.

Figure 5.11 Calculation out-of-phase component decoded with low frequency modulation selected.

In a simplified system, the out-of-phase component (V_{90}^{LF}) could be used alone, without its in-phase counterpart, for the temperature measurement, removing the need for calculating I_{oxygen}. Though this would give a temperature measurement dependent upon the ruby fluorescence intensity, this should have excellent stability, as explained above.

By updating the control electronics and software algorithm to alternately operate at high and low excitation modulation frequencies, the state of temperature and oxygen indictors could be independently determined, providing the dual measurement.

5.2.3. Extended Rapid Lifetime Detection Sensing Scheme for Dual Temperature and Oxygen Measurement

Rapid Lifetime Detection is a sensing scheme based on direct analysis of the fluorescence decay curve observed following an excitation pulse. Fluorescent light is accumulated during two time windows to make measurements. This sensing scheme may also be adapted for dual measurement simply by operating alternately at time windows defined within the first 10μs after the excitation pulse (rapid time scale, for oxygen measurements), then using delayed windows within the 10ms following the excitation flash (slow time scale, for temperature measurements).

During operation at the slow time scale, the time windows are set to monitor light arriving more than 600μs after the end of the excitation pulse. Therefore by the time interval A opens, the fluorescence from the membrane (which has an effective decay time of 1-3μs depending on oxygen concentration) will have already decayed to a negligible degree (around $1x10^{-29}$ of its original value), leaving only the fluorescence signal from the ruby (this is shown schematically in Figure 5.12). Photons accumulated during these wide time windows (initially window A was set to open between 600μs and 3ms, then window B between 3ms and 10ms after the excitation pulse) therefore represent the ruby fluorescence only. (This scheme is similar to that suggested in chapter 4 for reducing the effect on measurements of background fluorescence decays). This is shown in Figure 5.12.

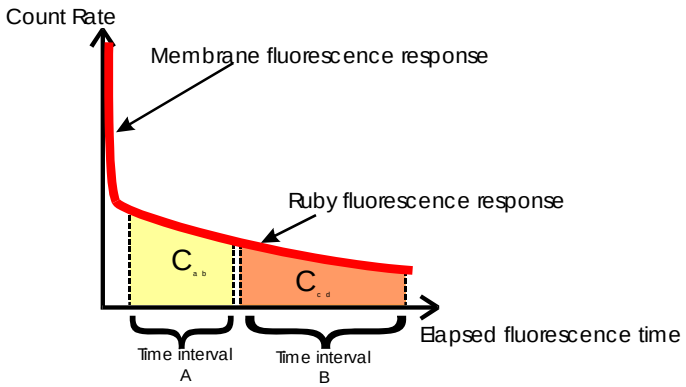

Figure 5.12 Interrogation of dual probe over long time-scale for oxygen indicator interrogation. For proof of principle, the time windows were set to between 600μs and 3ms (time interval A), then between 3ms and 10ms (time interval B)

When set for operation at the rapid time scale, the windows are assigned boundaries just after the excitation pulse (window A was defined between 2μs and 6μs, then window B between 6 and 11μs in the first system). As the ruby fluorescence decays by less than

0.5% during this 11µs time scale, it can be thought of as contributing a constant fluorescence background superimposed beneath the oxygen indicator decay, as shown schematically in Figure 5.13. This constant ruby contribution may be calculated from the long time scale measurements, and by subtracting this from the returned values, C_{ab} and C_{cd}, the prevailing oxygen concentration may be inferred.

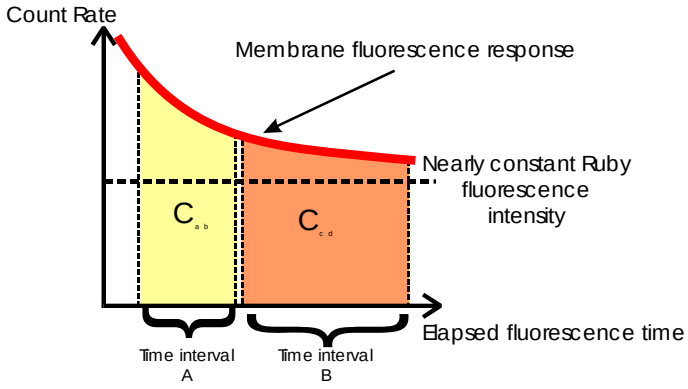

Figure 5.13 Interrogation of dual probe over short-time-scale for oxygen indicator interrogation. For proof of principle, the time windows were set to between 2 and 6µs (time interval A), then 6 and 11µs (time interval B)

5.3. Proof of principle – First Simultaneous, real-time, temperature and dissolved oxygen measurements

An initial experiment was performed to prove the dual measurement principle. Further analysis is required to fully optimise the sensor parameters and experimental setup.

The oxygenation rig described in chapter 4 was used to test the combined sensor. This bubbled air/nitrogen mixtures, via a sintered glass filter, into a 100ml water sample at a rate of 1 l/min. The bubbler was immersed in a temperature-controlled water bath for thermal control. The sensor's response to numerous pre-set levels of dissolved oxygen (0,25,50,75,100% [O_2], set by the gas mixture used) was obtained at the temperatures (30º,35º,40ºC).

In this first test, the decay curve interrogation sensing scheme was chosen to make the dual temperature and oxygen measurement. An averaging time constant of 100s for oxygenation and 15mins for temperature was applied, giving a good signal-to-noise ratio despite the rather low effective measurement duty cycle of 45% for O_2 measurement and 13% for temperature. This processing inefficiency was primarily due to initial software

limitations in the program which controlled the LED source repetition rate and data acquisition cycle. In particular, it appears advantageous to increase the duty cycle for the temperature measurement, which was only around 13% so far.

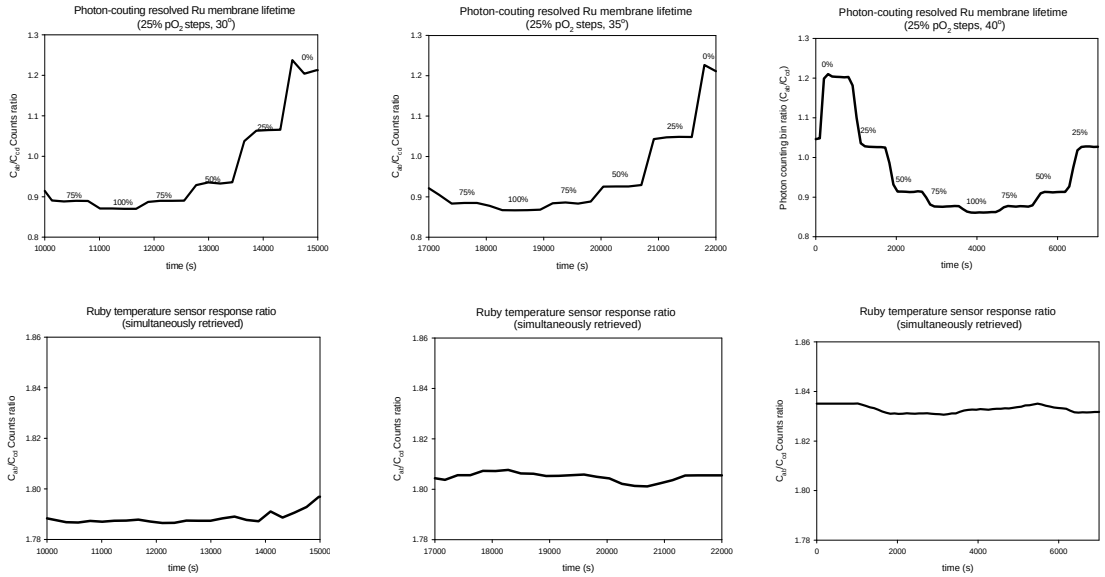

Figure 4a at 30°C **Figure 4b at 35°C** **Figure 4c at 40°C**

Figure 5.14 First results proving principle of dual oxygen and temperature measurement. An enhanced Rapid Lifetime Detection sensing algorithm, which interrogates the fluorescence state of an indicator by direct analysis of the decay curve was employed. Data was logged as the oxygenation level in a water sample held at 30, 35 and 40 degrees was cycled through profiles of 0, 25, 60, 75 and 100% [O_2]. The upper curves shows the count ratio measured from the oxygen indicator (showing the required DO sensitivity) while the lower curves show the count ratio measured from the optical temperature indicator (which shows desired thermal dependence).

5.4. Conclusions from chapter 6

In this chapter a novel scheme for optically monitoring the temperature of an optical oxygen indicator (first suggested as part of this study in 2000 [7]) was discussed. A small Cr^{3+} - doped sapphire (ruby) crystal, mounted close to a ruthenium-based oxygen indicator was demonstrated as a suitable adaptation for dual temperature and oxygen measurement. This has considerable advantages when compared with alternative clumsy electronic temperature monitoring solutions, which require an electrical connection between interrogator and probe tip, which implies associated electro-magnetic sensitivity and higher sensor cost.

Two sensing schemes for interrogation of the dual probe by delay monitoring and direct fluorescence curve analysis were suggested, which require minimal or no additional hardware compared with oxygen only sensors. To prove the principle, the combined probe

was interrogated by direct fluorescence decay curve analysis, using the same hardware as was previously described for oxygen and temperature only measurements in chapter 4.

The presence of the ruby crystal not only provides a temperature sensing element, but, by providing a stable fluorescence reference signal, may be used to indicate mechanical damage or membrane detachment. The reference also allows detection of gradual but more significant changes in fluorescence light output from the membrane (e.g. changes due to photo-degradation).

5.5. References for chapter 6

1. Opitz, N., Graf, H.J. and Lubbers, D.W., *Oxygen sensor for the temperature range 300 to 500K based on fluroescence quenching of indicator-treated silicone rubber membranes.* Sensors and Actuators B, 1988. **13**: p. 159-163.

2. McDonagh, C.*, et al.*, *Phase fluorometric dissolved oxygen sensor.* Sensors and Actuators B, 2001. **74**: p. 124-130.

3. Wolfbeis, O., *Oxygen Sensors - temperature effects*, in *Fiber optic chemical sensors and biosensors, volume II*, O. Wolfbeis, Editor. 1991, CRC Press, Inc. p. 27-28. ISBN 0-8493-5509-5

4. Tromans, D., *Temperature and pressure dependent solubility of oxygen in water : a thermodynamic analysis.* Hydometallurgy, 1998. **48**: p. 327-342.

5. Ocean-Optics, *FOXY Fiber Optic Oxygen Sensor - www.oceanoptics.com/products/foxysystem.asp*. 1996

6. PME, *Fast Dissolved Oxygen & Temperature Sensor (Clark Cell) www.pme.com/oxsensor.htm*. 2000

7. Austin, E. and Dakin, J. *Simultaneous sensing of dissolved oxygen and probe-tip temperature, using a ruby insert and compact photon counting receiver (postdeadline paper).* in *Optical Fibre Sensors 13* 11-13 October 2000 Venice, Italy,

8. Grattan, K.T.V. and Zhang, Z.Y., *Cr3+ Fluorescence Thermometers and Applications of PLD*, in *Fiber optic Fluorescence Thermometry*. 1995, Chapman and Hall. p. 83-103. ISBN 0-412-62470-2

9. Gibson, U. and Chernuschenko, M., *Ruby films as surface temperature and pressure sensors.* Optics Express, 1999. **4**(11): p. 443-448.

10. Nelson, D.F. and Sturge, M., *Relation between absorption and emission in the Region of the R lines of Ruby.* Physical Review, 1965. **137**(4A): p. A1117-A1130.

11. Alcala, J., S., L. and J, Z., *Real time frequency domain firbreoptic temperature sensor using ruby crystals.* Medical Engineering and Physics, 1996. **18**(1): p. 51-56.

6. CONCLUSIONS AND FURTHER WORK

6.1. Background

The aim of this work has been to devise methods to enhance the precision, response time and stability of measurements made by interrogation of fluorescent indicators. This has been mostly achieved by studying and optimising the processing schemes used, so the work presented has wider applicability to other fluorescence measurement systems or perhaps even further.

Several new interrogation and signal processing methods have been suggested, and experimentally confirmed using specially made bench-top sensor instrumentation. Starting from carefully designed basic systems similar to those described in the literature and available from the market place, the instrumentation was enhanced by inclusion of many novel features, including optimisation of the sensing scheme, dual optical thermal measurement, and a new calibration method. The instrument was used to make the first measurements with new anti-fouling coated fluorescent indicators (see appendix). This thesis was structured to describe each of the operational elements required to make measurements – firstly the fluorescent indicator, then the optical arrangement to promote and collect fluorescence, then finally the sensing scheme used to determine the measurement.

Fluorescence indicators were considered in chapter 2. To simplify the analysis, most of the work presented assumed measurement of a single measurand, as sensors for different measurands differ principally in the choice of fluorescent indicator. Because of its importance in natural, chemical and biological processes, measurement of oxygen concentration, principally when dissolved in water, was chosen. (A further compelling reason was that a large research contract, BOSS [1], was available to fund this area!) A ruthenium-based chemical complex formed the oxygen indicator, and this was fully described and characterised.

The ultimate performance of these sensors is clearly limited by the properties of the fluorescent indicator, so intensive research effort was devoted to improving and developing new chemical compositions and support layers by one of the BOSS collaborators. Attention here was therefore focussing on enhancing and optimising the

sensing scheme, which governs how the excitation source is generated and how the detected light is processed to decode the state of the fluorescent indicator.

Oxygen indicators, with their more complicated fluorescence response, were unsuitable for demonstration of some of the new methods. Titanium-doped-sapphire, a fluorescent crystal with similar optical properties to the oxygen indicator, but with exponential fluorescence decay curve, was therefore used as an alternative indicator. The use of Ti:sapphire, as a calibration probe for fluorescence interrogation instrumentation, was first suggested as part of this work, and forms one of the major contributions, [2] and [3].

In chapter 3, the optical part of the sensor was described. Illumination of the indicator with appropriate excitation light, and detection of the resultant fluorescence, is required to interrogate an indicator. An optical system comprising blue LED light source, optical filters, sensing probe, and optical detector (PMT and photodiode types were used) was developed and described. Several precautions were taken to ensure adequate operation of interrogation hardware; minimisation of optical cross-talk, measurement and minimisation of thermal dependence in optical components and minimisation of auto-fluorescence from optical filters and bonding epoxies.

The majority of the work in this thesis was concerned with optimisation and enhancement of the sensing scheme, which determines exactly what excitation waveform is used, and how the resulting fluorescence is interrogated to infer the state of the indicator. Optimisation of the sensing scheme can clearly improve the performance of the sensor, irrespective of the specific fluorescent indicator used. The new, and newly optimised, sensing schemes suggested and results, will each be summarised below. For each sensing scheme, suggested further work to develop the research will be described. Finally, work in other areas, which could form interesting further study, firstly to characterise the ageing process in oxygen indicator and secondly to adapt the instrumentation to sense pH will be briefly discussed.

6.2. Direct decay-curve analysis by enhanced Rapid Lifetime Detection (RLD)

The Rapid Lifetime Detection method is a very simple, yet elegant curve-fitting algorithm for rapid interrogation of fluorescence decays with modest hardware and software requirements. A new method was presented in chapter 4 for optimising measurements made using this method. Indicators with exponential decays (Ti:sapphire was used as an

example exponential fluorescence indicator) and the oxygen indicator, with considerably more complicated decay curve were both considered. An analytical error-propagation approach was adopted to model the precision of the RLD method as a function of excitation pulse length, window boundary times and experiment repetition rate. Using the model, the conditions for optimal high-repetition rate measurements of both of these were identified. This resulted in an **almost doubling** of signal-to-noise ratio, when compared with operating with settings previously believed to be optimal ($490Hz^{0.5}$ compared with next best $240Hz^{0.5}$ in a comparative test). The effectiveness of varying interrogator conditions to suit measurand level and background ambient light was investigated in detail. The effect of background fluorescence decays (e.g. from auto-fluorescence of optical components or fluorescence species in the analyte) was quantified. A method for reducing this effect (by up to 10^4 for short (<300ns) background decays) was discussed.

The theoretical model was verified by comparison with both a computer-based random (Poisson) noise generator, and with experimentally derived measurements from real indicators. The excellent agreement showed validity of the model. For measurement of a 3μs lifetime a signal to noise of **$280\ Hz^{0.5}$** (i.e. 280 in 1s averaging time) was achieved, when measuring a fluorescence signal with only 12.5pW peak power. When making oxygen measurements, a measurement uncertainty of **$1ppb\ Hz^{-0.5}$** was achieved for de-oxygenated measurements. For wide range measurements, (which require a different operating condition for optimal results), a measurement precision of 5ppb in 5s averaging time was achieved.

6.2.1. Possible further studies of the RLD sensing scheme.

Useful further theoretical work could be undertaken to identify optimum setup parameters for interrogating an intended fluorescence decay in the presence of other background fluorescence decays (e.g. from auto-fluorescence from optical filters, fluorescent species in the analyte, or even from other fluorescent indicators for other measurands included at the probe tip). This was briefly investigated in chapter 4, but, as background decays were engineered to be insignificant in the present system, it was necessary to fully pursue this work. The presented optimisation algorithm could also be used to improve measurements made with new two-dimensional oxygen flux sensors, which employ gated CCD detectors.

6.3. Fluorescence Interrogation by Monitoring the Delay Relative to an Intensity Modulated Excitation Source

Measurement of fluorescence by monitoring the delay between an intensity-modulated excitation source and the resultant fluorescence was investigated in chapter 5.

This technique has been widely used for the interrogation of fluorescent species, principally because of modest instrumentation requirements, and favourable immunity to background light. A ‘dual-phase’ system, where twin electronic multipliers are used to simultaneously decode in-phase and out-of-phase components is preferred, as the measurement is not affected by fluorescence light intensity. The instrumentation built here was designed using this principle.

It was found from theoretical study, that when square-wave shaped modulation is used, and when the detection system does not strongly band-limit the detected fluorescence signal to only the fundamental frequency of modulation, then the relationship between measured ‘phase delay’ (in general this measurement will not be a true phase delay, as waveforms are not identical) and fluorescence lifetime is complex. For this reason, in the past, an empirical calibration process has been used, where the response of a sensor to varying measurand value was logged to obtain a calibration curve. This does not require a full understanding of the system, and does nothing to reveal unexpected problems, such as thermally dependent delays, in the interrogation system. Therefore, here a more analytical approach was adopted, where the fluorescence signal, and the expected effect of the detection system on this signal, was calculated for any given modulation frequency and fluorescence lifetime by numerical simulation. This allowed, for the first time, realistic predictions of measured ‘phase delay’ without the need for experimental measurements. The importance of this analysis was demonstrated by comparison between the traditionally expected response and the new realistic version.

The modelling procedure was used to characterise the bench-top interrogator, and successfully predicted an observed fluorescence intensity waveform by modelling the delay and frequency response of the detection system. Performance limitations in the high-frequency analogue signal processing stage of the interrogator prevented accurate modelling of the complete sensor. (No analogue signal processing is required for

fluorescence decay-curve analysis systems as described in chapter 4, adding another major advantage to that approach.)

Optimal excitation frequencies for measurement of fluorescence lifetimes in the range 1-3μs, using dual and single-phase detection interrogation systems were calculated. For single-phase measurements, the results agreed with previously published results. A lower excitation frequency is required for optimal dual-phase measurements. This is believed to be a novel result.

The sources of random noise in the bench-top system were carefully identified and quantified as a function of detected fluorescence power. Using this expression, the expected precision of fluorescence lifetime measurements was calculated, and verified by comparison with experimental data. A lifetime precision of **2.3×10^{-10}s Hz$^{-0.5}$** was achieved when measuring a fluorescence lifetimes in the range 2.9-3.3μs at a peak power of 500±25pW. The predicted precision was **1.0×10^{-10}s Hz$^{-0.5}$**, verifying adequate operation of the model.

6.3.1. Further Studies of the modulated source interrogator

The major problem with optimising the sensing scheme arose from practical performance limitations in the high frequency electronic multiplier circuitry within the phase-delay monitoring system. Further work to improve either this aspect of the hardware, which was based on a bought-in design, or the theoretical model, would allow further characterisation and optimisation the interrogation system. The theoretical analysis required is possible, but would be extremely complicated.

Since the time of the initial design, greatly improved DSP (Digital Signal Processor) or computer based electronic-multiplier options have become more readily available. The analogue signal would be sampled at sufficient frequency to capture all required harmonics, then multiplied by +1 or –1 according to the state of the control signals. This is perhaps the most versatile approach, but requires high frequency sampling (>>1MHz) at high bit depths (for wide dynamic range of measurements) to allow faithful acquisition of the detected fluorescence signal. At the time of this research, such high bandwidth systems were still prohibitively expensive and complicated and so were not considered, but it is expected these will rapidly become viable alternatives with advances in digital technology.

An attempt was made to compare the modulated source interrogation system performance with that of the direct decay curve analysis system presented above, which showed the modulated analysis system giving 10 times improved precision, for normalised fluorescence power! This result is not significant however, and is not emphasised in this thesis, because different excitation spectra were used by each measurement system, and because a very much lower excitation power was used for the direct decay curve measurements. At such low received fluorescence power for the direct measurements (12.5pW) background ambient light, fluorescence and statistical variations in the detection electronics were proportionally far more significant that for the much higher power (500pW) modulated source experiments. With differing excitation spectra, different overall fluorescence yields were obtained. Significant further research would therefore be required to adequately compare the two methods.

6.4. Optical Temperature Compensation in Fluorescence Interrogation systems

A novel scheme for optically monitoring the temperature of an optical oxygen indicator (first suggested as part of this study in 2000 [4]) was discussed in chapter 6. A small Cr^{3+} - doped sapphire (ruby) crystal, mounted close to a ruthenium-based oxygen indicator, was demonstrated as a dual temperature and oxygen sensor. This has considerable advantages when compared with alternative less elegant electronic temperature monitoring solutions, which require an (undesirable) electrical connection between the interrogator instrumentation and the probe tip.

Sensing schemes for interrogation of the dual probe, by either excitation modulation or by direct fluorescence curve analysis were both suggested. Both methods require minimal or no additional hardware when compared with oxygen only sensors. To prove the principle, the combined probe was successfully interrogated and temperature and oxygen were measured, essentially simultaneously by direct fluorescence decay curve analysis, using the same hardware as used for oxygen and temperature only measurements in chapter 4.

6.4.1. Further Work to improve the dual measurement system

Further work could be done to fully optimise and test the sensing schemes suggested, making fuller use of the analysis techniques described in chapters 4 and 5. Time did not

permit all these to be tried. The possibility of dual or perhaps multi-variable measurements of other measurands using different indicators could also be explored.

6.5. Ongoing New Work

This chapter also describes other possibly ongoing work in areas where preliminary studies have already been done. Two main areas will be discussed, firstly work to characterise the ageing process in oxygen indicators and secondly modifications made to the instrumentation for sensing of pH, which has already resulted in a publication [5].

6.5.1. Ageing of optical oxygen sensors

The useful operation lifetime of an optical oxygen sensor employing fluorescent indicators is limited by ageing of the indicator itself. Light induced damage (sometimes called photo-bleaching) can shorten this lifetime to an extent dependent upon the indicator used and the excitation power. Photo-bleaching occurs when luminophores become damaged (generally through the presence of singlet oxygen from previous excitation processes), such that they no longer produce fluorescence.

This effect was observed when measurements of the oxygen indicator were initially made using an excitation power of 25μW/mm^2. An 11% fall in measured fluorescence intensity was observed over a 4 hour test period.

To confirm photo-degradation was the cause of this, the membrane was exposed to the 25μW mm^{-2} illumination intensity over a 600μm diameter circular illumination area for a 16 hour overnight test. The indicator was then illuminated over its full area with light from a blue LED (shown in Figure 6.1), then photographed through a 590nm long-pass optical filter (Schott OG590) in Figure 6.2, to show fluorescence across the whole membrane surface. The figure shows the membrane fluorescing strongly at all points, except for an area of greatly reduced fluorescence (the black circle) corresponding to the previously illuminated area. This confirmed severe photo-degradation of the indicator. For later work, this was alleviated by simply reducing the excitation power to an average of 6.2μW mm^{-2} reducing the effect by approximately 4 times.

Figure 6.1 Oxygen probe illuminated with 470nm blue LED light after 16 hour test. The sensing membrane is the smaller disc glued to the end of the probe

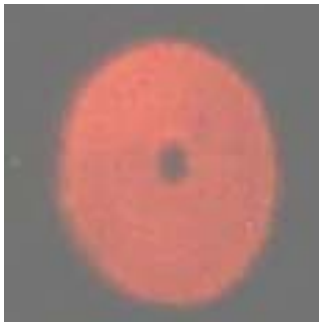

Figure 6.2 Zoomed view of the membrane photographed through a red (590nm cross-over long-pass) filter to show fluorescence. The black spot corresponds with the end of the fibre and shows complete photo-degradation of the sensing region.

6.5.1.1. Investigation of photo-degradation

As, for example, polymers degrade rapidly under UV light, it was thought that the wavelength of excitation light could effect the speed of this photo-degradation. Shorter wavelength photons, which convey more energy, may damage the indicator or support matrix faster than longer wavelengths. A preliminary investigation into this relationship was therefore attempted, in collaboration with a visiting researcher, in the later period of the work. If faster degradation were observed at lower wavelengths, the operating life-span of the sensor could be improved by attenuating the shorter wavelengths emitted from the LED excitation source.

To accelerate the degradation process, the indicator was exposed to light from an argon-ion laser, achieving an illumination intensity of 700μW/mm^2. The resultant fluorescence intensity was logged as the laser was set to produce different excitation wavelengths, thereby measuring the speed of photo-degradation as a function of excitation light wavelength.

Unfortunately, in the time available, the experiments did not produce particularly repeatable results. This was due to several complicating factors. Firstly, the poor uniformity of the immobilisation matrix and the concentration of dye within it (which was very high for these membranes) made the photo-degradation response vary widely not only between different sample membranes, but also between different sections within the same membrane. One proposed method for overcoming this was to illuminate the same area on the same membrane with different excitation wavelengths, whilst monitoring the rate of fluorescence light reduction (see Figure 6.5 for a typical initial result). This also proved inadequate, due to the heterogeneity of the matrix, which caused pockets of luminophores with differing degradation characteristics. This was observed from seeing varying rates of degradation, even when the membrane was exposed to a single excitation wavelength.

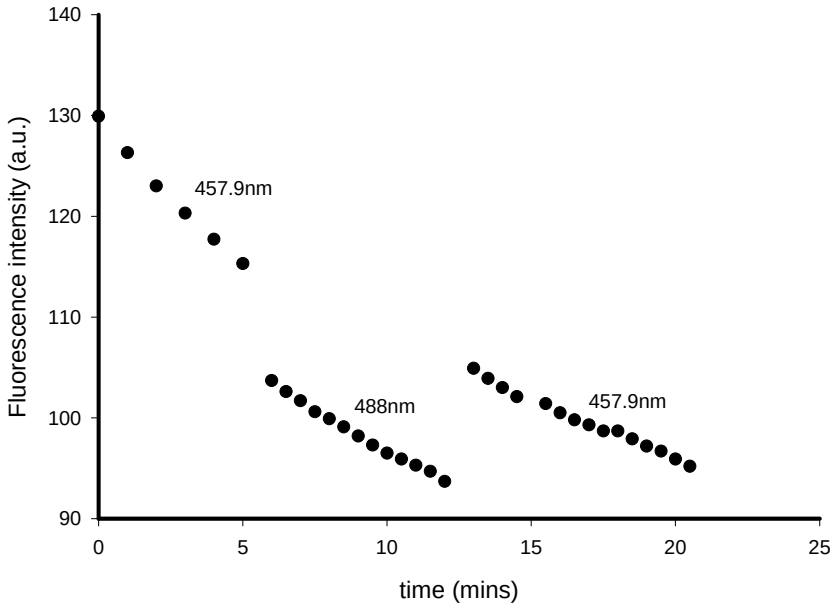

Figure 6.3 Initial results from accelerated photo-degradation study. The excitation radiance was 700μW mm^{-2} at both wavelengths.

After these initial studies, it was decided that this test was complicated enough to be worthy of its own thesis! (Parameters include temperature, wavelength, layer thickness, dye concentration and heterogeneity, support matrix composition, and beam intensity profile). Time did not allow further experimentation, but further work could tackle these problems and quantify any excitation wavelength dependence of the photo-degradation.

6.5.2. Measurement of pH using alternative fluorescent indicators

In this section, recent measurements using novel pH sensitive fluorescent indicators are briefly given. This section is included to underline the versatility of the work presented by demonstrating indirect fluorescence sensing of an alternative measurand.

The fluorescent indicators used were examples of new $Eu^{3+}$and BTB doped sol-gel layers produced by A.Lobnik *et. al.* of the University of Maribor, Slovenia. This novel composition, based on combining a novel fluorescent europium complex (with convenient long-wavelength absorption, at 370nm) with a standard bromothymolblue (BTB) non-fluorescent pH indicator, was described in [6]. The composition was therefore suitable for excitation by state-of-the-art UV LEDs. (Most other pH indicators have had excitation maxima well below 340nm). Successful interrogation of this dye was, for the first time, reported (as a product of this research) in [5].

Here the optical arrangement used and the results gained will be given.

6.5.2.1. Instrumentation and experiment for interrogation of pH sensing fluorescent indicator

For first testing of the very weak fluorescence light produced by the indicator, a bulk experimental arrangement was used, as shown in Figure 6.4. Light from the filtered UV LED (Nichia type NSHU590E, samples available for evaluation only presently) fell directly onto the indicator, which was completely immersed in a pH buffer solution. This increased the illumination intensity by removing optical power loss in the launch optics in comparison to remote fibre designs. It allowed the illumination of a large coating area, and reduced background auto-fluorescence generated within the launch optics. The main excitation peak occurred at 370 nm, which falls in the absorption band of the new pH indicator.

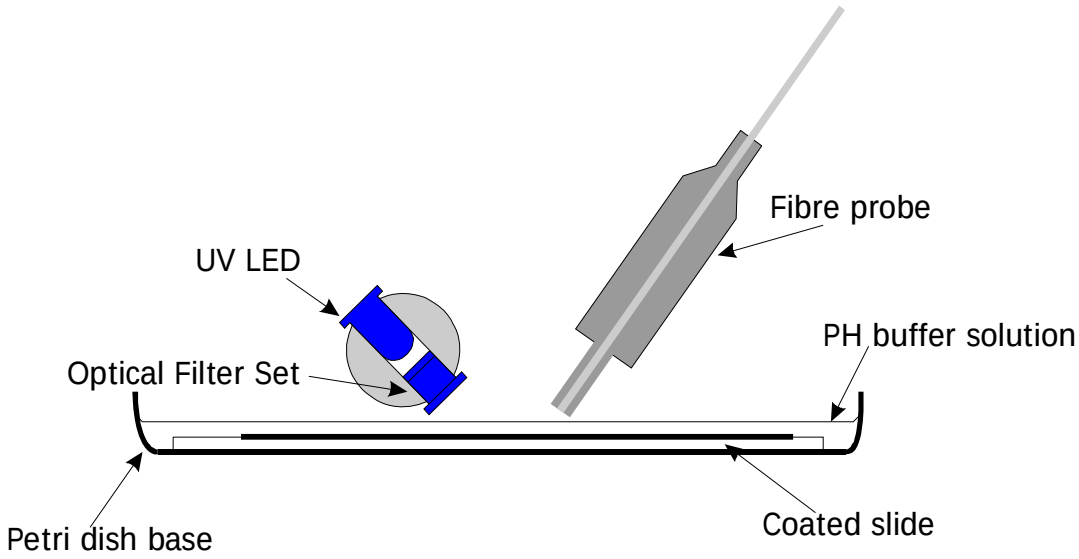

Figure 6.4 Optical arrangement for the interrogation of weak fluorescence signals.

Resulting fluorescence, collected by the fibre probe, was then conveyed back to the interrogation system, where fluorescence decay curves were captured using a photon counting PMT detector, as described in detail in chapter 4.

Fluorescence decay curves from the Eu-complex-impregnated coating (type 'A' made from 2ml TMOS, 2.5 ml EtOH+Eu-complex (2mg) and 1ml HCL 10^{-3}) were examined whilst the coatings were immersed in three pH buffers (pH 4, pH 7, pH 9). The pH of the buffer solutions was verified with a commercial electrode-type pH meter (Jenway 3030) before each experiment.

Fluorescence decay times, taken at the three different pH values, are plotted in fig 2. Two results were taken at a pH of 7.

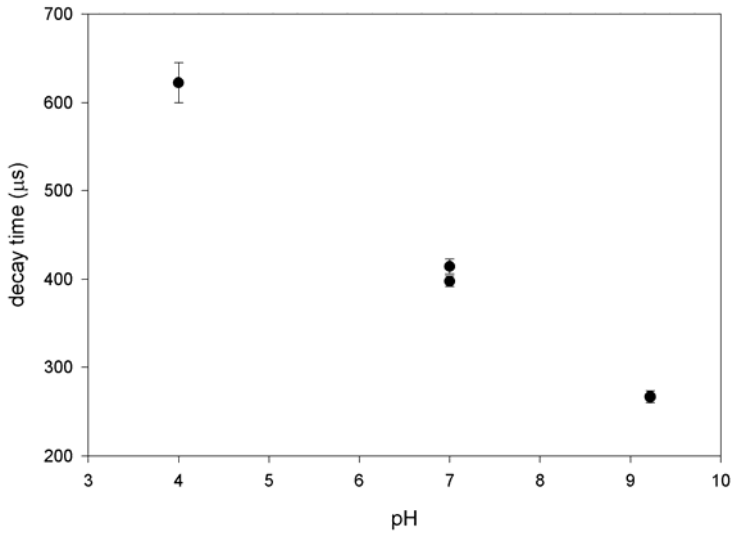

Figure 6.5 Fluorescent decay times of layer after 15 minutes soaking time

6.5.2.2. Conclusions from pH measurements.

These measurements clearly show that the fluorescence decay lifetime of the new indicator varies strongly with pH, proving that other measurands can be addressed with very similar hardware to that described elsewhere in this thesis.

Further work is required in two areas to improve the pH measurement. Firstly, due to the poor photo-degradation performance of initial indicators, they did not last long enough to apply the optimisation algorithms described in chapter 4. It is expected that newly developed layers should have greater photo-resilience, allowing this work to be done. Secondly, the optical arrangement, which was used to improve signal-to-noise and reduce self-fluorescence, was considered to be only an interim step on the way to developing an all-fibre system for illumination and collection of light. Clearly similar gains in signal can be achieved by using larger input and output fibres or fibre bundles, and self-fluorescence can be reduced by use of separate fibre cables for incident and fluorescent light.

6.6. References for chapter 7

1. BOSS, *(Biocompatible Optical Sensor Systems), BRITE RuRAM Project no BE-4311*. Jan. 1997 - Dec 2000

2. Austin, E., Dakin, J. and Strong, A.P. *Use of transition-metal-doped sapphire crystals to calibrate and thermally compensate fluorescent-lifetime chemical detectors (keynote communication).* in *EUROPT(R)ODE V* 16-19 April 2000 Lyon, France, KC9,

3. Austin, E.A.D. and Dakin, J.P. *Opto-electronic systems for addressing Ru oxygen sensors:their design optimization and calibration process (invited).* in *SPIE: Fiber Optic Sensor Technology and Applications* 28 October - 2 November 2001 Boston,USA, 4578-06,

4. Austin, E. and Dakin, J. *Simultaneous sensing of dissolved oxygen and probe-tip temperature, using a ruby insert and compact photon counting receiver (postdeadline paper).* in *Optical Fibre Sensors 13* 11-13 October 2000 Venice, Italy,

5. Austin, E., Dakin, J., Lobnik, A. and Uray, G. *Interrogation of optical pH sensor based on sol-gel doped new luminexcent europium chelate with compact photon counting system*. in *EUROPT(R)ODE VI* 7-10 April 2002 Manchester, UK, P15,

6. Lobnik, A., Majcen, N., Niederreiter, K. and Uray, G., *Optical pH sensor based on the absorption of antenna generated europium luminescence by bromothymolblue in a sol-gel membrane.* Sensors and Actuators B, 2001. **74**: p. 200-206.

7. APPENDIX

7.1. First measurements with anti-fouling coated membranes

As mentioned in the main thesis, this research was funded by a Brite-Euram technical collaborative, called Biocompatible Optical Sensor Systems (BOSS). The project demonstrated the possibility of using biocompatible, anti-fouling coatings to enhance optical sensors. Though most of the work in this thesis was conducted using uncoated membranes, results from one of the first tests using coated oxygen indicators are included here, for the interested reader. The test showed that the coated oxygen indicator still had almost equivalent oxygen sensitivity to an uncoated version.

These joint tests were conducted at the 'Institut fur Bioprozess und Analysenmesstechnik e. V.' (IBA) in Heiligenstadt, Germany.

Two oxygen sensing optrodes, one incorporating anti-fouling PC coating and one without any coating, were exposed to a series of biologically fouling media. By comparing their responses before, after, and during exposure, it was hoped that the effect of PC coating on probe performance and resistance to fouling could be explored. Here only results from exposure to a protein solution consisting 1g/l Bovine Serum Albumin (BSA) in 0.9% NaCl are given.

7.1.1. Procedure

6mm diameter discs were cut from coated and uncoated indicators and glued to the probe tips with General Electric type RTV615A room-temperature-vulcanising silicone glue. To aid vulcanisation of the silicone, newly glued probes were baked in an oven at 40 degrees overnight.

A bio-reactor was used to house the test solution, probes, commercial Clark cell oxygen sensor (for an independent oxygen level reading), thermometer, and frit for bubbling gas. Initially, it was intended to pump the test solution through flow cells housing the probes, but it proved impossible to realise this setup during the joint test period.

As only one fluorescence interrogation unit was available to measure both probes, the two probe responses were logged by alternately connecting each probe to the interrogator

whilst continuously logging results. Due to exposure of the interrogator optics to high levels of background light during this procedure, and the averaging algorithm built into the control software, there was a settling time of 30-60s after each probe swap (which has been removed from the data).

7.1.2. Results

The results from this 6 hour test are shown in Figure 7.1. The response of the coated and uncoated probes have been separated and plotted on separate sets of axis. Before starting to log results, air was bubbled through the solution, so the first values logged are the responses of the probes to an air saturated solution. Then nitrogen was bubbled, causing the response from both probes to increase to a maximum value, when the protein solution is de-oxygenated. Of course, the protein could not be damaged by this procedure. At the time shown, the flow of nitrogen was switched off and the bio-reactor left for 4.5 hours while air slowly dissolved into the solution. Finally, the nitrogen flow was switched on again, de-oxygenating the test solution again.

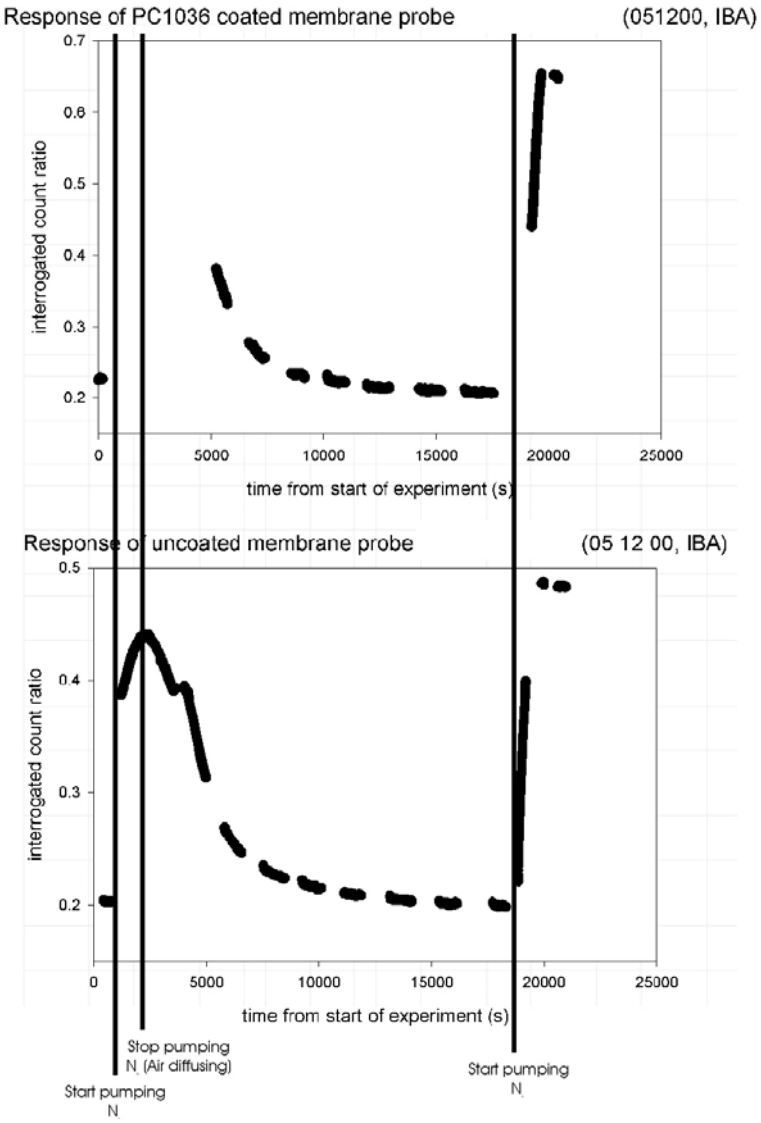

Figure 7.1 Results from measurement of the oxygenation level within a protein saline solution during a six-hour test. First air, then nitrogen gases were bubbled through the solution at the times indicated. Bubbling was switched of, allowing oxygen to diffuse back into the solution. Finally nitrogen was again bubbled through the solution. These results show the probe with anti-fouling coating has similar sensitivity to oxygen as the uncoated probe.

7.1.3. Conclusions

These results show that the presence of a PC coating on its sensing tip does not effect the oxygen measuring capability of these probes. This is a positive result, as it shows no significant degradation in probe performance arising from the anti-fouling coating. No effects of fouling on the probes were observed for either the uncoated or coated probe, due to the short time-scale available for the test.

7.2. Fluorescence interrogation by direct decay curve analysis technical description

7.2.1. Circuit description

An explanation of the electronics and software designed for fluorescence interrogation by direct decay curve analysis, hereafter the 'photon-counting fluorometer', is presented here. For a more detailed explanation of the scientific aspects of the sensor system, refer to chapter 4

The photon counting fluorometer measures fluorescence decay lifetime by accumulating, in 16 bit counters, over a number of repetitions, the number of resultant fluorescence photons arriving in two pre-defined time windows after an LED flash.

The required timing for an acquisition cycle is shown in Figure 7.2. First, the CLR_CNTRS line (active low) goes low-to-high to reset the counters ready for a new acquisition. Then, the LED_drive signal (active low) is sent low for a period to flash the LED and excite the fluorescent material. The T_ab line is sent high to enable the first counter and hence accumulate the fluorescence photons occurring in time window A. Subsequently, the T_cd line is used to count photons arriving in the second time window (B), by enabling the other counter. Such an LED flash, window A, window B, cycle is repeated a number of times for statistical averaging purposes, then the LATCH_CNTRS line is pulled high to store the counted values in registers ready for relay to the control computer.

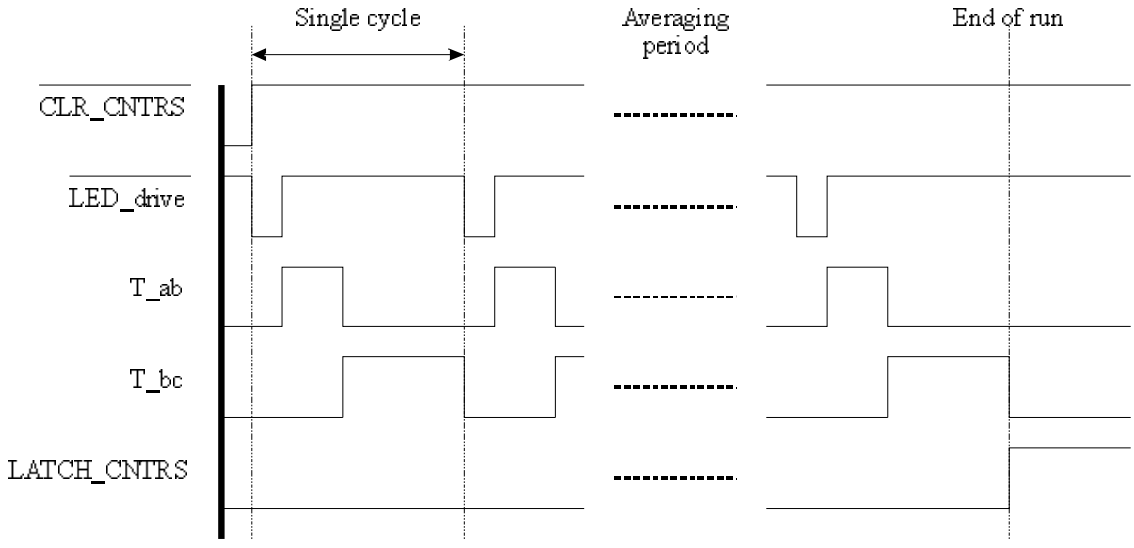

Figure 7.2 Timing of photon counter control signals during an acquisition cycle

The required control timings are achieved by pre-programming a static RAM with a look-up table of control information, like that shown in Table 5. By connecting the data bits of the RAM to the control inputs of the other circuitry, then clocking through the RAM addresses, any desired event timing pattern can be achieved. The last data byte (10000000) is an end-stop byte to signify the end of the control table. This is needed because the control information may not entirely fill available RAM addresses, so the clocking hardware must stop stepping before all the addresses have been accessed.

Address	LED_drive (active low) state	T_ab state	T_cd	Resultant data byte
h000	H	L	L	00000100
h001	L	L	L	00000000
h002	H	H	L	00000110
h003	H	H	L	00000110
h004	H	L	H	00000101
h005	H	L	H	00000101
h006	L	L	L	00000000
h007	H	H	L	00000110
…	…	…	…	…
hFFF	H	L	L	10000000

Table 5 Example look-up-table contents

The interface between PC and hardware is achieved by means of a NI-DAQ LAB-PC+ interface card, which utilises the popular 8255 PIO, giving three bi-directional 8-bit ports, called PA, PB and PC (this is of course different to Personal Computer…).

The modes of hardware operation are described in Table 6, and are selected by setting the upper 4bit nibble of PB (PB.4-7) appropriately.

mode Id.	**PB value (bin)**	**PA ownership**	**PB ownership**	**PC ownership**	**Action**	**notes**
0	x000xxx	hardware	hardware	hardware	In Experiment	Pull down Rs put

	x				Run mode	Y0 low
1	x001xxx x	computer	computer	computer	write data to RAM	WE on RAM low
2	x010xxx x	“	“	“	Write to control register	clk to on-board register low
3	x011xxx x	“	“	“	Read the window B counter value	Read Cntrs High, Read T_AB low
4	x100xxx x	“	“	“	Write to 8-bit cycles clock	clk on cycle 163 high
5	x101xxx x	“	“	“	Not used	cycle-163 clk low
6	x110xxx x	“	“	“	Not used	cycle-163 clk low
7	x111xxx x	“	“	“	Read the window A counter value	Read cntrs high, read TAB high

Table 6 Hardware mode action table

7.2.1.1. mode 1: RAM programming and setup mode

Before an acquisition cycle can occur, the contents of the RAM (U8), and other settings of the hardware must be setup by the control computer. In mode 1, the computer takes ownership of PA, PB and PC, using PA and the top 4-bit nibble of PB to control the address lines of the RAM, and uses PC to set the required data byte for each address location. By cycling through address values, a look-up table of timing information similar to that shown in Table 5 is programmed into the RAM.

7.2.1.2. mode 2: RAM programming and setup mode

To set other hardware control aspects, the 8-bit register U4 is programmed using control mode 2. The register setting controls the overall selection of clock frequency, by setting the divisor inputs on U5, the RAM page according the 3 MSB inputs on the RAM (U8), and two test outputs for diagnosis purposes according to the bit-masks shown in Figure 7.3.

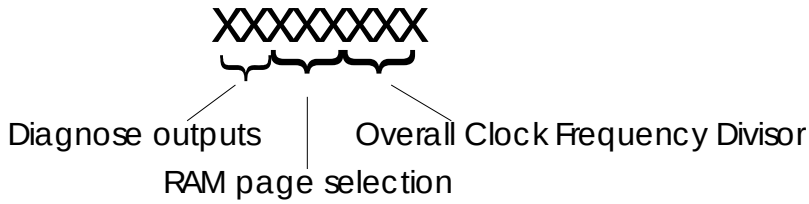

Figure 7.3 Photon-counting fluorometer control register (U4) functions

7.2.1.3. mode 4 : Write to 8-bit cycles clock

By selecting to this mode then switching to another mode, the contents of PA, as set by the control computer, is loaded into the ‘163 type cycles counter. This sets the overall number of RAM cycles to be performed during the acquisition cycle.

7.2.1.4. modes 3 and 7: Reading from window counters

These modes are used in conjunction with the MSB of PB (PB.7) to read the accumulated counts in each window after an acquisition cycle. In these modes, the hardware takes ownership of PA and applies the lower or upper byte of either of the windows appropriately. These values are read by the control computer and used as the product of the acquisition cycle.

7.2.2. Circuit diagrams

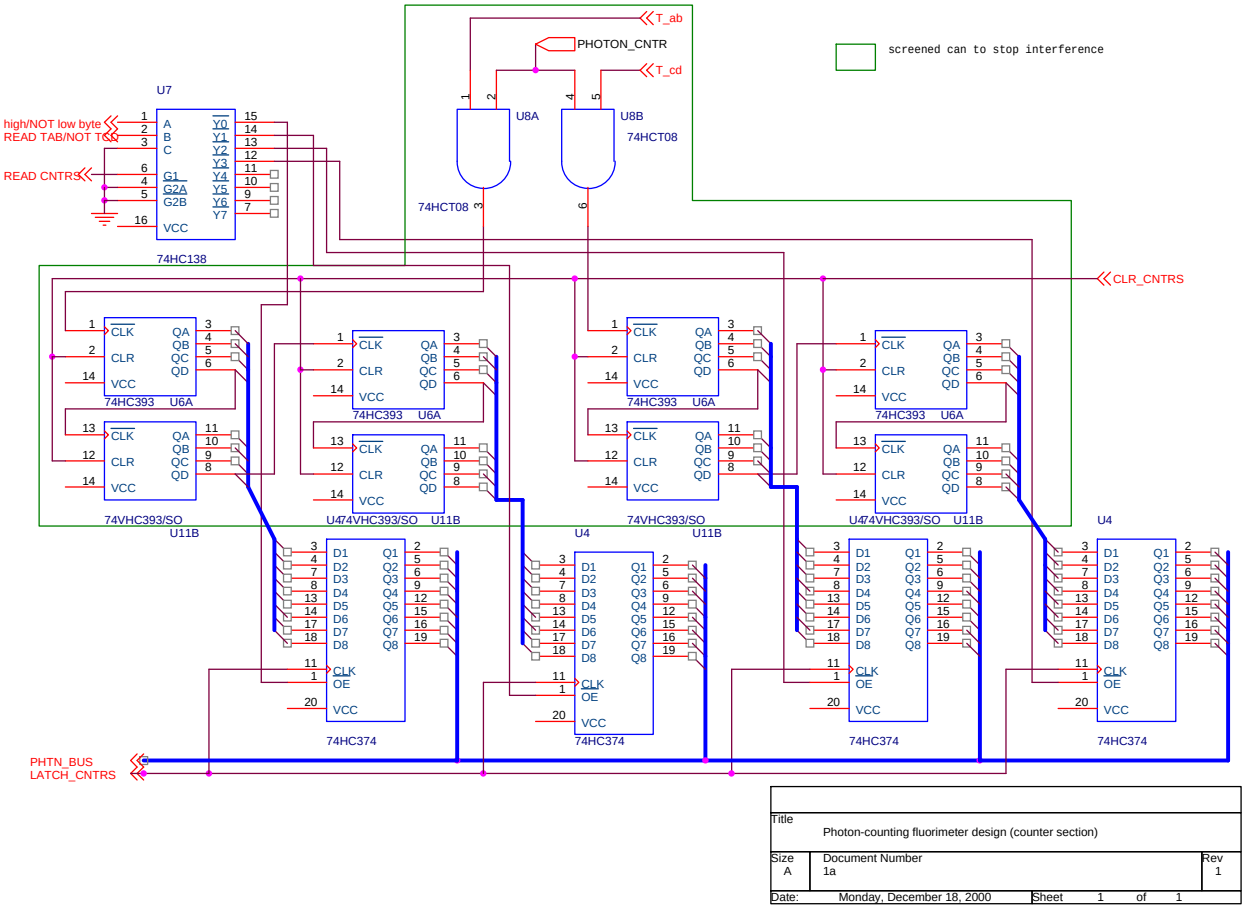

Figure 7.4 Photon counter fluoremeter counter section schematic

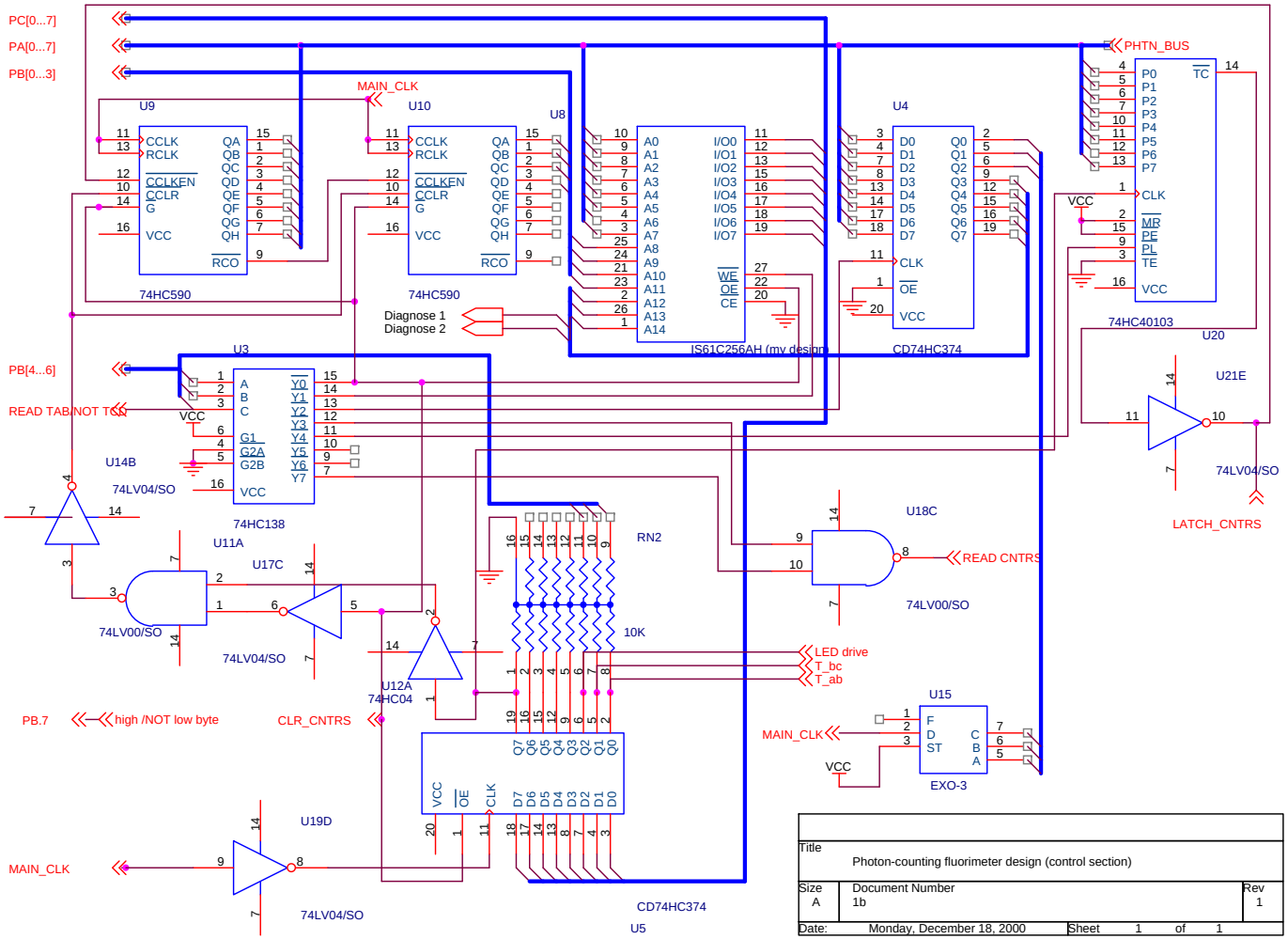

Figure 7.5 Photon counting fluorometer control section schematic

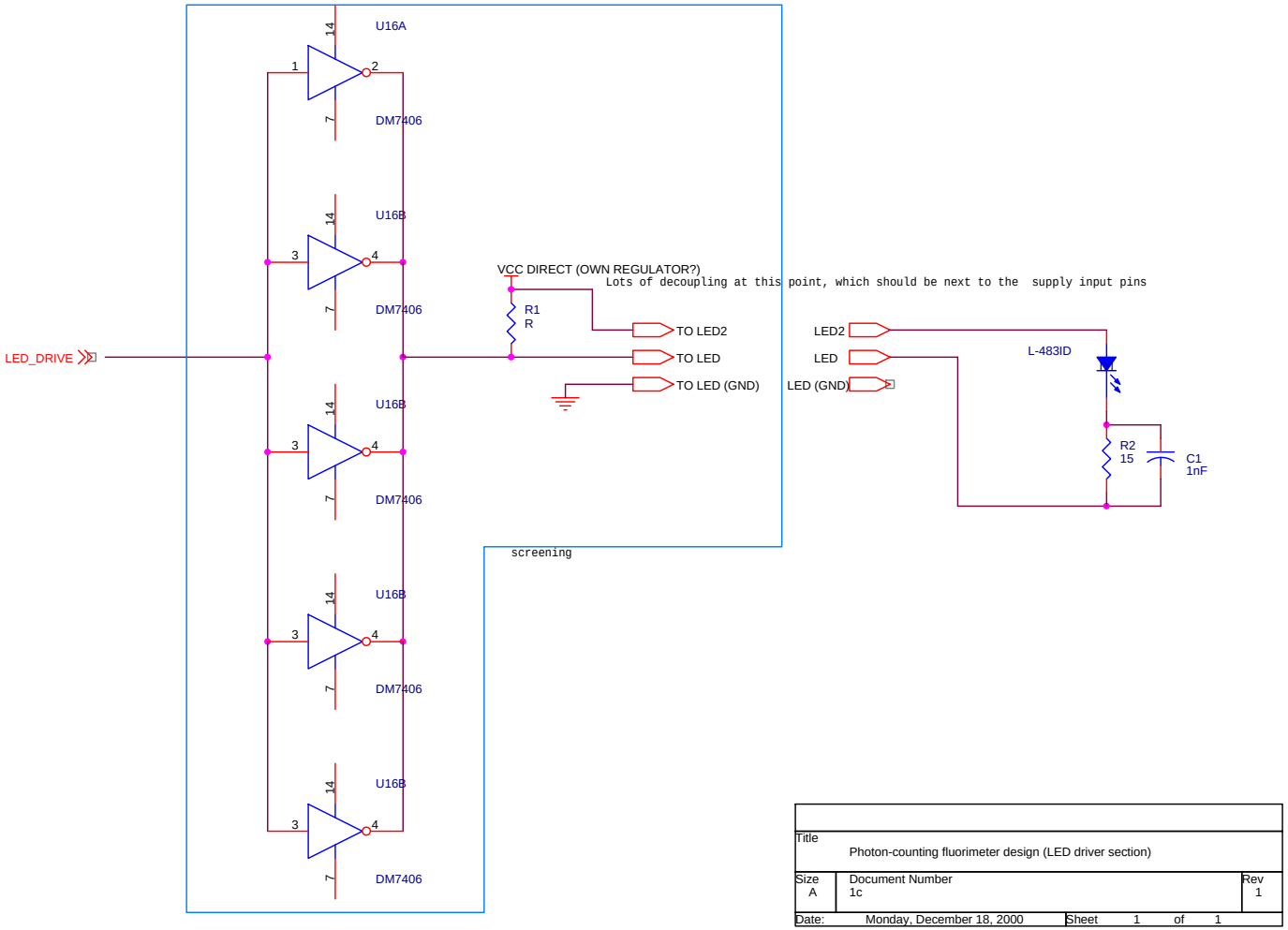

Figure 7.6 Photon counter fluorometer LED driver section

7.2.3. Software description

Software was written in National Instruments' Lab Windows program development environment for controlling the hardware. The software allows two overall views over the experiment. In 'Response' view, the hardware is operated with many small sequential windows so that a time-resolved plot of fluorescence decay can be easily recovered. A schematic representation of a fluorescence response plot during acquisition is shown in Figure 7.7. The two brief time windows are defined adjacently, and an acquisition cycle is performed. The number of photons arriving in each time interval are plotted as a point on the fluorescence decay graph. The two time intervals are re-defined adjacently to the previous time windows, another acquisition cycle is performed and two more points are plotted on the fluorescence decay plot. This view is extremely useful for probe and optics diagnostics, and, by means of suitable curve fitting software, analysis of indicator decay function.

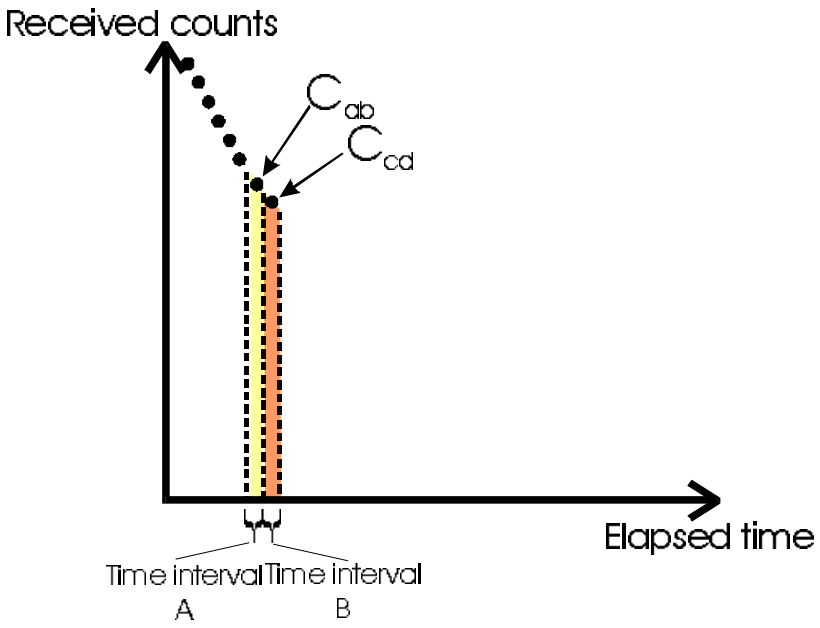

Figure 7.7 Recovering a time-resolved plot of fluorescence decay function by plotting points at sequentially defining small time intervals.

The second software view is called 'delay view', where the count ratio (which is related to the decay lifetime) of the fluorescent material or materials is recovered and displayed in real time. This is achieved by operating the interrogator with wide time windows and dividing the counts accumulated in window A by those in window B (as described in chapter 4) To retrieve the fluorescence decay from the two separate fluorescence materials, two sets of window parameters are programmed at run-time to operate the

hardware at difference window intervals and clock-frequency for retrieving interrogating each of the materials.

7.3. Phase-delay resolving fluorometer design detail

An overview of this fluorometer was given in chapter 5, so only a brief technical circuit description, the circuit diagrams and associated C source code is included here.

Fluorescence light is detected with a BP65RT type silicon PIN diode detector. A specially designed transimpedance amplifier stage (designed and constructed by B. Theobald of Theooptics) with 100M transimpedance (170KHz B/W) is connected to the input of the lock-in circuitry shown in Figure 7.8. After a variable gain stage, twin quadrature lock-in amplifiers, with servo DC offset rejection systems, decode in-phase and out-of-phase components. These voltages are then low pass filtered (with response time 62ms) before application to control PC via a NI-DAQ Lab-PC+ data acquisition card. Further digital filtering of the voltages and calculation of fluorescence phase delay is carried out within the computer.

Digital control signals are synthesised by the circuit shown in Figure 7.9. The original design was produced by sub-contracted to an external design organisation, but extensive re-design was required to achieve acceptable performance.

For dual frequency measurements, a simple computer controlled logic circuit transfers the drive signals from one of two separate oscillator modules to the main input (see Figure 7.9)

Software was developed in National Instruments LAB windows for control and logging tasks.

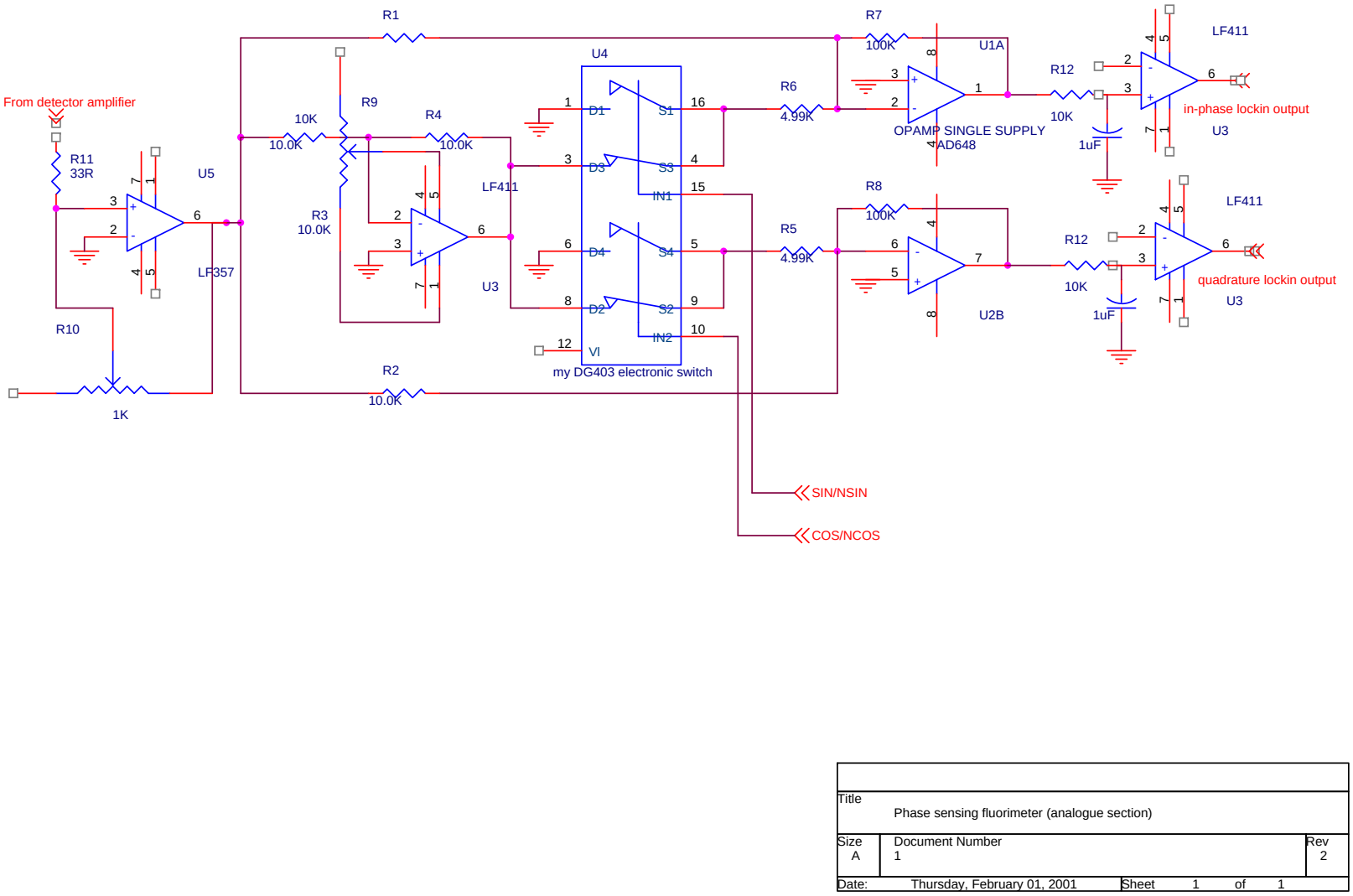

Title: Phase sensing fluorimeter (analogue section)		
Size: A	Document Number: 1	Rev: 2
Date: Thursday, February 01, 2001	Sheet 1 of 1	

Figure 7.8 phase-delay discriminating fluorescence lifetime interrogator circuit diagram (analogue section)). In the final version, R7 and R8 were replaced with 10KΩ versions and pin 2 should be connected to pin6 on U3.

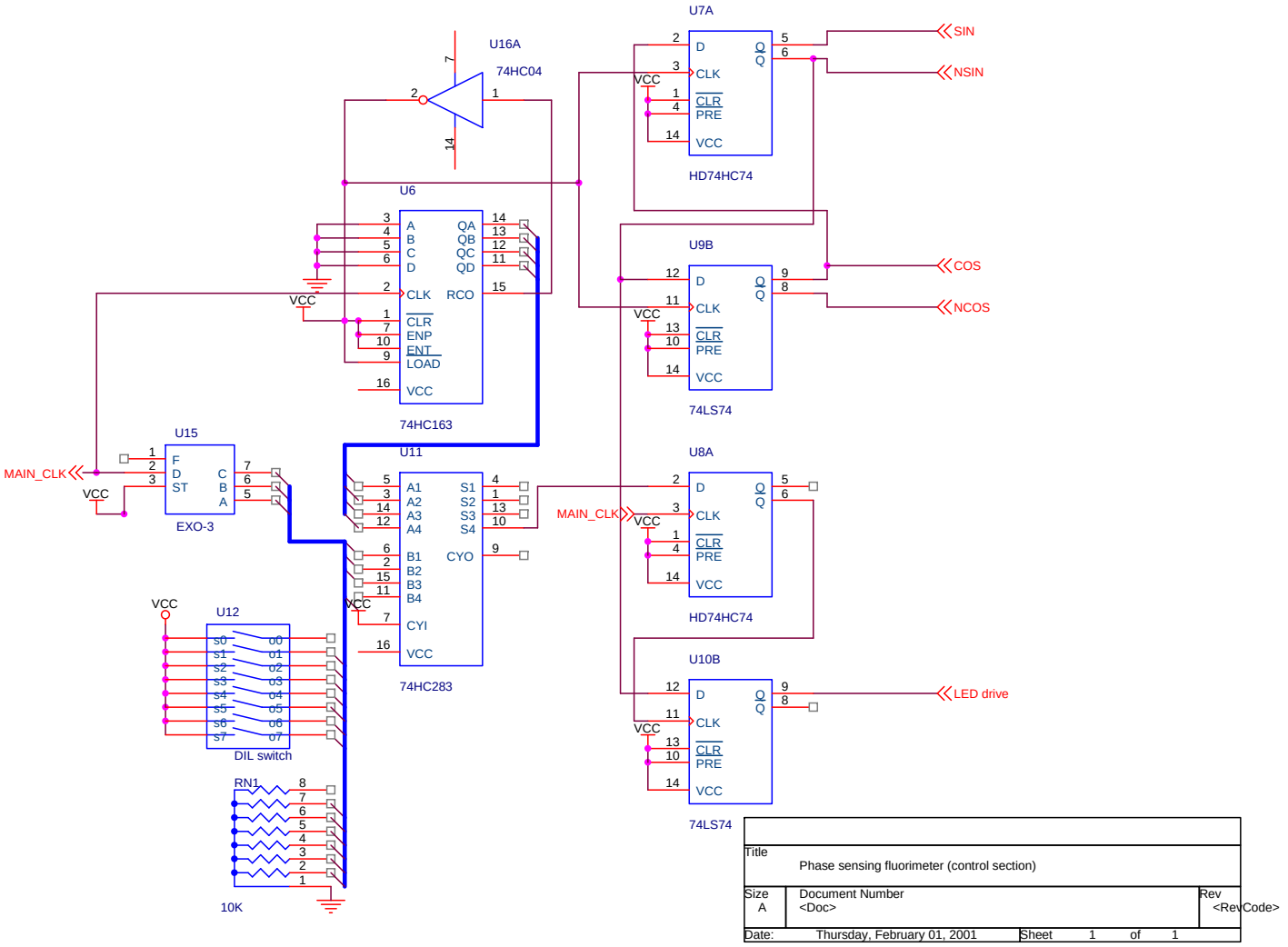

Figure 7.9 phase-delay discriminating fluorescence lifetime interrogator circuit diagram (digital section)

7.4. Optimisation of exponential measurements using the RLD method – Mathcad sheet

In this section, the optimisation programme written in Mathsoft Mathcad 2001 for identifying optimal conditions for exponential measurements is presented. The same general function was re-written in C++ for faster computation, then extended to optimisation of the oxygen measurement case.

Optimised interrogation of mono-exponential decays using the generalised RLD sensing scheme

First define global variables:

$torr\_range := 2, 2.1 .. 5$ for graph display $nfactor := 0$ initially no background $I\_sat := 1$ intensity term in Mcps $\tau\_global := 3$ lifetime (microseconds)

First define the returning fluroescence function from an individual flash (t_off is flash duration, torr is lifetime, t is current time)

$$I\_1(t, t\_off, \tau) := I\_sat \cdot \tau \cdot \left(1 - e^{\frac{-t\_off}{\tau}}\right) \cdot e^{\frac{-(t - t\_off)}{\tau}}$$

Now define the function **I**, which is the overall fluorescence intensity function seen, taking into account the contributions from four previous flashes (t_rep is the overall repeition time)

$$I(t, t\_off, \tau, t\_rep) := I\_1(t, t\_off, \tau) + I\_1(t + t\_rep, t\_off, \tau) + I\_1(t + 2t\_rep, t\_off, \tau) \ldots$$
$$+ I\_1(t + 3t\_rep, t\_off, \tau) + I\_1(t + 4 \cdot t\_rep, t\_off, \tau)$$

Now graph the single flash result, and the repetition result

$t\_range := 0 .. 10$

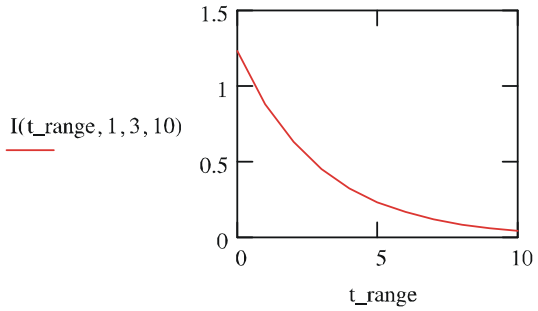

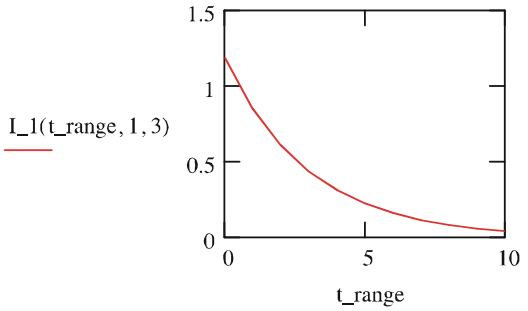

Now define the functions C_ab and C_cd, which accumulate the intensity arriving in the two time windows.

$$C\_ab(t\_1, t\_2, t\_off, \tau, t\_rep) := \int_{t\_1}^{t\_2} I(t, t\_off, \tau, t\_rep)\, dt \qquad C\_cd(t\_3, t\_4, t\_off, \tau, t\_rep) := \int_{t\_3}^{t\_4} I(t, t\_off, \tau, t\_rep)\, dt$$

now write the count values measured Cm_ab and Cm_cd (i.e. the ideal C_ab and C_cd plus the background light contribution.

$$Cm\_ab(t\_1, t\_2, t\_3, t\_4, t\_off, \tau, t\_rep) := C\_ab(t\_1, t\_2, t\_off, \tau, t\_rep) + (t\_2 - t\_1) \cdot nfactor$$

$$Cm\_cd(t\_1, t\_2, t\_3, t\_4, t\_off, \tau, t\_rep) := C\_cd(t\_3, t\_4, t\_off, \tau, t\_rep) + (t\_4 - t\_3) \cdot nfactor$$

Now write down the ratio of counts calculated in the computer, which takes away the background counts.

$$r(t\_1, t\_2, t\_3, t\_4, t\_off, \tau, t\_rep) := \frac{C\_ab(t\_1, t\_2, t\_off, \tau, t\_rep)}{C\_cd(t\_3, t\_4, t\_off, \tau, t\_rep)}$$

now calculate the expected noise in r

$$noiser(t\_1, t\_2, t\_3, t\_4, t\_off, \tau, t\_rep) := \sqrt{\frac{r(t\_1, t\_2, t\_3, t\_4, t\_off, \tau, t\_rep) \cdot (1 + r(t\_1, t\_2, t\_3, t\_4, t\_off, \tau, t\_rep))}{Cm\_cd(t\_1, t\_2, t\_3, t\_4, t\_off, \tau, t\_rep)}}$$

we have the noise in r, noiser, and we have r as a function of τ, so to find the noise in τ, we must multiply the noise in r by the dependence of τ on a small change in r (remembering the noise must be positive)

$$\text{noisetorr}(t\_1, t\_2, t\_3, t\_4, t\_off, \tau, t\_rep) := \sqrt{\left[\left(\frac{d}{d\tau} r(t\_1, t\_2, t\_3, t\_4, t\_off, \tau, t\_rep)\right)^{-1} \cdot \text{noiser}(t\_1, t\_2, t\_3, t\_4, t\_off, \tau, t\_rep)\right]^2}$$

now we have the uncertainty of measurement of torr, we need to account for the time it took to make that measurement of torr, (remembering that we are working in microseconds):

$$\text{noiset\_torr}(t\_1, t\_2, t\_3, t\_4, t\_off, \tau, t\_rep) := \frac{\sqrt{t\_rep} \cdot \text{noisetorr}(t\_1, t\_2, t\_3, t\_4, t\_off, \tau, t\_rep)}{1000}$$

and now converting the noise to a proportion of the measured torr value (signal to noise measurement of torr)

$$\text{SN\_t\_torr}(t\_1, t\_2, t\_3, t\_4, t\_off, \tau, t\_rep) := \frac{\tau}{\text{noiset\_torr}(t\_1, t\_2, t\_3, t\_4, t\_off, \tau, t\_rep)}$$

$$\text{SN\_t\_storr}(t\_1, t\_2, t\_3, t\_4, t\_off, t\_rep) := \text{SN\_t\_torr}(t\_1, t\_2, t\_3, t\_4, t\_off, \tau\_global, t\_rep)$$

before we can maximise this, need to specify initial values (in microseconds)

$t\_1 := 1$ $t\_2 := 2$ $t\_3 := 3$ $t\_4 := 5$ $t\_rep := 5$ $t\_off := 1$

and constraints

Given

$t\_off \le t\_1$

$t\_off > 0$

$t\_2 > t\_1$

$t\_3 \ge t\_1$

$t\_4 > t\_3$

$t\_rep \ge t\_4$

and finally perform maximisation

$max\_o := \text{Maximize}(SN\_t\_storr, t\_1, t\_2, t\_3, t\_4, t\_off, t\_rep)$

$$max\_o = \begin{pmatrix} 6.057 \\ 7.793 \\ 11.218 \\ 19.769 \\ 6.057 \\ 19.769 \end{pmatrix}$$

is the optimum point

$SN\_t\_storr\left(max\_o_0, max\_o_1, max\_o_2, max\_o_3, max\_o_4, max\_o_5\right) = 501.306$

is the optimum SNR